STUDY AND EVALUATION OF POLYANILINE–REDUCED GRAPHENE OXIDE COMPOSITES AND POROUS CARBON ELECTRODE MATERIALS FOR SUPERCAPACITORS

THESIS
SUBMITTED IN PARTIAL FULFILMENT OF THE
REQUIREMENTS FOR THE AWARD OF THE DEGREE OF

DOCTOR OF PHILOSOPHY

IN

PHYSICS

BY

MACHERLA NAGARAJU

[ROLL NO: 716187]

UNDER THE SUPERVISION OF

PROF. L. RAM GOPAL REDDY & Dr. KUSUM KUMARI

DEPARTMENT OF PHYSICS
NATIONAL INSTITUTE OF TECHNOLOGY
WARANGAL-506004, TELANGANA, INDIA
JULY-2022

DEDICATED TO

MY PARENTS & TEACHERS

NATIONAL INSTITUTE OF TECHNOLOGY
WARANGAL - 506004, TELANGANA, INDIA

APPROVAL SHEET

This thesis entitled **"Study and Evaluation of Polyaniline–Reduced Graphene Oxide Composites and Porous Carbon Electrode Materials for Supercapacitors"** by **Mr. MACHERLA NAGARAJU** (Roll No.: 716187) is approved for the degree of **Doctor of Philosophy**.

Ayan Roy Chaudhuri
Dr. Ayan Roy Chaudhuri
(External Examiner)
Associate Professor,
Materials Science Centre,
IIT Kharagpur-721302, INDIA

Prof. L. Ram Gopal Reddy
(Research supervisor)
Professor,
Department of Physics,
NIT Warangal.

Kusum
Dr. Kusum Kumari
(Research supervisor)
Assistant Professor,
Department of Physics,
NIT Warangal.

Dr. T Venkatappa Rao
(Chairman & Head)
Associate Professor,
Department of Physics,
NIT Warangal.

Date: 18/07/2022.

DECLARATION

This is to certify that the work presented in the thesis entitled “**STUDY AND EVALUATION OF POLYANILINE–REDUCED GRAPHENE OXIDE COMPOSITES AND POROUS CARBON ELECTRODE MATERIALS FOR SUPERCAPACITORS**” is a bonafide work done by me under the supervision of Prof. L. Ram Gopal Reddy and Dr. Kusum Kumari, and was not submitted elsewhere for the award of any degree.

I declare that this written submission represents my ideas in my own words and where others' ideas or words have been included, I have adequately cited and referenced the original sources. I also declare that I have adhered to all principles of academic honesty and integrity and have not misrepresented or fabricated or falsified any idea/data/fact/source in my submission. I understand that any violation of the above will be a cause for disciplinary action by the Institute and can also evoke penal action from the sources which have thus not been properly cited or from whom proper permission has not been taken when needed.

Macherla Nagaraju

(Roll No. 716187)

Date:18-07-2022.

CERTIFICATE

This is to certify that the work presented in the thesis entitled “**STUDY AND EVALUATION OF POLYANILINE–REDUCED GRAPHENE OXIDE COMPOSITES AND POROUS CARBON ELECTRODE MATERIALS FOR SUPERCAPACITORS**” is a bonafide work carried out by **Mr. Macherla Nagaraju (Roll No. 716187)** under our supervision and was not submitted elsewhere for the award of any degree.

Prof. L. RAM GOPAL REDDY
Research supervisor
Professor,
Department of Physics,
National Institute of Technology,
Warangal.

Dr. KUSUM KUMARI
Research supervisor
Assistant Professor,
Department of Physics,
National Institute of Technology,
Warangal.

Date:18-07-2022.

ACKNOWLEDGEMENT

First and foremost, I'd like to express my gratitude to the Almighty for providing me with this opportunity, strength, and good health to complete all of my research work without difficulty.

I express my heartfelt gratitude to my supervisors, Prof. L. Ram Gopal Reddy, professor, and Dr. Kusum Kumari, Assistant professor, Department of Physics, National Institute of Technology Warangal, for their guidance, unrelenting support, and motivation, which encouraged me to progress and complete my Ph.D. Their valuable advice and conversations always helped me to focus and achieve the purpose of this study.

I thank Prof. N. V. Ramana Rao, Director, NITW for allowing me to pursue my Ph. D in this reputed institute.

I also thank Prof. D. Dinakar, Head, Department of Physics, NITW for providing the necessary support during my Ph. D tenure. I would also like to take this opportunity to express my gratitude to the former heads of the Department of Physics at NITW for their invaluable assistance and support.

I ought to show my thankfulness to my Doctoral Scrutiny Committee members, Prof. K. V. Gobi, Department of Chemistry, and Prof. K. Venugopal Reddy, Department of Physics, Prof. D. Dinakar, Department of Physics, NITW, for their insightful comments and suggestions that aided the progress of my Ph. D work.

I am thankful to farmer faculty members of our department, Prof. S.V.S. Ramana Reddy, Prof. Sai Sankar, and Prof. R. L. N. Sai Prasad, for their encouragement and support.

I extend my sincere gratitude to the faculty members, Prof. K. Venu Gopal Reddy, Dr. B. Sobha, Dr. T. Venkatappa Rao, Dr. P. Abdul Azeem, Dr. P. Syam Prasad, Dr. Sourabh Roy, Dr. Thangaraju, Dr. D Haranath, Dr. D. Paul Joseph, Dr. V. Jayalakshmi, Dr. R. Rakesh Kumar, Dr. K. Uday Kumar, Dr. Vijay Kumar, Dr. Surya K. Ghosh, Dr. Hitesh Borkar, Dr. Aalu Boda, Department of Physics, National Institute of Technology, Warangal for their valuable advice, encouragement and moral support in my career.

I especially thank Dr. Kuldeep Singh Kakran, Senior Scientist, CSIR - Central Electrochemical Research Institute (CSIR CECRI), for his guidance, support, and motivation throughout my Ph. D thesis work. His extensive research ideologies have always inspired me to approach a scientific problem in a significant and simple manner.

This thesis work was supported by Empowerment and Equity Opportunities for Excellence in Science program, Science and Engineering Research Board, Department of

Science & Technology, Government of India (project no. EEQ/2016/000723), and Technology Mission Division, Department of Science & Technology, Government of India (project no. DST/TMD/SERI/S56(C)). I express my sincere thanks to MHRD, New Delhi for the financial support in the form of fellowship.

I am very much thankful to Dr. Satyender Singh, Associate professor, JNU I thank the Head, UGC-NRC, School of Physics, the University of Hyderabad for allowing me to utilize the FESEM facility.

I would also like to extend my sincere thanks to Head of Materials and Metallurgical engineering, Dr. Bontha Srinivasa Rao, and Dr. Rangadhara Chary, for extending their help to carryout electrochemical studies.

I am also indebted to the following friends and research colleagues for various reasons related to my Ph. D work, all of whom deserve special mention: Dr. Rajkumar, Dr. T Ramesh, Dr. Himamahesh, Dr. Ashish Kumar, Dr. PVN Kishore, Dr. P Kishore, Dr. Harikrishna, Dr. Mohan Babu, Dr. Ramarajan, Dr. N. Purushotham Reddy, Dr. Lalsingh guguloth, Mrs. N Manjula, Mr. Gnyaneshwar Dasi, Mr. B Ramesh, Ms. Mahalakshmi, Mrs. Madhurima, Mrs. Ramadevi, Ms. T Lavanya, Mr. Akshay Kranth, Mr. G. Buchaiah, Mr. R. Muniramaiah, Mrs. P Prasad, and Mr. Rohit.

I also express my thankfulness to all other present and past research scholars of Department of Physics NITW and all the teaching and non-teaching staff of the Dept. of Physics for their constant support during my Ph.D.

I express my special thanks to Dr. Banty Rani from Kakatiya University, who motivated me to study Ph.D. I extend my sincere thanks to the senior research scholars, Dr. Chandarrao and Dr. Ravinder from Kakatiya University Warangal, for their suggestion and encouragement to pursue Ph.D in this institute.

I take this opportunity to show my deepest gratitude to my gurus from my schooling to till today for not only educating me and also made me strong enough to face the challenges encountered during my entire life.

I am infinitely indebted to my loving parents Mrs. M. Bhagya and Mr. M. Rajaswamy, without their motivation I would not have been what I am. Their unconditional love and affection always inspired me to achieve my goals and gave strength and confidence to complete impossible tasks more than my strength, including my Ph.D. I always remember and cherish the encouragement and inspiration provided by my mother and father during the course of my research work.

I would like to thank my sister, Mrs. Navatha, and brother-in-law, Mr. Shekar, for their moral support. Special thanks to my nephew and niece, Mr. Suprith, Miss. Sahasra for making me happy, relax and feel fresh all the time to pursue my research work with full of confidence.

Finally, I'd like to express my deepest gratitude to my soul mate Mrs. Manjula for her constant support, healthy discussions about the research problem, and for lifting my confidence with her motivational words and lots of love to my baby daughter Miss. Jaisvi, who recently arrived in our life.

MACHERLA NAGARAJU

Date: 18/07/2022.

ABSTRACT

Energy storage has become one of the primary requirements in our day-to-day lives. Increased energy consumption, depletion of fossil fuels, and increased pollution have sparked a surge in interest in electrochemical energy storage devices (EESs). Batteries, fuel cells, and supercapacitors are examples of EES systems that are emerging as promising contenders for efficient energy storage. Supercapacitor (SC) is one of the EES system that converts the chemical energy into electrical energy and vice versa. However, the energy density of SCs is well below 50 W h/kg, which is a major issue that needs to be addressed to compete with the other energy storage systems such as Li-ion batteries. The energy density of SCs can be enhanced either by increasing specific capacitance or operating voltage of SC. The specific capacitance is mainly depending on the properties of the electrode materials. Significant research works have been conducted on various kinds of electrode materials to enhance the specific capacitance. In this direction, conducting polymers (CPs) have been showing promising electrochemical properties by storing the energy via pseudocapacitive nature. Significant research is being conducted over the years to enhance the energy density and cyclic stability using various CPs as electrode materials.

Polyaniline (PANI), a conducting polymer, is believed to be a potential pseudocapacitive material to utilize as electrode material owing to its distinctive properties. The electrochemical performance of PANI electrode materials has been showing an increasing trend over the years. However, structural degradation is been the main drawback for PANI which restricts its practical application. To address these draw backs, research has been focused on the development of composites comprising carbon materials with PANI. These combined composite materials offering not only enhanced specific capacitance but also enhanced cyclic stability. The state-of-the-art specific capacitance of supercapacitors made of PANI/carbon composite materials is approximately 500 F/g in a two-electrode system. However, along with high specific capacitance and cyclic stability, the production cost is also extremely important for their commercial applications. Accordingly, international R & D efforts have been devoted to the development of binary composites, with proper selection of composite materials with easy and economically viable synthesis methods. So far different combinations of PANI-carbon composites such as PANI-activate carbon, PANI-carbon nanotubes, PANI-graphene, etc., have been studied. Among the various carbon materials, graphene is a 2D layered structure material having advantages like high electrical conductivity, excellent

chemical stability, high mechanical strength, lightweight, and flexibility. However, the synthesis of graphene in its pure form and bulk production are extremely important to use in commercial applications. Chemical reduction of graphene oxide (GO) is a promising approach for the bulk production of reduced graphene oxide (rGO). In addition, rGO is a suitable candidate to composite with PANI to improve the chemical stability and electrochemical performance of electrode materials. However, the presence of residual oxygen functional groups and stacked graphene layers in rGO decreases the conductivity and surface area accessible for electrolyte ions. Meanwhile, heteroatom doping in graphene networks is an effective strategy to overcome the drawbacks and improve the characteristics of rGO. In this direction, there is a wide scope for enhancing the electrochemical properties of PANI using graphene-based materials. Hence, the present work is focused on preparing PANI composite materials using simple synthesis methods. The present thesis provides a detailed study of the effect of synthesis process on the material's properties as well as the electrochemical performance when it is used in a supercapacitor. In addition, it also explains the interaction between the carbon 2D materials with PANI and how the incorporated materials have significantly improved their performance.

The thesis is comprised of synthesis of 2D materials such as GO, rGO, and heteroatom (Nitrogen & Sulfur) doped rGO [N-rGO & S-rGO]. Further, these 2D materials were successfully incorporated into PANI for enhancing the electrochemical properties of the composites. Here, the composite materials, namely, PANI/rGO, PANI/N-rGO, and PANI/S-rGO have been synthesized via a simple *in-situ* chemical polymerization method, and optimized for achieving improved electrochemical properties. Subsequently symmetric supercapacitor cells were assembled using PANI composite electrode materials, and their electrochemical performances were examined using different techniques. All these composites have shown enhanced performances compared to their counterparts. PANI/rGO composite with 2 wt.% of GO based electrode material has delivered maximum specific capacitance of 299 F/g at a current density of 0.5 A/g. Besides, this composite has shown good rate capability and capacitance retention (88%) at a current density of 2 A/g after 2000 charge-discharge cycles. An improved specific capacitance is achieved for the PANI/N-rGO composite compared to PANI/rGO. For PANI/N-rGO, a maximum specific capacitance of 322 F/g at 1 A/g is achieved. Further, it has been found that PANI/S-rGO composite with 10 wt.% of S-rGO, has shown the best and enhanced specific capacitance of 348 F/g at 1 A/g with better cyclic stability (~89% capacitance retention after 2500 cycles) among all other composite materials.

In addition, porous carbons prepared from biomass/biowaste have attracted a lot of research attention over the years because of their low cost, natural abundance, renewable nature, and importance in "waste to wealth" applications. The type of precursor material, activation process, and activation conditions play major roles in determining the properties of the resulting porous carbons including porosity, pore-size distribution, surface area, and surface chemistry. In this direction, in this thesis, utilization of nature's abundant biowaste of corn husk as raw material for the preparation of porous carbons has been presented. The effect of activation temperature on the specific surface area and pore structure of the resultant carbons is studied. Along with the high specific surface area, abundant micro and mesoporosity are achieved for the corn husk derived porous carbon (CHPC) activated at 800 ^{o}C (CHPC-800). CHPC-800 electrode material has delivered a maximum specific capacitance of 133 F/g at a current density of 1 A/g. Further, CHPC-800 also showed good cyclic stability, with 93% of capacitance retention after 4500 cycles.

This thesis presents simple synthesis methods for designing efficient PANI composite electrode materials for supercapacitors, which are very promising for practical application in the energy storage field.

TABLE OF CONTENTS

LIST OF ABBREVIATIONS & SYMBOLS

ABBEVIATION	DESCRIPTION
EESs	Electrochemical Energy Storage Systems
SCs	Supercapacitors
FSCs	Flexible Supercapacitors
EDLCs	Electrical Double Layer Capacitors
IHP	Inner Helmholtz Layer
OHP	Outer Helmholtz Layer
PSCs	Pseudocapacitors
HSCs	Hybrid Supercapacitors
CPs	Conducting Polymers
TMO	Transition Metal Oxide
1D	One Dimensional
2D	Two Dimensional
3D	Three Dimensional
NFs	Nanofibers
NRs	Nanorods
NSs	Nanosheets
AC	Activated Carbon
CNFs	Carbon Nanofibers
CNTs	Carbon Nanotubes
GN	Graphene
PC	Porous Carbon
PANI	Polyaniline
An	Aniline
PPy	Polypyrrole
PAN	Polyacrylonitrile
PVA	Polyvinyl alcohol
PMMA	Polymethylmethacrylate
PI	Polyimide
PVP	Polyvinylpyrrolidone
GO	Graphene Oxide
cGO	crumbled Graphene Oxide
rGO	reduced Graphene Oxide

rcGO	reduced crumbled Graphene Oxide
N-rGO	Nitrogen-doped reduced Graphene Oxide
S-rGO	Sulphur-doped reduced Graphene Oxide
CH	Corn Husk
CHBC	Corn Husk Biochar
CHPC	Corn Husk Porous Carbon
PRGO	Polyaniline/reduced crumbled Graphene Oxide
PANI/rGO	Polyaniline/reduced Graphene Oxide
PANI/rGO	Polyaniline-/N-doped reduced Graphene Oxide
SPANI	Naphthalene sulfonic acid doped Polyaniline
SPANI/S-rGO	Naphthalene sulfonic acid doped Polyaniline/S- doped reduced Graphene Oxide
XRD	X-Ray Diffraction
FESEM	Field Emission Scanning Electron Microscopy
HRTEM	High Resolution Transmission Electron Microscopy
FTIR	Fourier Transform Infrared Spectroscopy
Raman	Raman spectroscopy
XPS	X-Ray Photoelectron Spectroscopy
B.E.	Binding Energy
K.E.	Kinetic energy
TGA	Thermogravimetry analysis
CV	Cyclic Voltammetry
GCD	Galvanostatic Charge-Discharge
EIS	Electrochemical Impedance Spectroscopy
C_{cell}	Total capacitance of a cell
A	Surface area
ε_o	Permittivity of free space
ε_r	Relative permittivity of electrolyte
C_{dl}	Double-layer capacitance
C_H	Stern layer capacitance

C_{diff}	Diffusion layer capacitance
C_{sp}	Specific Capacitance
E_m	Specific Energy
P_m	Specific Power
R_s	Equivalent Series Resistance
R_{ct}	Charge Transfer Resistance
λ	X-ray wavelength
ϕ	Work function
υ	Frequency
h	Plank constant
BET	Brunauer-Emmett-Teller
DFT	Density Functional Theory
BJH	Barret-Joyner-Halenda
P/P_o	Relative pressure
S_{tot}	specific surface area
S_{mic}	micropore surface area
S_{meso}	Mesopore surface area
V_t	Total pore volume
V_{mic}	micropore volume
s	scan rate
m	Mass of the electrode
ΔV	Voltage window
Δt	Discharge time
I	Current
mg	Milli gram
mL	Milli liter
L	Liter
DI	Deionized
M	Molarity
kg	kilogram
cm	centimeter
g	gram
CO_2	Carbon Dioxide
H_2SO_4	Sulfuric acid
Na_2SO_4	Sodium sulphate

NaOH	Sodium Hydroxide
KOH	Potassium Hydroxide
KCl	Potassium Chloride
HCl	Hydrochloric Acid
H_2O_2	Hydrogen Peroxide
RuO_2	Ruthenium Oixde
MnO_2	Manganese Oxide
Fe_2O_3	Iron Oxide
$Ni(OH)_2$	Nickel Hydroxide
SnO_2	Tin Oxide
ZnO	Zinc Oxide
ZnS	Zinc Sulfide
V_2O_5	Vanadium Pentoxide
NiO	Nickel oxide
$NaBH_4$	Sodium borohydride
CB	Carbon Black
PTFE	Polytetrafluoroethylene

LIST OF FIGURES

CHAPTER 1

CHAPTER 2

CHAPTER 3

CHAPTER 4

CHAPTER 5

CHAPTER 6

LIST OF TABLES

CHAPTER 1

CHAPTER 2

CHAPTER 3

CHAPTER 4

CHAPTER 5

CHAPTER 6

CHAPTER 7

CHAPTER 1

INTRODUCTION

1.1 Energy and its environmental challenges

The use of electrical energy storage systems (EESs) is drastically increasing with the innovations in electronic gadgets, the internet of things, and the automobile industry. The future technology is heading towards green, efficient, and portable EESs to make world clean by eliminating fossil fuels and other environment polluting resources. However, the statistical review of world energy 2020 showed that the 84% of global energy is generated from fossil fuels including Oil, Natural gas, and Coal [1]. The world energy intake is expected to be doubled by the middle and tripled by the end of the century [2]. The consumption of fossil fuels releases CO_2 and other hazardous greenhouse gasses. Particularly, the CO_2 emission from fossil fuels is showing an increasing trend over the years and global energy-related CO_2 emission reached 31.5 Gt in 2020. The CO_2 and other hazardous greenhouse gasses increase environmental pollution, cause unexpected climate changes, and spoil human health [3]. Therefore, it is necessary to reduce the use of fossil fuels to control the damage done by them.

The production of renewable energy is a better alternative to declining the use of fossil fuels. Renewable energy can be produced from natural resources (solar energy, wind energy, hydro energy, tidal energy, etc.) and is less harmful to the environment. However, uninterrupted driving forces are required for the production of electrical energy which is limited and not available all the time. In addition, the energy storage requirements are different in different places. Sometimes, we need to store the energy and utilize it as a continuous power supply in some places where ever required. Therefore, the energy generated from renewable resources has to be effectively stored for future usage. Hence the search for clean and efficient electrochemical energy storage systems (EES).

In EES, innovations have to come in such a way that they should provide high energy density, high power density, longer life, environment-friendly operation, easy maintenance, etc. From Figure 1.1, Ragone plot presents the state of art characteristics of different EES systems. Batteries and Fuel cells are capable to store more energy and have greater energy density. Li-ion batteries are known for their high energy density, but they also have a low power density and cycle life. Moreover, Li sources are also limited around the globe and they will become more costly in the nearby future. In contrast, a conventional capacitor provides high power output. On the other hand, supercapacitors (SCs) have been emerging as a future energy storage device owing to their fast charge and discharge capability, high power density, and longer cycle life. In terms of energy and power density characteristics, SCs lie in between Batteries and Capacitors as shown in Figure 1.1. SCs can be a potential candidate to fulfil the gap between batteries and conventional capacitors. SCs can offer several orders of magnitude higher energy density than a conventional capacitor. Significant research has been carried out recently to further enhance its energy density without affecting its power density.

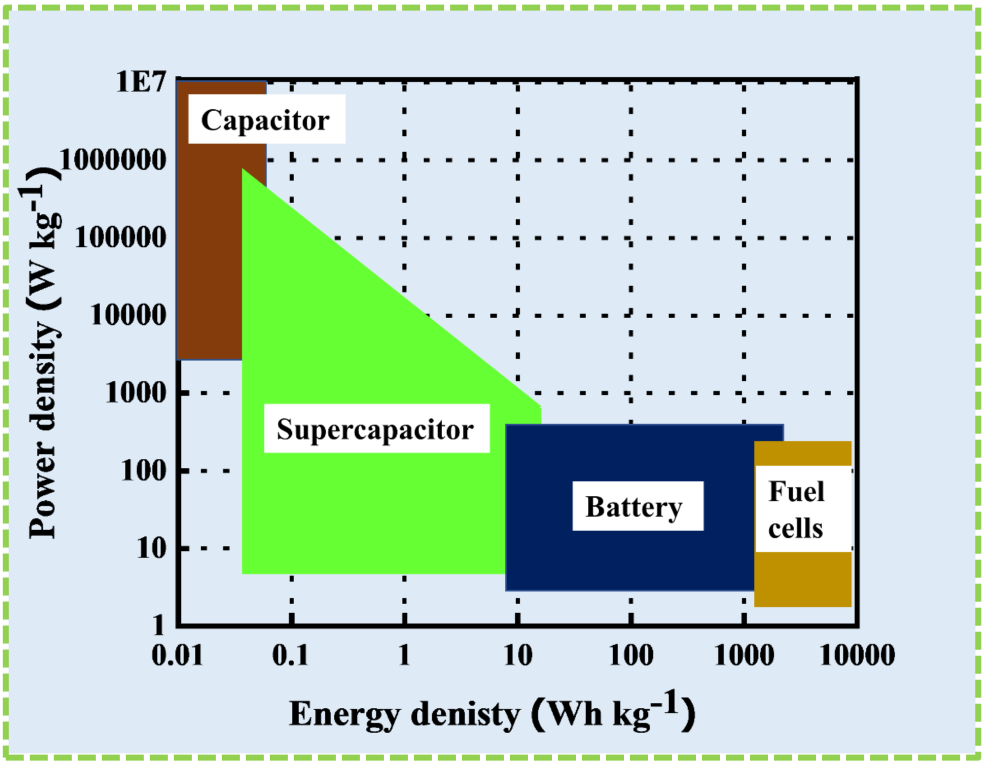

Figure 1.1 Ragone plot presents the energy and power characteristics of various EESs.

1.2 Supercapacitor

The name “Supercapacitor or Ultracapacitor” is used because of its ability to store and deliver a high capacitance usually in farads. Even though the concept of charge storage in supercapacitor in double-layer form is introduced in 19th century by von Helmholtz in his pioneer work on colloidal suspension. But it was first demonstrated practically in early 1950s by the General electric engineers’ group based on their work on porous carbon electrodes and patented by H.I. Becker of General Electric in 1957 [4]. They found a high capacitance value based on the charge adsorption at the pores of carbon materials. Later, in 1966, a research team of standard oil of Ohio observed the similar phenomena of charge storage while they designed a fuel cell using two layers of activated charcoal which are isolated electrically by an insulating paper. Finally, in 1978, NEC named a supercapacitor based on the EDLC behaviour, and they used it in power backup for computer maintenance [5]. Since the early 1990s, research on SCs has exploded to better understand how they might be used in various applications.

Generally, SCs are comprised of two working electrodes, electrolyte solution, ion-permeable, and electrically resistive separator and current collectors. The basic schematic of a supercapacitor is given in Figure 1.2. The charge storage of the supercapacitor is governed by a similar basic principle as a conventional capacitor. SC gets completely charged by the accumulation of charges at electrolyte/electrode interface. The electrolyte ions get adsorbed onto the surface of electrodes with opposite charges, i.e., anions from electrolyte, move toward the cathode (negative electrode) and cations attract to anode (positive electrode) while discharging these charges desorb and relieve from the interface. Different type of charge storage processes is observed in different types of electrode materials and electrolytes used. The next section provides a general classification of supercapacitors based on their charge storing mechanism.

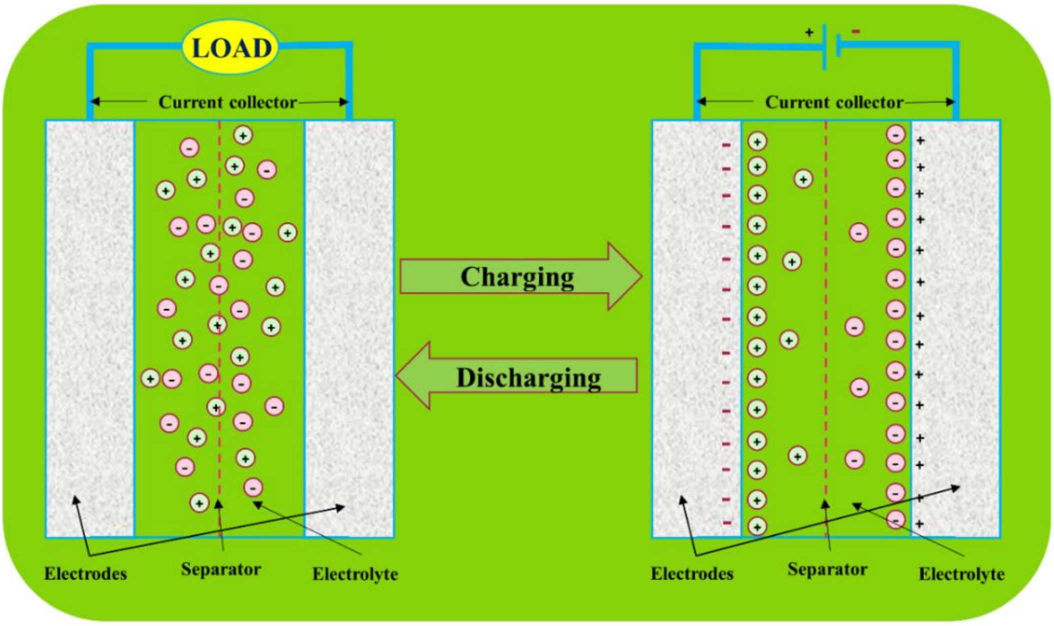

Figure 1.2 Basic supercapacitor design and working principle.

SCs are divided into three categories based on the charge storage phenomenon and electrode materials used: electrical double-layer capacitors (EDLCs), pseudocapacitors (PCs), and hybrid supercapacitors (HSCs).

1.2.1 Electrical Double Layer Capacitors (EDLCs)

In EDLCs, charge storage is occurred by the physical adsorption of charges which is purely electrostatic. Opposite charge layers formation has occurred at the interface of electrode and electrolyte with an atomic size distance; hence it is called an electrical double-layer capacitor (Figure 1.3). In EDLCs, the energy storage does not involve any charge transfer reaction. It mainly works on the principle of electrostatic adsorption of opposite charges. When an external potential is applied, in the vicinity of electrode and electrolyte solution, a thin layer of charges (electrons or holes) appeared at the electrode surface and the opposite charge cations/anions are get accumulate in the vicinity of electrode surface from the electrolyte solution. The formation of arrays of opposite charges at the one electrode represents a capacitor and the EDL capacitance at one electrode can be obtained by the following equation:

$$C = \varepsilon_r \varepsilon_o \frac{A}{d} \qquad (1.1)$$

Where A is surface area, d is the distance from electrode surface to the center of adsorbed ions and, ε_o is permittivity of free space; ε_r is relative permittivity of electrolyte [6].

The EDL formation happened simultaneously on both electrodes for a complete cell which resembles two capacitors connected in series. hence the total capacitance of a cell (C_{cell}) can be assessed by using the equation:

$$\frac{1}{C_{cell}} = \frac{1}{C_1} + \frac{1}{C_2} \qquad (1.2)$$

Where C_1 and C_2 are the capacitance of two individual electrodes. Unlike traditional supercapacitors, capacitance of EDLCs depends on the applied potential because charge balance does not happen exactly at the electrode-electrolyte interface. The ionic charge layer is diffused into the electrolyte. Various models have been proposed to understand the storage mechanism in EDLCs, as shown in Figure 1.4.

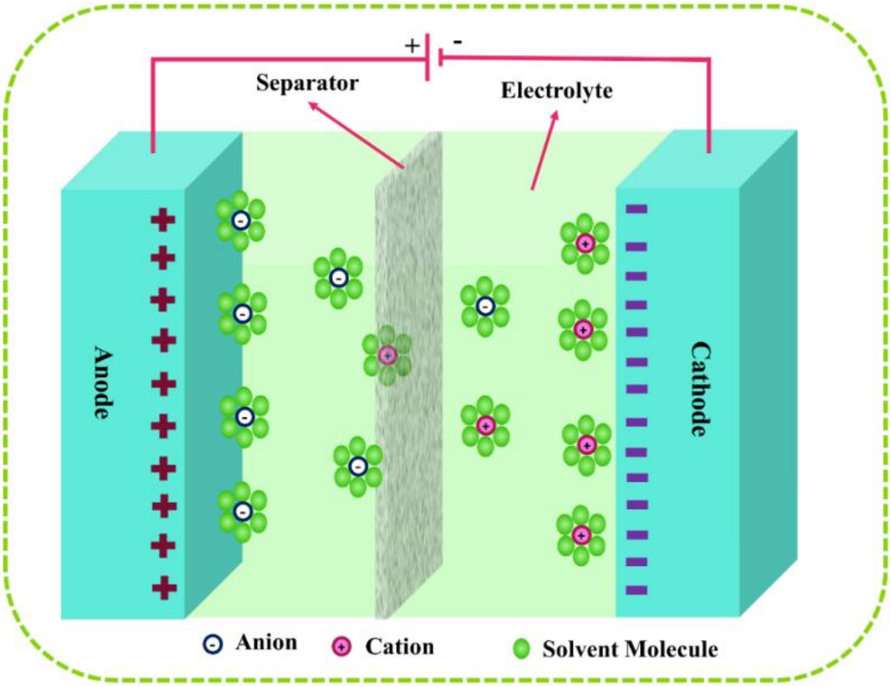

Figure 1.3 Schematic representation of EDLC.

The origin of double-layer charge storage phenomenon is first realized by von Helmholtz in the nineteenth century [7]. According to Helmholtz's double-layer model, when porous electrodes materials are dipped into an electrolyte, formation of double layers of opposite charges occurs at the interface, which he called Helmholtz layers. Helmholtz's model explains the charge storage is same as a conventional capacitor. The charge balance occurs at a distance of d from the surface of electrode as given in Figure 1.4. The amount of charge adsorbed at the interface is directly proportional to the applied voltage ($\Psi = \Psi_o$). Later, Gouy and Chapman modified the Helmholtz model and named it as diffuse layer model [8–10]. In Gouy and Chapman's model, the static adsorbed layer of electrolyte ions is modified into a diffuse layer. This model stated that the ions in the electrolyte cannot adsorb specifically instead these ions (cations and anions) diffuse into the electrolyte due to thermal motion. Finally, Stern introduced a new model that incorporates both Helmholtz and Gouy-Chapman models. The stern model explains the formation of static adsorbed layer and diffuse layer. He proposed the existence of the Helmholtz layer and diffuse layer in two different regions as shown in Figure 1.4. Helmholtz layers were formed at the interface which he represented as stern region where the specifically adsorbed ions represented as inner Helmholtz layer (IHP) and non-specifically adsorbed counter ions as outer Helmholtz layer (OHP). Some of the non-specifically adsorbed ions diffuse into the electrolyte solution due to the thermal agitation of electrolyte solution, which is referred to as diffuse layer. The total double-layer capacitance (C_{dl}) can be the series capacitance of stern layer capacitance (C_H) and diffusion layer capacitance (C_{diff}).

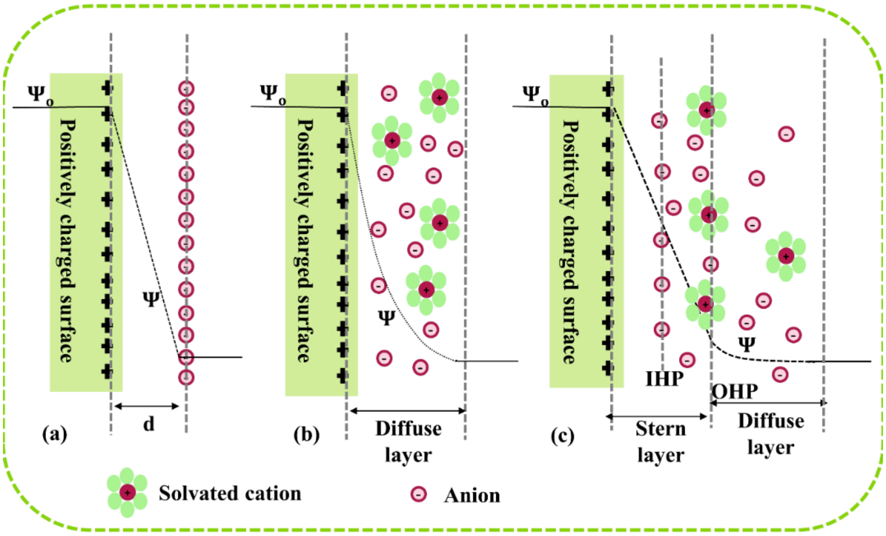

Figure 1.4 EDLC Models (a) Helmholtz model, (b) Gouy-Chapman model, and (c) Stern model.

EDLCs offer rapid charge-discharge, due to physical adsorption of charges at the interface. EDLCs have a much high power density and cycle life of over 100,000 cycles than batteries [11]. Carbon compounds have been the most widely utilised electrode materials in EDLCs for many years. The performance of EDLCs is primarily determined by their surface area, electrical conductivity, and porosity of carbon materials.

1.2.2 Pseudocapacitors (PCs)

In PCs, charge storage is governed by a rapid and reversible redox process that takes place between surface, near-surface of electrodes, and specifically adsorbed electrolyte ions. The mechanism of charge storage is not electrostatic in origin as EDLCs. The basic charging process of PCs is shown in Figure 1.5. Three basic types of charge storage mechanisms that occur in PCs are namely underpotential deposition, redox reaction, and intercalation process. PCs deliver high specific capacitance compared to EDLCs as the electrolyte ions undergo a charge transfer process. Pseudocapactiance arises under a special thermodynamic state where the change in charge (dq) is directly proportional to the change in electrode potential (dV). Hence the capacitance of PCs can be written as C= (dq/dV) [12]. However, the charge transfer kinetics of PCs are slower than EDLCs which limits the power capabilities. Metal oxides/hydroxides, metal sulphides/selenides and conducting polymers are the most commonly studied electrode materials for PCs.

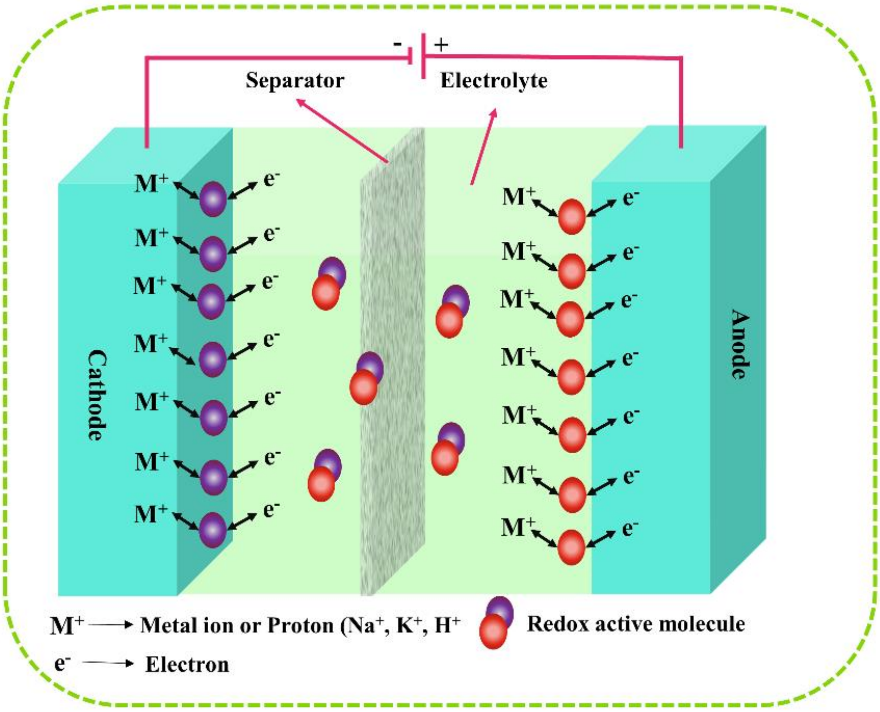

Figure 1.5 Schematic of Pseudocapacitor.

Conducting polymers are the extensively studied electrode material for PCs. The most commonly used CPs include polypyrrole, polyaniline, and polythiophene. The pseudocapacitance that arises in CPs is due to charge transfer between polymer chain and specifically adsorbed electrolyte counter ions. When a conducting polymer is charged, it loses electrons and forms polycations, causing anions in the solution to intercalate into it to preserve electro-neutrality [12,13]. CPs are prone to deliver high specific capacitance than carbon-based EDLCs owing to such a fast charge transfer process. In addition, CPs can offer flexibility so that they are commonly used for improving the capacitance as well as designing flexible SCs. But CPs have a critical challenge concerning cyclic stability and rate capability due to volume alterations in the polymer chain throughout the charging-discharging process.

Metal oxides provide high energy density due to the faradaic process at the interface. RuO_2 is one of the first and extensively studied electrode materials due to its high reversible faradaic reaction kinetics, high specific capacitance, and energy density [14]. However, the high cost and toxic nature of RuO_2 are forced to search for an alternative to RuO_2. Many other kinds of other metal oxides/hydroxide and metal sulfide/selenides are explored to assess their potential application in PCs. Some of the most commonly studied materials are MnO_2, Co_3O_4, Fe_3O_4, NiO, $Ni(OH)_2$, SnO_2, NiS_2, CoS_2, NiSe, CoSe etc. However, the specific capacitance achieved with the offered mentioned materials falls short compared to RuO_2 and still needs to be enhanced. Metal oxides, on the other hand, reveal cracking of electrodes with repeated charge-discharge, resulting in short-term stability [15].

1.2.3 Hybrid Supercapacitor (HSCs)

HCs are developed by using a combination of both EDLC and PCs electrodes. In which charge storage happens by a simultaneous process. It uses both reversible faradaic and non-faradaic processes to obtain high energy storage and better cycling stability [16,17]. HSCs are further divided into three main types: asymmetric, composite, and battery-type.

Asymmetric and battery type supercapacitor has two distinct types of electrode materials. In asymmetric SC, one of the electrodes is from EDLC and the other one is Pseudocapacitive. Whereas in battery type SC one of the electrodes is EDLC, and the other one is the battery electrode. Carbon-based materials serve as the negative electrodes in asymmetric and battery-type SCs [6]. Because simultaneous charge storage occurs in two dissimilar electrodes, these types of supercapacitors are capable to deliver high power and energy density. Compared to symmetric supercapacitors, these capacitors display better energy density and cyclic stability. However, two different materials need to be developed and understand their individual properties to explore them ins SCs.

Composite hybrid electrode materials are made of a combination of EDL electrode materials and pseudocapacitive electrode materials. The primary objective of composite hybrid electrode materials is to improve specific capacitance and cycling stability by combining the benefits of separate materials. As stated in section 1.2.1, EDLCs offer high power density and rapid charge-discharge because the merits of carbon materials include high surface area, better conductivity, and great mechanical strength. However, it shows poor energy density compared to commercially used lead-acid batteries and lithium-ion batteries. Whereas in PSCs, metal oxides and conducting polymers compete with batteries in storing charge, and thus energy but they display low surface area and poor structural stability. In a composite hybrid, Carbon will serve as a charge transport route, while the metal oxide/conducting polymer will store charge through redox processes, resulting in higher specific capacitance and high energy density [6]. In this thesis work, we have attempted to study the properties of composite hybrid materials by combining the carbon material with conducting polymer. The selection and the properties of individual materials play a vital role which deciding the properties of the obtained composite electrode materials. To select these materials, understanding of basic properties of these individual materials is extremely important.

1.3 Applications of SCs

SCs are ideal for applications that need frequent charge and discharge cycles, high working temperatures, or the quick release of large amounts of energy. Electric vehicles needed a large amount of energy to accelerate and for a quick start. Therefore, SCs are often combined with batteries to combine the features of both power density and charge storage capability. This arrangement provides a balance between charge time and enhances the distance travelled by the electrical vehicle. SCs operate at a wide temperature (roughly from -40 F to 150 F) which makes it possible for vehicles to function properly even in the dead of winter or the hottest days of summer. SCs are also used in automobiles, buses, trains, cranes and elevators, where they are used for regenerative braking, short-term energy storage, or burst-mode power delivery [18]. SCs has found a wide range of power-stabilizing applications, including backup systems and power buffers. SCs provide power for digital camera flashes and LED flashlights which can be charged in much shorter times. Tecate group has developed SC system to use in various military application [19,20].

1.4 Literature review on electrode material for supercapacitor

The energy and power characteristics of SCs are largely determined by the materials used in the electrodes. The sections that follow give an overview of the different types of electrode materials being used in SCs.

1.4.1 Carbon-based electrode materials

Carbon materials have been most widely employed electrode materials in SCs that stores energy by EDL capacitive behaviour. From the Eqn. 1.1, EDL specific capacitance is directly proportional to the electrode surface area. Hence, high specific area carbon materials are finding major applications as electrodes for supercapacitors. Apart from the surface area, other properties such as pore structure, pore distribution, morphology, surface functionalities, crystal structure, mechanical strength, and electrical conductivity are important properties that play a vital role in deciding the performance of carbon-based electrode materials. A wide variety of carbon materials has been developed over the years and explored SCs. Some of the main types of carbon materials studied in SCs are discussed in the following sections.

1.4.1.1 Activated carbons

Activated carbons (ACs) have been most popularized form of carbon-based electrode materials for energy storage. The fascinating features of ACs are high surface area, porous structure, tunable pore size distribution, surface functionalities, etc. The above-mentioned properties of activated carbons are mostly depending on the precursor materials and synthesis process. Activated carbons can be produced from fossil fuels (petroleum and coal) and biomass or biowaste precursors. Production of ACs from fossil fuels is usually an expensive and environmentally hazardous process. ACs derived from biomass or biowaste are of special interest because of their high carbon content, low cost, natural abundance, sustainable availability, and scalable, etc.

Biomass is always referring to animal or plant-based materials derived from nature [21,22]. The biomass precursors are undergone different carbonization (pyrolysis, and hydrothermal) and activation processes (physical, and chemical) to produce valuable porous carbons [23,24]. Various synthesis approaches and respective synthesis conditions are illustrated in Figure 1.6. To enhance the electrochemical properties of biomass-based carbon materials, advanced synthesis strategies are explored to produce carbon materials with different dimensions. For example, Hao et al., prepared 3D meso and microporous carbon nanofiber networks taking Bacterial cellulose biomass by following silica assisted strategy referred to as the ‘confine nano space’ pyrolysis process. The obtained carbon fibres displayed a maximum specific capacitance of 302 F/g at 0.5 A/g, along with high-rate capability and good cyclic stability [25]. Xie et al., produced hierarchical porous carbon microtubes using willow catkins via carbonization and subsequent KOH activation. The carbon microtubes activated at 800 ^{o}C possessed high surface area of 1775.7 m^2/g with a pore volume of 0.8516 cm^3/g and delivered a maximum specific capacitance of 292 F/g at 1 A/g in 6 M KOH electrolyte [26]. Zhou et al., synthesised porous carbon nanosheets from biomass-reed by using a hydrothermal process combined with chemical activation. They found a specific capacitance of 147 F/g at 1 A/g in 1-Ethyl-3-methylimidazolium tetrafluoroborate (EMIM BF4) electrolyte [27]. Hao et al. prepared 3D hierarchical porous CAs from bagasse and a specific capacitance of 142.1 F/g is obtained at 0.5 A/g in symmetric solid-state assembly. This solid-state SC also displayed capacitance retention of 93.9% over 5000 cycles [28]. Table 1.1 summarizes recent research work carried out on various biomass-derived ACs for supercapacitors. Even though the ACs are vastly studied materials in supercapacitors due to their large surface area (1000–3000 m^2/g) but the real-time energy storage capability is still very much below compared of Li-ion batteries [29,30]. The major factors effecting the properties of AC materials are: (i) limited ion diffusion and (ii) poor electron delivery and slow charge transfer. These problems arise due to less accessibility of micropores to the electrolyte ions and the inherent low electrical conductivity (10–100 S/m) [31,32].

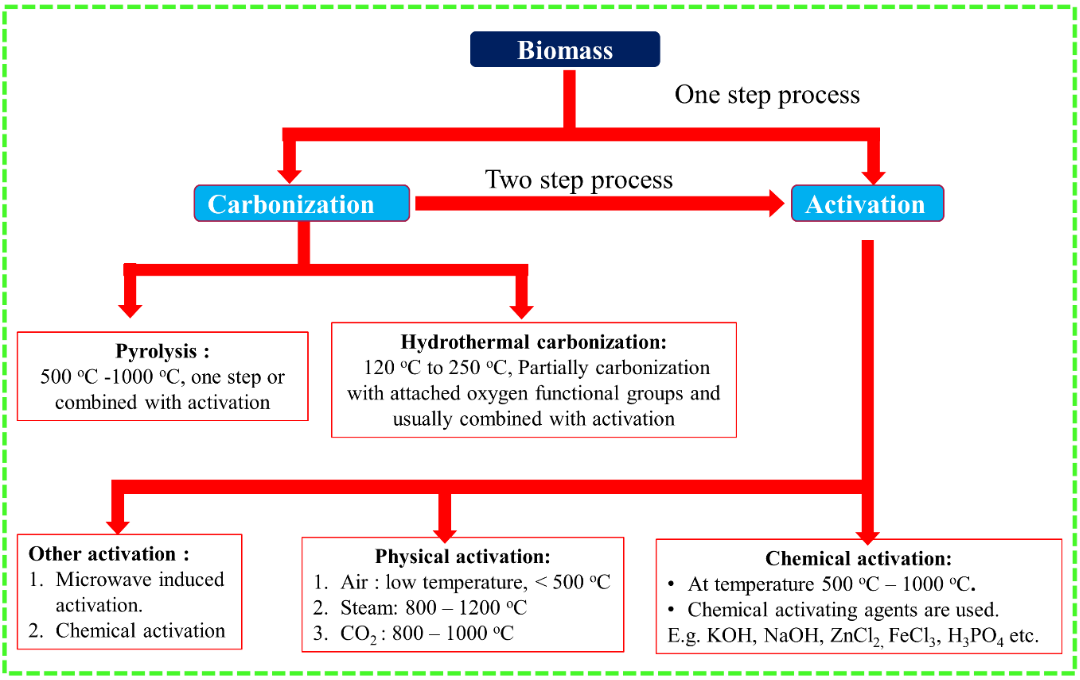

Figure 1.6 Common synthesis methods of converting biomass to carbon material [23].

To further enhance the specific capacitance and energy density of ACs, heteroatom doped porous carbons are also been developed. Doping has been carried out externally by adding hetero atom containing precursors and internally by selecting the hetero atom containing biomass materials. Again, the properties of obtained heteroatom doped carbon materials are strongly influenced by the precursor material, synthesis conditions, and heteroatom doping agents. For instance, Yu et al., subjected protein-rich soybeans to low-temperature pre-carbonization, hydrothermal stabilization, and KOH activation to obtain N, O, P, and S co-doped porous carbons. They achieved a high specific capacitance of 685.1 F/g at 0.5 current density of A/g in 2 M KOH and 439.5 F/g at 1 A/g in 1 M H_2SO_4 electrolyte, respectively. The heteroatom-containing porous carbon materials also have shown excellent cycling stability of 80% after 13,000 cycles [33]. Cao et al., compared the electrochemical performance of nitrogen-doped biomass-derived hierarchical porous carbon materials synthesized using different nitrogen-containing compounds (NH_4Cl, $(NH_4)_2CO_3$, and urea) as both activation agents and dopants. Among them, a highest specific capacitance of 300 F/g at 1 A/g is achieved for the porous carbon obtained using urea while a maximum capacitance retention rate of 95.2% after 10,000 cycles is achieved with the porous carbon derived by NH_4Cl [34]. Recently, Zhang et al., used watermelon rind as the carbon source to design diverse dimensional carbon materials such as 3D hierarchical honeycomb nanoporous carbon architecture, 2D carbon nanoflakes, and 1D needle-shaped carbon nano bars with/without different dopants. One step activation process is followed and 2D flakes are produced without additional doping agents. The presence of ammonium citrate tribasic and sodium alginate can modulate the dimensional morphology with more heteroatom contents for 3D hierarchical porous honeycomb structures and 1D needle-like architectures, respectively. The prepared flexible electrode using 1D carbon nano bars exhibited higher areal capacitance of ∼2245 F/cm^2 at 1 mA/cm^2 with outstanding cycling stability of 99.5% after 20,000 cycles [35]. Further, extensive studies are also been carried out to combine ACs with other carbon materials (e.g. CNTs, Graphene), metal oxide, and conducting polymers to further improve the electrochemical properties [36–42].

Table 1.1 Literature survey on various biomass-derived ACs for SCs.

Raw material	**Specific capacitance/ Measured condition**	**Electrolyte/ Electrode system**	**REF.**
Onion	158 F/g at 0.5 A/g	3 M KNO_3 /2-ele	[43]
wheat husk	271.5 F/g at 0.5 A/g	6 M KOH /3-ele	[44]
rice husk	198.4 F/g at 1 A/g	0.5 M K_2SO_4 /3-ele	[45]
nettle leaf	163 F/g at 0.5 A/g	EMIM BF_4 /2-ele	[46]
Miscanthus grass	112 F/g at 0.5 A/g	6 M KOH/3-ele	[47]
Pine nut shells	324 F/g at 0.05 A/g	6 M KOH /3-ele	[48]
Waste bagasse	455 F/g at 0.5 A/g	6 M KOH /3-ele	[49]
cotton	283 F/g at 1 A/g	6 M KOH /3-ele	[50]
citrus peel fibre waste	565 F/g at 0.5 A/g	2M KOH /3-ele	[51]
Corncob	338 F/g at 0.5 A/g	1 M H_2SO_4 /3-ele	[52]
Hibiscus sabdariffa fruits	29 F/g at 0.5 A/g	0.5 M Na_2SO_4/	[53]
Mangosteen peel	76.8 F/g at 1 A/g	1 M Li_2SO_4 /2-ele	[54]
Onion	158 F/g at 0.5 A/g	3 M KNO_3/2-ele	[43]
Rice straw	156 F/g at 0.5 A/g	1 M H_2SO_4/2-ele	[55]
Corn silk	160 F/g at 1 A/g	6 M KOH/2-ele	[56]
Fish seed	250 F/g at 1 A/g	6 M KOH/2-ele	[57]
Buckwheat husk	75 F/g at 1 A/g	6 M KOH/2-ele	[58]
Gardenia Jasminoides Ellis	153.7 F/g at 0.5 A/g	6 M KOH/2-ele	[59]
Flax seed residue	76 F/g at 0.5 A/g	6 M KOH/2-ele	[60]
Nettle leaf	163 F/g at 0.5 A/g	EMIM BF_4/2-ele	[46]
Waste tea	89.3 F/g at 1 A/g	6 M KOH/2-ele	[61]
American poplar fruits	58.71 F/g at 1 A/g	6 M KOH/2-ele	[62]

1.4.1.2 Carbon aerogel

Carbon aerogels (CAs) are three-dimensional nanostructured porous carbon materials derived from the pyrolysis of organic aerogels at elevated temperatures. The CAs are composed of small carbon particles or polymer chains that are covalently bonded together. The synthesis of CAs from organic aerogels involves four sequential steps i.e., sol-gel polymerization, aging, drying, and pyrolysis [63]. The physicochemical properties of CAs are greatly influenced by the type of precursor organic polymers and above-mentioned synthesis steps [64].

CAs have received substantial research as electrode material in SCs due to their attractive characteristics such as 3D hierarchical structure, low density, high surface area, porosity, and lightweight. CAs derived from the organic aerogel of resorcinol/formaldehyde are the most explored electrode materials in SCs [65]. Other organic aerogel precursors such as melamine/formaldehyde, melamine-resorcinol/formaldehyde and cresol/formaldehyde are also used for the preparation of CAs and evaluated as electrode material for supercapacitor [66–68]. Despite its advantages, the precursor formaldehyde, a carcinogen derived from the petroleum industry, is hazardous to the human body. Furthermore, resorcinol is an expensive chemical, and supercritical drying is an energy-intensive method that is too expensive for large-scale commercial production [63,69]. Alternatively, various low-cost biomass precursors (cellulose, chitosan, lignin, tannin and biowaste) are effectively utilized for the synthesis of CAs with improved properties [63]. The biomass precursors are relatively cheap and abundant raw materials for the preparation of CAs. For example, Hao et al., derived hierarchical porous CAs using bagasse as raw material. The resulting CAs possessed a specific surface area of 1892.4 m^2/g along with micro, meso, and macroporous structures. They found a comparable specific capacitance of about 142.1 F/g at 0.5 A/g [28]. In addition, heteroatom doping, and combining with other pseudocapacitive materials are also been investigated to further enhance the performance of CAs for SC electrodes. Table 1.2 summarizes some of the recent works carried out on CAs and their composite electrode materials for SCs.

Table 1.2 Literature review on CA electrode materials for SCs.

Precursors (or) Electrode Materials	**Specific capacitance/ Measured condition**	**Electrolyte/ Electrode system**	**REF.**
resorcinol/formaldehyde	110.06 F/g at 1 mV/s	6 M KOH /3-ele	[64]

resorcinol/formaldehyde	201 F/g at 0.1 A/g	1 M H_2SO_4/2-ele	[70]
Melamine-resorcinol/formaldehyde	139 F/g at 0.5 A/g	2 M KOH /3-ele	[71]
Melamine-resorcinol/formaldehyde (N-CA)	208 F/g at 5 mV/s	6 M KOH /2-ele	[72]
CA-Co_3O_4	180.8 F/g at 1 A/g	PVA-KOH gel/2-ele	[73]
N doped CA	166 F/g at 0.1 A/g	1 M H_2SO_4/2-ele	[74]
Cellulose CA	328 F/g, 0.5 A/g	1 M H_2SO_4/3-ele	[75]
Chitin CA	188.3 F/g at 1 A/g	6 M KOH /2-ele	[76]
CA-GO	120 F/g at 500 mV/s	1 M H_2SO_4/3-ele	[77]
Lignin CA-Ni	26.6 F/cm^2 at 1 mA/cm^2	6 M KOH /3-ele	[78]
CA/polypyrrole	268.5 F/g at 0.5 A/g	1 M H_2SO_4/2-ele	[79]

1.4.1.3 Carbon nanofibers

Carbon nanofibers (CNFs) have received considerable research interest due to the efficient 1D electron-transport path along the axial direction and short ionic-diffusion distance along radial direction [80–82]. Carbon fibres are most commonly prepared by electrospinning of polymers (polyacrylonitrile (PAN), polyvinyl alcohol (PVA), polymethylmethacrylate (PMMA), Polyimide (PI), Polyvinylpyrrolidone (PVP), and cellulose, etc.) [82,83]. In this method, polymers dissolved in suitable solvents are initially subjected to electrospinning to obtain polymer fibres with uniform size and thickness. Then subsequent high-temperature heat treatment of these polymer fibres produces carbon fibres. The thickness and size of the CNFs are affected by experimental parameters such as precursor concentration, spinning voltage, and pyrolysis temperature.

CNFs have been widely studied as electrode materials SCs. Various new strategies are also been followed increasing the degree of graphitization, adjusting the pore structure, and introducing heteroatoms, which have been investigated to improve the performance of CNFs [84–86]. For example, Li et al., developed porous nitrogen-doping CNFs by electrospinning of polyacrylonitrile/ polyvinylpyrrolidone, followed by a stabilization and carbonization process. They achieved a high specific capacitance of 148 F/g at 1 A/g in a symmetric cell [87]. Recently, Jiang et al. followed a novel way to produce free-standing N-doped CNFs via carbonization and subsequent pyrolysis of PVP-based CNFs in the presence of g-C_3N_4. They found a maximum specific capacitance of 265 F/g at 1 A/g along with high-rate capability (131 F/g at 16 A/g). They found that the incorporation of foreign atoms in CNFs is beneficial to enhance the electrochemical properties [88]. Further, the carbon fibers are also been blended with other pseudocapacitive materials to extract improved electrochemical properties for SCs [89,90]. Table 1.3 summarizes the research work carried out on CNFs and their composite electrode materials for SCs.

Table 1.3 Literature survey on CNFs and their composite electrode materials for SCs.

Precursors (or) Materials	Specific capacitance/ Measured condition	Electrolyte/ Electrode system	REF.
PAN -H_3PO_4	156 F/g at 0.5 A/g	6 M KOH /2-ele	[91]
PAN	103 F/g at 1 A/g	1 M Na_2SO_4/3-ele	[92]
PANI-polysulfone	257 F/g at 0.25 A/g	6 M KOH /2-ele	[85]
polyamic acid-poly(diaryloxyphosphazene)	182 F/g at 1 A/g	6 M KOH /2-ele	[93]
PAN-PMMA	140 F/g at 0.5 A/g	6 M KOH /2-ele	[94]
PAN-PVP	148 F/g at 1 A/g	6 M KOH /2-ele	[87]
PAN- PVP	252.6 F/g at 0.5 A/g	1 M H_2SO_4/3-ele	[95]
PAN/pitch-based CNFs/MnO2	188 F/g at 1 mV/s	6 M KOH /3-ele	[96]
PAN-based CNFs/CNTs	464.2 F/g at 0.5 A/g	6 M KOH /3-ele	[97]
PAN-based CNFs/CNTs	61.1 F/g at 5 mV/s	2 M H_2SO_4/3-ele	[98]
Cellulose derived CNFs/rGO	46 F/cm^3 at 5 mV/s	6 M KOH /2-ele	[99]
lignin/(PAN)-based CNFs/N, S -doped graphene	267.32 F/g at 5 mV/s	6 M KOH /2-ele	[100]
PAN-PVP based CNFs/graphene	249 F/g at 1 A/g	6 M KOH /3-ele	[101]
PAN/Fe(acac)$_3$ -based CNFs/CNT/MnO_2	~635 F/g at 0.9 A/g	1 M Na_2SO_4/3-ele	[102]
PAN-based CNFs/PANI	257 F/g at 5 mV/s	PVA-H_2SO_4 /2-ele	[103]
Polyacrylonitrile-CNFs/PANI	~149 F/g at 1 A/g	1 M H_2SO_4/3-ele	[104]
PAN-based CNFs/PANI	234 F/g at 1 A/g	1 M H_2SO_4/2-ele	[105]
PAN/PANI- based CNFs/PANI	260 F/g at 1 A/g	1 M H_2SO_4/3-ele	[106]
PAN/SiO_2-based CNFs/PANI	339.3 F/g at 0.1 A/g	PVA-H_3PO_4 /2-ele	[107]

1.4.1.4 Carbon nanotubes

Carbon nanotubes (CNTs) are graphene sheets that have been cylindrically rolled. CNTs are made of sp^2 hybridized carbon networks and they can be single-walled CNTs or MWCNTs based on the number of graphene sheets present in the materials. CNTs offer excellent stability, high electrical conductivity, flexibility, and lightweight. Because of these excellent properties, extensive research has been conducted on CNTs for their use in SCs. Although CNTs are proved their potential application in SC, difficulty in synthesis and synthesis costs involve costly equipment facilities. Besides, the high contact resistance between the electrode and current collector, as well as inefficient interaction with electrolyte due to low dispersion ability, result in unsatisfactory practical performance [108,109]. Alternatively, acid etching and heteroatom doping increases the defects and enhances the wettability thus improving electrochemical performance [110]. Further, CNTs composites are also been developed to boost electrochemical performance. For instance, Roy et al., prepared NiO/CNT binary composite and realise a high specific capacitance of 878.19 F/g at a scan rate of 2 mV/s [111]. Luo et al., demonstrated a maximum specific capacitance of 818 F/g at a scan rate of 1 mV/s with CeO_2/CNT composite electrodes [112]. Ding et al., reported developed functionalized graphene nanosheets/carbon nanotubes (G/CNTs) networks via chemical oxidation with a subsequent low-temperature reduction method. They achieved five times higher specific capacitance than pure CNTs (40 F/g) with functionalized graphene/CNTs composite electrode (202 F/g) at 0.5 A/g [113]. Jiang et al., designed mutually intercalated flexible films with a ternary composite of polyaniline/ graphene oxide /CNTs, and a specific capacitance of 729.3 F/g is obtained at 1 A/g [114]. Table 1.4 reviews the research work carried out on CNTs-based electrode materials for SCs.

Table 1.4 Literature review on CNTs-based electrode materials for SCs.

Sample	Specific capacitance/ Measured condition	Electrolyte/ Electrode system	REF.
N doped CNTs	146 F/g	1 M KCl /3-ele	[110]
RuO_2/CNT/CC	179 F/g at 2 A/g	1 M H_2SO_4 /2-ele	[115]
CNT/WO_3	496 F/g at 0.5 A/g	0.5 M H_2SO_4 /3-ele	[116]
AC/CNT/RGO	101 F/g at 0.2 A/g	1 M $LiClO_4$ /2-ele	[117]
NiCo hydroxide/CNT	139.3 F/g at 1 A/g	6 M KOH/2-ele	[118]
$CuCo_2S_4$/CNTs	557.5 F/g at 1 A/g	2 M KOH/3-ele	[119]
3D graphene/MWNT	286 F/g at 1.78 mA/cm^2	6 M KOH/2-ele	[120]
CNTs/GNFs	270 F/g at 1 A/g	6 M KOH/3-ele	[121]
NiO/CNTs	258 F/g at 1 A/g	2 M KOH/3-ele	[122]
Fe_2O_3/CNTs	204 F/g at 0.5 A/g	1 M Na_2SO_4/2-ele	[123]
CNT@N-porous carbon	244 F/g at 1 A/g	6 M KOH/3-ele	[124]

1.4.1.5 Graphene

Graphene is an allotropic form of carbons. It is a two-dimensional (2D) atomic size thin monolayer of graphite. It is often referred to as a “wonder material” because of its exceptional electrical, and mechanical properties and unique structure. Graphene has a hexagonal lattice structure formed with sp^2 hybridized carbon atoms. The unique and attractive properties of Graphene are its high surface area (2630 m^2/g), high electrical conductivity, high intrinsic strength (~130 GPa) and mechanical strength (~1.0 TPa), chemical stability, lite weight, flexibility. These extraordinary properties make it the strongest material for energy storage applications.

Graphene is firstly discovered by the pioneering work of Geim and Novoselov which laid a foundation for the research community to realize potential applications. Since then, various synthesis strategies are explored for developing graphene materials [125]. Graphene synthesis is mainly categorised into two types: ‘bottom-up’ and ‘top-down’. In bottom-up method, gas-phase carbon precursors are used for the production of graphene, the methods included in bottom-up approach are epitaxial growth [126], chemical vapour deposition [127,128], substrate-free gas-phase synthesis [129], template route [130] and total organic synthesis [131]. Although most of the bottom-up methods produce high-quality graphene materials they usually require sophisticated equipment setup and high production cost. Whereas in top-down approach, graphite is transformed into graphene. The top-down methods are mechanical exfoliation [125], arc discharge [132], oxidative exfoliation-reduction [133,134], liquid-phase exfoliation [135,136] and unzipping of CNT [137]. Bulk production of graphene is possible with some of the top-down approaches but often ended with the low quality and defective graphene materials which deteriorate its physicochemical properties [138].

Graphene has become one of the most popular carbon-based electrode materials for supercapacitor electrodes owing to its excellent properties. A single layer of graphene can carry a specific capacitance of ~21 $\mu F/cm^2$and the gravimetric corresponding capacitance of ~550 F/g when its surface area is completely utilized [139–141]. However, the practically obtained specific capacitance is lower than the estimated theoretical value. To realize the enhanced experimental performance, preparation of graphene in its pure form and bulk production are extremely important.

The chemical oxidized form of graphene i.e., graphene oxide (GO) is a suitable starting material for the bulk production of graphene as reduced graphene oxide (rGO) always has a few layers with attached residual oxygen functional groups attached to the graphene skeleton. rGO treated as a derivative of graphene has also been proven to be a promising material to act as electrode material for SCs [142,143]. However, the main troubles raised with graphene-based materials are its serious agglomeration and more tendency of restacking of graphene sheets to form graphitic structure, during synthesis and electrode fabrication processes. Agglomeration and restacking of graphene layers eventually decline the specific surface area accessible to electrolyte ions. These shortcomings could be addressed by following various strategies. The promising approaches are developing porous three-dimensional structures, doping with heteroatom and composites with other capacitive materials. Three-dimensional graphene networks were developed to reduce restacking and enhance the surface area. 3D porous graphene networks facilitate fast electron transfer, enhanced accessible surface area to electrolyte ions and fast electrolyte networks [144,145]. For example, Zhang et al., developed graphene hydrogels by hydrothermal reduction of GO dispersion then chemically reduced by hydrazine or hydroiodic acid. They obtained a high specific capacitance of 220 F/g at 1 A/g when the Graphene hydrogel is tested in a supercapacitor cell [146]. Hao et al., reported 3D graphene with an open pore network and having a pore size in the range of dozens of nanometres to hundred nanometres. The continuously cross-link structured 3D graphene has exhibited a high specific capacitance of 231 F/g at 1 A/g [147]. Li et al., produced porous graphene paper via a thermal stock of layer structure graphene self-assembled on Cu foil under nitrogen flowing. A maximum specific capacitance of 100 F/g is reported at a scan rate of 100 mV/s [148].

The second approach to enhancing the properties of graphene-based materials is hetero atoms (Nitrogen, Sulphur, Phosphorous, Boron, etc.) doping. Introducing heteroatoms into graphene has shown significant changes in its physicochemical properties. Doping induced bandgap in graphene thus makes it either N-type or P-type material. Even though addition of heteroatoms creates defective structures, these defective structures act as electroactive sites to interact with electrolyte ions thus enhancing their capacitive behavior. Besides that, different bonding configurations of heteroatoms in the graphene network actively engage in charge transfer reactions with electrolyte ions, providing additional pseudocapacitance. In particular, nitrogen (N) is a suitable dopant for graphene because of its comparable atomic size and provides an additional p-electron to the π-system of graphene making it n-type [149–151]. Previous reports have also demonstrated that N-doping is a beneficial route to decorating graphene for the reason that doping can increase the charge carrier concentration thus providing high electrical conductivity [151]. Moreover, the presence of a high electronegative N atom can improve surface wettability, which is beneficial for efficient charge transportation at the electrode/electrolyte interface [152]. Doping of the N atom can exist mainly in three different forms, namely pyridinic-N, pyrrolic-N, and quaternary-N [153,154]. Pyridinic-N and pyrrolic-N increase the surface wettability of electrodes and participate in charge transfer reaction with electrolyte ions, hence, generate additional pseudocapacitance, whereas the quaternary N atom is a substitution to the carbon atom in benzene ring which enriches the local electron density, consequently exhibit high electrical conductivity [154]. For example, Shin-Ming et al., reported the synthesis of N-doped rGO (N-rGO) via a simple thermal exfoliation combined with covalent transformation of melamine-graphene oxide mixture and achieved higher capacitance than rGO [155]. Sliwak et al., followed hydrothermal method for the synthesis of N-rGO where amitrole is used as a reducing agent as well as a nitrogen source. N doping concentration is obtained in the range of 10.9 to 13.4 at% at different hydrothermal temperatures. They found a specific capacitance of 244 F/g at a scan rate of 100 mV/s for the N-rGO with the highest nitrogen content [152]. Santhosh et al., developed N-doped porous rGO and studied its capacitive behaviour using all solid-state flexible supercapacitors. They attained a maximum specific capacitance of 230 F/g at 1 A/g with good capacitance retention [156]. Fan et al., prepared P-doped three-dimensional rGO hydrogels by a one-step hydrothermal process. The obtained P-doped rGO delivered a specific capacitance of 384 F/g at 1 mA/cm^2 [157]. Similarly, Sulfur doping is proved to improves catalytic activity. From the reported studies, the S-doping is also a recommended approach to increase capacitive performances of supercapacitor [158,159]. The C-S bonds and thiophens (C-SO$_x$-C) formation in graphene lattice creates defective structure which subsequently produce active sites for additional pseudo capacitance [158–160]. Duraivel et al., synthesized S-doped rGO via refluxing method where sodium borohydride ($NaBH_4$) and sodium sulfide (Na_2S) are used as reducing agent and sulfur sources respectively. They have shown a high specific capacitance of 392 F/g at 0.05 mA/cm^2 along with good cyclic stability (91% after 2000 cycles) using S-rGO electrodes [161]. Nurul et al., produced S-doped rGO by following a microwave-assisted method and obtained a high specific capacitance of 237.6 F/g at 0.1 A/g [158]. Recently, Arvas et al., proposed a one-step electrochemical method to prepare different heteroatom (-S, -N, -Cl) doped GO electrodes. They obtained the specific capacitances of 206.4, 533.2 and 1098 mF/cm^2 at 10 mA/cm^2, with -S, -N and -Cl doped graphene oxide electrodes respectively [162]. Several composite materials have also been developed by combining graphene-based materials with other pseudocapacitive materials [163–165]. The improved performance is realized with the composite materials by the synergistic effect of both EDLC and Pseudocapactiance. Various composite materials have been developed with graphene-metal oxide composites, and graphene-conducting polymer composites and achieved excellent electrochemical performance. Table 1.5 summarizes some of the recent research work reported on graphene and its composite electrode materials for SCs.

Table 1.5 Literature review on graphene-based electrode materials for SCs.

Sample	Specific capacitance/ Measured condition	Electrolyte/ Electrode system	REF.
3D Graphene hydrogel	220 F/g at 1 A/g	6 M KOH/2-ele	[146]
3D graphene	231 F/g at 1 A/g	1 M H_2SO_4 /3-ele	[147]
Porous graphene	100 F/g at 100 mV/s	1 M H_2SO_4 /2-ele	[148]
N-doped rGO	239 F/g at 0.2 A/g	6 M KOH/3-ele	[152]
N-doped porous rGO	230 F/g at 1 A/g	PVA- H_2SO_4 gel/2-ele	[156]
P-doped rGO	285 F/g at 1 mA/cm^2	1 M H_2SO_4 /3-ele	[157]
S-doped rGO	392 F/g at 0.05 mA/cm^2	1 M Na_2SO_4 /3-ele	[161]
S-doped rGO	237.6 F/g at 0.1 A/g	1 M H_2SO_4 /2-ele	[158]
α-Fe_2O_3/rGO	533 F/g at 1 A/g	2 M KOH/3-ele	[166]
MnO2/N-rGO	453 F/g at 2 A/g	0.5 M Na_2SO_4 /3-ele	[167]
Co_3O_4@MnO_2/rGO	347 F/g at 0.5 A/g	6 M KOH /3-ele	[168]
PANI@MnO_2/ Graphene	743.8 F/g at 1 A/g	1 M H_2SO_4 /3-ele	[169]
PANI/rGO-HT	420 F/g at 0.2 A/g	1 M H_2SO_4 /3-ele	[170]
rGO/PANI	99 F/g at 0.5 mA	PVA- H_2SO_4 gel/2-ele	[171]
3D graphene/PANI	352 F/g at 10 mV/s	1 M Na_2SO_4 /3-ele	[172]
ERGO/CNT	290F/g at 50 mV/s	0.5 M Na_2SO_4 /3-ele	[173]

1.4.2 Conducting polymers

Polymers are organic insulating materials made up of repeated monomer units. But the conductivity can be imposed onto some of the pi- conjugated polymers up on disturbing the local charge density of saturated macro molecules. Conductivity of a polymer can be realised in two basic ways i.e., extrinsically by adding conducting fillers into polymer matrix and intrinsically by disturbing the local electron distribution. The concept of intrinsic conductivity of polymers is realized by the discovery of conductivity in polyacetylene in 1970s [174]. The pioneer work of Hideki Shirakawa, Alan J. Heeger, and Alan G. MacDiarmid research group paved a way for the new field of conducting polymers (CPs) and they jointly honoured with Nobel Prize in Chemistry in 2000. Since the discovery of conducting polyacetylene, fundamental research on synthesis of many new kinds of CPs, conduction mechanism, properties evaluation and application of these polymers in various fields has been emerged. The basic structures of some of most popular CPs are illustrated in Figure 1.7.

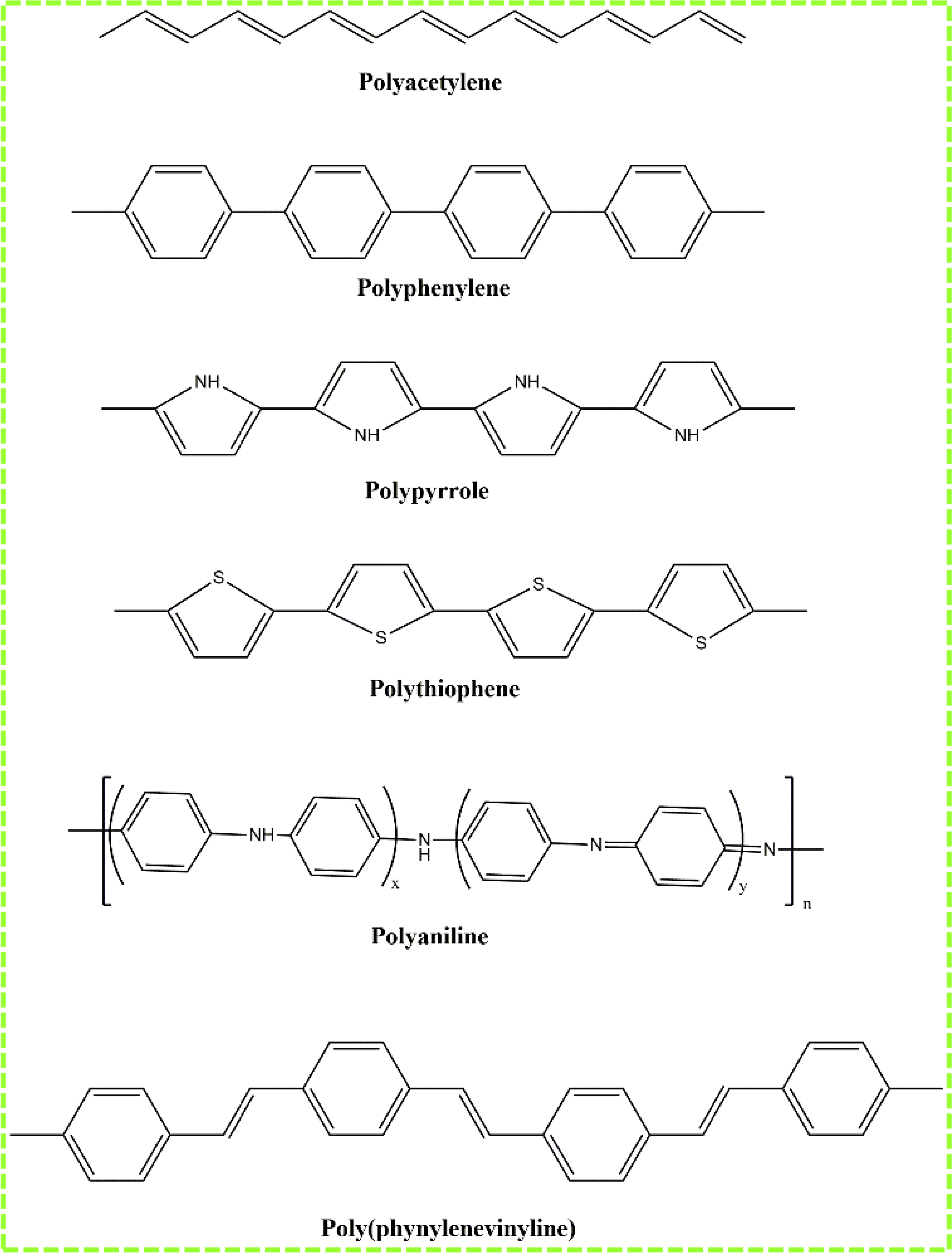

Figure 1.7 Molecular structures of some of the most common CPs.

Doping transforms the π-conjugated polymers from low conducting insulators to semiconducting or even into metallic regions (Figure 1.8). The conductivity depends on the doping level of polymers. Intrinsic CPs are having saturated macromolecules with a system of alternate single and double bonds leading to a continuous sp^2 hybridized carbon center. Upon withdrawal an electron i.e., oxidizing the polymer with a suitable oxidant, makes a positive ‘hole’ in polymer backbone (p-doping), and leftover electrons within the partially filled band become more mobiles and thereby induce conductivity. Similarly, upon adding an electron, i.e., reducing the same conjugated polymer in the presence of a reducing agent makes it n-doping. To maintain electroneutrality, the polymer electrode must also accept ions through a process known as polymer doping (p-doping), which is an ion insertion process that raises the polymer's redox state and electronic conductivity [175]. The majority of conductive polymers can be oxidatively doped to produce p-type materials, whereas n-doped polymers are less common.

CPs also grab significant research interest to use as pseudocapacitive electrode materials for SCs [176–178]. The attractive properties of CPs are their ability to store a high amount of energy, low cost, simple synthesis process, and lightweight. Besides CPs are also lightweight and offer flexibility which allows considerable design flexibility SCs. Polypyrrole, polyaniline, Polythiophene etc. are more frequently studied CPs in SCs. The CPs can store or release charge through fast redox doping/dedoping process associated with the π-conjugated polymer chain [13,179–181]. During the charge-discharge process, most of the common conducting polymers switch between their different doping states (p-type/n-type). The polymer backbone gets oxidized (p-doping) by the interaction of polycations with the anions (A^-) from the electrolyte. Similarly, the conducting polymers are reduced (n-doped) during discharge by the attraction of cations (M^+) from the electrolyte. In this way, charge neutrality occurs in conducting polymer electrodes. Unlike metal oxides, the complete backbone of conducting polymers will contribute to the charge transfer process thus resulting in high specific capacitance. Even though the charge storage capacity of CPs is higher than EDLCs and some of the metal oxides, the same process of charge storage is also a flaw for the CPs due to the damage of polymer structure upon continuous doping/dedoping in the entire polymer during charge-discharge which shortening the overall life [182,183].

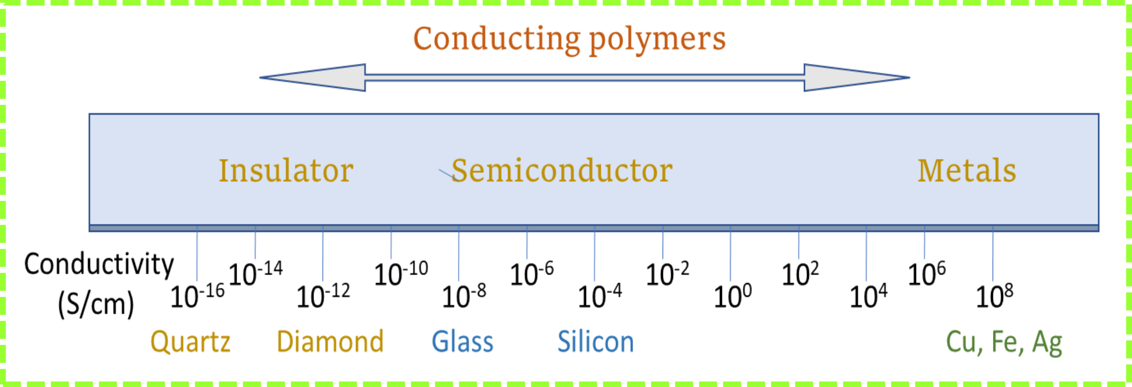

Figure 1.8 Conductivity of some metals, semiconductors, insulators and conjugated polymers.

1.4.2.1 Polyaniline

Polyaniline (PANI) is among the most widespread studies that have been conducted on CPs, with a unique doping mechanism and a variety of forms. Even though the early discovery of PANI occurred in 1862, which is named aniline black but the electrical conductivity properties were realized in 1985. The electrical conductivity of PANI is first experimentally measured by MacDiarmid which is prepared by chemical oxidization of aniline in 1 M HCl acid by ammonium peroxydisulfate (APS). The obtained green powder of PANI displays the conductivity of 3 S/cm [184]. PANI can be easily prepared from aniline monomer by chemical oxidative polymerization using an oxidizing agent. As an example, the general steps involved in the synthesis of PANI are given in Figure 1.9. The basic molecular structure of PANI is composed of Benzenoid and quinoid rings. Unlike other CPs, PANI can exist in three different states depending on its oxidation state: Leucoemeraldine, emeraldine, and pernigraniline, which are totally reduced, half-oxidized, and totally oxidized forms, respectively [185,186]. Different forms of PANI are shown in Figure 1.9 [187]. Interestingly, PANI can also show electrochromic properties, because of its appearance in different colours (transparent, yellow, violet, blue, and green) in different oxidation states.

The conductivity of PANI is realized upon conversion of emeraldine base of PANI into emeraldine salt form by protonic acid doping as shown in Figure 1.9 [188]. Only Emeraldine salt form of PANI possesses conductivity and other forms of PANI are insulators even after protonation. Protonic doping makes PANI as a special kind of CP because the doping does not impose any addition and removal of electrons from the polymer backbone. In this process, externally, electrons do not take any part in creating PANI conductive. The conductivity is induced by the formation of charged segments or species, such as radical cations (polarons), and dications (bipolarons) [189]. More clearly, in the doping process, a proton is bound to the imine N nitrogen atom of a quinone ring of the polymer chain. The quinone ring is then reduced to a benzene ring and the polymer chain is positively charged (polaron). An anion later enters the polymer chain to maintain electron neutrality [186]. The extent of protonation of imine nitrogen relies on the oxidation state and pH of the aqueous acid and complete protonation of it gives rise to doubly charged bi-polaron that simultaneously dissociates into delocalized polysemiquinone radical cations or two polarons with a rise in conductivity [188,190].

The existence of multiple redox states and the special proton exchange doping mechanism of PANI have grabbed the attention to extend its use in various domains of energy storage applications [186]. Polyaniline is an extensively investigated electrode material for supercapacitors owing to its easy synthesis, better electrical conductivity, multiple redox states, high doping level (~0.5), flexibility, and good environmental stability [180]. Because of multiple redox states, PANI is believed to deliver high specific capacitance. PANI has a high specific capacitance in protonic acid and protic ILs electrolytes due to protonic doping. A single PANI electrode can deliver a relatively high theoretical capacitance of 2000 F/g in 1.0 M H_2SO_4 under the redox potentials of 0.15-0.76 V versus SCE. However, the experimentally obtained values were much lower because of various synthesis and other experimental conditions. moreover, the cycle life of PANI-based devices is limited due to the tendency of volume change with the continuous charge/discharge process. The continuous doping/dedoping of counterions during charge-discharge causes the shrinkage/swelling of polymer resulting in mechanical failure of the polymer electrodes at higher cycles. Another issue with PANI is that it is susceptible to oxidative degradation, which results in poor performance even after minor overcharging. The conductivity and morphology of PANI have greatly influenced the electrochemical nature of resultant PANI.

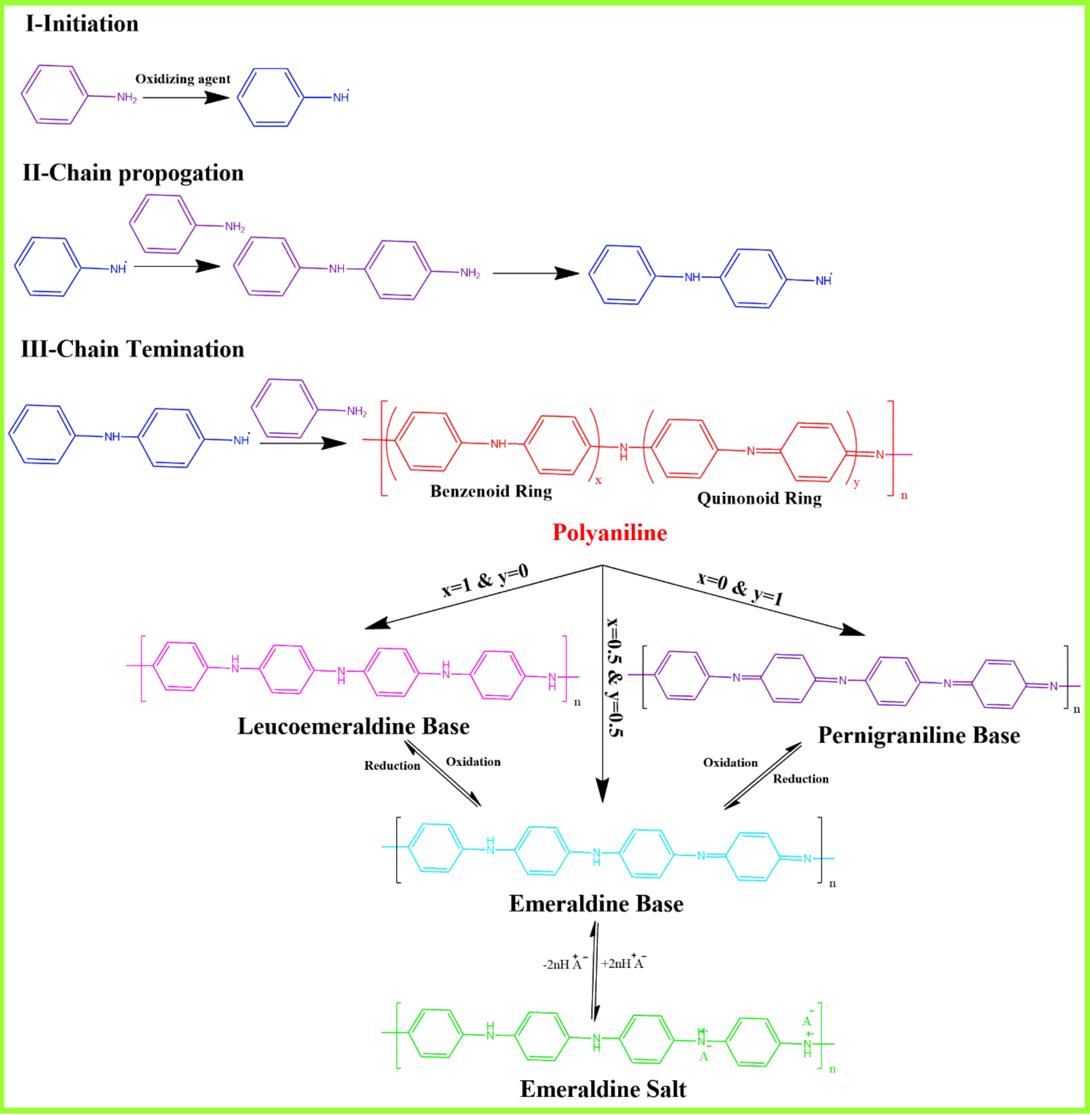

Figure 1.9 Mechanism of polymerization of PANI and different forms of PANI.

To improve PANI's electrochemical performance, mainly, two different strategies have been used. The first strategy is the construction of nanostructured PANI with different morphologies (nanofibers, nanorods, nanotube, nanosheets, nanospheres, etc.) and porous structures (3D conducting PANI porous networks, PANI hydrogel, PANI aerogel structures). Various synthesis methods are followed to prepare these different morphologies of PANI nanostructures and achieved enhanced electrochemical properties as SCs electrodes. These PANI nanostructures provide a larger surface area, high utilization efficiency, and decrease the transport pathways of ions and electrons [191–194]. The literature review on various types of nanostructured PANI and porous PANI structures reported is presented in **Table 1.6**.

Table 1.6 Literature review on PANI-based electrode materials for SCs.

Material	Electrolyte/ Electrode system	Specific capacitance	Ref.
PANI NFs	1 M H_2SO_4/3 ele.	239 F/g at 0.5 A/g	[195]
PANI NRs	1 M H_2SO_4/3 ele.	297 F/g at 1 A/g	[196]
PANI NSs	1 M H_2SO_4/3 ele.	272 F/g at 1 A/g	[197]
PANI NRs	0.5 M H_2SO_4/3 ele.	106 F/g at 1 A/g	[198]
3D porous PANI	1 M H_2SO_4/3 ele.	350 F/g at 1 A/g	[199]
Porous PANI	1 M H_2SO_4/3 ele. PVA/ H_2SO_4/2 ele.	455 F/g at 0.5 A/g 149.3 F/g at 0.2 A/g	[200]
PANI hydrogel	1 M H_2SO_4/3 ele.	252 F/g at 0.5 A/g	[201]
PANI aerogel	1 M H_2SO_4/3 ele.	184 F/g at 0.5 A/g	[202]
PANI/rGO	1 M H_2SO_4/2 ele.	220 F/g at 0.2 A/g	[170]
PANI/MWCNT	1 M H_2SO_4/3 ele.	431 F/g at 1.4 A/g	[203]
γ-MnO_2/PANI	0.5 M H_2SO_4/3 ele.	493 F/g at 0.5 A/g	[204]
V_3O_7-rGO-PANI	1 M H_2SO_4/3 ele.	579 F/g at 0.2 A/g	[205]
Ti_3C_2/PANI	1 M H_2SO_4/2 ele.	300.8 F/g at 0.1 A/g	[206]
rGO/PANI	1 M H_2SO_4/2 ele.	438 F/g at 0.5A/g	[207]
graphene/PANI	1 M H_2SO_4/3 ele.	357 F/g at 0.1A/g	[208]
Graphene/PANI	1 M H_2SO_4/3 ele.	257 F/g at 0.1 A/g	[209]
PANI NWAs/3D graphene	1 M H_2SO_4/2 ele.	72.3 F/g at 1 A/g	[210]
PANI/rGO	1 M H_2SO_4/3 ele.	250 F/g at10 mV/s	[211]
PANI/GNRs	1 M H_2SO_4/2 ele.	340 F/g at 0.25 A/g	[212]
rGO/PANI	1 M H_2SO_4/3 ele.	72 F/g at 2 mV/s	[213]
PANI/RGO	1 M H_2SO_4/3 ele.	431 F/g at 0.1 A/g	[214]
PANI/rGO	PVA/H_2SO_4/2 ele.	264 F/g at 1.8 A/g	[215]
PANI-RGO	1 M H_2SO_4/2 ele.	288 F/g @ 0.1 A/g	[216]
NG/PANI	1 M H_2SO_4/2 ele.	93.2 F/g at 1 A/g	[217]
N-GNS-PdNP-PANI	1 M H_2SO_4/2 ele.	230 F/g at 0.1 A/g	[218]
PANI/BG	1 M H_2SO_4/2 ele.	241 F/g at 0.5 A/g	[219]
N-3D-rGO/PANI	1 M H_2SO_4/3 ele.	282 F/g at 1 A/g	[220]
NG / PANI	1 M H_2SO_4/3 ele.	1058 F/cm^3 at 0.5 A/g	[221]
3D NG/PANI	1 M H_2SO_4/2 ele.	528 F/g at 0.1 A/g	[222]
H-NrGO-PANI	10% PVA-H_2SO_4/2 ele.	510 F/g at 1 A/g	[223]
N/SGH/PANI	1 M H_2SO_4/3 ele.	236.5 F/g @ 0.5 A/g	[224]
SG/PANI	1 M H_2SO_4/3 ele.	478 F/g @ 0.5 A/g	[225]
N-carbon /PANI	1 M H_2SO_4/2 ele.	285 F/g at 0.5 A/g	[226]
PANI/N-carbon	2 M KOH /3 ele.	276 F/g at 0.2 A/g	[227]
rGO-Au@PANI	1 M H_2SO_4/2 ele.	212.8 F/g at 1 A/g	[228]
CF@RGO/PANI	1 M H_2SO_4/2 ele.	868.5 F/g at 1 A/g	[229]

CC–PANI–CBf	1 M H_2SO_4/2 ele.	1039 F/g at 0.3 A/g	[230]
PF-rGO/PANI	1 M H_2SO_4/2 ele.	489 F/g at 0.5 A/g	[231]
PANI-IPDI-rGO	PVA/H_2SO_4/2 ele.	485 F/g at 1 A/g	[232]
PANI/GECF	1 M H_2SO_4/2 ele.	976.5 F/g at 0.1 A/g	[233]
PANI-FA	1 M H_2SO_4/2 ele.	208 F/g at 2.5 A/g	[234]
ZnS/RGO/PANI	6 M KOH/2 ele.	722 F/g at 1 A/g	[235]
PANI-RGO-ZnO	1 M H_2SO_4/2 ele.	40.5 F/g at 0.05 A/g	[236]
PANI/NiO/SGO	PVA-KOH/2 ele.	308.8 F/g at 1 A/g	[237]
Polyaniline-Acetylene black-Copper cobaltite	1M KOH/2 ele.	135 F/g at 1 mA/cm^2	[238]
PANI-rGO-Azo	1 M H_2SO_4/2 ele.	310 F/g @ 0.25 A/g	[239]
PANI-NG-$CuCr_2O_4$	1 M H_2SO_4/3 ele.	443.4 F/g at 1 A/g	[240]

The second important approach to improving the properties of PANI materials is designing PANI composites with carbons [42,241,242], CNTs [203,243], graphene [244,245], or even with metal or metal oxides [246–250]. Carbon composites are particularly effective at increasing the cyclic stability and power capability of the electrode. The presence of carbon in the composite increases the electrical conductivity of the electrode, especially when the polymer is in its less conductive neutral (undoped) state. The use of carbonaceous additives with PANI improves electrolyte percolation into the bulk active material, increasing utilization of the polymer surface to participate in the fast charge/discharge process, increasing mechanical strength; and the carbon itself may contribute additional double-layer capacitance [251]. PANI/graphene composites are of special interest because of the specific advantageous properties of graphene discussed in section 1.4.1.5. Graphene-based materials support the growth of PANI nanostructures and improve chemical stability. The crystalline nature of graphene improves the structural stability of the composites. The formation of PANI nanostructures on graphene layers declines the agglomeration and restacking and increases the specific surface area accessible for the electrolyte ions. Table 1.6 summarizes the research work reported on PANI composite-based electrode materials used in SCs.

PANI-Graphene composites studies have revealed promising properties in terms of increased specific capacitance and cyclic stability, when it is employed as electrode material for SCs. However, in desire to use graphene in real world applications, it must be synthesised in its original form and produced in large quantities. Chemical reduction of GO is a promising method for producing rGO in high quantities (rGO) [133]. In addition, rGO is a suitable candidate to composite with PANI to improve the chemical stability and electrochemical performance of electrode material [252–254]. The presence of excess oxygen functional groups and stacked graphene layers in rGO, on the other hand, minimise the conductivity and surface area accessible to electrolyte ions. Meanwhile, heteroatom doping in graphene networks is an effective technique for mitigating the disadvantages and improving the properties of rGO. Doping of heteroatoms causes rGO to become pseudocapacitive, and doping generates trap centers in the graphene lattice to store charge carriers, leading to higher energy storage capacity [149,255,256]. Recent studies are also reported an enhance performance with PANI/Hetero atom doped rGO composites compared to PANI/rGO. For instance, Gopalakrishnan et al. produced N-rGO/PANI composite with a 1:6 ratio using in-situ polymerization and achieved a specific capacitance of 715 F/g at a current density of 0.5 A/g in a three-electrode setup. In this experiment, N doping is achieved by thermal annealing at 900 °C in a N_2 environment. [257]. Zhisen Liu et al. investigated electrochemical properties of N-3D-rGO/PANI nanowire composites, a specific capacitance of 282 F/g at a current density of 1 A/g is found in a three-electrode system where N-rGO is produced using high-temperature thermal treatment. [220]. Liu et al., produced a holey N-rGO Holey nitrogen-doped reduced graphene oxide (H-NrGO) via refluxing GO with $NH_3.H_2O$ as doping reagent and H_2O_2 as etching reagent, followed by chemical reduction. H-NrGO is hybridized with PANI using simple chemical polymerization method. In a symmetric cell configuration, they found that the specific capacitance of H-NrGO/PANI composite (510 F/g at 1 A/g) is higher than the PANI/rGO composite electrodes (426 F/g at 1 A/g) [223]. Hao et al., have reported on sandwich-like polyaniline/B-doped graphene material for SC. The SC behaviour of the prepared electrode materials were evaluated in two different electrolyte systems using symmetric cell assembly. A maximum specific capacitance of 241 and 189 F/g is obtained at 0.5 A/g in 1 M H_2SO_4 and 6 M KOH electrolytes, respectively [219]. Fan et al., synthesized sulfonated graphene/polyaniline nanocomposite paper and studied its electrochemical properties for SC. They found high specific capacitance of 478 F/g at 0.5 A/g in three-electrode configurations [225]. Recently, Du et al., have prepared N, S-co-doped graphene/polyaniline composite hydrogel. The resultant composite delivered a maximum specific capacitance of 236.5 F/g at 0.5 A/g based on a three-electrode configuration [224]. Even though PANI/graphene based composite materials are found to be one of the best electrode materials for SCs, but the specific capacitance is fall below 300 F/g in symmetric configuration (Table 1.6). Therefore, based on this literature, we have been motivated to develop PANI/rGO and PANI-heteroatom doped reduced graphene oxide-based composite materials using a simple and easy synthesis process for obtaining enhanced properties as electrode materials for supercapacitors.

1.5 Objectives of the present study:

The main objectives of the present work are given as follows.

- To develop efficient electrode materials for supercapacitors such as PANI/rGO based composites and biowaste-derived porous carbon.
- To enhance the electrochemical properties of PANI/rGO composite-based electrode materials by doping reduced graphene oxide with nitrogen (N) and sulfur (S).
- To fabricate supercapacitors (in symmetric geometry) by using respective PANI/rGO based composites, and porous carbon as electrode materials, to achieve improved specific capacitance and better cyclic stability.
- **Experimental work carried out:**

1. Preparation of GO using modified Hummers' method, reduced Graphene Oxide (rGO), and heteroatom (N, S) doped rGO is synthesized using hydrothermal reduction method.
2. Preparation of PANI/rGO composite-based electrode materials using in-situ polymerization.
3. The effect of heteroatoms doped rGO on structural and electrochemical properties of PANI composites has been studied.
4. Synthesis of porous carbon using nature abundant biowaste of corn husk by carbonization and chemical activation method.
5. Flexible electrodes are prepared using respective polyaniline-reduced graphene oxide composites and porous carbon materials and their electrochemical properties are evaluated for symmetric supercapacitor.

1.6 Structure of the Thesis

The present thesis explores the utilization of carbon 2D materials for improving the performance of polyaniline composite electrode materials for supercapacitors. The studies on the effect of synthesis method on the structural and electrochemical properties of materials are thoroughly investigated. Further, this study also includes the preparation of porous carbon electrode material from biowaste corn husk for supercapacitors.

- C**hapter 1** has provided an overview of energy demand and the necessity for effective electrochemical energy storage systems. It covers the history of a supercapacitor, types of storage mechanisms that exist, and how they work, as well as the advantages and disadvantages of each type. It also includes information on the types of supercapacitors based on device geometry. In addition, a review of the literature on several types of electrode materials is presented. In particular, polyaniline and polyaniline - graphene composite-based electrode materials for supercapacitors are described. A comparison table of supercapacitor performance based on polyaniline composite electrode materials will be presented. Finally, the objectives and plan of the work are discussed in this chapter.

- **Chapter 2** provides detailed information on the material synthesis and the characterization techniques used in the present study. It includes the preparation of GO using modified Hummers' method, synthesis of rGO, N-rGO, and S-rGO using hydrothermal reduction method, and synthesis of polyaniline, polyaniline reduced graphene oxide-based composites using in-situ polymerization method. It also includes the synthesis of porous carbons using corn husk biowaste as raw material. Further, the details of the characterization and electrochemical techniques used in the present work have been discussed in this chapter. Structural and morphological characterization by X-ray Diffraction (XRD), Fourier transform infrared spectroscopy (FTIR), Raman spectroscopy, X-ray photoelectron spectroscopy (XPS), and Field emission scanning electron microscope (FESEM), High-resolution transmission electron microscopy (HRTEM). The surface area and pore structure of the materials is investigated using N_2 adsorption-desorption measurements. The electrochemical properties are evaluated using cyclic voltammetry (CV), galvanostatic charge-discharge (GCD), and electrochemical impedance spectroscopy (EIS) methods.
- **Chapter 3** describes the structural, morphological, and electrochemical properties of polyaniline-reduced graphene oxide composites (PRGO) which are synthesized using in-situ polymerization followed by low-temperature hydrothermal treatment. During polymerization, aniline monomer gets adsorbed onto the layers of GO easily due to the presence of oxygen functional groups. These adsorbed aniline molecules subsequently get polymerized. Further, the hydrothermal treatment of polymeric solution leads to the reduction of GO and forms a densely packed nanocluster of PANI. The FESEM studies revealed the higher wt.% of GO used in the synthesis of PRGO composite leads to a more densely packed structure which declines the capacitive performance. XRD studies confirm the reduction of GO and the formation of PANI nanostructures on graphene layers. FTIR and Raman studies show that the existence of strong interfacial contact between the polymer chain and graphene layer

leads to improve electrochemical properties. A symmetrical supercapacitor is assembled using a Swagelok cell for evaluating the electrochemical properties of prepared electrodes in 1 M H_2SO_4 electrolyte. PRGO composite with 2 wt.% of GO based electrode material has delivered a maximum specific capacitance of 299 F/g at a current density of 0.5 A/g. Besides, this composite has shown good rate capability and capacitance retention (88%) at a current density of 2 A/g after 2000 charge-discharge cycles.

- **Chapter 4** deals with the structural, morphological, and electrochemical properties of polyaniline-N doped reduced graphene oxide (PANI/N-rGO) composite. Initially, N-rGO is synthesized using hydrothermal method at 180 ^{o}C where urea is used as a reducing agent as well as an N-containing precursor. GO reduction and N doping into graphene lattice is confirmed using XRD, FTIR, Raman, and XPS analysis. *In-situ* polymerization is followed to synthesize PANI/N-rGO composite. The properties of the PANI/N-rGO composite are compared with the pristine PANI and PANI/rGO. From the FESEM studies, the long-range interconnected network morphology is observed for PANI/N-rGO composite which leads to an increase in surface area. N_2 adsorption studies confirm the high surface area of 82.80 m^2/g for PANI/N-rGO owing to the long-range interconnected network-like structure. Flexible electrodes are prepared to study the electrochemical properties of the composite material. In a symmetrical supercapacitor configuration, PANI/N-rGO exhibited enhanced electrochemical properties compared to PANI and PANI/rGO composite. A specific capacitance value of 322 F/g is obtained for PANI/N-rGO composite at a current density of 1 A/g. Further, PANI/N-rGO demonstrates better rate capability and enhanced cycling stability (93% capacitance retention after 1000 cycles).
- **Chapter 5** describes the properties of a facile grown well-aligned sulfonic acid doped polyaniline nanostructures on S-doped reduced graphene oxide (SPANI/S-rGO). S-rGO is synthesized using hydrothermal reduction at 180 ^{o}C where sodium sulfide is used as a reducing agent as well as S containing precursor. *In-situ* polymerization method is used for the growth of PANI nanostructures on S-rGO sheets. The effect of different wt.% of S-rGO on the structural, morphology, and electrochemical performance of SPANI/S-rGO composites is evaluated. The XPS survey spectra of S-rGO contains peak related to S 2p in addition to C 1s and O 1s peaks confirming the successful doping of Sulphur spaces in the graphene network. From the XRD plots of SPANI/S-rGO composites, it is noticed that the intensity of diffraction peak at 25^{o} is

increased with increasing concentration of S-rGO, indicating the successful incorporation of S-rGO nanosheets in the composites. An additional small intensity peak is also observed at 2θ of 43° in SPANI/S-rGO composites, which is related to the graphitic phase of S-rGO. For PANI, vertically aligned nanoarray morphology is observed. In PANI/S-rGO10 (10 wt.% of S-rGO), the growth of PANI nanostructures is more prominent and is vertically aligned in all directions with the support of S-rGO sheets. Further increase in wt.% of S-rGO leads to overlapping of PANI nanostructures with S-rGO which restricts the electroactive surface area accessible for electrolyte ions. The well-aligned nanostructures of SPANI/S-rGO10 composite could result in high contact area for the electrolyte ions to diffuse and enhance the charge transfer property of the material. Flexible electrodes are prepared to study the electrochemical properties of the composite material using the Swagelok cell. The SPANI/S-rGO10 composite electrode delivered a high specific capacitance of 348 F/g at a current density of 1 A/g in a symmetrical supercapacitor. Further, this composite electrode revealed impressive cyclic stability of 89% after 2500 cycles at a current density of 2 A/g. The enhanced performance is attributed to the optimum loading of S-rGO in designing binary composites and the well-aligned growth of SPANI nanostructures on S-rGO sheets.

- **Chapter 6** explains the detailed synthesis of porous carbons from nature-abundant biowaste of corn husk using carbonization and chemical activation process. Initially, the corn husk is subjected to carbonization at 800 °C to prepare corn husk biochar, and then it was subjected to chemical activation by mixing 1:4 wt.% of KOH at different activation temperatures from 600 °C to 800 °C. The effect of activation temperature on the specific surface area and pore structure of the resultant carbons is studied. Along with the high specific surface area, abundant micro and mesoporosity are achieved for the CHPC activated at 800 °C (CHPC-800). FTIR and XPS results revealed the existence of surface oxygen functional groups attached to the carbon network which can improve the surface wettability of the electrodes. In a symmetrical supercapacitor, CHPC-800 electrode material has delivered a maximum specific capacitance of 133 F/g at a current density of 1 A/g. Further, CHPC-800 also showed good cyclic stability, with 93% of capacitance retention after 4500 charge-discharge cycles at a current density of 5 A/g. The improved performance of CHPC-800 is attributed to the combination of both high surface area and porous structure of the material.

- In this Chapter 7, the summary and conclusions of the current thesis work are presented. The scope for future work to expand in the field of research work has also been suggested.

References

[1] BP, Statistical Review of World Energy 2020, 69th edition, (2020) 1–66. https://www.bp.com/content/dam/bp/business-sites/en/global/corporate/pdfs/energy-economics/statistical-review/bp-stats-review-2020-full-report.pdf.

[2] Q. Abbas, M. Mirzaeian, M.R.C. Hunt, P. Hall, R. Raza, Current State and Future Prospects for Electrochemical Energy Storage and Conversion Systems, Energies. 13 (2020) 5847. https://doi.org/10.3390/en13215847.

[3] J. Lelieveld, K. Klingmüller, A. Pozzer, R.T. Burnett, A. Haines, V. Ramanathan, Effects of fossil fuel and total anthropogenic emission removal on public health and climate, Proc. Natl. Acad. Sci. U. S. A. 116 (2019) 7192–7197. https://doi.org/10.1073/pnas.1819989116.

[4] H.I. Becker, US2800616 Low voltage electrolytic capacitor patent, (1954).

[5] Conway B. E., Electrochemical Supercapacitors_ Scientific Fundamental s and Technological Applications, Springer, Boston, MA, 1999. https://doi.org/10.1007/978-1-4757-3058-6_1.

[6] S. Najib, E. Erdem, Current progress achieved in novel materials for supercapacitor electrodes: Mini review, Nanoscale Adv. 1 (2019) 2817–2827. https://doi.org/10.1039/c9na00345b.

[7] L. Zhang, X.S. Zhao, Carbon-based materials as supercapacitor electrodes, Chem. Soc. Rev. 38 (2009) 2520–2531. https://doi.org/10.1039/b813846j.

[8] M. Gouy, Sur la constitution de la charge électrique à la surface d'un électrolyte, J. Phys. Théorique Appliquée. 9 (1910) 457–468. https://doi.org/10.1051/jphystap:019100090045700.

[9] D.L. Chapman, LI. A contribution to the theory of electrocapillarity, London, Edinburgh, Dublin Philos. Mag. J. Sci. 25 (1913) 475–481. https://doi.org/10.1080/14786440408634187.

[10] R. Dubey, V. Guruviah, Review of carbon-based electrode materials for supercapacitor energy storage, Ionics (Kiel). 25 (2019) 1419–1445. https://doi.org/10.1007/s11581-019-02874-0.

[11] Q. Meng, K. Cai, Y. Chen, L. Chen, Research progress on conducting polymer based supercapacitor electrode materials, Nano Energy. 36 (2017) 268–285. https://doi.org/10.1016/j.nanoen.2017.04.040.

[12] B.E. Conway, V. Birss, J. Wojtowicz, The role and utilization of pseudocapacitance for energy storage by supercapacitors, J. Power Sources. 66 (1997) 1–14. https://doi.org/10.1016/S0378-7753(96)02474-3.

[13] C. Peng, S. Zhang, D. Jewell, G.Z. Chen, Carbon nanotube and conducting polymer composites for supercapacitors, Prog. Nat. Sci. 18 (2008) 777–788. https://doi.org/10.1016/j.pnsc.2008.03.002.

[14] C.C. Hu, K.H. Chang, M.C. Lin, Y.T. Wu, Design and tailoring of the nanotubular

arrayed architecture of hydrous RuO2 for next generation supercapacitors, Nano Lett. 6 (2006) 2690–2695. https://doi.org/10.1021/nl061576a.

[15] A.L.M. Reddy, S. Ramaprabhu, Nanocrystalline metal oxides dispersed multiwalled carbon nanotubes as supercapacitor electrodes, J. Phys. Chem. C. 111 (2007) 7727–7734. https://doi.org/10.1021/jp069006m.

[16] V.S. Marin Halper James C Ellenbogen, Supercapacitors: A Brief Overview, in: The MITRE Corporation, McLean, Virginia, USA, 2006. http://www.mitre.org/tech/nanotech (accessed March 14, 2022).

[17] M.Y. HO, P.S. KHIEW, D. ISA, T.K. TAN, W.S. CHIU, C.H. CHIA, a Review of Metal Oxide Composite Electrode Materials for Electrochemical Capacitors, Nano. 09 (2014) 1430002. https://doi.org/10.1142/s1793292014300023.

[18] Z. Tehrani, D.J. Thomas, T. Korochkina, C.O. Phillips, D. Lupo, S. Lehtimäki, J. O'Mahony, D.T. Gethin, Large-area printed supercapacitor technology for low-cost domestic green energy storage, Energy. 118 (2017) 1313–1321. https://doi.org/10.1016/j.energy.2016.11.019.

[19] Tecate Group - Markets & Applications., (n.d.). https://www.tecategroup.com/markets/?market=Military-Aerospace (accessed April 23, 2022).

[20] M.E. Şahin, F. Blaabjerg, A. Sangwongwanich, A Comprehensive Review on Supercapacitor Applications and Developments, Energies. 15 (2022) 674. https://doi.org/10.3390/en15030674.

[21] Z. Bi, Q. Kong, Y. Cao, G. Sun, F. Su, X. Wei, X. Li, A. Ahmad, L. Xie, C.M. Chen, Biomass-derived porous carbon materials with different dimensions for supercapacitor electrodes: A review, J. Mater. Chem. A. 7 (2019) 16028–16045. https://doi.org/10.1039/c9ta04436a.

[22] A. Mohammad-Khah, R. Ansari, Activated charcoal: Preparation, characterization and applications: A review article, Int. J. ChemTech Res. 1 (2009) 859–864.

[23] H. Lu, X.S. Zhao, Biomass-derived carbon electrode materials for supercapacitors, Sustain. Energy Fuels. 1 (2017) 1265–1281. https://doi.org/10.1039/C7SE00099E.

[24] S. Sundriyal, V. Shrivastav, H.D. Pham, S. Mishra, A. Deep, D.P. Dubal, Advances in bio-waste derived activated carbon for supercapacitors: Trends, challenges and prospective, Resour. Conserv. Recycl. 169 (2021) 105548. https://doi.org/10.1016/j.resconrec.2021.105548.

[25] X. Hao, J. Wang, B. Ding, Y. Wang, Z. Chang, H. Dou, X. Zhang, Bacterial-cellulose-derived interconnected meso-microporous carbon nanofiber networks as binder-free electrodes for high-performance supercapacitors, J. Power Sources. 352 (2017) 34–41. https://doi.org/10.1016/j.jpowsour.2017.03.088.

[26] L. Xie, G. Sun, F. Su, X. Guo, Q. Kong, X. Li, X. Huang, L. Wan, W. Song, K. Li, C. Lv, C.M. Chen, Hierarchical porous carbon microtubes derived from willow catkins for supercapacitor applications, J. Mater. Chem. A. 4 (2016) 1637–1646. https://doi.org/10.1039/c5ta09043a.

[27] D. Zhou, H. Wang, N. Mao, Y. Chen, Y. Zhou, T. Yin, H. Xie, W. Liu, S. Chen, X. Wang, High energy supercapacitors based on interconnected porous carbon nanosheets with ionic liquid electrolyte, Microporous Mesoporous Mater. 241 (2017) 202–209. https://doi.org/10.1016/j.micromeso.2017.01.001.

[28] P. Hao, Z. Zhao, J. Tian, H. Li, Y. Sang, G. Yu, H. Cai, H. Liu, C.P. Wong, A. Umar, Hierarchical porous carbon aerogel derived from bagasse for high performance supercapacitor electrode, Nanoscale. 6 (2014) 12120–12129. https://doi.org/10.1039/c4nr03574g.

[29] P. Wang, G. Zhang, M.Y. Li, Y.X. Yin, J.Y. Li, G. Li, W.P. Wang, W. Peng, F.F. Cao, Y.G. Guo, Porous carbon for high-energy density symmetrical supercapacitor and lithium-ion hybrid electrochemical capacitors, Chem. Eng. J. 375 (2019) 122020. https://doi.org/10.1016/j.cej.2019.122020.

[30] B. Li, F. Dai, Q. Xiao, L. Yang, J. Shen, C. Zhang, M. Cai, Nitrogen-doped activated carbon for a high energy hybrid supercapacitor, Energy Environ. Sci. 9 (2016) 102–106. https://doi.org/10.1039/c5ee03149d.

[31] C. Li, X. Zhang, Z. Lv, K. Wang, X. Sun, X. Chen, Y. Ma, Scalable combustion synthesis of graphene-welded activated carbon for high-performance supercapacitors, Chem. Eng. J. 414 (2021) 128781. https://doi.org/10.1016/j.cej.2021.128781.

[32] C. Largeot, C. Portet, J. Chmiola, P.L. Taberna, Y. Gogotsi, P. Simon, Relation between the ion size and pore size for an electric double-layer capacitor, J. Am. Chem. Soc. 130 (2008) 2730–2731. https://doi.org/10.1021/ja7106178.

[33] J. Yu, X. Li, Z. Cui, D. Chen, X. Pang, Q. Zhang, F. Shao, H. Dong, L. Yu, L. Dong, Tailoring in-situ N, O, P, S-doped soybean-derived porous carbon with ultrahigh capacitance in both acidic and alkaline media, Renew. Energy. 163 (2021) 375–385. https://doi.org/10.1016/j.renene.2020.08.066.

[34] L. Cao, H. Li, Z. Xu, H. Zhang, L. Ding, S. Wang, G. Zhang, H. Hou, W. Xu, F. Yang, S. Jiang, Comparison of the heteroatoms-doped biomass-derived carbon prepared by one-step nitrogen-containing activator for high performance supercapacitor, Diam. Relat. Mater. 114 (2021) 108316. https://doi.org/10.1016/j.diamond.2021.108316.

[35] R. Zhang, W. Zhang, M. Shi, H. Li, L. Ma, H. Niu, Morphology controllable synthesis of heteroatoms-doped carbon materials for high-performance flexible supercapacitor, Dye. Pigment. 199 (2022) 109968. https://doi.org/10.1016/j.dyepig.2021.109968.

[36] B. Sriram, A. Sathiyan, S.F. Wang, E. Elanthamilan, X.B. Joseph, J.N. Baby, J.P. Merlin, J.C. Ezhilarasi, Synergistic effect of Co3O4 nanoparticles with Bauhinia vahlii dry fruits derived activated carbon on energy storage applications, J. Solid State Chem. 295 (2021) 121931. https://doi.org/10.1016/j.jssc.2020.121931.

[37] T. Yumak, D. Bragg, E.M. Sabolsky, Effect of synthesis methods on the surface and electrochemical characteristics of metal oxide/activated carbon composites for supercapacitor applications, Appl. Surf. Sci. 469 (2019) 983–993. https://doi.org/10.1016/j.apsusc.2018.09.079.

[38] Sowmya, M. Selvakumar, Multilayered electrode materials based on polyaniline/activated carbon composites for supercapacitor applications, Int. J. Hydrogen Energy. 43 (2018) 4067–4080. https://doi.org/10.1016/j.ijhydene.2017.10.106.

[39] K.S. Lee, M.S. Park, J.D. Kim, Nitrogen doped activated carbon with nickel oxide for high specific capacitance as supercapacitor electrodes, Colloids Surfaces A Physicochem. Eng. Asp. 533 (2017) 323–329.

https://doi.org/10.1016/j.colsurfa.2017.09.008.

[40] K.S. Lee, C.W. Park, J.D. Kim, Synthesis of ZnO/activated carbon with high surface area for supercapacitor electrodes, Colloids Surfaces A Physicochem. Eng. Asp. 555 (2018) 482–490. https://doi.org/10.1016/j.colsurfa.2018.06.077.

[41] F. Wang, J. Ma, K. Zhou, X. Li, MoS2/corncob-derived activated carbon for supercapacitor application, Mater. Chem. Phys. 244 (2020) 122215. https://doi.org/10.1016/j.matchemphys.2019.122215.

[42] L. Gao, L. Xiong, D. Xu, J. Cai, L. Huang, J. Zhou, L. Zhang, Distinctive Construction of Chitin-Derived Hierarchically Porous Carbon Microspheres/Polyaniline for High-Rate Supercapacitors, ACS Appl. Mater. Interfaces. 10 (2018) 28918–28927. https://doi.org/10.1021/acsami.8b05891.

[43] N.M. Musyoka, B.K. Mutuma, N. Manyala, Onion-derived activated carbons with enhanced surface area for improved hydrogen storage and electrochemical energy application, RSC Adv. 10 (2020) 26928–26936. https://doi.org/10.1039/d0ra04556j.

[44] M.M. Baig, I.H. Gul, Conversion of wheat husk to high surface area activated carbon for energy storage in high-performance supercapacitors, Biomass and Bioenergy. 144 (2021) 105909. https://doi.org/10.1016/j.biombioe.2020.105909.

[45] K. Le Van, T.T. Luong Thi, Activated carbon derived from rice husk by NaOH activation and its application in supercapacitor, Prog. Nat. Sci. Mater. Int. 24 (2014) 191–198. https://doi.org/10.1016/j.pnsc.2014.05.012.

[46] W. Fan, H. Zhang, H. Wang, X. Zhao, S. Sun, J. Shi, M. Huang, W. Liu, Y. Zheng, P. Li, Dual-doped hierarchical porous carbon derived from biomass for advanced supercapacitors and lithium ion batteries, RSC Adv. 9 (2019) 32382–32394. https://doi.org/10.1039/c9ra06914c.

[47] G.A. Yakaboylu, C. Jiang, T. Yumak, J.W. Zondlo, J. Wang, E.M. Sabolsky, Engineered hierarchical porous carbons for supercapacitor applications through chemical pretreatment and activation of biomass precursors, Renew. Energy. 163 (2021) 276–287. https://doi.org/10.1016/j.renene.2020.08.092.

[48] L. Guan, L. Pan, T. Peng, C. Gao, W. Zhao, Z. Yang, H. Hu, M. Wu, Synthesis of Biomass-Derived Nitrogen-Doped Porous Carbon Nanosheests for High-Performance Supercapacitors, ACS Sustain. Chem. Eng. 7 (2019) 8405–8412. https://doi.org/10.1021/acssuschemeng.9b00050.

[49] P. Yu, Y. Liang, H. Dong, H. Hu, S. Liu, L. Peng, M. Zheng, Y. Xiao, Y. Liu, Rational Synthesis of Highly Porous Carbon from Waste Bagasse for Advanced Supercapacitor Application, ACS Sustain. Chem. Eng. 6 (2018) 15325–15332. https://doi.org/10.1021/acssuschemeng.8b03763.

[50] P. Cheng, T. Li, H. Yu, L. Zhi, Z. Liu, Z. Lei, Biomass-Derived Carbon Fiber Aerogel as a Binder-Free Electrode for High-Rate Supercapacitors, J. Phys. Chem. C. 120 (2016) 2079–2086. https://doi.org/10.1021/acs.jpcc.5b11280.

[51] M. Mondal, D.K. Goswami, T.K. Bhattacharyya, Lignocellulose based Bio-waste Materials derived Activated Porous Carbon as Superior Electrode Materials for High-Performance Supercapacitor, J. Energy Storage. 34 (2021) 102229. https://doi.org/10.1016/j.est.2020.102229.

[52] M. Karnan, K. Subramani, P.K. Srividhya, M. Sathish, Electrochemical Studies on

Corncob Derived Activated Porous Carbon for Supercapacitors Application in Aqueous and Non-aqueous Electrolytes, Electrochim. Acta. 228 (2017) 586–596. https://doi.org/10.1016/j.electacta.2017.01.095.

[53] H.A. Hamouda, S. Cui, X. Dai, L. Xiao, X. Xie, H. Peng, G. Ma, Synthesis of porous carbon material based on biomass derived from hibiscus sabdariffa fruits as active electrodes for high-performance symmetric supercapacitors, RSC Adv. 11 (2020) 354–363. https://doi.org/10.1039/d0ra09509e.

[54] V. Yang, R.A. Senthil, J. Pan, A. Khan, S. Osman, L. Wang, W. Jiang, Y. Sun, Highly ordered hierarchical porous carbon derived from biomass waste mangosteen peel as superior cathode material for high performance supercapacitor, J. Electroanal. Chem. 855 (2019) 113616. https://doi.org/10.1016/j.jelechem.2019.113616.

[55] N. Sudhan, K. Subramani, M. Karnan, N. Ilayaraja, M. Sathish, Biomass-derived activated porous carbon from rice straw for a high-energy symmetric supercapacitor in aqueous and nonaqueous electrolytes, Energy and Fuels. 31 (2017) 977–985. https://doi.org/10.1021/acs.energyfuels.6b01829.

[56] T. Mitravinda, K. Nanaji, S. Anandan, A. Jyothirmayi, V.S.K. Chakravadhanula, C.S. Sharma, T.N. Rao, Facile Synthesis of Corn Silk Derived Nanoporous Carbon for an Improved Supercapacitor Performance, J. Electrochem. Soc. 165 (2018) A3369–A3379. https://doi.org/10.1149/2.0621814jes.

[57] Y. Lu, F. Xu, L. Sun, Y. Wu, Y. Xia, X. Cai, N. Zhong, H. Zhang, B. Li, H. Chu, Facile method for preparation of porous carbon derived from biomass for high performance supercapacitors, Int. J. Electrochem. Sci. 14 (2019) 11199–11211. https://doi.org/10.20964/2019.12.54.

[58] L. Qiang, Z. Hu, Z. Li, Y. Yang, X. Wang, Y. Zhou, X. Zhang, W. Wang, Q. Wang, Buckwheat husk-derived hierarchical porous nitrogen-doped carbon materials for high-performance symmetric supercapacitor, J. Porous Mater. 26 (2019) 1217–1225. https://doi.org/10.1007/s10934-019-00723-z.

[59] C. Qin, S. Wang, Z. Wang, K. Ji, S. Wang, X. Zeng, X. Jiang, G. Liu, Hierarchical porous carbon derived from Gardenia jasminoides Ellis flowers for high performance supercapacitor, J. Energy Storage. 33 (2021) 102061. https://doi.org/10.1016/j.est.2020.102061.

[60] Y. Li, D. Zhang, Y. Zhang, J. He, Y. Wang, K. Wang, Y. Xu, H. Li, Y. Wang, Biomass-derived microporous carbon with large micropore size for high-performance supercapacitors, J. Power Sources. 448 (2020) 227396. https://doi.org/10.1016/j.jpowsour.2019.227396.

[61] S. Yaglikci, Y. Gokce, E. Yagmur, Z. Aktas, The performance of sulphur doped activated carbon supercapacitors prepared from waste tea, Environ. Technol. (United Kingdom). 41 (2020) 36–48. https://doi.org/10.1080/09593330.2019.1575480.

[62] T.R. Kumar, R.A. Senthil, Z. Pan, J. Pan, Y. Sun, A tubular-like porous carbon derived from waste American poplar fruit as advanced electrode material for high-performance supercapacitor, J. Energy Storage. 32 (2020) 101903. https://doi.org/10.1016/j.est.2020.101903.

[63] D.K. Sam, E.K. Sam, A. Durairaj, X. Lv, Z. Zhou, J. Liu, Synthesis of biomass-based carbon aerogels in energy and sustainability, Carbohydr. Res. 491 (2020)

107986. https://doi.org/10.1016/j.carres.2020.107986.

[64] J. Li, X. Wang, Q. Huang, S. Gamboa, P.J. Sebastian, Studies on preparation and performances of carbon aerogel electrodes for the application of supercapacitor, J. Power Sources. 158 (2006) 784–788. https://doi.org/10.1016/j.jpowsour.2005.09.045.

[65] F. Li, L. Xie, G. Sun, Q. Kong, F. Su, Y. Cao, J. Wei, A. Ahmad, X. Guo, C.M. Chen, Resorcinol-formaldehyde based carbon aerogel: Preparation, structure and applications in energy storage devices, Microporous Mesoporous Mater. 279 (2019) 293–315. https://doi.org/10.1016/j.micromeso.2018.12.007.

[66] Y. Zhu, H. Hu, W.C. Li, X. Zhang, Cresol-formaldehyde based carbon aerogel as electrode material for electrochemical capacitor, J. Power Sources. 162 (2006) 738–742. https://doi.org/10.1016/j.jpowsour.2006.06.049.

[67] R.W. Pekala, J.C. Farmer, C.T. Alviso, T.D. Tran, S.T. Mayer, J.M. Miller, B. Dunn, Carbon aerogels for electrochemical applications, J. Non. Cryst. Solids. 225 (1998) 74–80. https://doi.org/10.1016/S0022-3093(98)00011-8.

[68] D. Salinas-Torres, A.F. Léonard, V. Stergiopoulos, Y. Busby, J.J. Pireaux, N. Job, Effect of nitrogen doping on the pore texture of carbon xerogels based on resorcinol-melamine-formaldehyde precursors, Microporous Mesoporous Mater. 256 (2018) 190–198. https://doi.org/10.1016/j.micromeso.2017.08.004.

[69] N. Job, A. Théry, R. Pirard, J. Marien, L. Kocon, J.N. Rouzaud, F. Béguin, J.P. Pirard, Carbon aerogels, cryogels and xerogels: Influence of the drying method on the textural properties of porous carbon materials, Carbon N. Y. 43 (2005) 2481–2494. https://doi.org/10.1016/j.carbon.2005.04.031.

[70] C. Li, X. Yang, G. Zhang, Mesopore-dominant activated carbon aerogels with high surface area for electric double-layer capacitor application, Mater. Lett. 161 (2015) 538–541. https://doi.org/10.1016/j.matlet.2015.09.003.

[71] C. Lu, Y.H. Huang, J.S. Hong, Y.J. Wu, J. Li, J.P. Cheng, The effects of melamine on the formation of carbon xerogel derived from resorcinol and formaldehyde and its performance for supercapacitor, J. Colloid Interface Sci. 524 (2018) 209–218. https://doi.org/10.1016/j.jcis.2018.04.006.

[72] M. Mirzaeian, Q. Abbas, D. Gibson, M. Mazur, Effect of nitrogen doping on the electrochemical performance of resorcinol-formaldehyde based carbon aerogels as electrode material for supercapacitor applications, Energy. 173 (2019) 809–819. https://doi.org/10.1016/j.energy.2019.02.108.

[73] W. Liu, X. Li, M. Zhu, X. He, High-performance all-solid state asymmetric supercapacitor based on Co3O4 nanowires and carbon aerogel, J. Power Sources. 282 (2015) 179–186. https://doi.org/10.1016/j.jpowsour.2015.02.047.

[74] F.Y. Zeng, Z.Y. Sui, S. Liu, H.P. Liang, H.H. Zhan, B.H. Han, Nitrogen-doped carbon aerogels with high surface area for supercapacitors and gas adsorption, Mater. Today Commun. 16 (2018) 1–7. https://doi.org/10.1016/j.mtcomm.2018.03.015.

[75] H. Zhuo, Y. Hu, X. Tong, L. Zhong, X. Peng, R. Sun, Sustainable hierarchical porous carbon aerogel from cellulose for high-performance supercapacitor and CO2 capture, Ind. Crops Prod. 87 (2016) 229–235. https://doi.org/10.1016/j.indcrop.2016.04.041.

[76] Z. Zhai, B. Ren, Y. Xu, S. Wang, L. Zhang, Z. Liu, Nitrogen self-doped carbon aerogels from chitin for supercapacitors, J. Power Sources. 481 (2021) 228976. https://doi.org/10.1016/j.jpowsour.2020.228976.

[77] G. Ramos-Fernández, M. Canal-Rodríguez, A. Arenillas, J.A. Menéndez, I. Rodríguez-Pastor, I. Martin-Gullon, Determinant influence of the electrical conductivity versus surface area on the performance of graphene oxide-doped carbon xerogel supercapacitors, Carbon N. Y. 126 (2018) 456–463. https://doi.org/10.1016/j.carbon.2017.10.025.

[78] S. Guo, H. Li, X. Zhang, H. Nawaz, S. Chen, X. Zhang, F. Xu, Lignin carbon aerogel/nickel binary network for cubic supercapacitor electrodes with ultra-high areal capacitance, Carbon N. Y. 174 (2021) 500–508. https://doi.org/10.1016/j.carbon.2020.12.051.

[79] X. Zhang, H. Li, W. Zhang, Z. Huang, C.P. Tsui, C. Lu, C. He, Y. Yang, In-situ growth of polypyrrole onto bamboo cellulose-derived compressible carbon aerogels for high performance supercapacitors, Electrochim. Acta. 301 (2019) 55–62. https://doi.org/10.1016/j.electacta.2019.01.166.

[80] J. Tan, Y. Han, L. He, Y. Dong, X. Xu, D. Liu, H. Yan, Q. Yu, C. Huang, L. Mai, In situ nitrogen-doped mesoporous carbon nanofibers as flexible freestanding electrodes for high-performance supercapacitors, J. Mater. Chem. A. 5 (2017) 23620–23627. https://doi.org/10.1039/c7ta07024a.

[81] L.F. Chen, Y. Lu, L. Yu, X.W. Lou, Designed formation of hollow particle-based nitrogen-doped carbon nanofibers for high-performance supercapacitors, Energy Environ. Sci. 10 (2017) 1777–1783. https://doi.org/10.1039/c7ee00488e.

[82] X. Wu, R. Liu, J. Zhao, Z. Fan, Advanced carbon materials with different spatial dimensions for supercapacitors, Nano Mater. Sci. 3 (2021) 241–267. https://doi.org/10.1016/j.nanoms.2021.01.002.

[83] J. Liang, H. Zhao, L. Yue, G. Fan, T. Li, S. Lu, G. Chen, S. Gao, A.M. Asiri, X. Sun, Recent advances in electrospun nanofibers for supercapacitors, J. Mater. Chem. A. 8 (2020) 16747–16789. https://doi.org/10.1039/d0ta05100d.

[84] Q. Yu, J. Lv, Z. Liu, M. Xu, W. Yang, K.A. Owusu, L. Mai, D. Zhao, L. Zhou, Macroscopic synthesis of ultrafine N–doped carbon nanofibers for superior capacitive energy storage, Sci. Bull. 64 (2019) 1617–1624. https://doi.org/10.1016/j.scib.2019.08.008.

[85] H.H.H. Wang, W. Wang, H.H.H. Wang, X. Jin, H. Niu, H.H.H. Wang, H. Zhou, T. Lin, High Performance Supercapacitor Electrode Materials from Electrospun Carbon Nanofibers in Situ Activated by High Decomposition Temperature Polymer, ACS Appl. Energy Mater. 1 (2018) 431–439. https://doi.org/10.1021/acsaem.7b00083.

[86] Y. Liu, J. Zhou, L. Chen, P. Zhang, W. Fu, H. Zhao, Y. Ma, X. Pan, Z. Zhang, W. Han, E. Xie, Highly Flexible Freestanding Porous Carbon Nanofibers for Electrodes Materials of High-Performance All-Carbon Supercapacitors, ACS Appl. Mater. Interfaces. 7 (2015) 23515–23520. https://doi.org/10.1021/acsami.5b06107.

[87] X. Li, Y. Zhao, Y. Bai, X. Zhao, R. Wang, Y. Huang, Q. Liang, Z. Huang, A Non-Woven Network of Porous Nitrogen-doping Carbon Nanofibers as a Binder-free Electrode for Supercapacitors, Electrochim. Acta. 230 (2017) 445–453.

https://doi.org/10.1016/j.electacta.2017.02.030.

[88] Q. Jiang, M. Liu, C. Shao, X. Li, H. Liu, X. Li, Y. Liu, Nitrogen doping polyvinylpyrrolidone-based carbon nanofibers via pyrolysis of g-C3N4 with tunable chemical states and capacitive energy storage, Electrochim. Acta. 330 (2020) 135212. https://doi.org/10.1016/j.electacta.2019.135212.

[89] A.P. Tiwari, S.H. Chae, G.P. Ojha, B. Dahal, T. Mukhiya, M. Lee, K. Chhetri, T. Kim, H.Y. Kim, Three-dimensional porous carbonaceous network with in-situ entrapped metallic cobalt for supercapacitor application, J. Colloid Interface Sci. 553 (2019) 622–630. https://doi.org/10.1016/j.jcis.2019.06.070.

[90] D. Tian, X. Lu, G. Nie, M. Gao, N. Song, C. Wang, Growth of polyaniline thorns on hybrid electrospun CNFs with nickel nanoparticles and graphene nanosheets as binder-free electrodes for high-performance supercapacitors, Appl. Surf. Sci. 458 (2018) 389–396. https://doi.org/10.1016/j.apsusc.2018.07.103.

[91] M. Zhi, S. Liu, Z. Hong, N. Wu, Electrospun activated carbon nanofibers for supercapacitor electrodes, RSC Adv. 4 (2014) 43619–43623. https://doi.org/10.1039/c4ra05512h.

[92] Y.J. Heo, H.I. Lee, J.W. Lee, M. Park, K.Y. Rhee, S.J. Park, Optimization of the pore structure of PAN-based carbon fibers for enhanced supercapacitor performances via electrospinning, Compos. Part B Eng. 161 (2019) 10–17. https://doi.org/10.1016/j.compositesb.2018.10.026.

[93] X. Yan, H. You, W. Liu, X. Wang, D. Wu, Free-standing and heteroatoms-doped carbon nanofiber networks as a binder-free flexible electrode for high-performance supercapacitors, Nanomaterials. 9 (2019) 1189. https://doi.org/10.3390/nano9091189.

[94] G. He, Y. Song, S. Chen, L. Wang, Porous carbon nanofiber mats from electrospun polyacrylonitrile/polymethylmethacrylate composite nanofibers for supercapacitor electrode materials, J. Mater. Sci. 53 (2018) 9721–9730. https://doi.org/10.1007/s10853-018-2277-5.

[95] W. Na, J. Jun, J.W. Park, G. Lee, J. Jang, Highly porous carbon nanofibers co-doped with fluorine and nitrogen for outstanding supercapacitor performance, J. Mater. Chem. A. 5 (2017) 17379–17387. https://doi.org/10.1039/c7ta04406b.

[96] C.M. Yang, B.H. Kim, Highly conductive pitch-based carbon nanofiber/MnO 2 composites for high-capacitance supercapacitors, J. Alloys Compd. 749 (2018) 441–447. https://doi.org/10.1016/j.jallcom.2018.03.305.

[97] T. Kshetri, T.D. Thanh, S.B. Singh, N.H. Kim, J.H. Lee, Hierarchical material of carbon nanotubes grown on carbon nanofibers for high performance electrochemical capacitor, Chem. Eng. J. 345 (2018) 39–47. https://doi.org/10.1016/j.cej.2018.03.143.

[98] Z.Y. Yang, Y.H. Wang, Z. Dai, Z.W. Lu, X.Y. Gu, H. Zhao, G.Z. Sun, W. Lan, Z.X. Zhang, X.J. Pan, J.Y. Zhou, E.Q. Xie, Nature of improved double-layer capacitance by KOH activation on carbon nanotube-carbon nanofiber hierarchical hybrids for supercapacitors, Carbon N. Y. 146 (2019) 610–617. https://doi.org/10.1016/j.carbon.2019.02.057.

[99] V. Kuzmenko, N. Wang, M. Haque, O. Naboka, M. Flygare, K. Svensson, P. Gatenholm, J. Liu, P. Enoksson, Cellulose-derived carbon nanofibers/graphene composite electrodes for powerful compact supercapacitors, RSC Adv. 7 (2017)

45968–45977. https://doi.org/10.1039/c7ra07533b.

[100] Z. Dai, P.G. Ren, Y.L. Jin, H. Zhang, F. Ren, Q. Zhang, Nitrogen-sulphur Co-doped graphenes modified electrospun lignin/polyacrylonitrile-based carbon nanofiber as high performance supercapacitor, J. Power Sources. 437 (2019) 226937. https://doi.org/10.1016/j.jpowsour.2019.226937.

[101] X. Li, X. Chen, Y. Zhao, Y. Deng, J. Zhu, S. Jiang, R. Wang, Flexible all-solid-state supercapacitors based on an integrated electrode of hollow N-doped carbon nanofibers embedded with graphene nanosheets, Electrochim. Acta. 332 (2020) 135398. https://doi.org/10.1016/j.electacta.2019.135398.

[102] J. Zhou, J. Chen, S. Han, H. Zhao, J. Bai, Z. Yang, X. Mu, Y. Liu, D. Bian, G. Sun, Z. Zhang, X. Pan, E. Xie, Constructing optimized three-dimensional electrochemical interface in carbon nanofiber/carbon nanotube hierarchical composites for high-energy-density supercapacitors, Carbon N. Y. 111 (2017) 502–512. https://doi.org/10.1016/j.carbon.2016.10.036.

[103] F. Miao, C. Shao, X. Li, N. Lu, K. Wang, X. Zhang, Y. Liu, Polyaniline-coated electrospun carbon nanofibers with high mass loading and enhanced capacitive performance as freestanding electrodes for flexible solid-state supercapacitors, Energy. 95 (2016) 233–241. https://doi.org/10.1016/j.energy.2015.12.013.

[104] X. Li, A. Rafie, Y.Y. Smolin, S. Simotwo, V. Kalra, K.K.S. Lau, Engineering conformal nanoporous polyaniline via oxidative chemical vapor deposition and its potential application in supercapacitors, Chem. Eng. Sci. 194 (2019) 156–164. https://doi.org/10.1016/j.ces.2018.06.053.

[105] M. Yanilmaz, M. Dirican, A.M. Asiri, X. Zhang, Flexible polyaniline-carbon nanofiber supercapacitor electrodes, J. Energy Storage. 24 (2019) 100766. https://doi.org/10.1016/j.est.2019.100766.

[106] H. Sun, S. Li, Y. Shen, F. Miao, P. Zhang, G. Shao, Integrated structural design of polyaniline-modified nitrogen-doped hierarchical porous carbon nanofibers as binder-free electrodes toward all-solid-state flexible supercapacitors, Appl. Surf. Sci. 501 (2020) 144001. https://doi.org/10.1016/j.apsusc.2019.144001.

[107] D. Yang, W. Ni, J. Cheng, Z. Wang, C. Li, Y. Zhang, B. Wang, Omnidirectional porous fiber scrolls of polyaniline nanopillars array-N-doped carbon nanofibers for fiber-shaped supercapacitors, Mater. Today Energy. 5 (2017) 196–204. https://doi.org/10.1016/j.mtener.2017.06.011.

[108] C. Zheng, W. Qian, C. Cui, G. Xu, M. Zhao, G. Tian, F. Wei, Carbon nanotubes for supercapacitors: Consideration of cost and chemical vapor deposition techniques, J. Nat. Gas Chem. 21 (2012) 233–240. https://doi.org/10.1016/S1003-9953(11)60358-7.

[109] T. Chen, L. Dai, Carbon nanomaterials for high-performance supercapacitors, Mater. Today. 16 (2013) 272–280. https://doi.org/10.1016/j.mattod.2013.07.002.

[110] A.R. John, P. Arumugam, Open ended nitrogen-doped carbon nanotubes for the electrochemical storage of energy in a supercapacitor electrode, J. Power Sources. 277 (2015) 387–392. https://doi.org/10.1016/j.jpowsour.2014.11.151.

[111] A. Roy, A. Ray, S. Saha, M. Ghosh, T. Das, B. Satpati, M. Nandi, S. Das, NiO-CNT composite for high performance supercapacitor electrode and oxygen evolution reaction, Electrochim. Acta. 283 (2018) 327–337. https://doi.org/10.1016/j.electacta.2018.06.154.

[112] Y. Luo, T. Yang, Q. Zhao, M. Zhang, CeO2/CNTs hybrid with high performance as electrode materials for supercapacitor, J. Alloys Compd. 729 (2017) 64–70. https://doi.org/10.1016/j.jallcom.2017.09.165.

[113] B. Ding, D. Guo, Y. Wang, X. Wu, Z. Fan, Functionalized graphene nanosheets decorated on carbon nanotubes networks for high performance supercapacitors, J. Power Sources. 398 (2018) 113–119. https://doi.org/10.1016/j.jpowsour.2018.07.063.

[114] Q. Jiang, Y. Shang, Y. Sun, Y. Yang, S. Hou, Y. Zhang, J. Xu, A. Cao, Flexible and multi-form solid-state supercapacitors based on polyaniline/graphene oxide/CNT composite films and fibers, Diam. Relat. Mater. 92 (2019) 198–207. https://doi.org/10.1016/j.diamond.2019.01.004.

[115] S. Asim, M.S. Javed, S. Hussain, M. Rana, F. Iram, D. Lv, M. Hashim, M. Saleem, M. Khalid, R. Jawaria, Z. Ullah, N. Gull, RuO2 nanorods decorated CNTs grown carbon cloth as a free standing electrode for supercapacitor and lithium ion batteries, Electrochim. Acta. 326 (2019) 135009. https://doi.org/10.1016/j.electacta.2019.135009.

[116] J. Di, H. Xu, X. Gai, R. Yang, H. Zheng, One-step solvothermal synthesis of feather duster-like CNT@WO 3 as high-performance electrode for supercapacitor, Mater. Lett. 246 (2019) 129–132. https://doi.org/10.1016/j.matlet.2019.03.070.

[117] X. Li, Y. Tang, J. Song, W. Yang, M. Wang, C. Zhu, W. Zhao, J. Zheng, Y. Lin, Self-supporting activated carbon/carbon nanotube/reduced graphene oxide flexible electrode for high performance supercapacitor, Carbon N. Y. 129 (2018) 236–244. https://doi.org/10.1016/j.carbon.2017.11.099.

[118] Q. Zhou, T. Fan, Y. Li, D. Chen, S. Liu, X. Li, Hollow–structure NiCo hydroxide/carbon nanotube composite for High–Performance supercapacitors, J. Power Sources. 426 (2019) 111–115. https://doi.org/10.1016/j.jpowsour.2019.04.035.

[119] H. Li, Z. Li, Z. Wu, M. Sun, S. Han, C. Cai, W. Shen, X.T. Liu, Y.Q. Fu, Enhanced electrochemical performance of CuCo 2 S 4 /carbon nanotubes composite as electrode material for supercapacitors, J. Colloid Interface Sci. 549 (2019) 105–113. https://doi.org/10.1016/j.jcis.2019.04.056.

[120] W. Wang, S. Guo, M. Penchev, I. Ruiz, K.N. Bozhilov, D. Yan, M. Ozkan, C.S. Ozkan, Three dimensional few layer graphene and carbon nanotube foam architectures for high fidelity supercapacitors, Nano Energy. 2 (2013) 294–303. https://doi.org/10.1016/J.NANOEN.2012.10.001.

[121] Y. Zhou, P. Jin, Y. Zhou, Y. Zhu, High-performance symmetric supercapacitors based on carbon nanotube/graphite nanofiber nanocomposites, Sci. Rep. 8 (2018) 1–7. https://doi.org/10.1038/s41598-018-27460-8.

[122] V. Sannasi, K.U. Maheswari, C. Karthikeyan, S. Karuppuchamy, H2O2-assisted microwave synthesis of NiO/CNT nanocomposite material for supercapacitor applications, Ionics (Kiel). 26 (2020) 4067–4079. https://doi.org/10.1007/s11581-020-03563-z.

[123] L. Yue, S. Zhang, H. Zhao, M. Wang, J. Mi, Y. Feng, D. Wang, Microwave-assisted one-pot synthesis of Fe2O3/CNTs composite as supercapacitor electrode materials, J. Alloys Compd. 765 (2018) 1263–1266. https://doi.org/10.1016/j.jallcom.2018.06.283.

[124] X. Fu, A. Chen, Y. Yu, S. Hou, L. Liu, Carbon Nanotube@N-Doped Mesoporous Carbon Composite Material for Supercapacitor Electrodes, Chem. - An Asian J. 14 (2019) 634–639. https://doi.org/10.1002/asia.201801865.

[125] K.S. Novoselov, A.K. Geim, S. V. Morozov, D. Jiang, Y. Zhang, S. V. Dubonos, I. V. Grigorieva, A.A. Firsov, Electric field in atomically thin carbon films, Science (80-.). 306 (2004) 666–669. https://doi.org/10.1126/science.1102896.

[126] H. Huang, S. Chen, A.T.S. Wee, W. Chen, Epitaxial growth of graphene on silicon carbide (SiC), in: V.S. Alan B. Kaiser (Ed.), Graphene Prop. Prep. Characterisation Devices, 3rd editio, Woodhead Publishing, 2014: pp. 3–26. https://doi.org/10.1533/9780857099334.1.3.

[127] R.M. Jacobberger, R. Machhi, J. Wroblewski, B. Taylor, A.L. Gillian-Daniel, M.S. Arnold, Simple Graphene Synthesis via Chemical Vapor Deposition, J. Chem. Educ. 92 (2015) 1903–1907. https://doi.org/10.1021/acs.jchemed.5b00126.

[128] M. Son, M.H. Ham, Low-temperature synthesis of graphene by chemical vapor deposition and its applications, FlatChem. 5 (2017) 40–49. https://doi.org/10.1016/j.flatc.2017.07.002.

[129] A. Dato, M. Frenklach, Substrate-free microwave synthesis of graphene: Experimental conditions and hydrocarbon precursors, New J. Phys. 12 (2010) 125013. https://doi.org/10.1088/1367-2630/12/12/125013.

[130] Y. Yang, R. Liu, J. Wu, X. Jiang, P. Cao, X. Hu, T. Pan, C. Qiu, J. Yang, Y. Song, D. Wu, Y. Su, Bottom-up Fabrication of Graphene on Silicon/Silica Substrate via a Facile Soft-hard Template Approach, Sci. Rep. 5 (2015) 1–7. https://doi.org/10.1038/srep13480.

[131] V. Singh, D. Joung, L. Zhai, S. Das, S.I. Khondaker, S. Seal, Graphene based materials: Past, present and future, Prog. Mater. Sci. 56 (2011) 1178–1271. https://doi.org/10.1016/j.pmatsci.2011.03.003.

[132] X. Wu, Y. Liu, H. Yang, Z. Shi, Large-scale synthesis of high-quality graphene sheets by an improved alternating current arc-discharge method, RSC Adv. 6 (2016) 93119–93124. https://doi.org/10.1039/c6ra22273k.

[133] C.K. Chua, M. Pumera, Chemical reduction of graphene oxide: A synthetic chemistry viewpoint, Chem. Soc. Rev. 43 (2014) 291–312. https://doi.org/10.1039/c3cs60303b.

[134] T.F. Emiru, D.W. Ayele, Controlled synthesis, characterization and reduction of graphene oxide: A convenient method for large scale production, Egypt. J. Basic Appl. Sci. 4 (2017) 74–79. https://doi.org/10.1016/j.ejbas.2016.11.002.

[135] Ö. Güler, S.H. Güler, V. Selen, M.G. Albayrak, E. Evin, Production of graphene layer by liquid-phase exfoliation with low sonication power and sonication time from synthesized expanded graphite, Fullerenes Nanotub. Carbon Nanostructures. 24 (2016) 123–127. https://doi.org/10.1080/1536383X.2015.1114472.

[136] S. Haar, M. Bruna, J.X. Lian, F. Tomarchio, Y. Olivier, R. Mazzaro, V. Morandi, J. Moran, A.C. Ferrari, D. Beljonne, A. Ciesielski, P. Samorì, Liquid-Phase Exfoliation of Graphite into Single- and Few-Layer Graphene with α-Functionalized Alkanes, J. Phys. Chem. Lett. 7 (2016) 2714–2721. https://doi.org/10.1021/acs.jpclett.6b01260.

[137] A.M. Dimiev, A. Khannanov, I. Vakhitov, A. Kiiamov, K. Shukhina, J.M. Tour,

Revisiting the Mechanism of Oxidative Unzipping of Multiwall Carbon Nanotubes to Graphene Nanoribbons, ACS Nano. 12 (2018) 3985–3993. https://doi.org/10.1021/acsnano.8b01617.

[138] X.J. Lee, B.Y.Z. Hiew, K.C. Lai, L.Y. Lee, S. Gan, S. Thangalazhy-Gopakumar, S. Rigby, Review on graphene and its derivatives: Synthesis methods and potential industrial implementation, J. Taiwan Inst. Chem. Eng. 98 (2019) 163–180. https://doi.org/10.1016/j.jtice.2018.10.028.

[139] M.F. El-Kady, Y. Shao, R.B. Kaner, Graphene for batteries, supercapacitors and beyond, Nat. Rev. Mater. 1 (2016) 16033. https://doi.org/10.1038/natrevmats.2016.33.

[140] Y. Sun, Q. Wu, G. Shi, Graphene based new energy materials, Energy Environ. Sci. 4 (2011) 1113–1132. https://doi.org/10.1039/c0ee00683a.

[141] M.D. Stoller, S. Park, Y. Zhu, J. An, R.S. Ruoff, Graphene-Based Ultracapacitors, Nano Lett. 8, (2008) 3498–3502. https://doi.org/10.1021/nl802558y.

[142] C. Wang, J. Zhou, F. Du, Synthesis of Highly Reduced Graphene Oxide for Supercapacitor, J. Nanomater. 2016 (2016) 1–8. https://doi.org/10.1155/2016/4840301.

[143] F.T. Johra, W.G. Jung, Hydrothermally reduced graphene oxide as a supercapacitor, Appl. Surf. Sci. 357 (2015) 1911–1914. https://doi.org/10.1016/j.apsusc.2015.09.128.

[144] C. Li, X. Zhang, K. Wang, H.T. Zhang, X.Z. Sun, Y.W. Ma, Three dimensional graphene networks for supercapacitor electrode materials, Xinxing Tan Cailiao/New Carbon Mater. 30 (2015) 193–206. https://doi.org/10.1016/S1872-5805(15)60185-8.

[145] J. Zeng, C. Xu, T. Gao, X. Jiang, X. Bin Wang, Porous monoliths of 3D graphene for electric double-layer supercapacitors, Carbon Energy. 3 (2021) 193–224. https://doi.org/10.1002/cey2.107.

[146] L. Zhang, G. Shi, Preparation of highly conductive graphene hydrogels for fabricating supercapacitors with high rate capability, J. Phys. Chem. C. 115 (2011) 17206–17212. https://doi.org/10.1021/jp204036a.

[147] J. Hao, Y. Liao, Y. Zhong, D. Shu, C. He, S. Guo, Y. Huang, J. Zhong, L. Hu, Three-dimensional graphene layers prepared by a gas-foaming method for supercapacitor applications, Carbon N. Y. 94 (2015) 879–887. https://doi.org/10.1016/j.carbon.2015.07.069.

[148] Q. Li, X. Guo, Y. Zhang, W. Zhang, C. Ge, L. Zhao, X. Wang, H. Zhang, J. Chen, Z. Wang, L. Sun, Porous graphene paper for supercapacitor applications, J. Mater. Sci. Technol. 33 (2017) 793–799. https://doi.org/10.1016/j.jmst.2017.03.018.

[149] R. Santhosh, S.R.S.S. Raman, S. Murali, V. Sandhya, S. Ghosh, N. Kumar, S. Punniyakoti, M. Karthik, P. Kollu, S. Kwan, A. Nirmala, S.M. Krishna, S. sai Ravuri, V. Sandhya, S. Ghosh, N.K. Sahu, S. Punniyakoti, M. Karthik, P. Kollu, S.K. Jeong, A.N. Grace, Heteroatom doped graphene based hybrid electrode materials for supercapacitor applications, Electrochim. Acta. 276 (2018) 284–292. https://doi.org/10.1016/j.electacta.2018.04.142.

[150] H. Liu, Y. Liu, D. Zhu, Chemical doping of graphene, J. Mater. Chem. 21 (2011) 3335–3345. https://doi.org/10.1039/c0jm02922j.

[151] D. Usachov, O. Vilkov, A. Grüneis, D. Haberer, A. Fedorov, V.K. Adamchuk, A.B. Preobrajenski, P. Dudin, A. Barinov, M. Oehzelt, C. Laubschat, D. V. Vyalikh, Nitrogen-doped graphene: Efficient growth, structure, and electronic properties, Nano Lett. 11 (2011) 5401–5407. https://doi.org/10.1021/nl2031037.

[152] A. Śliwak, B. Grzyb, N. Díez, G. Gryglewicz, Nitrogen-doped reduced graphene oxide as electrode material for high rate supercapacitors, Appl. Surf. Sci. 399 (2017) 265–271. https://doi.org/10.1016/j.apsusc.2016.12.060.

[153] H. Xu, L. Ma, Z. Jin, Nitrogen-doped graphene: Synthesis, characterizations and energy applications, J. Energy Chem. 27 (2018) 146–160. https://doi.org/10.1016/j.jechem.2017.12.006.

[154] L. Sun, L. Wang, C. Tian, T. Tan, Y. Xie, K. Shi, M. Li, H. Fu, Nitrogen-doped graphene with high nitrogen level via a one-step hydrothermal reaction of graphene oxide with urea for superior capacitive energy storage, RSC Adv. 2 (2012) 4498–4506. https://doi.org/10.1039/c2ra01367c.

[155] S.M. Li, S.Y. Yang, Y.S. Wang, H.P. Tsai, H.W. Tien, S.T. Hsiao, W.H. Liao, C.L. Chang, C.C.M. Ma, C.C. Hu, N-doped structures and surface functional groups of reduced graphene oxide and their effect on the electrochemical performance of supercapacitor with organic electrolyte, J. Power Sources. 278 (2015) 218–229. https://doi.org/10.1016/j.jpowsour.2014.12.025.

[156] S.K. Singh, V.M. Dhavale, R. Boukherroub, S. Kurungot, S. Szunerits, N-doped porous reduced graphene oxide as an efficient electrode material for high performance flexible solid-state supercapacitor, Appl. Mater. Today. 8 (2017) 141–149. https://doi.org/10.1016/j.apmt.2016.10.002.

[157] X. Fan, H. Xu, S. Zuo, Z. Liang, S. Yang, Y. Chen, Preparation and supercapacitive properties of phosphorus-doped reduced graphene oxide hydrogel, Electrochim. Acta. 330 (2020) 135207. https://doi.org/10.1016/j.electacta.2019.135207.

[158] N.H.A. Rosli, K.S. Lau, T. Winie, S.X. Chin, C.H. Chia, Synergistic effect of sulfur-doped reduced graphene oxide created via microwave-assisted synthesis for supercapacitor applications, Diam. Relat. Mater. 120 (2021) 108696. https://doi.org/10.1016/j.diamond.2021.108696.

[159] S.S. Balaji, J. Anandha Raj, M. Karnan, M. Sathish, Supercritical fluid assisted synthesis of S-doped graphene and its symmetric supercapacitor performance evaluation using different electrolytes, Synth. Met. 255 (2019) 116111. https://doi.org/10.1016/j.synthmet.2019.116111.

[160] A.S. Rajpurohit, N.S. Punde, A.K. Srivastava, A dual metal organic framework based on copper-iron clusters integrated sulphur doped graphene as a porous material for supercapacitor with remarkable performance characteristics, J. Colloid Interface Sci. 553 (2019) 328–340. https://doi.org/10.1016/j.jcis.2019.06.031.

[161] M. Duraivel, S. Nagappan, B. Balamuralitharan, S. Selvam, S.N. Karthick, K. Prabakar, C.S. Ha, H.J. Kim, Superior one-pot synthesis of a doped graphene oxide electrode for a high power density supercapacitor, New J. Chem. 42 (2018) 11093–11101. https://doi.org/10.1039/c8nj01672k.

[162] M.B. Arvas, H. Gürsu, M. Gencten, Y. Sahin, Preparation of different heteroatom doped graphene oxide based electrodes by electrochemical method and their supercapacitor applications, J. Energy Storage. 35 (2021) 102328. https://doi.org/10.1016/j.est.2021.102328.

[163] S.W. Bokhari, A.H. Siddique, P.C. Sherrell, X. Yue, K.M. Karumbaiah, S. Wei, A. V. Ellis, W. Gao, Advances in graphene-based supercapacitor electrodes, Energy Reports. 6 (2020) 2768–2784. https://doi.org/10.1016/j.egyr.2020.10.001.

[164] S. Yadav, A. Devi, Recent advancements of metal oxides/Nitrogen-doped graphene nanocomposites for supercapacitor electrode materials, J. Energy Storage. 30 (2020) 101486. https://doi.org/10.1016/j.est.2020.101486.

[165] H. Kumar, R. Sharma, A. Yadav, R. Kumari, Recent advancement made in the field of reduced graphene oxide-based nanocomposites used in the energy storage devices: A review, J. Energy Storage. 33 (2021) 102032. https://doi.org/10.1016/j.est.2020.102032.

[166] S. Zhu, X. Zou, Y. Zhou, Y. Zeng, Y. Long, Z. Yuan, Q. Wu, M. Li, Y. Wang, B. Xiang, Hydrothermal synthesis of graphene-encapsulated 2D circular nanoplates of α-Fe2O3 towards enhanced electrochemical performance for supercapacitor, J. Alloys Compd. 775 (2019) 63–71. https://doi.org/10.1016/j.jallcom.2018.10.085.

[167] H.R. Naderi, P. Norouzi, M.R. Ganjali, Electrochemical study of a novel high performance supercapacitor based on MnO 2 /nitrogen-doped graphene nanocomposite, Appl. Surf. Sci. 366 (2016) 552–560. https://doi.org/10.1016/j.apsusc.2016.01.058.

[168] S. Ramesh, K. Karuppasamy, H.S. Kim, H.S. Kim, J.H. Kim, Hierarchical Flowerlike 3D nanostructure of Co3O4@MnO2/N-doped Graphene oxide (NGO) hybrid composite for a high-performance supercapacitor, Sci. Rep. 8 (2018) 1–11. https://doi.org/10.1038/s41598-018-34905-7.

[169] Y. Wang, B. Hu, J. Luo, Y. Gu, X. Liu, Synthesis of Polyaniline@MnO2/Graphene Ternary Hybrid Hollow Spheres via Pickering Emulsion Polymerization for Electrochemical Supercapacitors, ACS Appl. Energy Mater. 4 (2021) 7721–7730. https://doi.org/10.1021/acsaem.1c01087.

[170] A. Moyseowicz, G. Gryglewicz, Hydrothermal-assisted synthesis of a porous polyaniline/reduced graphene oxide composite as a high-performance electrode material for supercapacitors, Compos. Part B Eng. 159 (2019) 4–12. https://doi.org/10.1016/j.compositesb.2018.09.069.

[171] K. Gholami laelabadi, R. Moradian, I. Manouchehri, Facile Method of Fabricating Interdigitated and Sandwich Electrodes for High-Performance and Flexible Reduced Graphene Oxide@Polyaniline Nanocomposite Supercapacitors, ACS Appl. Energy Mater. 4 (2021) 6697–6710. https://doi.org/10.1021/acsaem.1c00754.

[172] T. Zhao, X. Ji, P. Bi, W. Jin, C. Xiong, A. Dang, H. Li, T. Li, S. Shang, Z. Zhou, In situ synthesis of interlinked three-dimensional graphene foam/polyaniline nanorod supercapacitor, Electrochim. Acta. 230 (2017) 342–349. https://doi.org/10.1016/j.electacta.2017.02.021.

[173] W. Yang, Y. Chen, J. Wang, T. Peng, J. Xu, B. Yang, K. Tang, Reduced Graphene Oxide/Carbon Nanotube Composites as Electrochemical Energy Storage Electrode Applications, Nanoscale Res. Lett. 13 (2018) 1–7. https://doi.org/10.1186/s11671-018-2582-6.

[174] M. Audenaert, G. Gusman, R. Deltour, Electrical conductivity of in doped polyacetylene, Phys. Rev. B. 24 (1981) 7380–7382. https://doi.org/10.1103/PhysRevB.24.7380.

[175] P. Novák, K. Müller, K.S.V. Santhanam, O. Haas, Electrochemically active polymers for rechargeable batteries, Chem. Rev. 97 (1997) 207–281. https://doi.org/10.1021/cr941181o.

[176] I. Weissman, D. Aurbach, Nonaqueous Electrochemistry, Marcel Dekker, 1999. https://doi.org/10.1201/9780824741389.ch1.

[177] H.S. Nalwa, Handbook of organic conductive molecules and polymers, Handb. Org. Conduct. Mol. Polym. (1997) 87.

[178] J.R. Terje A. Skotheim, ed., Handbook of Conducting Polymers, 2 Volume Set, 3rd Editio, CRC Press, 2007. https://doi.org/10.1201/b12346.

[179] A. Laforgue, P. Simon, J.F. Fauvarque, J.F. Sarrau, P. Lailler, Hybrid Supercapacitors Based on Activated Carbons and Conducting Polymers, J. Electrochem. Soc. 148 (2001) A1130–A1134. https://doi.org/10.1149/1.1400742.

[180] H. Li, J. Wang, Q. Chu, Z. Wang, F. Zhang, S. Wang, Theoretical and experimental specific capacitance of polyaniline in sulfuric acid, J. Power Sources. 190 (2009) 578–586. https://doi.org/10.1016/j.jpowsour.2009.01.052.

[181] Y. Fang, J. Liu, D.J. Yu, J.P. Wicksted, K. Kalkan, C.O. Topal, B.N. Flanders, J. Wu, J. Li, Self-supported supercapacitor membranes: Polypyrrole-coated carbon nanotube networks enabled by pulsed electrodeposition, J. Power Sources. 195 (2010) 674–679. https://doi.org/10.1016/j.jpowsour.2009.07.033.

[182] H. Wang, J. Lin, Z.X. Shen, Polyaniline (PANi) based electrode materials for energy storage and conversion, J. Sci. Adv. Mater. Devices. 1 (2016) 225–255. https://doi.org/10.1016/j.jsamd.2016.08.001.

[183] G. Lota, K. Fic, E. Frackowiak, Carbon nanotubes and their composites in electrochemical applications, Energy Environ. Sci. 4 (2011) 1592–1605. https://doi.org/10.1039/c0ee00470g.

[184] J.C. Chiang, A.G. MacDiarmid, "Polyaniline": Protonic acid doping of the emeraldine form to the metallic regime, Synth. Met. 13 (1986) 193–205. https://doi.org/10.1016/0379-6779(86)90070-6.

[185] J.E. De Albuquerque, L.H.C. Mattoso, R.M. Faria, J.G. Masters, A.G. MacDiarmid, Study of the interconversion of polyaniline oxidation states by optical absorption spectroscopy, Synth. Met. 146 (2004) 1–10. https://doi.org/10.1016/j.synthmet.2004.05.019.

[186] Y. Luo, R. Guo, T. Li, F. Li, Z. Liu, M. Zheng, B. Wang, Z. Yang, H. Luo, Y. Wan, Application of Polyaniline for Li-Ion Batteries, Lithium–Sulfur Batteries, and Supercapacitors, ChemSusChem. 12 (2019) 1591–1611. https://doi.org/10.1002/cssc.201802186.

[187] A. Samadi, M. Xie, J. Li, H. Shon, C. Zheng, S. Zhao, Polyaniline-based adsorbents for aqueous pollutants removal: A review, Chem. Eng. J. 418 (2021) 129425. https://doi.org/10.1016/j.cej.2021.129425.

[188] A.G. MacDiarmid, "synthetic metals": A novel role for organic polymers, Curr. Appl. Phys. 1 (2001) 269–279. https://doi.org/10.1016/S1567-1739(01)00051-7.

[189] W.J. Feast, J. Tsibouklis, K.L. Pouwer, L. Groenendaal, E.W. Meijer, Synthesis, processing and material properties of conjugated polymers, Polymer (Guildf). 37 (1996) 5017–5047. https://doi.org/10.1016/0032-3861(96)00439-9.

[190] H.N. Heme, M.S.N. Alif, S.M.S.M. Rahat, S.B. Shuchi, Recent progress in

polyaniline composites for high capacity energy storage: A review, J. Energy Storage. 42 (2021) 103018. https://doi.org/10.1016/j.est.2021.103018.

[191] P. Liu, J. Yan, Z. Guang, Y. Huang, X. Li, W. Huang, Recent advancements of polyaniline-based nanocomposites for supercapacitors, J. Power Sources. 424 (2019) 108–130. https://doi.org/10.1016/j.jpowsour.2019.03.094.

[192] P. Fan, S. Wang, H. Liu, L. Liao, G. Lv, L. Mei, Polyaniline nanotube synthesized from natural tubular halloysite template as high performance pseudocapacitive electrode, Electrochim. Acta. 331 (2020) 135259. https://doi.org/10.1016/j.electacta.2019.135259.

[193] K. Zhou, Y. He, Q. Xu, Q. Zhang, A. Zhou, Z. Lu, L.K. Yang, Y. Jiang, D. Ge, X.Y. Liu, H. Bai, A Hydrogel of Ultrathin Pure Polyaniline Nanofibers: Oxidant-Templating Preparation and Supercapacitor Application, ACS Nano. 12 (2018) 5888–5894. https://doi.org/10.1021/acsnano.8b02055.

[194] A. Sumboja, U.M. Tefashe, G. Wittstock, P.S. Lee, Investigation of Charge Transfer Kinetics of Polyaniline Supercapacitor Electrodes by Scanning Electrochemical Microscopy, Adv. Mater. Interfaces. 2 (2015) 1400154. https://doi.org/10.1002/admi.201400154.

[195] V.R. Gedela, V.V.S.S. Srikanth, Polyaniline nanostructures expedient as working electrode materials in supercapacitors, Appl. Phys. A Mater. Sci. Process. 115 (2014) 189–197. https://doi.org/10.1007/s00339-013-7920-z.

[196] X. Wang, J. Deng, X. Duan, D. Liu, J. Guo, P. Liu, Crosslinked polyaniline nanorods with improved electrochemical performance as electrode material for supercapacitors, J. Mater. Chem. A. 2 (2014) 12323–12329. https://doi.org/10.1039/c4ta02231a.

[197] Y. Ma, C. Hou, H. Zhang, M. Qiao, Y. Chen, H. Zhang, Q. Zhang, Z. Guo, Morphology-dependent electrochemical supercapacitors in multi-dimensional polyaniline nanostructures, J. Mater. Chem. A. 5 (2017) 14041–14052. https://doi.org/10.1039/c7ta03279j.

[198] M. Suba Lakshmi, S.M. Wabaidur, Z.A. Alothman, D. Ragupathy, Novel 1D polyaniline nanorods for efficient electrochemical supercapacitors: A facile and green approach, Synth. Met. 270 (2020) 116591. https://doi.org/10.1016/j.synthmet.2020.116591.

[199] Y. Gawli, A. Banerjee, D. Dhakras, M. Deo, D. Bulani, P. Wadgaonkar, M. Shelke, S. Ogale, 3D Polyaniline Architecture by Concurrent Inorganic and Organic Acid Doping for Superior and Robust High Rate Supercapacitor Performance, Sci. Rep. 6 (2016) 1–10. https://doi.org/10.1038/srep21002.

[200] Y. He, X. Wang, H. Huang, P. Zhang, B. Chen, Z. Guo, In-situ electropolymerization of porous conducting polyaniline fibrous network for solid-state supercapacitor, Appl. Surf. Sci. 469 (2019) 446–455. https://doi.org/10.1016/j.apsusc.2018.10.180.

[201] H. Huang, X. Zeng, W. Li, H. Wang, Q. Wang, Y. Yang, Reinforced conducting hydrogels prepared from the in situ polymerization of aniline in an aqueous solution of sodium alginate, J. Mater. Chem. A. 2 (2014) 16516–16522. https://doi.org/10.1039/c4ta03332a.

[202] H.B. Zhao, L. Yuan, Z.B. Fu, C.Y. Wang, X. Yang, J.Y. Zhu, J. Qu, H.B. Chen, D.A. Schiraldi, Biomass-Based Mechanically Strong and Electrically Conductive

Polymer Aerogels and Their Application for Supercapacitors, ACS Appl. Mater. Interfaces. 8 (2016) 9917–9924. https://doi.org/10.1021/acsami.6b00510.

[203] G. Otrokhov, D. Pankratov, G. Shumakovich, M. Khlupova, Y. Zeifman, I. Vasil'Eva, O. Morozova, A. Yaropolov, Enzymatic synthesis of polyaniline/multi-walled carbon nanotube composite with core shell structure and its electrochemical characterization for supercapacitor application, Electrochim. Acta. 123 (2014) 151–157. https://doi.org/10.1016/j.electacta.2013.12.089.

[204] A. Xie, F. Tao, C. Jiang, W. Sun, Y. Li, L. Hu, X. Du, S. Luo, C. Yao, A coralliform-structured γ-MnO2/polyaniline nanocomposite for high-performance supercapacitors, J. Electroanal. Chem. 789 (2017) 29–37. https://doi.org/10.1016/j.jelechem.2017.02.032.

[205] K.Y. Yasoda, A.A. Mikhaylov, A.G. Medvedev, M.S. Kumar, O. Lev, P. V. Prikhodchenko, S.K. Batabyal, Brush like polyaniline on vanadium oxide decorated reduced graphene oxide: Efficient electrode materials for supercapacitor, J. Energy Storage. 22 (2019) 188–193. https://doi.org/10.1016/j.est.2019.02.010.

[206] W. Wu, C. Wang, C. Zhao, D. Wei, J. Zhu, Y. Xu, Facile strategy of hollow polyaniline nanotubes supported on Ti3C2-MXene nanosheets for High-performance symmetric supercapacitors, J. Colloid Interface Sci. 580 (2020) 601–613. https://doi.org/10.1016/j.jcis.2020.07.052.

[207] X. Hong, B. Zhang, E. Murphy, J. Zou, F. Kim, Three-dimensional reduced graphene oxide/polyaniline nanocomposite film prepared by diffusion driven layer-by-layer assembly for high-performance supercapacitors, J. Power Sources. 343 (2017) 60–66. https://doi.org/10.1016/j.jpowsour.2017.01.034.

[208] M.K. Chini, S. Chatterjee, FlatChem Hydrothermally reduced nano porous graphene – polyaniline nanofiber composites for supercapacitor, FlatChem. 1 (2016) 1–5. https://doi.org/10.1016/j.flatc.2016.08.001.

[209] Z.F. Li, H. Zhang, Q. Liu, L. Sun, L. Stanciu, J. Xie, Fabrication of high-surface-area graphene/polyaniline nanocomposites and their application in supercapacitors, ACS Appl. Mater. Interfaces. 5 (2013) 2685–2691. https://doi.org/10.1021/am4001634.

[210] X. Gao, H. Zhang, H. Yue, F. Yao, X. Zhang, E. Guo, Y. Ma, Z. Wang, Y. Wang, A Novel Polyaniline Nanowire Arrays/Three-Dimensional Graphene Composite for Supercapacitor, ChemistrySelect. 5 (2020) 11004–11009. https://doi.org/10.1002/slct.202002801.

[211] N.A. Kumar, H.J. Choi, Y.R. Shin, D.W. Chang, L. Dai, J.B. Baek, Polyaniline-grafted reduced graphene oxide for efficient electrochemical supercapacitors, ACS Nano. 6 (2012) 1715–1723. https://doi.org/10.1021/nn204688c.

[212] L. Li, A.R.O. Raji, H. Fei, Y. Yang, E.L.G. Samuel, J.M. Tour, Nanocomposite of polyaniline nanorods grown on graphene nanoribbons for highly capacitive pseudocapacitors, ACS Appl. Mater. Interfaces. 5 (2013) 6622–6627. https://doi.org/10.1021/am4013165.

[213] Shruthi, K.M. Vighnesha, Sandhya, D.N. Sangeetha, M. Selvakumar, Synthesis and Characterization of Reduced Graphene Oxide- Polyaniline Composite for Supercapacitor Applications, Surf. Eng. Appl. Electrochem. 54 (2018) 359–366. https://doi.org/10.3103/S106837551804018X.

[214] M. Kim, C. Lee, J. Jang, Fabrication of highly flexible, scalable, and high-performance supercapacitors using polyaniline/reduced graphene oxide film with enhanced electrical conductivity and crystallinity, Adv. Funct. Mater. 24 (2014) 2489–2499. https://doi.org/10.1002/adfm.201303282.

[215] H.H. Chien, C.Y. Liao, Y.C. Hao, C.C. Hsu, I.C. Cheng, I.S. Yu, J.Z. Chen, Improved performance of polyaniline/reduced-graphene-oxide supercapacitor using atmospheric-pressure-plasma-jet surface treatment of carbon cloth, Electrochim. Acta. 260 (2018) 391–399. https://doi.org/10.1016/j.electacta.2017.12.060.

[216] A.A. Alamin, A.E.M. Abd Elhamid, W.R. Anis, A.M. Attiya, Fabrication of symmetric supercapacitor based on relatively long lifetime polyaniline grown on reduced graphene oxide via Fe2+ oxidation sites, Diam. Relat. Mater. 96 (2019) 182–194. https://doi.org/10.1016/j.diamond.2019.05.013.

[217] M. Ge, H. Hao, Q. Lv, J. Wu, W. Li, Hierarchical nanocomposite that coupled nitrogen-doped graphene with aligned PANI cores arrays for high-performance supercapacitor, Electrochim. Acta. 330 (2020) 135236. https://doi.org/10.1016/j.electacta.2019.135236.

[218] P.K. Kalambate, C.R. Rawool, S.P. Karna, A.K. Srivastava, Nitrogen-doped graphene/palladium nanoparticles/porous polyaniline ternary composite as an efficient electrode material for high performance supercapacitor, Mater. Sci. Energy Technol. 2 (2019) 246–257. https://doi.org/10.1016/j.mset.2018.12.005.

[219] Q. Hao, X. Xia, W. Lei, W. Wang, J. Qiu, Facile synthesis of sandwich-like polyaniline/boron-doped graphene nano hybrid for supercapacitors, Carbon N. Y. 81 (2015) 552–563. https://doi.org/10.1016/j.carbon.2014.09.090.

[220] Z. Liu, D. Li, Z. Li, Z. Liu, Z. Zhang, Nitrogen-doped 3D reduced graphene oxide/polyaniline composite as active material for supercapacitor electrodes, Appl. Surf. Sci. 422 (2017) 339–347. https://doi.org/10.1016/j.apsusc.2017.06.046.

[221] Z. Fan, Z. Cheng, J. Feng, Z. Xie, Y. Liu, Y. Wang, Ultrahigh volumetric performance of a free-standing compact N-doped holey graphene/PANI slice for supercapacitors, J. Mater. Chem. A. 5 (2017) 16689–16701. https://doi.org/10.1039/c7ta04384h.

[222] J. Zhu, L. Kong, X. Shen, Q. Chen, Z. Ji, J. Wang, K. Xu, G. Zhu, Three-dimensional N-doped graphene/polyaniline composite foam for high performance supercapacitors, Appl. Surf. Sci. 428 (2018) 348–355. https://doi.org/10.1016/j.apsusc.2017.09.148.

[223] J. Liu, P. Du, Q. Wang, D. Liu, P. Liu, Mild synthesis of holey N-doped reduced graphene oxide and its double-edged effects in polyaniline hybrids for supercapacitor application, Electrochim. Acta. 305 (2019) 175–186. https://doi.org/10.1016/j.electacta.2019.03.049.

[224] X. Du, X. Shi, Y. Li, K. Cao, Construction of N, S-co-doped graphene/polyaniline composite as free-standing electrode material, Int. J. Energy Res. 45 (2021) 6227–6238. https://doi.org/10.1002/er.6243.

[225] T. Fan, S. Tong, W. Zeng, Q. Niu, Y. Liu, C. Kao, J. Liu, W. Huang, Y. Min, A.J. Epstein, Self-assembling sulfonated graphene / polyaniline nanocomposite paper for high performance supercapacitor, Synth. Met. 199 (2015) 79–86. https://doi.org/10.1016/j.synthmet.2014.11.017.

[226] Y. Hu, X. Tong, H. Zhuo, L. Zhong, X. Peng, Biomass-Based Porous N-Self-Doped Carbon Framework/Polyaniline Composite with Outstanding Supercapacitance, ACS Sustain. Chem. Eng. 5 (2017) 8663–8674. https://doi.org/10.1021/acssuschemeng.7b01380.

[227] K. Xie, M. Zhang, Y. Yang, L. Zhao, W. Qi, Synthesis and Supercapacitor Performance of Polyaniline/Nitrogen-Doped Ordered Mesoporous Carbon Composites, Nanoscale Res. Lett. 13 (2018) 1–8. https://doi.org/10.1186/s11671-018-2577-3.

[228] Z. Çıplak, A. Yıldız, N. Yıldız, Green preparation of ternary reduced graphene oxide-au@polyaniline nanocomposite for supercapacitor application, J. Energy Storage. 32 (2020) 101846. https://doi.org/10.1016/j.est.2020.101846.

[229] X. Hong, Y. Lu, S. Li, X. Wang, X. Wang, J. Liang, Carbon foam@reduced graphene oxide scaffold grown with polyaniline nanofibers for high performance symmetric supercapacitor, Electrochim. Acta. 294 (2019) 376–382. https://doi.org/10.1016/j.electacta.2018.10.133.

[230] J. Sarkar, S. Bhattacharyya, Application of graphene and graphene-based materials in clean energy-related devices Minghui, Arch. Thermodyn. 33 (2012) 23–40. https://doi.org/10.1002/er.

[231] Z. Hou, S. Zou, J. Li, Morphology and structure control of amine- functionalized graphene/polyaniline composite for high-performance supercapacitors, J. Alloys Compd. 827 (2020) 154390. https://doi.org/10.1016/j.jallcom.2020.154390.

[232] Y. Li, M. Zhou, Z. Xia, Q. Gong, X. Liu, Y. Yang, Q. Gao, Facile preparation of polyaniline covalently grafted to isocyanate functionalized reduced graphene oxide nanocomposite for high performance flexible supercapacitors, Colloids Surfaces A Physicochem. Eng. Asp. 602 (2020) 125172. https://doi.org/10.1016/j.colsurfa.2020.125172.

[233] S. He, X. Hu, S. Chen, H. Hu, M. Hanif, H. Hou, Needle-like polyaniline nanowires on graphite nanofibers: Hierarchical micro/nano-architecture for high performance supercapacitors, J. Mater. Chem. 22 (2012) 5114–5120. https://doi.org/10.1039/c2jm15668g.

[234] S.N. Karri, S.P. Ega, V. Perupogu, P. Srinivasan, Enhancing the Electrochemical Performance of Polyaniline Using Fly Ash of Coal Waste for Supercapacitor Application, ChemistrySelect. 6 (2021) 2576–2589. https://doi.org/10.1002/slct.202100513.

[235] Z. Xu, Z. Zhang, H. Yin, S. Hou, H. Lin, J. Zhou, S. Zhuo, Investigation on the role of different conductive polymers in supercapacitors based on a zinc sulfide/reduced graphene oxide/conductive polymer ternary composite electrode, RSC Adv. 10 (2020) 3122–3129. https://doi.org/10.1039/c9ra07842h.

[236] S. Palsaniya, H.B. Nemade, A.K. Dasmahapatra, Hierarchical PANI-RGO-ZnO ternary nanocomposites for symmetric tandem supercapacitor, J. Phys. Chem. Solids. 154 (2021) 110081. https://doi.org/10.1016/j.jpcs.2021.110081.

[237] C. Huang, C. Hao, W. Zheng, S. Zhou, L. Yang, X. Wang, C. Jiang, L. Zhu, Synthesis of polyaniline/nickel oxide/sulfonated graphene ternary composite for all-solid-state asymmetric supercapacitor, Appl. Surf. Sci. 505 (2020) 144589. https://doi.org/10.1016/j.apsusc.2019.144589.

[238] T. Das, B. Verma, Polyaniline - Acetylene black - Copper cobaltite based ternary

hybrid material with enhanced electrochemical properties and its use in supercapacitor electrodes, (2019) 1–16. https://doi.org/10.1002/er.4951.

[239] U. Male, J.K.R. Modigunta, D.S. Huh, Design and synthesis of polyaniline-grafted reduced graphene oxide via azobenzene pendants for high-performance supercapacitors, Polymer (Guildf). 110 (2017) 242–249. https://doi.org/10.1016/j.polymer.2016.12.031.

[240] A. Raghavan, S. Sarkar, S. Ghosh, Dnevelopment of PANI based ternary nanocomposite with enhanced capacity retention for high performance supercapacitor application, Electrochim. Acta. 388 (2021) 138564. https://doi.org/10.1016/j.electacta.2021.138564.

[241] M. Liu, S. He, W. Fan, Y.E. Miao, T. Liu, Filter paper-derived carbon fiber/polyaniline composite paper for high energy storage applications, Compos. Sci. Technol. 101 (2014) 152–158. https://doi.org/10.1016/j.compscitech.2014.07.008.

[242] H. Hu, S. Liu, M. Hanif, S. Chen, H. Hou, Three-dimensional cross-linked carbon network wrapped with ordered polyaniline nanowires for high-performance pseudo-supercapacitors, J. Power Sources. 268 (2014) 451–458. https://doi.org/10.1016/j.jpowsour.2014.06.074.

[243] D.D. Potphode, L. Sinha, P.M. Shirage, Redox additive enhanced capacitance: Multi-walled carbon nanotubes/polyaniline nanocomposite based symmetric supercapacitors for rapid charge storage, Appl. Surf. Sci. 469 (2019) 162–172. https://doi.org/10.1016/j.apsusc.2018.10.277.

[244] K. Li, X. Liu, S. Chen, W. Pan, J. Zhang, A flexible solid-state supercapacitor based on graphene/polyaniline paper electrodes, J. Energy Chem. 32 (2019) 166–173. https://doi.org/10.1016/j.jechem.2018.07.014.

[245] T.W. Chang, L.Y. Lin, P.W. Peng, Y.X. Zhang, Y.Y. Huang, Enhanced electrocapacitive performance for the supercapacitor with tube-like polyaniline and graphene oxide composites, Electrochim. Acta. 259 (2018) 348–354. https://doi.org/10.1016/j.electacta.2017.10.195.

[246] Z. Çıplak, N. Yıldız, Polyaniline-Au nanocomposite as electrode material for supercapacitor applications, Synth. Met. 256 (2019) 116150. https://doi.org/10.1016/j.synthmet.2019.116150.

[247] M. Ates, M. Yildirim, The synthesis of rGO/RuO2, rGO/PANI, RuO2/PANI and rGO/RuO2/PANI nanocomposites and their supercapacitors, Polym. Bull. 77 (2020) 2285–2307. https://doi.org/10.1007/s00289-019-02850-8.

[248] S. Rajkumar, E. Elanthamilan, J.P. Merlin, I.J. Daisy Priscillal, I.S. Lydia, Fabrication of a CuCo2O4/PANI nanocomposite as an advanced electrode for high performance supercapacitors, Sustain. Energy Fuels. 4 (2020) 5313–5326. https://doi.org/10.1039/d0se00913j.

[249] Y. Tan, Y. Liu, L. Kong, L. Kang, C. Xu, F. Ran, In situ doping of PANI nanocomposites by gold nanoparticles for high-performance electrochemical energy storage, J. Appl. Polym. Sci. 134 (2017) 45309. https://doi.org/10.1002/app.45309.

[250] Y. Ma, C. Hou, H. Zhang, Q. Zhang, H. Liu, S. Wu, Z. Guo, Three-dimensional core-shell Fe3O4/Polyaniline coaxial heterogeneous nanonets: Preparation and high performance supercapacitor electrodes, Electrochim. Acta. 315 (2019) 114–

123. https://doi.org/10.1016/j.electacta.2019.05.073.

[251] G.J. Wilson, M.G. Looney, A.G. Pandolfo, Enhanced capacitance textile fibres for supercapacitors via an interfacial molecular templating process, Synth. Met. 160 (2010) 655–663. https://doi.org/10.1016/j.synthmet.2009.12.022.

[252] K. Jin, W. Zhang, Y. Wang, X. Guo, Z. Chen, L. Li, Y. Zhang, Z. Wang, J. Chen, L. Sun, T. Zhang, In–situ hybridization of polyaniline nanofibers on functionalized reduced graphene oxide films for high-performance supercapacitor, Electrochim. Acta. 285 (2018) 221–229. https://doi.org/10.1016/j.electacta.2018.07.220.

[253] X. Duan, J. Deng, X. Wang, P. Liu, Preparation of rGO/G/PANI ternary nanocomposites as high performance electrode materials for supercapacitors with spent battery powder as raw material, Mater. Des. 129 (2017) 135–142. https://doi.org/10.1016/j.matdes.2017.05.031.

[254] F. Yang, M. Xu, S.J. Bao, H. Wei, H. Chai, Self-assembled hierarchical graphene/polyaniline hybrid aerogels for electrochemical capacitive energy storage, Electrochim. Acta. 137 (2014) 381–387. https://doi.org/10.1016/j.electacta.2014.06.017.

[255] T.K. Das, S. Banerjee, A. Kumar, A.K. Debnath, V. Sudarsan, Electrochemical performance of hydrothermally synthesized N-Doped reduced graphene oxide electrodes for supercapacitor application, Solid State Sci. 96 (2019) 105952. https://doi.org/10.1016/j.solidstatesciences.2019.105952.

[256] Z. Tian, J. Li, G. Zhu, J. Lu, Y. Wang, Z. Shi, C. Xu, Facile synthesis of highly conductive sulfur-doped reduced graphene oxide sheets, Phys. Chem. Chem. Phys. 18 (2015) 1125–1130. https://doi.org/10.1039/c5cp05475c.

[257] K. Gopalakrishnan, S. Sultan, A. Govindaraj, C.N.R. Rao, Supercapacitors based on composites of PANI with nanosheets of nitrogen-doped RGO, BC1.5N, MoS2 and WS2, Nano Energy. 12 (2015) 52–58. https://doi.org/10.1016/j.nanoen.2014.12.005.

EXPERIMENTAL DETAILS: PREPARATION, CHARACTERIZATION, & MEASUREMENTS

This chapter contains detailed information about the synthesis methods adopted for the preparation of PANI/rGO based composites and porous carbon electrode materials. Further, various structural, morphology techniques employed to study the properties of synthesized materials are discussed. It also explains the electrode fabrication and supercapacitor device assembly. Finally, the performance evaluated electrochemical characterization techniques used in this study are detailed in this chapter.

2.1 Materials

The chemicals and raw materials used in the present work are listed in the below table. These chemicals are used as such without any further purification.

Table 2.1 List of chemicals and raw materials used for the synthesis of nanocomposites and porous carbon electrode materials.

Chemicals	**Grade / Supplier**
Graphite powder	Sigma Aldrich
Aniline	Sigma Aldrich
Ammonium peroxy-di sulphate (APS)	Sigma Aldrich
Potassium permanganate ($KMnO_4$)	Merck chemicals
Hydrochloric Acid (HCl)	Merck chemicals
Sulfuric Acid (H_2SO_4)	Merck chemicals
Hydrogen Peroxide (H_2O_2)	Merck chemicals
Carbon Black	Alfa-Aesar
Polytetrafluoroethylene (PTFE (60 wt.%))	Sigma Aldrich
Urea	Merck chemicals
Sodium sulfide ($Na_2S.xH_2O$)	Merck chemicals
2- Naphthalene Sulfonic Acid (NSA)	Sigma-Aldrich
Corn Husk	Local Market

2.2 Materials synthesis

2.2.1 Synthesis of crumble Graphene Oxide

The crumbled graphene oxide (cGO) has been synthesized from graphite powder by following the modified Hummer's method [1–3]. In a typical procedure, 4 g of graphite powder was dispersed in 200 ml conc. H_2SO_4 (98%) at 0 °C and with constant stirring, followed by slow addition of 20 g of $KMnO_4$ and left the reaction mixture for 24 h with continuous stirring. Further, 500 ml of deionized

(DI) water ice was poured slowly into the reaction suspension to sustain the temperature of the solution under 70 °C followed by the addition of 20 ml of H_2O_2 into the reaction solution. Subsequently, vigorous bubbles appeared in the reaction solution, and the greenish reaction solution changes to yellow colour. Afterward, the solution was kept undisturbed for 5 to 6 h to settle down the precipitate and filtered. Further, it was washed with (10 %) HCl to remove MnO_2 and other metallic impurities, washed several times with DI water to bring pH ~ 7. the graphite oxide powder is obtained by filtering and drying the suspension in an oven at 60 °C for 24 h. Finally, cGO dispersion is prepared by dispersing the graphite oxide powder in DI water (2 mg/ml) using ultrasonication.

2.2.2 Synthesis of Polyaniline-reduced crumbled Graphene Oxide (PRGO) composites

Polyaniline-reduced graphene oxide nanocomposites (PRGO) were synthesized with different weight percentages of GO to Aniline. The wt.% of GO to Aniline is varied as 1 wt.% (1:100), 2 wt.% (1:50), 4 wt.% (1:25), and the corresponding composites are named PRGO1, PRGO2, and PRGO4, respectively. To prepare nanocomposite with 1 wt.% of GO, initially, 1 wt.% of graphite oxide powder (9.3 mg) was dispersed in 20 ml of DI water and ultra-sonicated to form a homogeneous solution of GO with no visible particle. The resulting GO dispersion was added to the mixture of 0.1 M Aniline containing 80 ml of 1 M HCl solution with continuous stirring and maintained the solution temperature of 5 ^{o}C through an ice bath. Once the GO solution is fully mixed uniformly, 0.1 M of 20 ml aqueous solution of APS was added slowly (dropwise) into the solution. As the reaction proceeds with time, the colour of the solution change from dark brown to dark green, indicating the formation of PANI (in Emeraldine form). As the polymerization was complete after 6 h, the reaction solution as such without filtration was transferred into Teflon lined stainless steel autoclave and hydrothermally treated at 120 °C for 12 h. Further, it was allowed to cool down to room temperature naturally. The precipitate was collected and washed with DI water and acetone until the filtrate becomes colourless. Finally, it was dried at 60 °C overnight and then ground into a fine powder. The schematic for the synthesis of PRGO composites is shown in Fig. 2.1. For comparison, pristine PANI is also prepared by the same method in absence of GO.

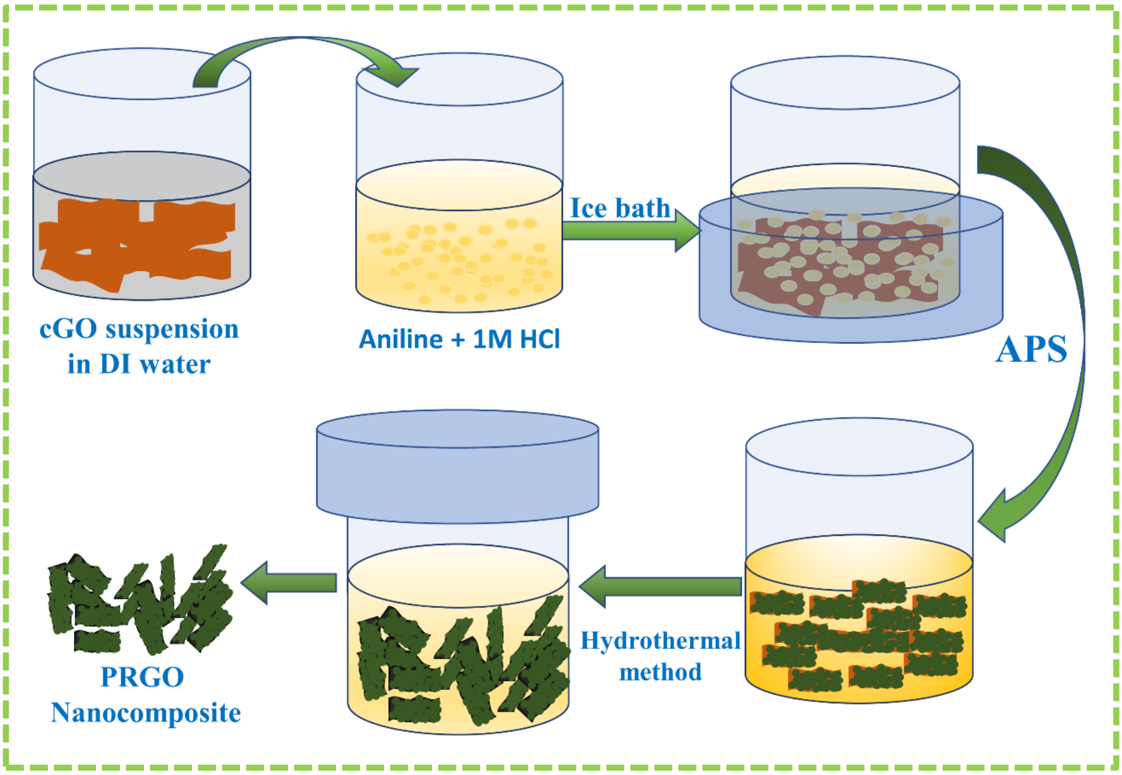

Figure 2.1 *Schematic representation for the synthesis of PRGO nanocomposites.*

2.2.3 Synthesis of N–doped reduced Graphene Oxide (N-rGO)

For the synthesis of N-rGO, 240 mg of graphite oxide powder is taken in 120 ml DI water and subjected to ultrasonic treatment for 30 min. to obtain a clear GO dispersion. Afterward, a desired amount of urea is mixed with GO dispersion and sonicated for another 30 min. Then, it was poured into a Teflon-lined autoclave and hydrothermally treated at 180 ^{o}C for 12 h. Further, the autoclave is allowed to cool naturally and the precipitate is filtered and washed with DI water and ethanol repeatedly to eliminate the unreacted reagents. The final product was obtained by drying the filtrate at 60 ^{o}C for 24 h. The rGO is also synthesized via a similar procedure by excluding reducing agents during the hydrothermal process.

2.2.4 Synthesis of PANI/N-rGO composite

The synthesis process of PANI/N-rGO nanocomposite is as follows. Initially, N-rGO sheets were dispersed in the mixture of DI water and ethanol (20 ml + 20 ml) under ultrasonication. 2 wt.% of N-rGO has been used for the synthesis of PANI/N-rGO composite. 50 ml of 1 M HCl containing 0.1 M aniline was prepared in another beaker and kept under continuous stirring. Then, N-rGO dispersion was added to the above mixture and it was transferred into an ice bath and cooled below 5 ^{o}C. After that 30 ml of 0.1 M of APS was dissolved in DI water and introduced drop by drop to the reaction mixture to initiate the polymerization. After 5 min. of reaction time, the solution is turned into a green color, which is the indication of the formation of conductive emeraldine salt form of polyaniline. Further, the polymerization is carried out for 24 h. After that, the solution was filtered and washed with DI water and ethanol several times and then dried at 60 ^{o}C overnight. The schematic of the synthesis process is shown in Fig. 2.2. For comparison, PANI/rGO is synthesized using a similar procedure by replacing N-rGO with rGO. Pure PANI is also prepared using a similar process.

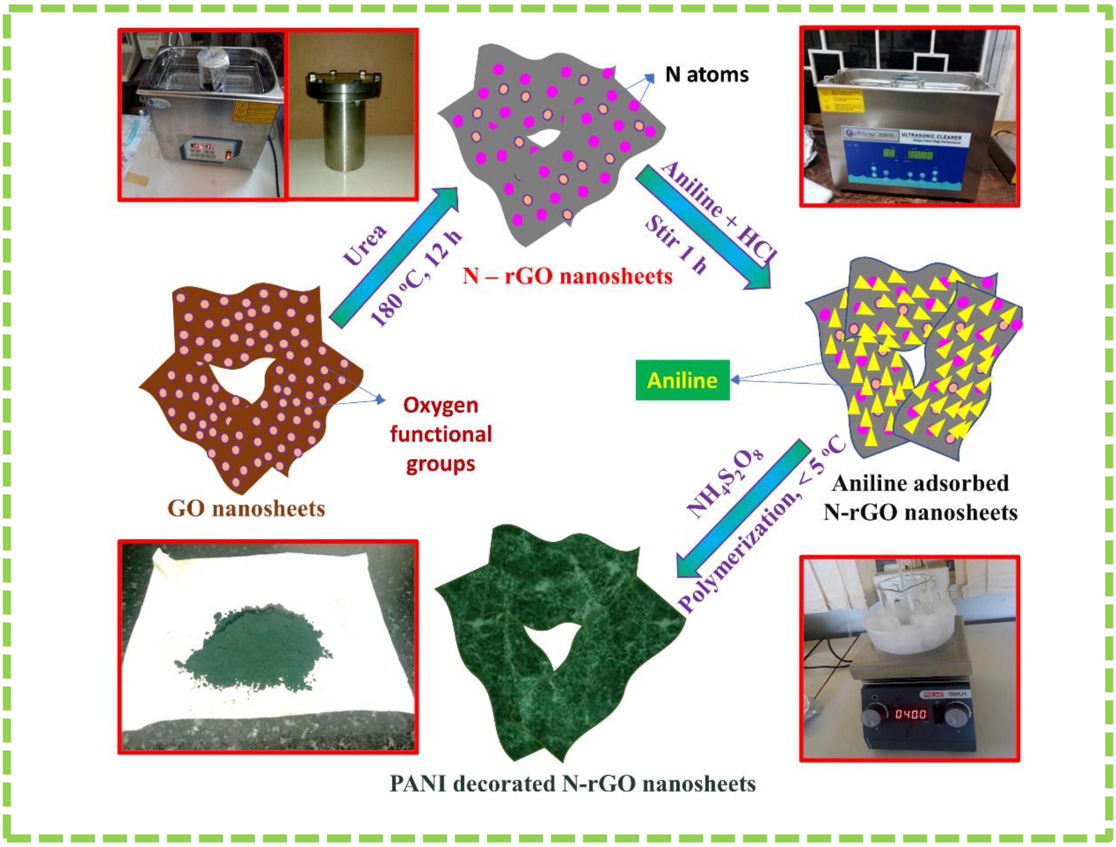

Figure 2.2 *Schematic representation for the synthesis of PANI/N-rGO nanocomposite.*

2.2.5 Synthesis of S – doped reduced graphene oxide (S-rGO)

For the synthesis of S – doped reduced graphene oxide (S-rGO), initially, graphite oxide is prepared from graphite powder using the modified Hummers method. The steps involved in the synthesis process of graphite oxide are explained in section 2.2.1. Then, graphene oxide (GO) dispersion was obtained by sonication of graphite oxide powder in deionized (DI) water (2 mg/ml) for 30 min. After that, Na_2S was mixed with the above GO dispersion (1:1 ratio with GO) and continuously sonicated for another 30 min. Then, it was transferred into 120 ml of Teflon vessel and kept in a stainless-steel autoclave. Further, the autoclave is heated at 180 ^{o}C for 12 h using a hot air oven. When the autoclave is reached room temperature, the precipitate formed at the bottom of the autoclave is collected and washed with DI water repeatedly. Finally, the obtained product was dried at 60 ^oC for 24 hr.

2.2.6 Synthesis of sulfonic acid doped polyaniline: S-doped reduced graphene oxide (SPANI/S-rGO) nanocomposites

The synthesis procedure of SPANI/S-rGO nanocomposites is as follows. In the first step, S-rGO is dispersed in the mixture of DI water and Ethanol (10 ml + 10 ml) under the sonication for 1 h and it is named solution A. Simultaneously, 5 mmol of 2-NSA solution (60 ml) containing 5 mmol of Aniline was prepared in another beaker under continuous stirring and it was named as solution B. After 1 h, the two solutions (solution A and solution B) are mixed and transferred into an ice bath and waited till the reaction mixture reached a temperature below 5 ^oC. After that, precooled 20 ml solution of APS (Aniline: APS = 1:1) was added dropwise to initiate polymerization in the solution and kept for continuous stirring for 12 h. Then the stirring is stopped and the solution was kept undisturbed for another 10 h to settle the final product at the bottom of the beaker. Further, the precipitate was separated from the solution and filtered with repeated washes using ethanol and DI water until the filtrate becomes colourless. Finally, the obtained product was dried at 80 ^oC for 24 h. The schematic of the synthesis process is shown in Fig. 2.3. The wt.% of S-rGO to Aniline was varied as 5 wt.%, 10 wt.%, 15 wt.%, and 20 wt.% and the corresponding nanocomposites were named as SPANI/S-rGO5, SPANI/S-rGO10, SPANI/S-rGO15, and SPANI/S-rGO20, respectively. For comparison, pristine SPANI is also synthesized using a similar method without the addition of S-rGO.

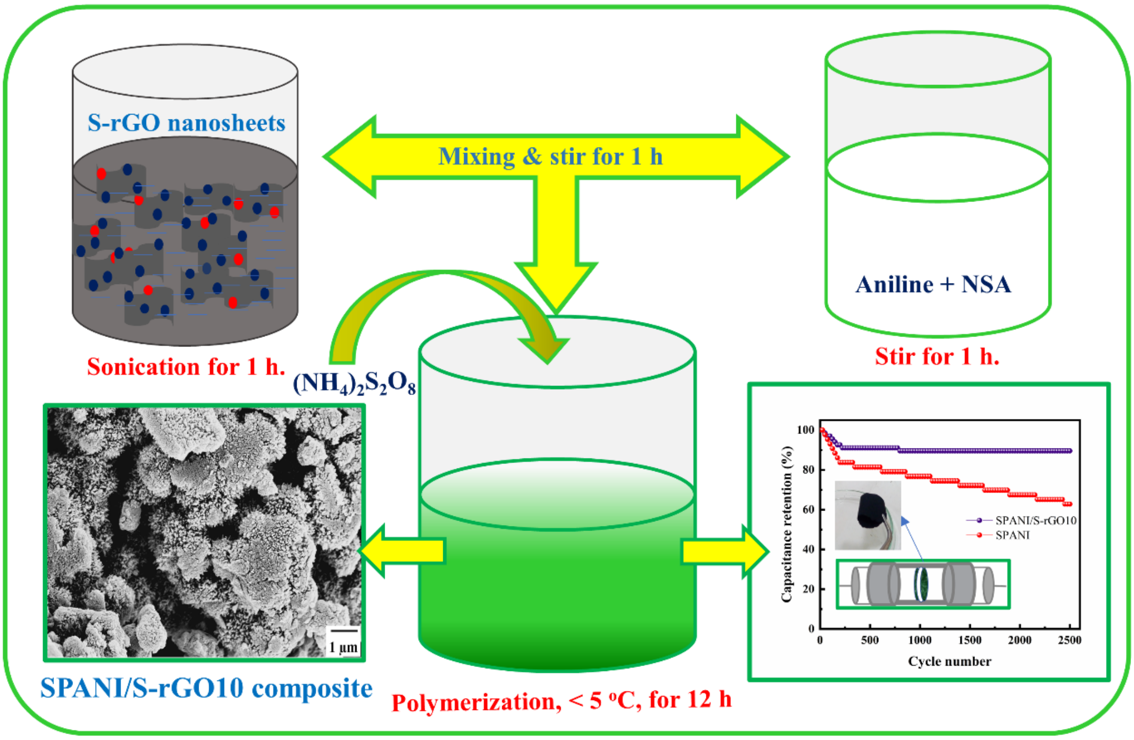

Figure 2.3 *Schematic of steps involved in the synthesis process of SPANI/S-rGO composites.*

2.2.7 Synthesis of corn husk derived porous carbon (CHPCs)

The synthesis of porous carbon is a two-step process, carbonization and then activation. Initially, the corn husk (CH) is sliced into small peace and cleaned thoroughly with tap water, ethanol, and then deionized water (DI water). The cleaned CH is dried in the oven at 120 °C for 24 h and then crushed into powder. Later, 10 g of dried CH powder is taken in an alumina boat and transferred into a tubular furnace, and subjected to carbonization at 800 °C for 1 h with a heating rate of 5 °C/min under N_2 atmosphere. Then, the obtained black CH biochar (CHBC) is washed with 1M HCl and DI water, repeatedly and kept on drying at 100 °C for 24 h. For chemical activation, 2 g of CHBC is mixed with KOH (1:4 ratio) in 20 ml of DI water and dried at 100 °C for 6 h. As the prepared mixture was shifted into an alumina boat and placed in a tubular furnace. Subsequently, it was calcinated at 800 °C for 1 h under N_2 gas flow with a heating rate of 5 °C/min. Finally, CH-derived porous carbon (CHPC) is obtained by following the similar cleaning steps used for biochar. The steps involved in the synthesis process of CHPC are shown in Fig. 2.4. Three different activation temperatures are used for the preparation of CHPCs and the corresponding samples are named CHPC-600, CHPC-700, and CHPC-800.

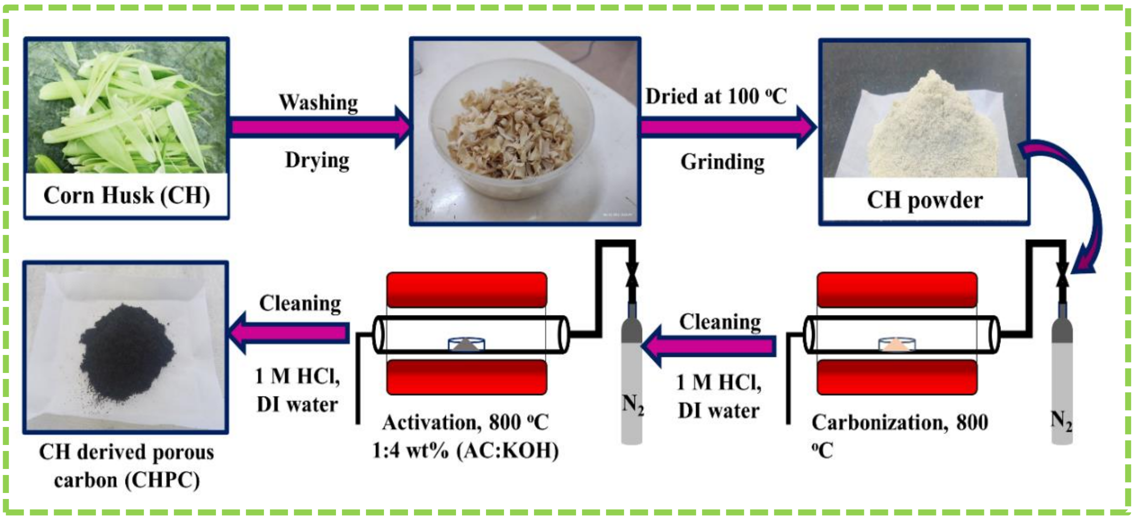

Figure 2.4 *Schematic of steps involved in the synthesis of CHPC.*

2.3 Materials Characterization

2.3.1 Scanning Electron Microscopy and Field Emission Scanning Electron Microscopy

Scanning Electron Microscope (SEM) is a microscopic technique that uses an electron beam instead of light to scan the surface of the material. It is an image processing technique that produces features of the specimen such as surface morphology, structure, and composition. The surface images are produced by scanning a high-energy focussed electron beam on the surface of the specimen. The beam of electrons is generated either by a thermionic gun where a tungsten filament is heated at high temperatures to produce electrons or a field emission gun where a high electric field is applied to the tungsten wire. The electron beam is focussed vertically onto the surface of the specimen by using an electromagnetic lenses system. When the electron beam interacts with the surface, it produces signals mainly secondary electrons, backscattered electrons, and characteristic x-rays. These secondary and backscattered electrons are collected and processed to produce surface images of the materials [4–7]. To produce high-quality images using SEM, the sample surface must be conductive to prevent the charging effect which blurs the image quality. To avoid this, generally, the surface of the sample is sputtered with the conducting surface layer. In this thesis, we have used FESEM (CARL ZEISS, ULTRA55) and SEM (TESCAN, VEGA-3 LMU). For sample preparation, a few mg of powder samples is spread over the copper adhesive tape and gold coating is performed using the sputtering technique.

2.3.2 Transmission Electron Microscopy

Transmission Electron Microscopy (TEM) is also a microscopy technique, similar to SEM, it also uses a highly focussed electron beam to produce the images of the specimen. In this technique, the specimen should be thin in such a way that it should pass the electron beam through the sample. Sample preparation is extremely important because this technique works on the transmission of electrons through the samples. In this technique, electron beam focussed on the sample is interacted with the sample and transmit through it. The interaction of electron beam transmitted through the specimen is further processed by an image detection system to produce the images of the samples. TEM is useful to evaluate the microstructure, pore arrangement, and crystallinity of the electrode material [8]. In this thesis, High-Resolution Transmission Electron Microscopy (HRTEM, Thermofisher, Talos F200S) is used to obtain the TEM images of the electrode materials. For sample preparation, powdered samples are dispersed in ethanol solvent by ultrasonication and drop cast over a Cu grid.

2.3.3 X-ray Diffraction

X-ray Diffraction (XRD) is one of the most traditional, basic non-destructive technique to analyse the crystal structure of the materials. The information about the crystal structure is obtained by the interaction of X-rays with the atoms in a crystal plane of the samples. When a monochromatic X-ray beam hits the sample and is diffracted at different angles, which are collected by the detector. The peak position i.e., the angle of diffraction and peak intensities are the important parameters to analyse the crystal structure. Bragg's stated that for every diffracted beam, there exists a set of crystal planes such that the diffracted beam appears to be spectacularly reflected from the set of planes [9,10]. The interference of these diffracted beams from the different crystal planes is used to identify the crystal structure by using the Bragg's law, i.e., the path difference between two x-ray beams that are diffracted from the two successive crystal planes is equal to the integral multiple of incident X-ray wavelength which is given in below equation.

$$2\mathrm{d}\sin\theta = n\lambda \tag{2.1}$$

Where n is an integer (n=1, 2, 3, etc) and λ is the wavelength of X-ray (λ= 1.5406 Å). In this thesis, XRD patterns of the powder samples are obtained by using a PAN Analytical powder X-ray diffractometer equipped with Cu Kα-radiation of wavelength 1.54 Å.

2.3.4 Fourier Transform Infrared Spectroscopy

Fourier Transform Infrared spectroscopy (FTIR) is also called vibrational spectroscopy which helps us to find out the functional groups present in the sample. It is a study on the interaction of infrared radiation with the material. FTIR works on the principle of interferometry. In this technique, the sample is irradiated with the IR light with variable frequency. Each functional group present in the sample has its characteristic vibrational frequency. When the frequency of incident radiation matches the vibrational frequency of the chemical bonds or functional group of molecules, the radiation gets absorbed. The absorption of energy causes a change in the vibrational state of the molecule from the ground state to an excited state. As a result, the dipole moment of the molecule has changed. When IR light is incident on the sample, part of the radiation gets absorbed and part of the radiation is transmitted. The transmitted light is collected with a detector and forms an interferogram where it is in the time domain. The detected signal is converted from time domain to frequency domain by Fourier transform computer-based programming. Finally obtained FTIR spectra is the plot between the transmittance or absorbance as a function of wavenumber. From the absorption peaks of FITR spectra, the chemical functional groups can be determined [11,12]. The intensity of an absorption peak is related to the population of a certain vibrational state, the number of molecules vibrating at that frequency, and the change in molecular dipole moment [13,14]. In this work, FTIR spectra were recorded on a PerkinElmer Spectrum-100 instrument in a wavenumber range of 400 – 4000 cm^{-1}. KBr pellets are prepared for the FTIR analysis.

2.3.5 Raman spectroscopy

Raman spectroscopy is a spectroscopic technique of special interest because of its ability to provide detailed information about the chemical structure, crystallinity, and molecular interactions of the material [15]. Raman spectroscopy is first discovered by the great Indian scientist Sir. C. V. Raman in 1928. He observed that when light strikes the matter, a fraction of light is scattered and has a different colour which was later named as Raman effect after his pioneering work. He was also awarded a noble prize in 1930 for the discovery of Raman effect. Raman effect is a consequence of inelastic scattering of incident light by the interaction of vibrational/rotational motion of the atoms/molecules. The interaction of incident light causes a change in polarizability with respect to vibrational motion, which induces a dipole movement in the molecule. As a result, we observe a change in the energy of light scattered by this induced dipole movement. When the light is scattered with the same energy as incident photon energy then it is called as Rayleigh's elastic scattering. When the scattered light energy is lower than the incident light energy, the corresponding transition is referred to as stokes line and the higher energy transition is called as anti-stokes line [16,17]. The shift in the frequency of light due to the interaction of vibrational/rotational motion of the molecules provides information about the chemical bonds, and structure of the materials. The Raman spectroscopic instrument consists of four major components, a laser source, sample illuminator, filter, and detector. When Laser light strikes the sample surface at sample illuminator and the light is scattered elastically or inelastically. The elastically scattered light is filtered and the detector process the inelastically scattered light and produces a spectrum consisting of change intensity as a function of change in frequency (Raman shift). The Raman shift is corresponding to the interaction of vibrational/rotational motion of the molecules providing information about the chemical bonds, and structure of the materials. In this research work, the Raman studies are obtained by the Enspectra R532 Raman spectrometer operated with laser light of excitation wavelength 532 nm at room temperature.

2.3.6 X-ray Photoelectron spectroscopy

X-ray photoelectron spectroscopy (XPS) is a widely employed spectroscopy tool to understand the surface elemental composition quantitatively, and chemical state of the sample being studied [18]. The XPS is a result of the interaction of x-rays with sample surface of the order of a few nanometres depth. XPS works on the principle of photoelectric effect. When the x-rays strike the atoms on the surface of the sample, core-shell photoelectrons are ejected. As a result, the XPS spectral lines are identified by which shell the electrons are emitted. The electrons present in each shell of atoms have their binding energies (B.E.). Therefore, the kinetic energy (K.E.) of the emitted electrons is given by K.E. = hυ-B.E.-ϕ where ϕ is the work function. An electron energy analyzer is used to measure the energy of the emitted photoelectrons [19,20]. From the binding energy and intensity of a photoelectron peak, the elemental identity, chemical state, and quantity of a detected element can be determined. The main components of an X-ray Photoelectron Spectrometer are the X-ray source, sample stage, electron energy analyzer, and detector. In the present study, XPS studies were carried out using a K-alpha electron spectrometer equipped with an *Al* X-ray beam source.

2.3.7 Thermogravimetric analysis

Thermogravimetric analysis (TGA) provides useful information about the thermal behavior of the material such as thermal stability, decomposition temperature, compositional analysis, etc. In this technique, change in the weight of the samples is monitored with increasing temperature. The precision of TGA results depends on the three main important measurements: change in weight, heating rate, and temperature [21]. In this study, a known weight sample is heated in an inert atmosphere to avoid unwanted reactions of samples with atmospheric impurities during heating. The constant heating rate is maintained by using a programmable heating furnace. The weight of the sample varied with an increase in temperature due to the thermal decomposition of the sample. The weight change is measured and plotted as a function of temperature to understand the thermal behaviour of the sample being studied. The main components of the TGA instrument are High precision weighing balance and a programmable heating furnace with a temperature controller. NETZSCH STA 2500 model thermogravimetry analyzer is used in the present study to evaluate the thermal properties of the samples.

2.3.8 N_2 adsorption-desorption studies

N_2 adsorption-desorption studies are useful to evaluate the surface area and pore size distribution of the prepared samples [22]. In this technique, during adsorption, the N_2 molecules get adsorbed on the available surface area of the sample with increased relative pressure. During desorption, N_2 is released with a decrease in relative pressure. The plot between the quantity adsorbed as a function of relative pressure is used to estimate the surface area and pore structure of the sample. Before proceeding with the measurements, the samples are subjected to degassing at a particular temperature below the thermal decomposition temperature of the sample for several hours (6 – 24 h) to remove surface adsorbed contaminations, because it is a surface-sensitive technique. The weight of the sample is recorded after cooling down to room temperature (approximately ~ 250 mg). After degassing, the sample was subjected to N_2 gas at variable pressures and constant temperature (generally at -196 ˚C). The amount of nitrogen gas adsorption/desorption with an increase/decrease in applied pressure is measured [23,24].

In this work, N_2 sorption/desorption has been carried out using a Micromeritics ASAP2020 analyzer. The specific surface area (S_{tot}) of the samples is calculated by a multiple-point Brunauer-Emmett-Teller (BET) model within the relative pressure ranges from 0.05 to 0.25 [22]. The micropore surface area and micropore volume are calculated using the t-plot method. The total pore volume of the materials is calculated at a relative pressure value of 0.99. The t-plot is used to calculate the micropore surface area (S_{mic}) and micropore volume (V_{mic}) [25,26]. The difference between S_{tot} and S_{mic} gives the external surface are which consists of mesopores and macropores. The density functional theory (DFT) model and Barret-Joyner-Halenda (BJH) methods are employed for pore size distribution of the material [27].

2.4 Electrochemical Characterization

The electrochemical properties of the electrode materials are evaluated in a two-electrode symmetric cell system. 1 M H_2SO_4 is used as an electrolyte for PANI composite-based systems whereas 6 M KOH electrolyte is used for porous carbon electrodes.

2.4.1 Electrode Fabrication and Cell Assembly

For the preparation electrodes, 40 mg of synthesized material, 4 mg of CB, and 10 µl of PTFE solution are mixed with the addition of a few drops of ethanol under ultrasonication for 30 min. Then it was mixed using a glass rod until it becomes a paste. After that, this paste was rolled into a thick film on a glass plate. After 5 min, the film electrode was peeled off from the glass plate and dried in a vacuum oven for 10 h. The photograph of the prepared flexible film electrode is shown in the insight of Fig. 2.5. The as-prepared flexible electrode is punched into 10 mm diameter pieces and was pressed at 10 MPa using a hydraulic press to give strength to the electrode. Two symmetric pieces are used as electrodes and filter paper is used as a separator. A symmetric supercapacitor device is assembled in a Swagelok cell by separating the electrodes with filter paper. The schematic of Swagelok cell and the photograph of Swagelok cell are given in Fig. 2.5. The electrochemical properties of the device are evaluated by performing electrochemical measurements such as cyclic voltammetry, Galvanostatic charge/discharge, electrochemical impedance spectroscopy measurements using PARSTAT 4000A, and Origa-flex 500u electrochemical workstations.

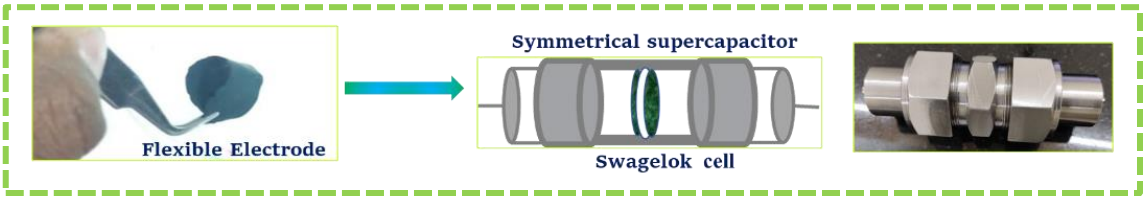

Figure 2.5 *Flexible electrode and SSC assembly.*

2.4.2 Cyclic Voltammetry

Cyclic voltammetry (CV) is an extensively adopted effective technique to understand the electrochemical behaviour of electrode materials. This technique is usually employed to identify the interaction of electrodes with electrolyte ions. It provides information about the faradaic/non-faradaic reaction at the interface of electrode and electrolyte as a function of applied voltage (V). The CV measurements were carried out by applying a voltage across the device at a constant scan rate (mV/s) within the specified voltage range, in both forward and reverse directions. The corresponding current (i) response is measured and plotted against the applied voltage is called as cyclic voltammogram. Generally, carbon-based electrodes exhibit rectangular or nearly rectangular shape CV curves whereas, for pseudocapacitive electrodes, we notice a deviation in CV curve rectangular with presence of redox peaks. The obtained CV plots are used to calculate the specific capacitance (C_{sp}) of the electrode material using the following equation (2.2)

$$C_{sp} = \frac{\int I(V)dV}{m*s*\Delta V}(\mathrm{F/g}) \qquad (2.2)$$

where $\int \boldsymbol{I(V)dv}$ is the integrated area under the CV curve, m is mass of the electrode, s is the scan rate (mV/s), and ΔV is the voltage window.

2.4.3 Galvanostatic charge-discharge

Galvanostatic charge-discharge (GCD) is a standard testing method for measuring the electrochemical characteristics of supercapacitors. This method is also called a chrono-potentiometry technique where a constant current is applied and the voltage response of the device is measured over time in a specified voltage range. A positive constant current is applied to charge the device to a set maximum voltage and then it is discharged by applying the same negative constant current until the voltage across the device becomes zero. The change in voltage with time is plotted and a complete loop of this charging-discharging is referred to as a cycle. This method is used to estimate the performance characteristics of the assembled supercapacitor such as specific capacitance (C_{sp}), specific energy (E_m), and specific power (P_m). The cyclic stability of the cell is measured by conducting GCD continuously over a large number of cycles. The specific capacitance values of electrodes are calculated from GCD measurements using the following equation [28–30].

$$C_{sp} = 2\,\frac{I*\Delta t}{m*\,\Delta V} \qquad (2.3)$$

Where I is the discharging current, Δt is the discharging time, *m* is the mass of a single electrode, Δt is the discharging time, and ΔV is the voltage window. Further, specific energy (E_m) and specific power (P_m) values are calculated using the following Eqn. (2.4) and (2.5), respectively [31,32].

$$E_m = \frac{1}{7.2} C_{sp} \Delta V^2 \text{ (Wh/kg)} \tag{2.4}$$

$$P_m = \frac{E_m}{\Delta t} X\ 3600 \text{ (W/kg)} \tag{2.5}$$

2.4.4 Electrochemical Impedance Spectroscopy

The electrochemical impedance spectroscopy (EIS) is a complementary electrochemical technique to understand the electrical properties of the electrode and the interfacial interaction of charge or ion with the electrode surface at a stationary condition. In this method, an AC sinusoidal voltage over a wide range of frequencies (0.01 to 10^5 Hz) is applied to the electrochemical cell and its corresponding AC sinusoidal current response is measured. The ratio and phase angle between the applied AC voltage and obtained current response provide information about the complex impedance Z, which consists of real (Resistor) and imaginary components. The variation of a real part and imaginary part of the impedance is plotted, it is called as Nyquist plot [33]. These Nyquist plots are used to estimate valuable parameters like cell resistance, double-layer capacitance, and charge transfer resistance by interpreting them with an equivalent circuit model with electrical components. In this research work, EIS studies are performed under open circuit potential conditions by applying the AC voltage of 10 mV amplitude in a frequency range of 0.01 Hz to 10 kHz.

2.5 Conclusions

In this chapter, we have given detailed information on the material synthesis and the characterization techniques used in the present study. It includes the preparation of GO using modified Hummers' method, synthesis of rGO, N-rGO, and S-rGO using hydrothermal reduction method, and synthesis of PANI, PANI/rGO based composites using *in-situ* polymerization method. It also includes the synthesis of porous carbons using corn husk biowaste as raw material. Further, the details of the characterization and electrochemical techniques used in the present work have been discussed in this chapter. Structural and morphological characterization by X-ray Diffraction (XRD), Fourier transform infrared spectroscopy (FTIR), Raman spectroscopy, X-ray photoelectron spectroscopy (XPS), and Field emission scanning electron microscope (FESEM), High-resolution transmission electron microscopy (HRTEM). The surface area and pore structure of the materials is investigated using N_2 adsorption-desorption measurements. The electrochemical properties are evaluated using cyclic voltammetry (CV), galvanostatic charge-discharge (GCD), and electrochemical impedance spectroscopy (EIS) methods.

References

[1] K. Krishnamoorthy, M. Veerapandian, K. Yun, S.J. Kim, The chemical and structural analysis of graphene oxide with different degrees of oxidation, Carbon N. Y. 53 (2013) 38–49. https://doi.org/10.1016/j.carbon.2012.10.013.

[2] K. Singh, A. Ohlan, V.H. Pham, R.B. Balasubramaniyan, S. Varshney, J. Jang, S.H. Hur, W.M. Choi, M. Kumar, S.K. Dhawan, B.S. Kong, J.S. Chung, Nanostructured graphene/Fe3O4 incorporated polyaniline as a high performance shield against electromagnetic pollution, Nanoscale. 5 (2013) 2411–2420. https://doi.org/10.1039/c3nr33962a.

[3] J. Dalal, S. Lather, A. Gupta, S. Dahiya, A.S. Maan, K. Singh, S.K. Dhawan, A. Ohlan, EMI shielding properties of laminated graphene and PbTiO3 reinforced poly(3,4-ethylenedioxythiophene) nanocomposites, Compos. Sci. Technol. 165 (2018) 222–230. https://doi.org/10.1016/j.compscitech.2018.07.016.

[4] M. de Assumpcão Pereira-da-Silva, F.A. Ferri, Scanning Electron Microscopy, in: Nanocharacterization Tech., Springer, Boston, MA, Boston, MA, 2017: pp. 1–35. https://doi.org/10.1016/B978-0-323-49778-7.00001-1.

[5] P. Echlin, Handbook of Sample Preparation for Scanning Electron Microscopy and X-Ray Microanalysis, Springer US, 2009. https://doi.org/10.1007/978-0-387-85731-2.

[6] G.R. Chalmers, R.M. Bustin, I.M. Power, Characterization of gas shale pore systems by porosimetry, pycnometry,surfacearea,andfield emission scanning electron microscopy/ transmission electron microscopy image analyses: Examples from the Barnett, Woodford, Haynesville, Marcellus,andDoig units, Am. Assoc. Pet. Geol. Bull. 96 (2012) 1099–1119. https://doi.org/10.1306/10171111052.

[7] J.M. Bonard, K.A. Dean, B.F. Coll, C. Klinke, Field Emission of Individual Carbon Nanotubes in the Scanning Electron Microscope, Phys. Rev. Lett. 89 (2002) 197602. https://doi.org/10.1103/PhysRevLett.89.197602.

[8] J. Ayache, L. Beaunier, J. Boumendil, G. Ehret, D. Laub, Sample Preparation Handbook for Transmission Electron Microscopy, Springer New York, 2010. https://doi.org/10.1007/978-0-387-98182-6.

[9] B.E. Warren, X-ray diffraction methods, J. Appl. Phys. 12 (1941) 375–383. https://doi.org/10.1063/1.1712915.

[10] C.G. Pope, X-ray diffraction and the bragg equation, J. Chem. Educ. 74 (1997) 129–131. https://doi.org/10.1021/ed074p129.

[11] S.G. Kazarian, K.L.A. Chan, Sampling approaches in fourier transform infrared imaging applied to polymers, Prog. Colloid Polym. Sci. 132 (2006) 1–6. https://doi.org/10.1007/2882_034.

[12] R. Bhargava, S.Q. Wang, J.L. Koenig, FTIR microspectroscopy of polymeric systems, Adv. Polym. Sci. 163 (2003) 137–191. https://doi.org/10.1007/b11052.

[13] H. Günzler, H.-U. Gremlich, H.W. Siesler, Y. Ozaki, S. Kawata, H.M. Heise, A. Williams, Handbook of Spectroscopy, Wiley, 2003. https://doi.org/10.1002/3527602305.

[14] B. Smith, Infrared Spectral Interpretation, CRC Press, 2018. https://doi.org/10.1201/9780203750841.

[15] G.F.S., A new radiation, J. Franklin Inst. 206 (1928) 276–277. https://doi.org/10.1016/s0016-0032(28)91546-x.

[16] H.A. Szymanski, RAMAN SPECTROSCOPY, THEORY AND PRACTICE, v 2., Springer US, Boston, MA, 1967. http://ebooks.cambridge.org/ref/id/CBO9781107415324A009%5Cnhttp://link.springer.com/10.1007/978-1-4684-3024-0 (accessed April 14, 2022).

[17] Practical Raman Spectroscopy, Springer Berlin Heidelberg, 1989. https://doi.org/10.1007/978-3-642-74040-4.

[18] C.J. Powell, P.E. Larson, Quantitative surface analysis by X-ray photoelectron spectroscopy, Appl. Surf. Sci. 1 (1978) 186–201. https://doi.org/10.1016/0378-5963(78)90014-4.

[19] J.D. Andrade, X-ray Photoelectron Spectroscopy (XPS), in: Surf. Interfacial Asp. Biomed. Polym., Springer, Boston, MA, Boston, MA, 1985: pp. 105–195. https://doi.org/10.1007/978-1-4684-8610-0_5.

[20] S. Oswald, X-Ray Photoelectron Spectroscopy in Analysis of Surfaces, in: Encycl. Anal. Chem., John Wiley & Sons, Ltd, 2013. https://doi.org/10.1002/9780470027318.a2517.pub2.

[21] R. Bottom, Thermogravimetric Analysis, in: Princ. Appl. Therm. Anal., John Wiley & Sons, Ltd, 2008: pp. 87–118. https://doi.org/10.1002/9780470697702.ch3.

[22] K.S.W. Sing, REPORTING PHYSISORPTION DATA FOR GAS/SOLID SYSTEMS., in: John Wiley & Sons, Ltd, 1984: pp. 567–583. https://doi.org/10.1002/9783527610044.hetcat0065.

[23] J. Cai, H. Niu, Z. Li, Y. Du, P. Cizek, Z. Xie, H. Xiong, T. Lin, High-Performance Supercapacitor Electrode Materials from Cellulose-Derived Carbon Nanofibers, ACS Appl. Mater. Interfaces. 7 (2015) 14946–14953. https://doi.org/10.1021/acsami.5b03757.

[24] Y. Dong, H. Lin, D. Zhou, H. Niu, Q. Jin, F. Qu, Synthesis of mesoporous graphitic carbon fibers with high performance for supercapacitor, Electrochim. Acta. 159 (2015) 116–123. https://doi.org/10.1016/j.electacta.2015.01.152.

[25] H. Demiral, I. Demiral, Surface properties of activated carbon prepared from wastes, in: Surf. Interface Anal., John Wiley & Sons, Ltd, 2008: pp. 612–615. https://doi.org/10.1002/sia.2716.

[26] A. Galarneau, F. Villemot, J. Rodriguez, F. Fajula, B. Coasne, Validity of the t-plot method to assess microporosity in hierarchical micro/mesoporous materials, Langmuir. 30 (2014) 13266–13274. https://doi.org/10.1021/la5026679.

[27] J. Jagiello, M. Thommes, Comparison of DFT characterization methods based on N2, Ar, CO2, and H2 adsorption applied to carbons with various pore size

distributions, in: Carbon N. Y., Pergamon, 2004: pp. 1227–1232. https://doi.org/10.1016/j.carbon.2004.01.022.

[28] Q. Hao, X. Xia, W. Lei, W. Wang, J. Qiu, Facile synthesis of sandwich-like polyaniline/boron-doped graphene nano hybrid for supercapacitors, Carbon N. Y. 81 (2015) 552–563. https://doi.org/10.1016/j.carbon.2014.09.090.

[29] F. Liu, S. Luo, D. Liu, W. Chen, Y. Huang, L. Dong, L. Wang, Facile processing of free-standing polyaniline/SWCNT film as an integrated electrode for flexible supercapacitor application, ACS Appl. Mater. Interfaces. 9 (2017) 33791–33801. https://doi.org/10.1021/acsami.7b08382.

[30] T. Hu, Y. Liu, Y. Zhang, M. Chen, J. Zheng, J. Tang, C. Meng, 3D hierarchical porous V3O7·H2O nanobelts/CNT/reduced graphene oxide integrated composite with synergistic effect for supercapacitors with high capacitance and long cycling life, J. Colloid Interface Sci. 531 (2018) 382–393. https://doi.org/10.1016/j.jcis.2018.07.060.

[31] Y. He, X. Wang, H. Huang, P. Zhang, B. Chen, Z. Guo, In-situ electropolymerization of porous conducting polyaniline fibrous network for solid-state supercapacitor, Appl. Surf. Sci. 469 (2019) 446–455. https://doi.org/10.1016/j.apsusc.2018.10.180.

[32] H. Kuzhandaivel, S. Manickam, S.K. Balasingam, M.C. Franklin, H.J. Kim, K.S. Nallathambi, Sulfur and nitrogen-doped graphene quantum dots/PANI nanocomposites for supercapacitors, New J. Chem. 45 (2021) 4101–4110. https://doi.org/10.1039/d1nj00038a.

[33] P. Abélard, J.F. Baumard ; Study Of The, A.C.; P. Abélard, J.F. Baumard ; London, U.G. Adam, J.H. Gibbs, ; E166-E172 R H Adrian, W.K. Chandler, A.L. Hodgkin, ; Y Aihara, J. Kuratomi, T. Bando, T. Iguchi, H. Yoshida, T. Ono, K. Kuwana, Impedance Spectroscopy, John Wiley & Sons, Inc., 2018. https://doi.org/10.1002/9781119381860.

CHAPTER 3

POLYANILINE/rGO COMPOSITE AS A FLEXIBLE ELECTRODE MATERIAL SUPERCAPACITORS

3.1 Introduction

Conducting Polymers (CPs) are well known for their electrochemical properties and are considered best suited for flexible or stretchable energy storage devices. The electrochemical properties of CPs can be tuned depending on the morphology, type, and size of polymers [1,2]. Hence, the design and development of highly efficient flexible electrode material for high energy are crucial for improving the performance of the supercapacitor [3]. Flexible supercapacitors (FSCs) possessing high mechanical strength, an optimum surface area along with high conductivity are the main parameter to meet the compliance in wearable, foldable, and flexible devices [4]. Nitrogen-wearing functional polymers like Polyaniline (PANI) is the best suitable candidate for the FSCs owing to their advantages like high flexibility, multiple oxidation states, tunable electrical properties, and environmental stability [5,6]. However, in PANI, there is huge volume expansion during the charge-discharge process at a high current which hampered the commercialization of PANI in supercapacitors [7,8]. To address the above problems, PANI composite with carbon nanofibers, Carbon nanotubes, graphene, and transition metal oxides, have been reported to enhance the electrochemical performance by increasing the conductivity and surface area [9–11]. PANI nanostructure incorporated with two-dimensional (2D) materials like GO or rGO (having high conductivity and high specific surface area of ~2300 m^2/g) leads to an increase in the specific capacitance and cyclic stability [12]. Several methods were reported for the synthesis of PANI/GO and PANI/rGO composite and have shown promising performance for the supercapacitor application [13–18]. Various studies were also have shown the performance of PANI/rGO composite is better than the PANI/GO composite [12,19]. Further, few studies are also reported on the synthesis of PANI/rGO using the hydrothermal method, and their improved electrochemical performance for supercapacitors [20–24]. However, we found that in most of these reported studies, either GO is reduced by employing a reducing agent before subjecting to the *in-situ* polymerization or high-temperature hydrothermal treatment (~180 ^oC) is used while synthesizing PANI/rGO composite. In these synthesis techniques, the reduction of GO done before *in-situ* polymerization causes the stacking of graphene layers, and therefore, the resultant rGO cannot be fully dispersed in DI water during the *in-situ* polymerization process of Aniline. Further, the usage of high reaction temperature (~180 ^{o}C) and reducing agents during hydrothermal synthesis also causes a reduction in PANI [21]. The reduced state of PANI was accompanied by the transformation of emeraldine salt form to non-conducting emeraldine base which decreases the electrochemical performance of supercapacitor. Therefore, here we have reported a simple facile procedure to synthesize PANI- reduced crumbled graphene oxide (rcGO) nanocomposites by varying the wt. % of Aniline to crumbled graphene oxide (cGO) using a reducing agent-free low-temperature hydrothermal method (120 ^{o}C) to avoid the reduction of PANI and to obtain the composite with better electrical conductivity. Further, the oligomers/dimers formed during the polymerization of Aniline in PANI/cGO solutions have been utilized for the reduction of cGO and simultaneously a solid-state charge transfer mechanism is happening between PANI chains and rcGO layers. Furthermore, hydrothermal reduction of cGO in PANI creates better interfacial contact between the laminated PANI/rcGO which prevents the restacking of graphene layers and offers exceptional electrochemical properties. With a little modification in reaction parameter, we can get high-performance PANI/rcGO composite at a lower temperature, making a more economically viable process for scale-up of polyaniline-reduced graphene oxide binary composite for supercapacitor application.

3.2 Results and Discussion

The preparation of PRGO nanocomposite is a two-step process, where first cGO synthesis was carried out and then *in-situ* polymerization followed by hydrothermal reaction at 120 °C. The *in-situ* oxidation polymerization of Aniline with cGO in the HCl medium leads to a homogeneous cross-linked polymer chain of PANI. During polymerization, dopant ions play a very directional role to form the morphology of nanostructure and modification of surface properties of PANI [25]. Due to the presence of functional groups (-COOH, -OH, and C-O-C) on graphene sheets, the PANI/cGO is hydrophilic and has a high degree of hydration. Once the polymerization is complete, the hydrothermal reduction of cGO through the dimer and oligomer present in the polymer solution leads to removable of functional groups to form more densely packed laminated with the fluffy structure of PRGO. This heat-assisted reduction of cGO in the presence of the PANI chain leads to more interfacial contact between the polymer chains and graphene layers providing more charge transfer and mechanical strength to the PRGO nanocomposites. The densely packed nanoclusters of PANI lead to more charge in a relatively shorter transmission path for electrolyte ions to interact with the electro-active surface of PANI and graphene layers in PRGO favour the enhanced electrochemical performance.

The powder XRD images of cGO, rcGO, PANI, PRGO1, PRGO2, and PRGO4 are shown in Fig. 3.1. The wide d-spacing (d =0.838 nm) corresponds to a peak related to (002) reflection at $2\theta = 10.3°$ confirming the oxidation of graphite powder to cGO whereas a broad diffraction peak at $2\theta = 24.5°$ was observed for rcGO (d= 0.359 nm). The hydrothermal reduction leads to a decrease in d -spacing from 0.838 nm to 0.359 nm due to the removal of oxygen-containing functional groups from the basal planes of cGO [26]. In the diffraction pattern, PANI exhibits three broad and less intensive diffraction peaks centered at $2\theta = 14.15°$, 20.27°, and 25.06° shows that PANI is having partial crystallinity with amorphous background [27]. The diffraction peaks at 14.5° and 19.25° are assigned to the periodicity perpendicular to the polymer chain, and the peak at 25° is due to the periodicity parallel to the polymer chain [28]. PRGO1, PRGO2, and PRGO4 possess a similar XRD pattern as that of PANI, and the diffraction peak related to cGO has disappeared. The XRD results suggested that the successful reduction of cGO and PANI nanostructures were firmly settled on the surface of the rcGO sheets and retained their crystal structure. Further, no extra peaks are observed in the synthesized composite reveals the graphene sheets are fully laminated by the PANI chains as supported by FESEM images.

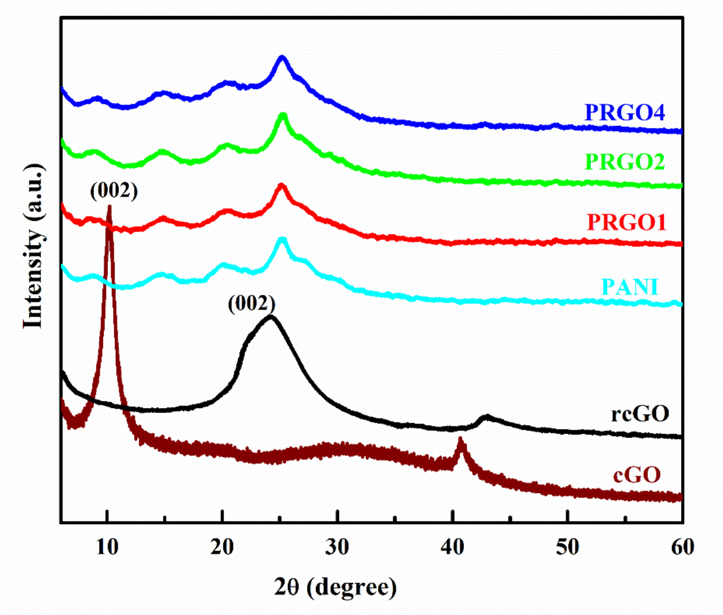

Figure 3.1 *XRD pattern of cGO, rcGO, PANI, PRGO1, PRGO2, and PRGO4 nanocomposites, respectively.*

The surface morphologies of cGO, rcGO, PANI, and PRGO2 composite were analyzed through FESEM as shown in Fig. 3.2. The cGO (Fig. 3.2a) shows crumbled layered morphology whereas rcGO possessed some aggregated sheets, which is linked to the restacking of graphene layers after hydrothermal reduction of cGO. From Fig. 3.2b, it is visible that the graphene layers are more agglomerated due to loss of oxygen-containing functional groups (-CO, -COOH, -C-O-C- and -OH) present on the surface of cGO leading to less porous structure and more Vander Waals interactions. For PANI, the APS initiates the oxidation polymerization of monomer Aniline in a hydrochloric medium at low temperature leading to interconnected nanostructures to form a continuous network (Fig. 3.2c). In composites, a short-range PANI nanostructure network is formed on the surface of graphene sheets which is more densely packed with increasing wt.% of cGO in PRGO composites (Fig. 3.2d-f). Due to the presence of crumbled layers of cGO and the presence of electronegative oxygen functional groups, aniline monomer gets adsorbed onto the layers of cGO easily. These adsorbed Aniline molecules on the graphene layers undergo oxidation to form positive free radical cation (anilinium cation) at the surface of graphene layers which combine with another ion to form a dimer and subsequently get polymerized and cover the surface by densely packed nanocluster of PANI in the form laminates. Further, the heat treatment of polymeric solution leads to the reduction of cGO and crosslinking of PANI chains with removable functional groups (-CO, -COOH, -C-O-C- and -OH) to form a fluffy structure of

PRGO composites (Fig. 3.2d-f). Furthermore, the reduction of cGO to form better interfacial contact between the polymer chains and graphene layers provides an improved charge-transfer mechanism to facilitate more active sites for enhanced electrochemical performance. Excess amount of cGO in PRGO4 composite (Fig. 3.2f) leads to the agglomerated graphene layers with a short range of interconnections and a more densely packed structure affects the electron transport properties of composite and decrease the specific capacitance.

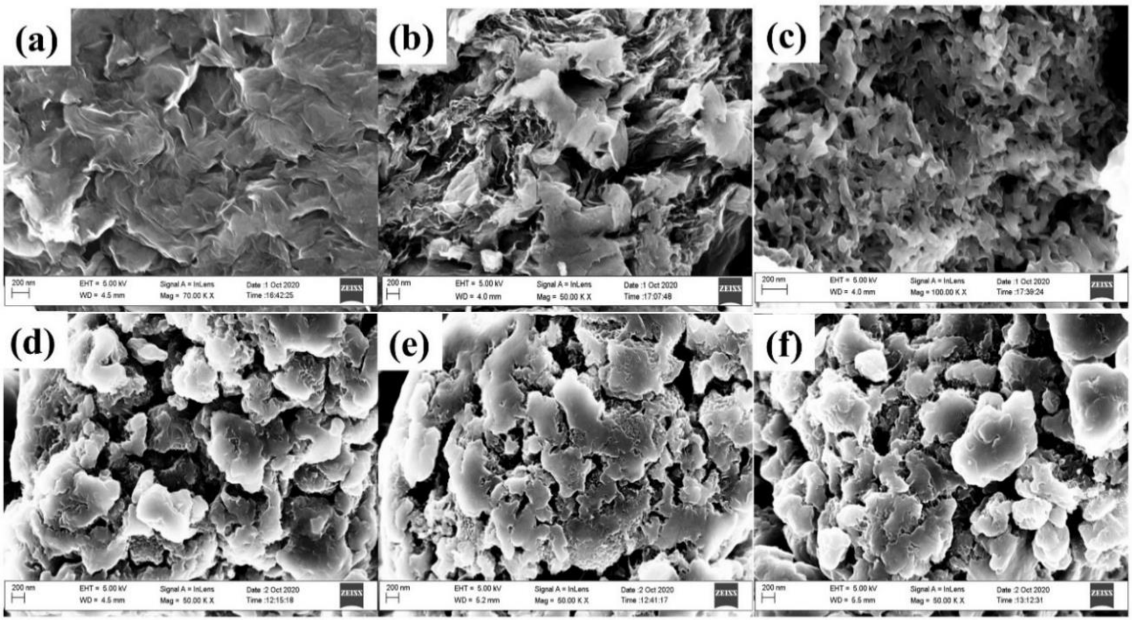

Figure 3.2 *FESEM images of (a) cGO, (b) rcGO (c) PANI, (d) PRGO1, (e) PRGO2 and (f) PRGO4.*

To get an insight view of synthesized material and strengthen the results obtained from the FESEM, pure PANI and PRGO2 composite are also analysed by TEM. Fig. 3.3a-d shows the TEM and HRTEM images of PANI and PRGO2 composite. From Fig. 3.3a, pristine PANI consists of short-range nanorods interconnected network which is agglomerated to form cluster whereas these interconnected networks of PANI nanostructures are fully covered the surface of graphene layers to form densely pack fluffy structure in PRGO (Fig. 3.3c). From Fig. 3.3d, we can observe the presence of both few-layer graphene covered by the amorphous PANI (as we have seen in Fig. 3.3b) at the boundary, which shows that cGO layers will provide favourable support for the growth of PANI nanostructures [28]. Such type of structural foundation improves the charge transport kinetics of the composite material, hence, it is more beneficial to develop a high-performance supercapacitor [21].

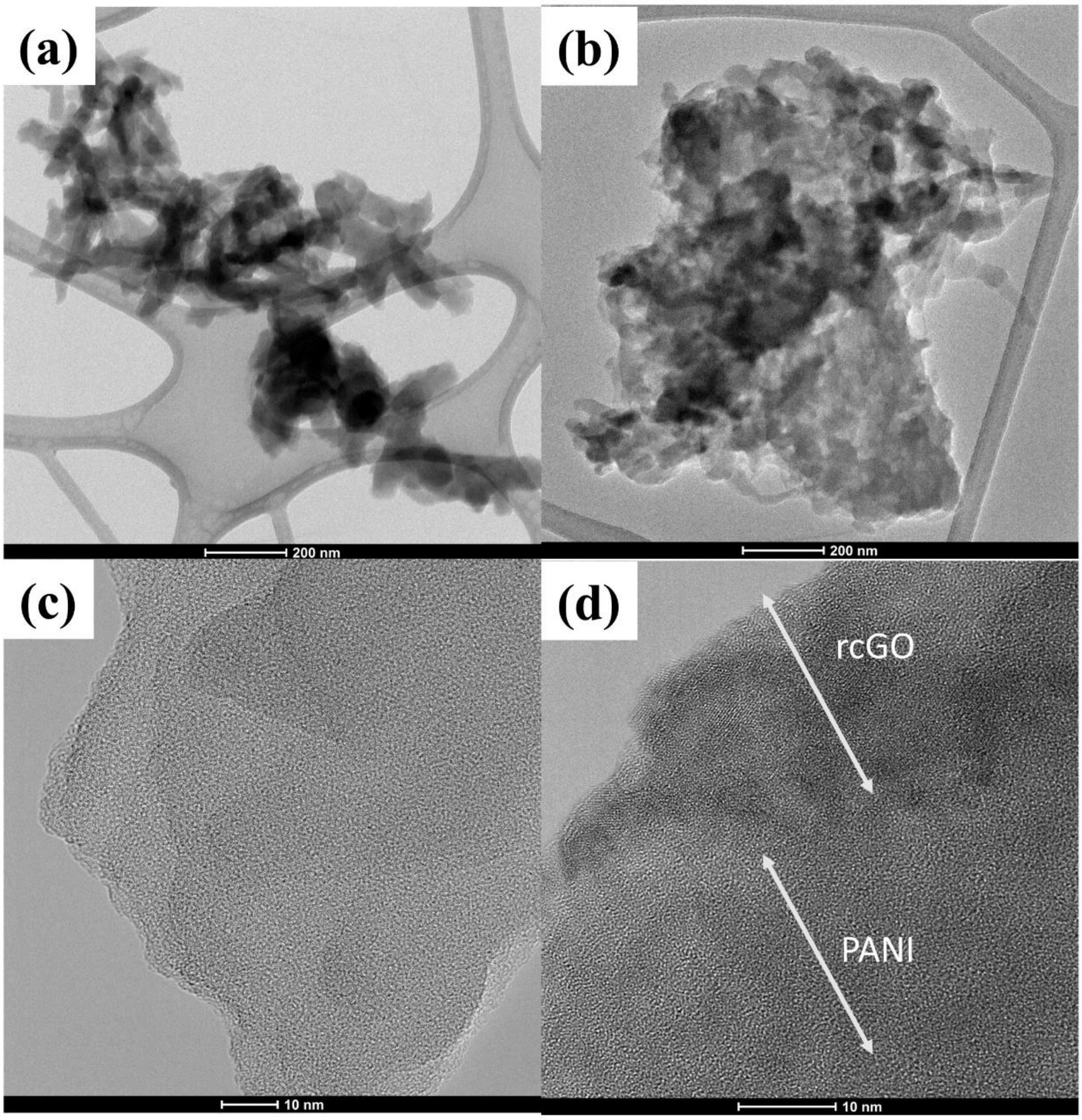

Figure 3.3 *TEM images of (a) PANI & (b) PRGO2 and HRTEM images of (c) PANI & (d) PRGO2.*

FTIR & Raman spectroscopy are very effective techniques to study detailed structural information about the functional groups present in the nanostructured material. The formation of rcGO in the PANI network has been measured through FTIR and Raman spectroscopy. FTIR spectrum of cGO, and rcGO are shown in Fig. 3.4 of supplementary information. The characteristic peaks of cGO related to aromatic (C=C), epoxide (C-O-C), and carbonyl (C=O) groups are observed at 1582 cm^{-1}, 1029 cm^{-1}, and 1719.54 cm^{-1}, respectively (Fig. 3.4). This is in line with the vibrational absorption peaks observed in the FTIR spectrum of a typical GO sample reported elsewhere [29]. After hydrothermal reduction, the intensity of all the peaks corresponding to oxygen functional groups is decreased, which indicates the heat treatment leads to the reduction of cGO to some extent (Fig. 3.4). The presence of a vibrational peak at 1580 cm^{-1} and the appearance of double peaks at 2943 cm^{-1}, and 2890 cm^{-1} confirms the restoration of sp^2 hybridized C=C groups in rcGO [30].

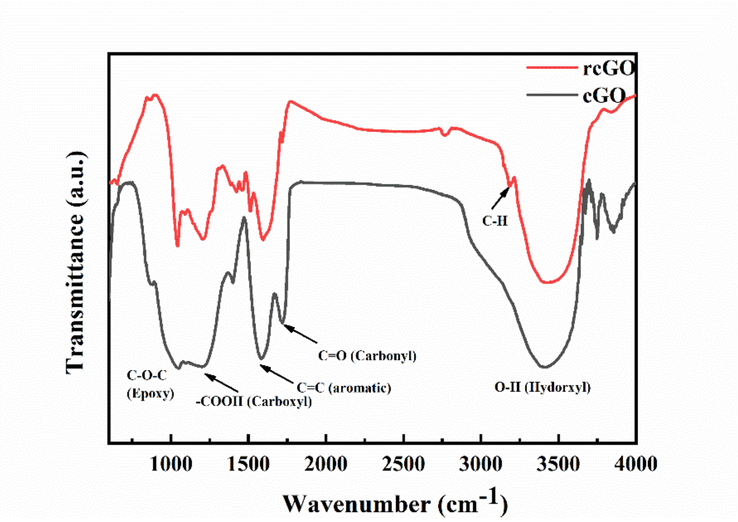

Figure 3.4 *FTIR spectrum of cGO and rcGO.*

FTIR spectrum of PANI, PRGO1, PRGO2, and PRGO4 are shown in Fig. 3.5a. For PANI, the absorption peaks at 1488 cm^{-1} and 1582 cm^{-1} are attributed to the aromatic C=C stretching of benzenoid ring and quinonoid ring of PANI, respectively [21]. The other absorption peak at 1296 cm^{-1} is related to the C-N stretching of secondary amines and the strong bond at 1122 cm^{-1} corresponds to C-H bending vibration of the benzene ring [13]. All the prominent peaks, which are related to the PANI, are retained in all the composites. After hydrothermal treatment, the peaks related to benzenoid and quinoid ring are red-shifted with the increasing concentration of cGO. This shifting phenomenon is indicating the strong interfacial contact between the rcGO and PANI [31,32]. The strong interaction between rcGO layers and PANI nanostructures facilitates high electron transport thus increasing the specific capacitance of the composite material.

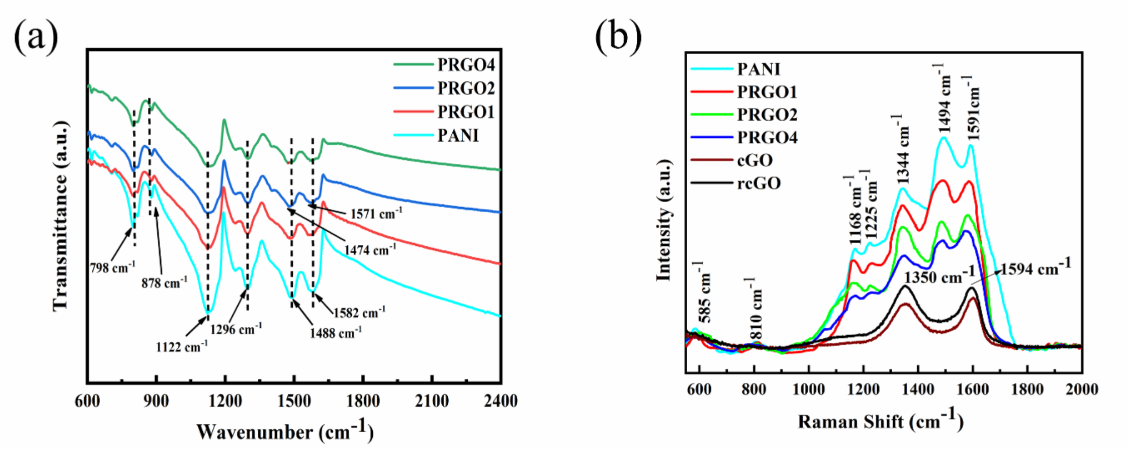

Figure 3.5 *(a) FTIR spectra of PANI, PRGO1, PRGO2, and PRGO4, and (b) Raman spectra of cGO, rcGO, PANI, PRGO1, PRGO2, and PRGO4 nanocomposites.*

Raman spectroscopy is an excellent tool to study the chemical structure of carbon-based materials [33]. Fig. 3.5b shows the Raman spectra of the samples. In the case of cGO and rcGO, the G band at 1594 cm^{-1} and D band at 1350 cm^{-1} are observed. The G band is linked to E_{2g} vibrations modes of sp^2 hybridized carbon domains while the D band is closely associated with the structural defects within the nanomaterial [34]. The I_D/I_G ratio is used to scrutinize the degree of defects present in the carbon material. The I_D/I_G of rcGO is 1.01, which is higher than that of cGO (0.89), this may be due to the partial restoration of graphitic structure and the addition of defects and disorder in the rcGO after reduction [35]. These defects rich frameworks facilitate sufficient contact between the electrode and electrolyte for ion diffusion [36]. A series of characteristic bands at 585 cm^{-1}, 810 cm^{-1}, 1168 cm^{-1}, 1225 cm^{-1}, 1344 cm^{-1}, 1494 cm^{-1}, and 1591 cm^{-1} are found in the Raman spectra of PANI. The C=N stretching vibrations are associated with the peak at 1494 cm^{-1} while the peak at 1591 cm^{-1} is associated with the C=C quinoid/benzene ring, respectively. The other peaks at 585, 810, 1168, 1225, and 1344 cm^{-1} are related to the ring deformation of the benzene/quinoid ring, C-H out of plane bending, C-H in-plane bending of the quinoid ring, C-N stretching mode of polaronic units, and protonic stretching of C-N$^+$ in quinoid ring, respectively [37]. For, PRGO composites, the peak at 1591 cm^{-1} is red-shifted to 1576 cm^{-1} and the corresponding intensity of all the peaks was reduced, confirming the solid-state charge transfer interaction between the rcGO nanosheets with PANI [25].

XPS analysis is further performed to obtain information about the surface elemental composition of the samples. The survey spectra of cGO, rcGO, PANI, and

PRGO2 composite are shown in Fig. 3.6 and the corresponding elemental composition is given in Table 3.1. The survey spectra of cGO and rcGO contain both the C1s and O1s peaks whereas additional peaks corresponding to N1s and Cl 2p are observed for both PANI and PRGO2 composite (Fig. 3.6). It is seen from the survey spectrum of the cGO prepared by the modified hummer method to contain a higher amount of oxygen functionalities and which was decreased after heat treatment at 120 °C in the case of rcGO (Fig. 3.6).

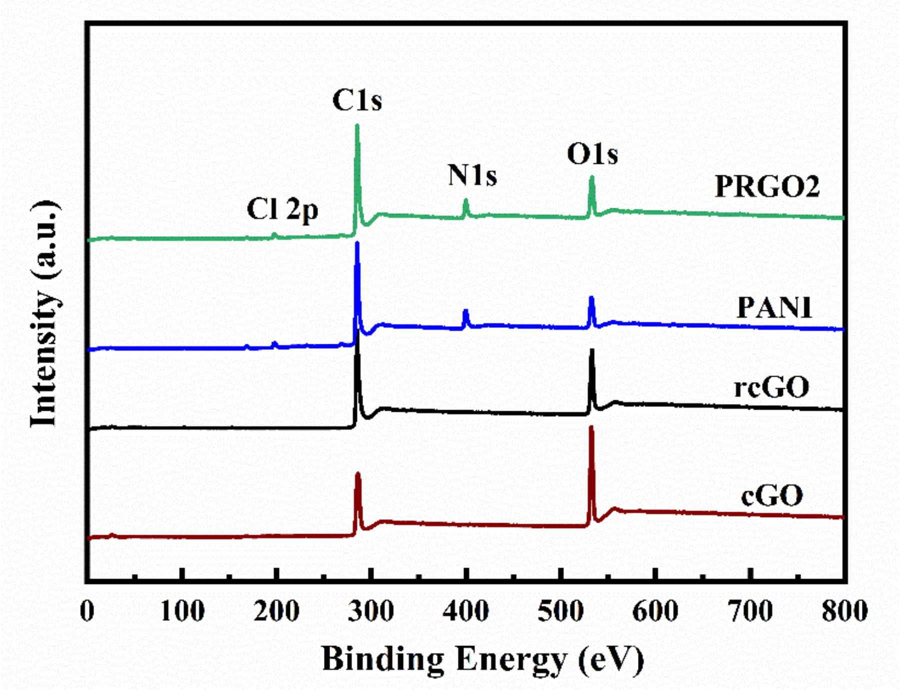

Figure 3.6 *XPS survey spectra of cGO, rcGO, PANI, and PRGO2.*

The high-resolution C1s spectra of cGO (Fig. 3.7a) has various bonding configurations such as C-C/C=C (284.5 eV), C-O (286.4 eV), C=O (287.5 eV), and O-C=O (288.8 eV) confirms the formation of cGO. Further, we found that there is a decrease in intensity of the peaks related to oxygen functionalities in high-resolution C1s spectra of rcGO (Fig. 3.7b) indicating the reduction of cGO after heat treatment. The high-resolution C1s spectra (Fig. 3.7c&d) of PANI and PRGO2 deconvoluted into three components related to C-C (284.5 eV), C-N/C=N (285.5 eV), and O-C=O (288.5 eV). The peak at 288.8 eV is shown the oxidation level of the sample surface, it is consistent with the reactive nature of most of the conjugate polymers [38]. Further, there is a notable increase in the carbon content associated with the C-C bond, and oxygen functionalities (O-C=O) are observed for PRGO2 composite confirming the presence of rcGO and the interaction of imine groups of PANI with the oxygen functional groups of cGO in the composites.

Table 3.1 Elemental composition of cGO, rcGO, PANI, and PRGO2.

Materials	C	N	O	-N=	-NH-	Doping level N$^+$/N	azane-type
	At. %	At. %	At. %	%	%	%	%
cGO	71.50	-	28.50	-	-	-	
rcGO	87.29	-	12.71	-	-	-	
PANI	82.87	10.74	6.39	6.51	58.36	27.44	7.68
PRGO2	86.94	5.39	7.67	12.73	55.59	26.99	4.67

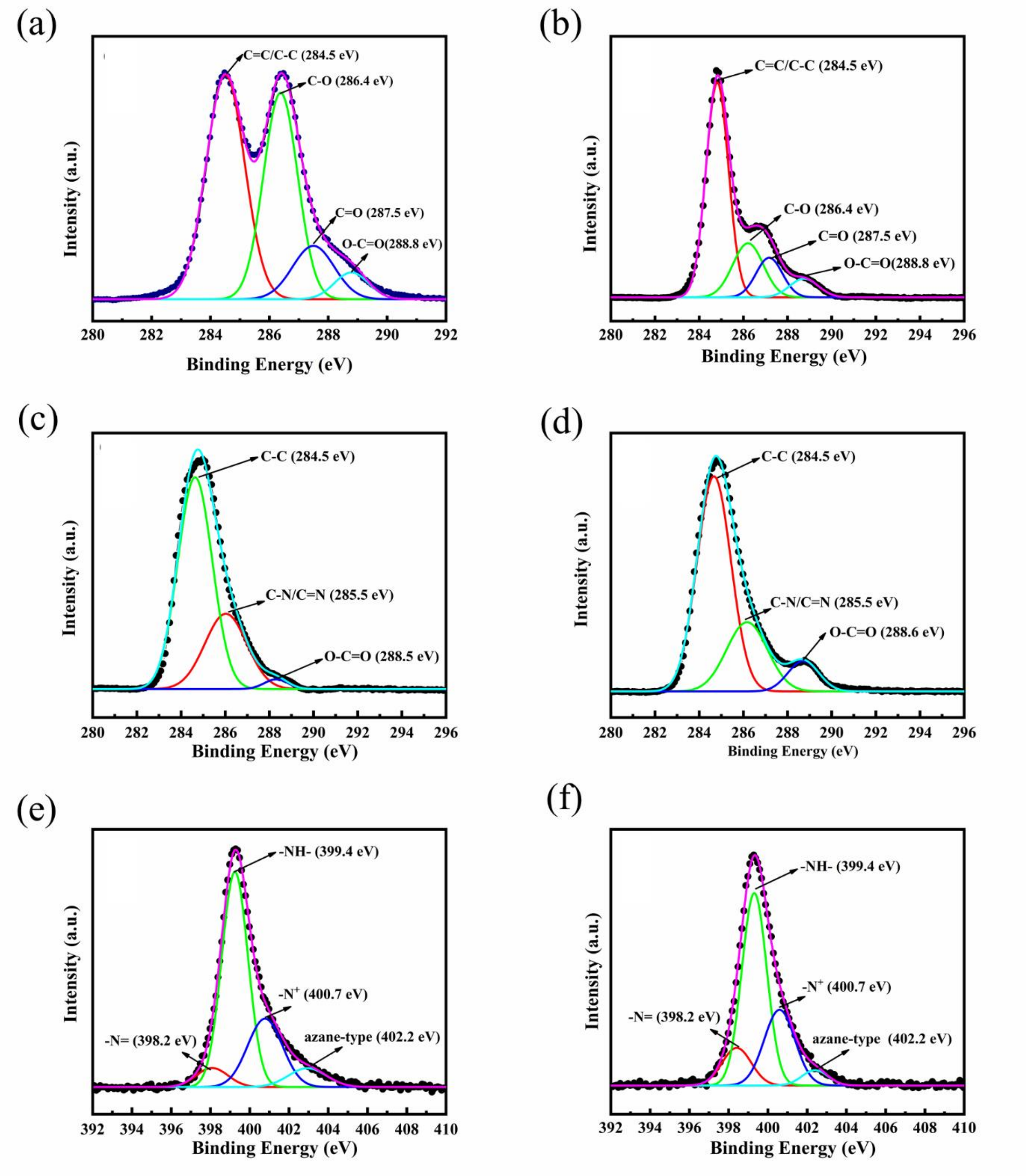

Figure 3.7 *High-resolution C1s spectrum of (a) cGO, (b) rcGO, (c) PANI, (d) PRGO2, and high-resolution N1s spectrum of (e) PANI, and (f) PRGO2.*

The deconvoluted N1s spectra of PANI and PRGO2 (Fig. 3.7e&f) contain the peaks related to quinoid imine (398.2 eV), and benzenoid amine (399.4 eV), protonated radical cation N^+ (400.7 eV), and azane-type (402.2 eV) state of nitrogen. Generally, the ratio of protonated nitrogen to overall nitrogen content (N^+/N) will give information about the doping level in polymer, responsible for the conductivity of PANI [20]. There is only a little decrease in the N^+/N ratio is observed for PRGO2 composite (26.99%) indicates the high doping level of composite with good electrical conductivity. Furthermore, the presence of azane-type nitrogen content has well supported the existence of crosslinking in both PANI and PRGO2 composite, in line with the FESEM and HRTEM results [37,39]. Moreover, there is a notable increase in the concentration of quinoid imine groups in PRGO2 composite clearly shows the strong π- π interaction of graphene layers with polymer chain as we observed in FTIR and RAMAN results.

The comparison of electrical conductivity of PRGO1, PRGO2, and PRGO4 samples with pristine rcGO and pure PANI has been represented in Fig. 3.8. Here, we found that the electrical conductivity for all the PANI/rcGO composite samples i.e., PRGO1 (σ=1.33 S/cm), PRGO2 (σ=4.81 S/cm), and PRGO4 (σ=3.83 S/cm), is relatively higher compared to the electrical conductivity of pristine rcGO (σ=0.22 S/cm) and pure PANI (σ=0.89 S/cm) samples. This is owing to the strong π-π stacking between the PANI nanostructures and rcGO layers [12,21]. Also, it is observed that PRGO2 has revealed the highest conductivity among all the three PANI/rcGO samples due to the better morphology of the PRGO2 samples compared to PRGO1 and PRGO4 samples as evident from the FESEM images shown in Fig. 3.2(d-f).

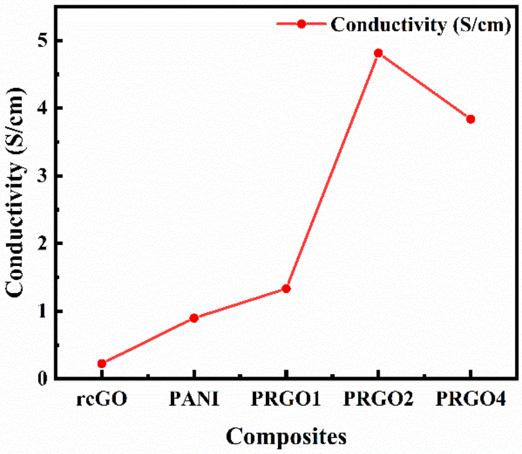

Figure 3.8 *Electrical conductivity of rcGO, PANI, PRGO1, PRGO2, and PRGO4, respectively.*

TGA of cGO, rcGO, PANI, and PRGO composites samples were evaluated in Argon atmosphere between 30 - 800 °C temperature range at a heating rate ~ 10 °C/min as shown in Fig. 3.9. All the samples have shown weight loss below 130 °C, which is mainly due to the loss of adsorbed water molecules. The major weight loss of about 80 % of cGO was observed at 200 °C, which is linked to the thermal disintegration of oxygen-containing functional groups [40]. Subsequently, after hydrothermal reduction, the mass loss was only 20 % after 200 °C, which is the mark for the removal of most of the oxygen-containing functional groups from the cGO during hydrothermal reduction. Meanwhile, PRGO composites show similar thermal behaviour as that of PANI, which confirms the formation of PANI nanostructures at the surface of rcGO layers. All PRGO nanocomposites and PANI has shown weight loss from 150 °C to 450 °C linked to the removal of dopant in the form of HCl gas and removal of lower weight fragments of the polymer chain [41]. Major weight loss after 450 °C is due to the complete breakdown of the polymer backbone. From the TGA graphs, it is observed that weight loss after 450 °C is decreased by increasing the wt.% of cGO which clearly shows that the presence of rcGO in the PANI matrix leads to an increase in thermal stability which in turn prevents the decomposition of the polymer.

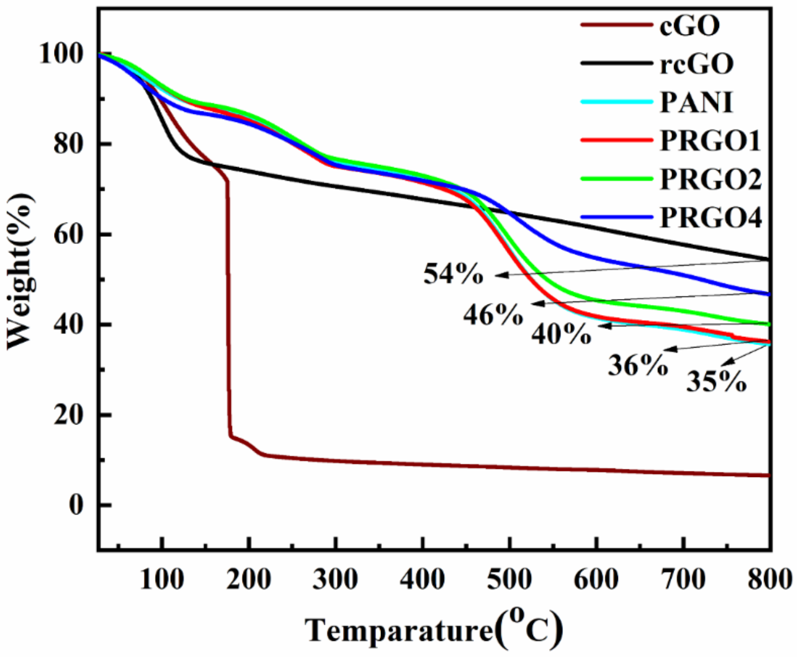

Figure 3.9 *TGA graphs of cGO, rcGO, PANI, PRGO1, PRGO2, and PRGO4 nanocomposites.*

The electrochemical performance of heat-assisted PRGO nanocomposites was investigated by CV, GCD, and EIS measurements by fabricating a two-electrode system (symmetrical cell). Typically, two or three-electrode configurations were used for electrode characterization where the two-electrode system gives more real and accurate results to conclude the performance of material as a supercapacitor [42,43]. In Fig. 3.10a. the CV curves of PANI, rcGO and PRGO composites in 1 M H_2SO_4 solution have shown at a scan rate of 5 mV/s. The CV curve of rcGO is almost rectangular, which is a typical EDLC characteristic behaviour of carbon materials. In the case of PANI, PRGO1, PRGO2, and PRGO4 composites two pairs of redox peaks were observed with rectangular shape credited for the conversion of Leucoemeraldine base to Emeraldine salt and Emeraldine salt to Pernigraniline base forms of PANI by redox reaction [44,45]. However, the oxidation and reduction cycles are not symmetric and rectangular in shape suggesting these composites possess combined features of both EDLC and pseudocapacitance. Moreover, the specific capacitance of electrode material can be evaluated from the area covered by the CV curve. The specific capacitance of electrode material can be evaluated from the cyclic voltammogram curves, using equation 2.2 [46]. The specific capacitance values of rcGO, PANI, PRGO1, PRGO2, and PRGO4 are 126, 205, 234, 287, and 257 F/g, respectively. PRGO2 shows superior capacitance behavior compare to other composites and pure PANI. The electrochemical behaviour of rcGO, PANI, and PRGO composite was further evaluated at higher scan rates as shown in Fig. 3.10 (b-f). The shape of the CV curve of rcGO has slightly deviated from the rectangular shape with increasing scan rate which is due to the presence of oxygen functionalities in rcGO (Fig. 3.10b). Whereas, we found a clear deviation in the CV curves of PANI (Fig. 3.10c), suggesting structural instability and poor rate capability of the PANI sample. The rate capability of PANI is increased with the incorporation of cGO, while the shape of CV in PRGO2 (Fig. 3.10e) composite remains the same even at a scan rate of 100 mV/s showing a higher rate capability of the composite material. Additionally, the total peak current density increases, demonstrating the exceptional capacitance behaviour and good rate property of the PRGO2 composite. The incorporation of rcGO into the PANI chain enhances the electrochemical properties as well as chemical stability. The augmentation in the area may happen due to more availability to the active sites and better-conducting channels owing to the formation of hydrogen bonding in PRGO2 [47]. The PRGO composites have shown better electrochemical properties due to properly oriented nanostructures and synergistic effects of well laminated densely packed PANI nanocluster with fluffy structure. This leads to a notable increase in electrical conductivity (Fig. 3.8) as well as high interfacial electrode/electrolyte interaction attributing to high rates of electrode reaction, subsequently resulting in a superior electrochemical activity. Secondly, the solid-state charge transfer reaction between the PANI chains and graphene also advances the faradaic movement and contributes to an increase in total capacitance.

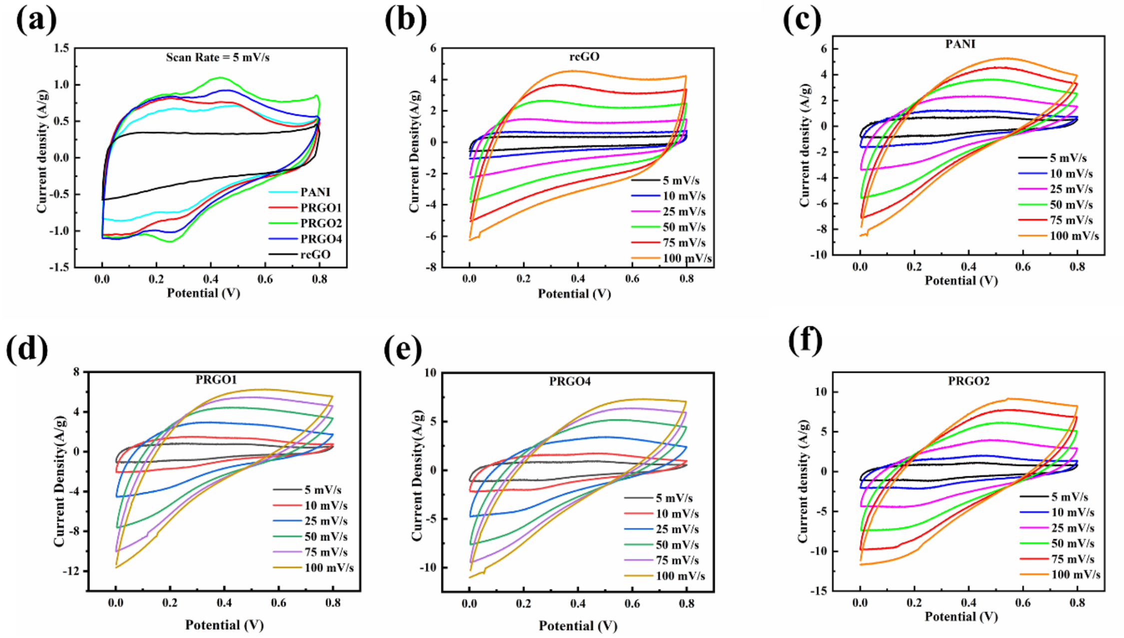

Figure 3.10 *(a) CV curves of PANI, PRGO1, PRGO2, PRGO4, and rcGO at 5 mV/s, CV curves at different scan rates at various scan rates in 1 M* H_2SO_4 *(b) rcGO, (c) PANI, (d) PRGO1, (e) PRGO2 and (f) PRGO4.*

EIS is a very powerful technique to probe the resistance behaviour of the materials. Figure 3.11a shows the Nyquist plots of all sample materials while the inset shows the zoomed area of the EIS spectrum in the high-frequency region. From the inset of Fig. 3.11a, it is undoubtedly visible that Nyquist plots are comprised of a semi-circle in the high-frequency range and a straight line in the low-frequency region [48]. Therefore, EIS is a sum of electrode resistance and electrolyte resistance, where a semi-circle offers the equivalent series resistance (R_S), which is the intercept point of the impedance spectrum on the real axis and charge transfer resistance (R_{ct}) at the interface between electrode and electrolyte, the diameter of the semi-circle at the high-frequency region. While in the low-frequency region, straight line corresponds to the capacitance behaviour of the material [14,21]. From the EIS curves, the R_s and R_{ct} values are derived for all the materials and shown in Table 3.2.

Table 3.2 Equivalent series resistance and charge transfer resistance of rcGO, PANI, PRGO1, PRGO2 & PRGO4 composites:

	rcGO	PANI	PRGO1	PRGO2	PRGO4
R_s (Ω)	1.28	1.41	1.38	1.02	1.25
R_{ct} (Ω)	3.08	4.32	3.57	1.97	2.16

R_{ct} is a vital parameter to estimate the electrochemical behaviour of the tested electrodes. PRGO2 composite possesses a smaller diameter semicircle than that of other electrode material, indicating favourable conducting pathways for the electrolyte ions. Therefore, PRGO2 composite has high charge transfer capabilities and enhanced conductivity compared to pure PANI. These results are also well supported by conductivity measurements (Fig. 3.8). Further, we have studied the resistance variation of PRGO2 composite to charge-discharge cycles. Figure 3.11b, shows the impedance spectra of PRGO2 composite before cycling and after running 2000 cycles. The variation in the R_{ct} of PRGO2 composite was very less even after 2000 cycles, which proves the high conductivity and high cyclic stability of the composite material.

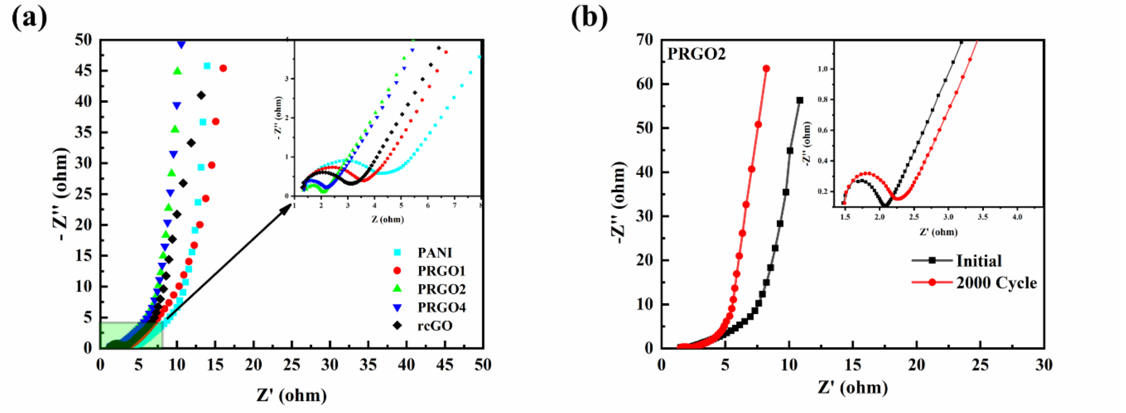

Figure 3.11 *(a) Nyquist plots of PANI, PRGO1, PRGO2, PRGO4, and rcGO whereas the inset shows the zoomed view of impedance in the high-frequency region, and (b) Nyquist plots of PRGO2 composite at the* 0^{th} *cycle and after 2000 cycles.*

To confirm the superior behaviour of the PRGO composite, the rate performance has been examined by charge-discharge plots at various current densities (Fig. 3.12). The GCD curve of rcGO, PANI, and PRGO composite electrodes at a discharge current density of 0.5 A/g is shown in Fig. 3.12a. The GCD curve of rcGO is triangular which suggests the ideal EDLC capacitive behaviour of carbon material. The GCD plots of PANI and PRGO composites show a nearly symmetrical charge-discharge curve with deviation from linearity. The deviation from the linearity in the GCD curve indicates the characteristic pseudocapacitive nature of the material [49]. PRGO composites (Fig. 3.12a) possess a longer discharging time compared to PANI (Fig. 3.12a), owing to the combined features of both EDLC and pseudocapacitance. The GCD data has been utilized to evaluate the specific capacitance (C_{sp}) of the samples using the following equation 2.3 [46,50]. The specific capacitance values of rcGO, PANI, PRGO1, PRGO2, and PRGO4 are 121, 248, 257, 299, and 287 F/g, which are consistent with the CV results. Here, the specific capacitance has increased in the case of the 2 wt.% cGO sample compared to 1 wt.% cGO sample, however, it decreases further when the cGO weight percentage has been increased to 4 wt.%. This is because higher wt.% of cGO may cover the electroactive sites of PANI nanostructures, which suppresses complete utilization of PANI resulting in a decrease of specific capacitance of PRGO4 composite [9]. The superior properties of PRGO2 composite based on the factor that the formation of PANI on the surface of cGO sheets, which inhibits the stocking of graphene layers during the hydrothermal reaction. Thus, it increases the utilization of electrode active area, enhances the conductive properties of the composite, and decreases the ion diffusion paths for the electrolyte. Figure 3.12b-e displays the GCD curves of PANI, PRGO1, PRGO2, and PRGO4 composites at various current densities. For PANI, the voltage drop is increased with increasing current density showing the poor rate capability of PANI which is due to the structural instability of polymer chain. Further, we observed that the voltage drop is decreased with the incorporation of rcGO in PRGO2 composite (Fig. 3.12d) proving the improved charge transfer kinetics and good electrical conductivity of the material.

Furthermore, to know the rate capability, the current density vs specific capacitance of PANI, PRGO1, PRGO2, and PRGO4 samples are plotted at different current densities as shown in Fig. 3.12f. From Fig. 3.12f, it is seen that PRGO2 composites shows superior rate capability compared to PANI, and retained a specific capacitance of 225 F/g even at high current density (5 A/g), which could be attributed to the presence of rcGO in the composite. For comparison with the work reported elsewhere, the specific capacitances of the similar composites under different electrolyte solutions are given in Table 3.3 [29,31,62-67]. This shows that the electrode has outstanding rate capability due to laminated floppy structure where the PANI chains have outstanding interfacial contact with the graphene layer which in turn leads to a high charge transfer mechanism within the PRGO composite. These results were attributed to the high conductivity and superior electrochemical performance of the composite and contributing high-performance electrode for next-generation wearable/ flexible power sources.

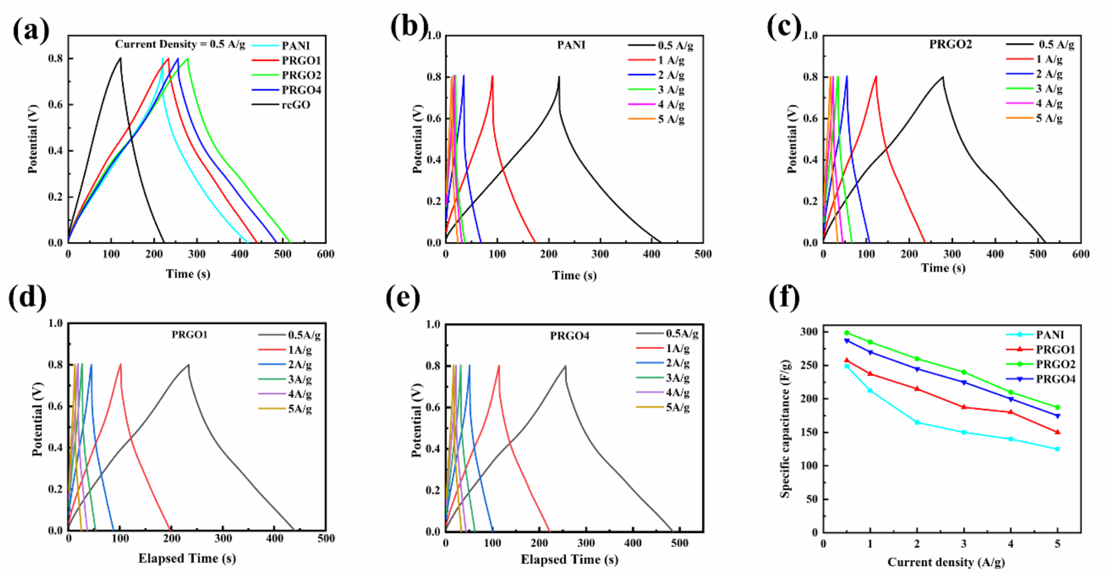

Figure 3.12 *(a) The GCD curves of PANI, PRGO1, PRGO2, PRGO4, and rcGO at 0.5 A/g, GCD curves at different current densities for (b) PANI c) PRGO1, (d) PRGO2, (e) PRGO4, and (f) Current density vs specific capacitance of PANI, PRGO1, PRGO2, and PRGO4.*

Further, the performance of composite materials is evaluated in terms of energy density and power density. The energy density (E_m, Wh/kg) and power density (P_m, W/kg) of the SC device is calculated from the specific capacitance values obtained from the GCD curves using the following equation 2.4 & 2.5, respectively [50]. The Ragone plots of all the composites are depicted in Fig. 3.13a. PRGO2 composite can deliver a high energy density of 24.45 Wh k/g at 0.5 A/g and the corresponding power density is 368 W/kg these values are higher than that of pristine PANI and rcGO indicates the superior charge storage behaviour of the composite material.

Table 3.3 Comparison of the specific capacitance of similar electrode materials.

Material	Electrolyte	Specific capacitance	Ref.
Porous PANI/rGO	1 M H_2SO_4 in 3 ele.	420 F/g at 0.2 A/g	[20]
rGO/PANI	1 M H_2SO_4in 2 ele.	438 F/g at 0.5A/g	[22]
Porous graphene-PANI NFs	1 M H_2SO_4 in 3 ele.	357 F/g at 0.1A/g	[51]
Graphene/PANI	1 M H_2SO_4 in 3 ele.	257 F/g at 0.1 A/g	[52]
PANI grafted rGO	1 M H_2SO_4 in 3 ele.	250 F/g at 10 mV/s	[53]
PANI-GNRs	1 M H_2SO_4 in 2 ele.	340 F/g at 0.25A/g	[54]
rGO/PANI	1 M H_2SO_4in 3 ele.	72 F/g at 2 mV/s	[55]
PANI/RGO	1 M H_2SO_4in 3 ele.	431 F/g at 0.1 A/g	[56]
Heat assisted PANI/rcGO	1 M H_2SO_4 in 2 ele.	299 F/g at 0.5A/g	Present work

For realizing the commercial application, cycling performance in a supercapacitor is a very important factor. As shown in Fig. 3.13b, the cycling stability studies were done at 2 A/g current density where pristine PANI has shown only 70% of capacitance retention, this low cyclic stability is due to the chemical redox reaction (doping/de-doping) in the polymer matrix during charging and discharging process. The repeated charge-discharge leads to the volumetric expansion due to swelling and shrinking in the skeleton of the polymer chain [57]. Whereas PRGO2 possesses high cycling stability compared to pure PANI. PRGO2 electrode retains 88% of capacitance after 2000 cycles. The increase in cycling stability of PRGO2 composite has probably come from the synergistic effect between rcGO nanosheets and PANI chains which ultimately leads to a decrease in volumetric changes and increases the mechanical strength and conductivity of the composite.

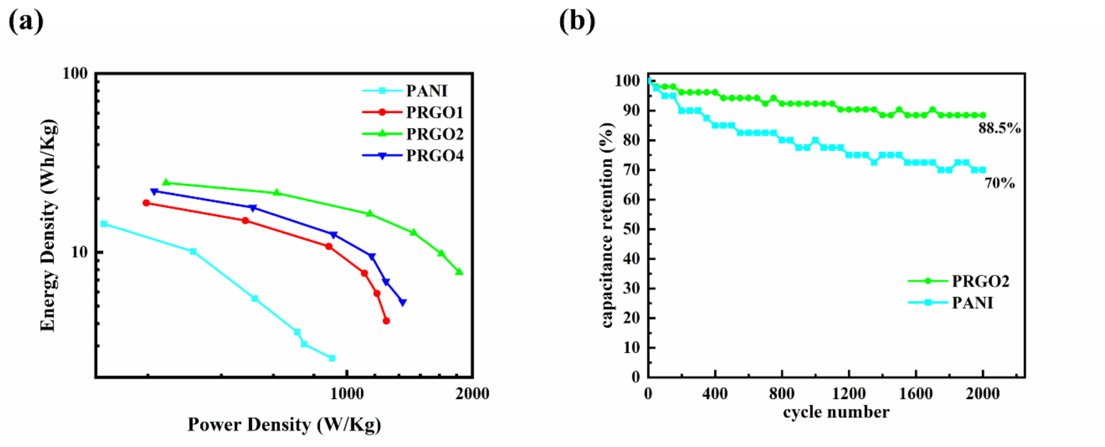

Figure 3.13 *(a) The Ragone plots of PANI, PRGO1, PRGO2, and PRGO4 nanocomposite, and (b) Cycling stability plot of PANI and PRGO2 composite.*

3.3 Conclusions

We have successfully designed heat-assisted polyaniline reduced crumbled graphene oxide (PANI/rcGO) composite as potential electrode material for flexible supercapacitors which can be used directly without any substrate. The heat-assisted reduction of graphene oxide in composite leads to lamination of graphene layers with densely packed PANI nanocluster which in turn provides good mechanical support as well as charge transfer for synergistic effects between graphene & PANI to extend the significant contribution in specific capacitance. The synergistic effect of PANI and rcGO assisted by heating leads to a 3D floppy network and contributes to high flexibility, good mechanical strength, and long cycle life with high energy density electrodes. PRGO2 composite with 2 wt.% of cGO was shown maximum specific capacitance of 299 F/g at current density of 0.5 A/g. Besides, these PRGO composite has shown high-rate capability and capacitance retention (88%) at current density of 2 A/g after 2000 charge/discharge cycles, which proves that the PRGO composite synthesized by low-temperature heat-assisted reduction of cGO is a potential candidate as electrode material in flexible supercapacitor to power wearable/ flexible electronic devices.

References

[1] T.H. Le, Y. Kim, H. Yoon, Electrical and electrochemical properties of conducting polymers, Polymers (Basel). 9 (2017). https://doi.org/10.3390/polym9040150.

[2] H.W. Park, T. Kim, J. Huh, M. Kang, J.E. Lee, H. Yoon, Anisotropic growth control of polyaniline nanostructures and their morphology-dependent electrochemical characteristics, ACS Nano. 6 (2012) 7624–7633. https://doi.org/10.1021/nn3033425.

[3] G. Wang, L. Zhang, J. Zhang, A review of electrode materials for electrochemical supercapacitors, Chem. Soc. Rev. 41 (2012) 797–828. https://doi.org/10.1039/c1cs15060j.

[4] Y. Wang, S. Tang, S. Vongehr, J. Ali Syed, X. Wang, X. Meng, High-Performance Flexible Solid-State Carbon Cloth Supercapacitors Based on Highly Processible N-Graphene Doped Polyacrylic Acid/Polyaniline Composites, Sci. Rep. 6 (2016) 1–10. https://doi.org/10.1038/srep12883.

[5] S. Bhadra, D. Khastgir, N.K. Singha, J.H. Lee, Progress in preparation, processing and applications of polyaniline, Prog. Polym. Sci. 34 (2009) 783–810. https://doi.org/10.1016/j.progpolymsci.2009.04.003.

[6] H. Wang, J. Lin, Z.X. Shen, Polyaniline (PANi) based electrode materials for energy storage and conversion, J. Sci. Adv. Mater. Devices. 1 (2016) 225–255.

https://doi.org/10.1016/j.jsamd.2016.08.001.

[7] L. Lizarraga, E.M. Andrade, F.V. Molina, Swelling and volume changes of polyaniline upon redox switching, J. Electroanal. Chem. 561 (2004) 127–135. https://doi.org/10.1016/j.jelechem.2003.07.026.

[8] M.M. Mezgebe, Z. Yan, G. Wei, S. Gong, F. Zhang, S. Guang, H. Xu, 3D graphene-Fe3O4-polyaniline, a novel ternary composite for supercapacitor electrodes with improved electrochemical properties, Mater. Today Energy. 5 (2017) 164–172. https://doi.org/10.1016/j.mtener.2017.06.007.

[9] P. Liu, J. Yan, Z. Guang, Y. Huang, X. Li, W. Huang, Recent advancements of polyaniline-based nanocomposites for supercapacitors, J. Power Sources. 424 (2019) 108–130. https://doi.org/10.1016/j.jpowsour.2019.03.094.

[10] H. Kwon, D. Hong, I. Ryu, S. Yim, Supercapacitive Properties of 3D-Arrayed Polyaniline Hollow Nanospheres Encaging RuO2 Nanoparticles, ACS Appl. Mater. Interfaces. 9 (2017) 7412–7423. https://doi.org/10.1021/acsami.6b14331.

[11] D. Yang, W. Ni, J. Cheng, Z. Wang, C. Li, Y. Zhang, B. Wang, Omnidirectional porous fiber scrolls of polyaniline nanopillars array-N-doped carbon nanofibers for fiber-shaped supercapacitors, Mater. Today Energy. 5 (2017) 196–204. https://doi.org/10.1016/j.mtener.2017.06.011.

[12] K. Zhang, L.L. Zhang, X.S. Zhao, J. Wu, Graphene/polyaniline nanofiber composites as supercapacitor electrodes, Chem. Mater. 22 (2010) 1392–1401. https://doi.org/10.1021/cm902876u.

[13] J. Li, J. Ren, Y. Xu, H. Ji, X. Zou, Facile synthesis and characterization of three-dimensional graphene/polyaniline composites with enhanced electrochemical properties, J. Mater. Sci. Mater. Electron. 30 (2019) 6650–6659. https://doi.org/10.1007/s10854-019-00974-1.

[14] Y. Li, M. Zhou, Z. Xia, Q. Gong, X. Liu, Y. Yang, Q. Gao, Facile preparation of polyaniline covalently grafted to isocyanate functionalized reduced graphene oxide nanocomposite for high performance flexible supercapacitors, Colloids Surfaces A Physicochem. Eng. Asp. 602 (2020) 125172. https://doi.org/10.1016/j.colsurfa.2020.125172.

[15] U. Male, P. Srinivasan, B.S. Singu, Incorporation of polyaniline nanofibres on graphene oxide by interfacial polymerization pathway for supercapacitor, Int. Nano Lett. 5 (2015) 231–240. https://doi.org/10.1007/s40089-015-0160-9.

[16] E. Mitchell, J. Candler, F. De Souza, R.K. Gupta, B.K. Gupta, L.F. Dong, High performance supercapacitor based on multilayer of polyaniline and graphene oxide, Synth. Met. 199 (2015) 214–218. https://doi.org/10.1016/j.synthmet.2014.11.028.

[17] D. Gui, C. Liu, F. Chen, J. Liu, Preparation of polyaniline/graphene oxide nanocomposite for the application of supercapacitor, Appl. Surf. Sci. 307 (2014) 172–177. https://doi.org/10.1016/j.apsusc.2014.04.007.

[18] Z. Luo, L. Zhu, H. Zhang, H. Tang, Polyaniline uniformly coated on graphene oxide sheets as supercapacitor material with improved capacitive properties, Mater. Chem. Phys. 139 (2013) 572–579. https://doi.org/10.1016/j.matchemphys.2013.01.059.

[19] Q. Zhou, T. Wei, J. Yue, L. Sheng, Z. Fan, Polyaniline nanofibers confined into

graphene oxide architecture for high-performance supercapacitors, Electrochim. Acta. 291 (2018) 234–241. https://doi.org/10.1016/j.electacta.2018.08.104.

[20] A. Moyseowicz, G. Gryglewicz, Hydrothermal-assisted synthesis of a porous polyaniline/reduced graphene oxide composite as a high-performance electrode material for supercapacitors, Compos. Part B Eng. 159 (2019) 4–12. https://doi.org/10.1016/j.compositesb.2018.09.069.

[21] L. Tang, Z. Yang, F. Duan, M. Chen, Fabrication of graphene sheets/polyaniline nanofibers composite for enhanced supercapacitor properties, Colloids Surfaces A Physicochem. Eng. Asp. 520 (2017) 184–192. https://doi.org/10.1016/j.colsurfa.2017.01.083.

[22] X. Hong, B. Zhang, E. Murphy, J. Zou, F. Kim, Three-dimensional reduced graphene oxide/polyaniline nanocomposite film prepared by diffusion driven layer-by-layer assembly for high-performance supercapacitors, J. Power Sources. 343 (2017) 60–66. https://doi.org/10.1016/j.jpowsour.2017.01.034.

[23] F. Yang, M. Xu, S.J. Bao, H. Wei, H. Chai, Self-assembled hierarchical graphene/polyaniline hybrid aerogels for electrochemical capacitive energy storage, Electrochim. Acta. 137 (2014) 381–387. https://doi.org/10.1016/j.electacta.2014.06.017.

[24] W. Tang, L. Peng, C. Yuan, J. Wang, S. Mo, C. Zhao, Y. Yu, Y. Min, A.J. Epstein, Facile synthesis of 3D reduced graphene oxide and its polyaniline composite for super capacitor application, Synth. Met. 202 (2015) 140–146. https://doi.org/10.1016/j.synthmet.2015.01.031.

[25] K. Singh, A. Ohlan, V.H. Pham, R.B. Balasubramaniyan, S. Varshney, J. Jang, S.H. Hur, W.M. Choi, M. Kumar, S.K. Dhawan, B.S. Kong, J.S. Chung, Nanostructured graphene/Fe3O4 incorporated polyaniline as a high performance shield against electromagnetic pollution, Nanoscale. 5 (2013) 2411–2420. https://doi.org/10.1039/c3nr33962a.

[26] Z. Bo, X. Shuai, S. Mao, H. Yang, J. Qian, J. Chen, J. Yan, K. Cen, Green preparation of reduced graphene oxide for sensing and energy storage applications, Sci. Rep. 4 (2014) 1–8. https://doi.org/10.1038/srep04684.

[27] J.P. Pouget, M.E. Józefowicz, A.J. Epstein, X. Tang, A.G. MacDiarmid, X-ray Structure of Polyaniline, Macromolecules. 24 (1991) 779–789. https://doi.org/10.1021/ma00003a022.

[28] M. Mitra, C. Kulsi, K. Chatterjee, K. Kargupta, S. Ganguly, D. Banerjee, S. Goswami, Reduced graphene oxide-polyaniline composites - Synthesis, characterization and optimization for thermoelectric applications, RSC Adv. 5 (2015) 31039–31048. https://doi.org/10.1039/c5ra01794g.

[29] F. Pendolino, N. Armata, Graphene Oxide in Environmental Remediation Process, SpringerBriefs in Applied Sciences and Technology, 2017. https://doi.org/10.1007/978-3-319-60429-9.

[30] P. Liu, Y. Huang, L. Wang, A facile synthesis of reduced graphene oxide with Zn powder under acidic condition, Mater. Lett. 91 (2013) 125–128. https://doi.org/10.1016/j.matlet.2012.09.085.

[31] S. Goswami, U.N. Maiti, S. Maiti, S. Nandy, M.K. Mitra, K.K. Chattopadhyay, Preparation of graphene-polyaniline composites by simple chemical procedure and its improved field emission properties, Carbon N. Y. 49 (2011) 2245–2252.

https://doi.org/10.1016/j.carbon.2011.01.055.

[32] S. Xiong, Y. Wang, J. Chu, X. Wang, R. Zhang, M. Gong, B. Wu, Z. Li, One-pot hydrothermal synthesis of polyaniline nanofibers/reduced graphene oxide nanocomposites and their supercapacitive properties, High Perform. Polym. 31 (2019) 1238–1247. https://doi.org/10.1177/0954008319845435.

[33] K.N. Kudin, B. Ozbas, H.C. Schniepp, R.K. Prud'homme, I.A. Aksay, R. Car, Raman spectra of graphite oxide and functionalized graphene sheets, Nano Lett. 8 (2008) 36–41. https://doi.org/10.1021/nl071822y.

[34] Z.S. Wu, W. Ren, L. Xu, F. Li, H.M. Cheng, Doped graphene sheets as anode materials with superhigh rate and large capacity for lithium ion batteries, ACS Nano. 5 (2011) 5463–5471. https://doi.org/10.1021/nn2006249.

[35] Z. Tian, J. Li, G. Zhu, J. Lu, Y. Wang, Z. Shi, C. Xu, Facile synthesis of highly conductive sulfur-doped reduced graphene oxide sheets, Phys. Chem. Chem. Phys. 18 (2015) 1125–1130. https://doi.org/10.1039/c5cp05475c.

[36] Y. Wang, C. Wang, Y. Wang, H. Liu, Z. Huang, Boric Acid Assisted Reduction of Graphene Oxide: A Promising Material for Sodium-Ion Batteries, ACS Appl. Mater. Interfaces. 8 (2016) 18860–18866. https://doi.org/10.1021/acsami.6b04774.

[37] Y. Zou, Z. Zhang, W. Zhong, W. Yang, Hydrothermal direct synthesis of polyaniline, graphene/polyaniline and N-doped graphene/polyaniline hydrogels for high performance flexible supercapacitors, J. Mater. Chem. A. 6 (2018) 9245–9256. https://doi.org/10.1039/c8ta01366g.

[38] H.R. Tantawy, B.A.F. Kengne, D.N. McIlroy, T. Nguyen, D. Heo, Y. Qiang, D.E. Aston, X-ray photoelectron spectroscopy analysis for the chemical impact of solvent addition rate on electromagnetic shielding effectiveness of HCl-doped polyaniline nanopowders, J. Appl. Phys. 118 (2015) 175501. https://doi.org/10.1063/1.4934851.

[39] Y.M. Lee, J.H. Kim, J.S. Kang, S.Y. Ha, Annealing effects of dilute polyaniline/NMP solution, Macromolecules. 33 (2000) 7431–7439. https://doi.org/10.1021/ma992004y.

[40] M.J. McAllister, J.L. Li, D.H. Adamson, H.C. Schniepp, A.A. Abdala, J. Liu, M. Herrera-Alonso, D.L. Milius, R. Car, R.K. Prud'homme, I.A. Aksay, Single sheet functionalized graphene by oxidation and thermal expansion of graphite, Chem. Mater. 19 (2007) 4396–4404. https://doi.org/10.1021/cm0630800.

[41] P. Saini, V. Choudhary, B.P. Singh, R.B. Mathur, S.K. Dhawan, Polyaniline-MWCNT nanocomposites for microwave absorption and EMI shielding, Mater. Chem. Phys. 113 (2009) 919–926. https://doi.org/10.1016/j.matchemphys.2008.08.065.

[42] T.C. Girija, M. V. Sangaranarayanan, Polyaniline-based nickel electrodes for electrochemical supercapacitors-Influence of Triton X-100, J. Power Sources. 159 (2006) 1519–1526. https://doi.org/10.1016/j.jpowsour.2005.11.078.

[43] M.D. Stoller, S. Park, Y. Zhu, J. An, R.S. Ruoff, Graphene-Based Ultracapacitors, Nano Lett. 8, (2008) 3498–3502. https://doi.org/10.1021/nl802558y.

[44] A. Gupta, S. Sardana, J. Dalal, S. Lather, A.S. Maan, R. Tripathi, R. Punia, K. Singh, A. Ohlan, Nanostructured Polyaniline/Graphene/Fe2O3Composites

Hydrogel as a High-Performance Flexible Supercapacitor Electrode Material, ACS Appl. Energy Mater. 3 (2020) 6434–6446. https://doi.org/10.1021/acsaem.0c00684.

[45] L. Wang, X. Li, G. Wang, Construction of an electrochemical stable conductive network to improve the pseudocapacitance of polyaniline, Electrochim. Acta. 331 (2020) 135279. https://doi.org/10.1016/j.electacta.2019.135279.

[46] Q. Hao, X. Xia, W. Lei, W. Wang, J. Qiu, Facile synthesis of sandwich-like polyaniline/boron-doped graphene nano hybrid for supercapacitors, Carbon N. Y. 81 (2015) 552–563. https://doi.org/10.1016/j.carbon.2014.09.090.

[47] X. Liu, P. Shang, Y. Zhang, X. Wang, Z. Fan, B. Wang, Y. Zheng, Three-dimensional and stable polyaniline-grafted graphene hybrid materials for supercapacitor electrodes, J. Mater. Chem. A. 2 (2014) 15273–15278. https://doi.org/10.1039/c4ta03077j.

[48] M.K. Singh, M. Suleman, Y. Kumar, S.A. Hashmi, A novel configuration of electrical double layer capacitor with plastic crystal based gel polymer electrolyte and graphene nano-platelets as electrodes: A high rate performance, Energy. 80 (2015) 465–473. https://doi.org/10.1016/j.energy.2014.11.087.

[49] K. Jin, W. Zhang, Y. Wang, X. Guo, Z. Chen, L. Li, Y. Zhang, Z. Wang, J. Chen, L. Sun, T. Zhang, In–situ hybridization of polyaniline nanofibers on functionalized reduced graphene oxide films for high-performance supercapacitor, Electrochim. Acta. 285 (2018) 221–229. https://doi.org/10.1016/j.electacta.2018.07.220.

[50] F. Liu, S. Luo, D. Liu, W. Chen, Y. Huang, L. Dong, L. Wang, Facile processing of free-standing polyaniline/SWCNT film as an integrated electrode for flexible supercapacitor application, ACS Appl. Mater. Interfaces. 9 (2017) 33791–33801. https://doi.org/10.1021/acsami.7b08382.

[51] M.K. Chini, S. Chatterjee, FlatChem Hydrothermally reduced nano porous graphene – polyaniline nanofiber composites for supercapacitor, FlatChem. 1 (2016) 1–5. https://doi.org/10.1016/j.flatc.2016.08.001.

[52] Z.F. Li, H. Zhang, Q. Liu, L. Sun, L. Stanciu, J. Xie, Fabrication of high-surface-area graphene/polyaniline nanocomposites and their application in supercapacitors, ACS Appl. Mater. Interfaces. 5 (2013) 2685–2691. https://doi.org/10.1021/am4001634.

[53] N.A. Kumar, H.J. Choi, Y.R. Shin, D.W. Chang, L. Dai, J.B. Baek, Polyaniline-grafted reduced graphene oxide for efficient electrochemical supercapacitors, ACS Nano. 6 (2012) 1715–1723. https://doi.org/10.1021/nn204688c.

[54] L. Li, A.R.O. Raji, H. Fei, Y. Yang, E.L.G. Samuel, J.M. Tour, Nanocomposite of polyaniline nanorods grown on graphene nanoribbons for highly capacitive pseudocapacitors, ACS Appl. Mater. Interfaces. 5 (2013) 6622–6627. https://doi.org/10.1021/am4013165.

[55] Shruthi, K.M. Vighnesha, Sandhya, D.N. Sangeetha, M. Selvakumar, Synthesis and Characterization of Reduced Graphene Oxide- Polyaniline Composite for Supercapacitor Applications, Surf. Eng. Appl. Electrochem. 54 (2018) 359–366. https://doi.org/10.3103/S106837551804018X.

[56] M. Kim, C. Lee, J. Jang, Fabrication of highly flexible, scalable, and high-performance supercapacitors using polyaniline/reduced graphene oxide film with enhanced electrical conductivity and crystallinity, Adv. Funct. Mater. 24 (2014)

2489–2499. https://doi.org/10.1002/adfm.201303282.

[57] L. Wang, Y. Ye, X. Lu, Z. Wen, Z. Li, H. Hou, Y. Song, Hierarchical nanocomposites of polyaniline nanowire arrays on reduced graphene oxide sheets for supercapacitors, Sci. Rep. 3 (2013) 1–9. https://doi.org/10.1038/srep03568.

CHAPTER 4

POLYANILINE/N-rGO COMPOSITE ELECTRODE MATERIAL FOR EFFICIENT FLEXIBLE SUPERCAPACITORS

4.1 Introduction

Among the different types of carbon electrode materials used in SCs, the prominent features of graphene (GN) such as high electrical conductivity, greater flexibility, high thermal and chemical stability, and other structural and optical properties, make it a superior material for the flexible supercapacitor application [1]. GN can deliver a high specific capacitance of 550 F/g with a high theoretical surface area of ~2600 m^2/g [2]. A cost-effective synthesis method for the large-scale production of GN with controlled surface chemistry is extremely important for its usage in practical applications. The reduction of graphene oxide (GO) with a suitable chemical reagent is a viable process for the bulk synthesis of reduced graphene oxide (rGO) compared to other synthesis methods [3]. Nevertheless, rGO exhibits relatively low specific capacitance as rGO produced via the reduction process contains the agglomeration of graphene sheets and residual oxygen functional groups. The presence of oxygen functional groups leads to poor electrical conductivity, and the agglomeration of graphene layers severely diminishes the active surface area accessible for the electrolyte ions leading to unsatisfactory practical performance. Much research attention has been given to boosting the electrochemical properties of rGO by adopting different techniques such as enhancing the specific surface area, doping with the hetero atom, increasing the electrical conductivity, controlled morphology, etc. [1,2,4]. Among them, doping with a heteroatom is proved to be an effective approach to varying the physical and chemical properties of rGO [2,4]. In particular, nitrogen (N) is a suitable dopant for graphene because of its comparable atomic size and provides an additional p-electron to the π-system of graphene making it n-type [4–6]. Previous reports have also demonstrated that N-doping is a beneficial route to decorating graphene for the reason that doping can increase the charge carrier concentration thus providing high electrical conductivity [6]. Moreover, the presence of a high electronegative N atom can improve surface wettability, which is beneficial for efficient charge transportation at the electrode/electrolyte interface [7]. Doping of the N atom can exist mainly in three different forms, namely pyridinic-N, pyrrolic-N, and quaternary-N [8,9]. Pyridinic-N and pyrrolic-N increase the surface wettability of electrodes and participate in charge transfer reaction with electrolyte ions, hence, generate additional pseudocapacitance, whereas the quaternary N atom is a substitution to the carbon atom in benzene ring which enriches the local electron density, consequently exhibit high electrical conductivity [9].

Chemical doping of N atoms into the graphene framework can be achieved via several synthesis routes such as chemical vapour deposition, plasma treatment, thermal annealing, hydrothermal synthesis, and so on [8]. Among them, the hydrothermal method is considered to be a simple, cost-effective, and promising method for N doping at relatively lower temperatures (< 200 ^{o}C) by mixing GO with N-containing precursors such as ammonia [10], hexamethylenetetramine [11], hydrazine hydrate [12], amino acids [13], urea [14], amitrole [7]. Moreover, recent studies have also demonstrated that N-rGO synthesized by the hydrothermal method can exhibit excellent surface activity and high chemical stability compared to rGO when it is used for supercapacitor application [14]. With the above-mentioned prominent features, N-rGO is considered to be a better choice than rGO to utilize as a substrate to load a pseudocapacitive material to further enlarge its electrochemical properties. On the other hand, polyaniline (PANI) from the conducting polymer family, is considered to be a potential pseudocapacitive material to merge with carbon material owing to its better environmental stability, flexibility, and greater theoretical capacitance [15–17]. For example, Gopalakrishnan *et al.* synthesized N-rGO/PANI composite with 1:6 ratio using *in-situ* polymerization, and it has delivered a specific capacitance of 715 F/g at a current density of 0.5 A/g in the three-electrode system where the N-rGO is prepared by thermal annealing at 900 ^{o}C under N_2 atmosphere [18]. Zhisen Liu *et al.* studied N-3D-rGO/PANI nanowire composites and achieved a specific capacitance of 282 F/g at a current density of 1 A/g in a three-electrode system, where N-rGO has been synthesized using high-temperature thermal treatment [19]. Zhimin Fan *et al.* prepared a free-standing N-doped holey graphene/PANI composite which delivered a volumetric capacitance of 1053 F/cm^3 at a current density of 0.5 A/g in the three-electrode system [20]. Zhu *et al.* synthesized 3D N-rGO/PANI foam using a hydrothermal method and obtained a specific capacitance of 528 F/g at a current density of 0.1 A/g in a three-electrode system [21]. More recently, Liu *et al.* developed a holey N-rGO/PANI composite with a high specific capacitance of 510 F/g at a current density of 1 A/g [22]. However, in most of the above-mentioned cases, electrochemical studies are obtained using the three-electrode system, and the N doping into graphene lattice is reportedly done by high-temperature heat treatment which needs an expensive instrument facility. It is worth noting that for practical applications, studies on the two-electrode system are more reliable compared to the three-electrode system. Moreover, according to our knowledge, only very few studies are explored the supercapacitor performance based on the flexible electrodes using N-rGO/PANI composites.

In this context, here, we report a simple and robust approach for a readily scalable synthesis method for the preparation of PANI/N-rGO nanocomposites. The reduction of GO and N doping into graphene lattice was done by the hydrothermal method. The hydrothermal synthesized N-rGO is readily dispersible in DI water due to the presence of residual oxygen functional groups and N groups which prevents the agglomeration of graphene sheets during the *in-situ* polymerization of aniline. The presence of electronegative N atoms and residual oxygen functional groups in N-rGO can facilitate the aniline monomer to get adsorbed onto the surface of N-rGO sheets. Therefore, the layers of N-rGO can act as a substrate for the growth of PANI nanostructures. During the polymerization process, PANI nanostructures were uniformly distributed over the surface of the N-rGO sheets, which reduces the restacking of N-rGO layers. To evaluate the electrochemical performance, self-standing flexible electrodes of PANI/N-rGO composite were assembled into a symmetrical supercapacitor and the electrochemical properties are compared with pristine PANI, N-rGO, and PANI/rGO composites. The PANI/N-rGO composite-based self-standing flexible electrodes delivered a high specific capacitance of 322 F/g at a current density of 1 A/g in a symmetrical supercapacitor assembly. Herein, PANI/N-rGO composite possesses combined features of both PANI and N-rGO providing more electroactive surface area and also decreasing the diffusion path length for the electrolyte ions, hence, resulting in high performance.

4.2 Results and Discussion

The surface morphology images of PANI, PANI/rGO, and PANI/N-rGO materials are shown in Fig. 4.1. Pristine PANI shows the rod-like morphology with irregularly grown and agglomerated interconnected clusters. (Fig. 4.1a&b). *In-situ* polymerization of PANI onto the rGO and N-rGO sheets in PANI/rGO and PANI/N-rGO composites leads to the homogeneous interconnected network of PANI nanorods (Fig. 4.1(c-f)). During the initial polymerization process, aniline monomers get adsorbed over the surface of rGO and N-rGO sheets. Once the polymerization is initiated by the addition of APS, these nanosheets in rGO and N-rGO act as a support system to grow PANI nanorods. As polymerization progresses, these initially grown nanorods act as nucleation sites for the secondary growth of PANI and finally end up with an extended interconnected chain-like network and in turn modified the surface of graphene sheets as we observed in Fig. 4.1(c-f). It is worth noting that the long-range interconnected network of PANI/N-rGO composite leads to an increase in porosity of the material in comparison with PANI/rGO. The increase in porosity in PANI/N-rGO composite increases the electrochemically active surface area available for the electrolyte ions which in turn results in enhanced performance for the supercapacitor.

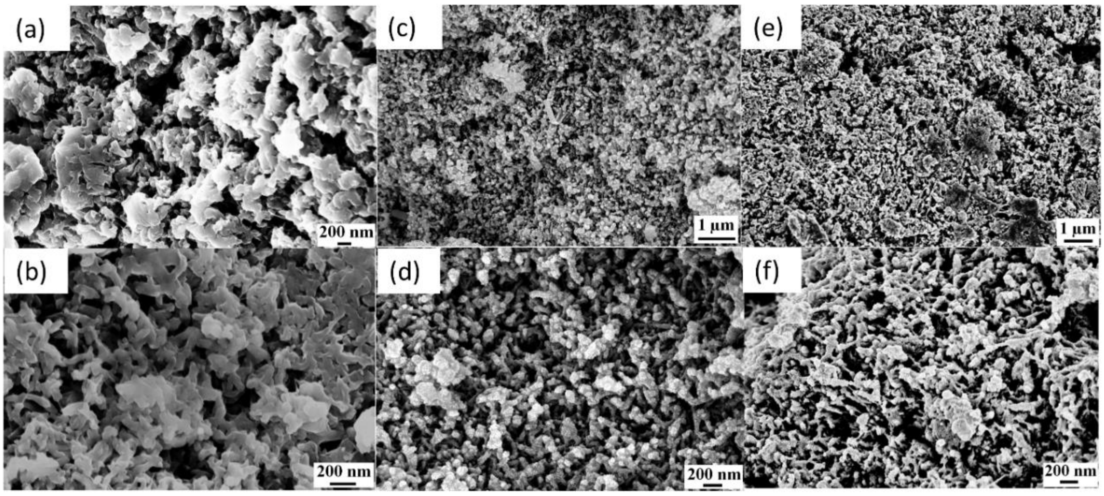

Figure 4.1 *FESEM images of (a)&(b) PANI, (c)&(d) PANI/rGO, and (e)&(f) PANI/N-rGO.*

The XRD plots of rGO, N-rGO, PANI, PANI/rGO, and PANI/N-rGO are shown in Fig. 4.2a. A characteristic diffraction peak of GO nanosheets is observed at 2θ ~10.3° attributed to the (002) plane reflection, showing the higher degree of oxidation level, and the corresponding interlayer spacing value (*d* = 0.85 nm) is calculated using Bragg's Law [23]. In contrast, when the GO is exposed to the hydrothermal treatment, the diffraction peak at 10.3° has vanished and a broad diffraction peak is detected at 2θ ~24.3° for rGO, and 2θ ~25.4° for N-rGO, and the interlayer spacing is found to decrease to 0.35 nm for rGO and 0.36 nm for N-rGO, confirms the removal of oxygen moieties and restoration of graphitic phase [4]. In addition, diffraction peak broadening for both rGO and N-rGO indicates the random orientation of graphene layers after the reduction process [24]. For PANI, three characteristic less intensive diffraction peaks at 2θ ~14°, ~20°, and 24° are observed which are corresponds to the (011), (020), (200) crystal planes of PANI [22,25,26]. The diffraction peaks at 14° and 24° are assigned to the periodicity parallel and perpendicular to the polymer chain, respectively [20]. Further, PANI/rGO and PANI/N-rGO possess a diffraction pattern similar to PANI, which implies that fully dispersed rGO and N-rGO sheets are utilized as a substrate for the formation of a polymer chain, respectively. Furthermore, the diffraction peak associated with the rGO and N-rGO might be overlapped with the peaks of PANI [27].

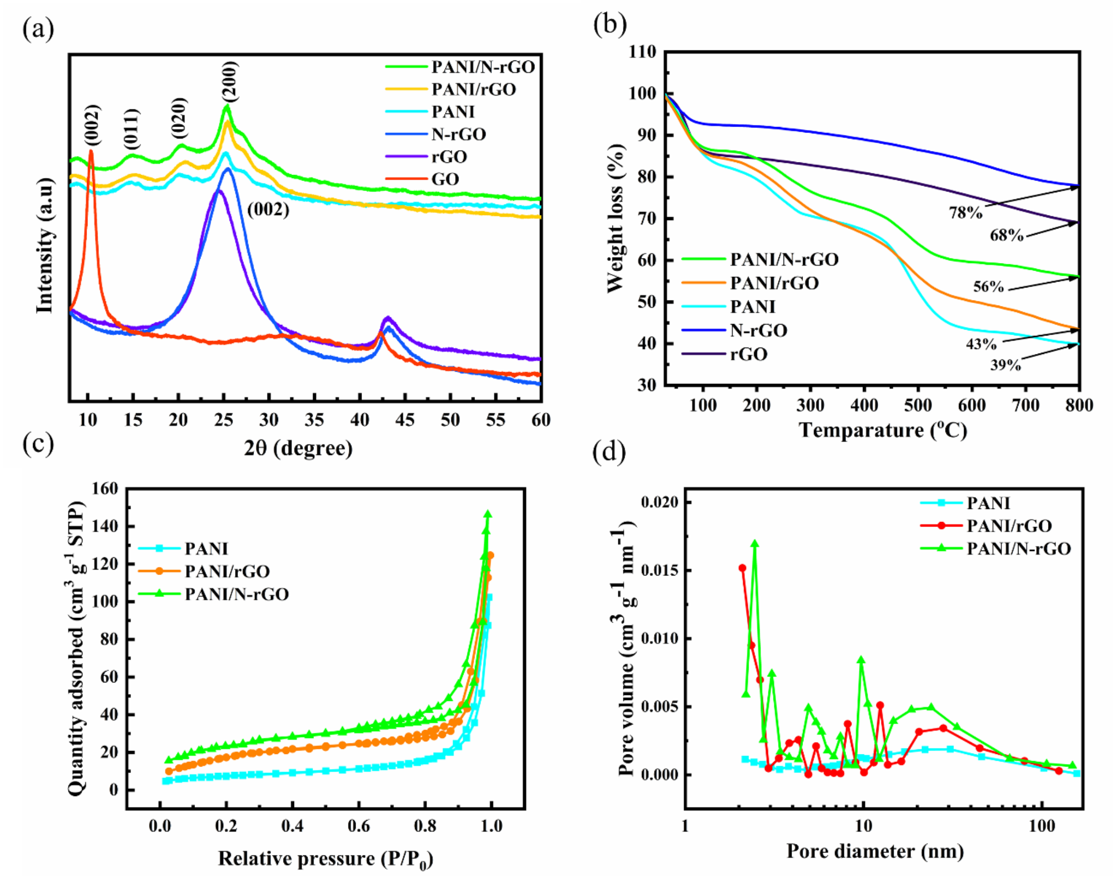

Figure 4.2 *(a) XRD patterns of GO, rGO, N-rGO, PANI, PANI/rGO, and PANI/N-rGO, (b) TGA plots of rGO, N-rGO, PANI, PANI/rGO, and PANI/N-rGO, (c)* N_2 *adsorption-desorption isotherms, and (d) Pore size distribution of PANI, PANI/rGO, and PANI/N-rGO.*

Thermogravimetric analysis (TGA) was carried out from room temperature to 800 °C with a heating rate of 5 °C/min in an inert atmosphere and the responses were shown in Fig. 4.2b. In the TGA analysis, initial weight loss at a temperature below 120 °C is attributed to the evaporation of absorbed moisture. Then weight loss in rGO and N-rGO from 120 °C to 800 °C originated from the removal of oxygen and N functional groups. In comparison with the TGA curve of rGO, there is a significant increase in thermal stability of N-rGO (78%), indicating that the reduction of GO is more effective in the presence of reducing agent and a higher number of oxygenated moieties were eliminated. From the TGA plots, it is noticed that the thermal behaviour of PANI/N-rGO and PANI/rGO is quite similar to PANI, all the samples possessed weight loss in two stages. At the initial stage in the temperature range 120 - 450 °C, the lower-weight fragments of polymer got eliminated and dopant ions were removed in the form of HCl gas [28]. Furthermore, maximum weight loss is observed after 450 °C, owing to the complete decomposition of the polymer chain at high temperatures. It is noteworthy that the disintegration of PANI is decreased for PANI/N-rGO, indicating that N-rGO could prevent the breakdown of the polymer chain and enhance its structural stability.

The microstructure of the pure PANI, PANI/rGO, and PANI/N-rGO composite is further investigated by conducting N_2 adsorption-desorption studies and the adsorption-desorption isotherms and pore size distribution curves are displayed in Fig. 4.2c. All three samples exhibited type IV isotherm [29]. Particularly a small hysteresis loop is observed at relatively high pressure, showing the presence of meso and micropores in the sample. The specific surface area and average pore diameter values are calculated using the BET method and BJH model, respectively. The BET surface area, total pore volume and average pore diameter values of all three samples are given in Table 4.1. The more agglomeration of nanorods in PANI leads to forming clusters as can be observed in FESEM (Fig. 4.1a) and 2(B)) and resulting in lower porosity and a small surface area of 26.62 m^2/g with the pore volume of 0.15 cm^3/g. Whereas, the uniform growth of PANI nanorods on the surface of rGO and N-rGO sheets in PANI/rGO and PANI/N-rGO composites results in increased surface area to 59.21 m^2/g and 82.80 m^2/g and the corresponding pore volumes are increased to 0.19 cm^3/g and 0.22 cm^3/g, respectively. The high surface area of PANI/N-rGO is attributed to the presence of a long-range interconnected chain-like network with increased porosity as can be observed in FESEM images (Fig. 4.1e&f). Doping of N atoms into the graphene network creates more defective sites and prevents the aggregation of neighbouring graphene layers which eventually results in increased surface area in PANI/N-rGO over PANI/rGO composite.[9] Further, the average pore diameter of PANI/N-rGO is smaller in comparison with the PANI and PAN/rGO which can be ascribed to the less agglomeration and uniform growth of PANI nanostructures on N-rGO sheets (Table 4.1). From the pore size distribution curve (Fig. 4.2d), PANI/N-rGO composite material has more pores lying in the range of meso to micropores region with smallest pore diameter contributing to possessing a higher BET surface area [30,31]. The presence of electronegative N-atoms in the basal planes of N-rGO creates more crosslinking between the polymer chain and graphene sheets as is evident in XPS spectra thus surface area is increased. The high surface area along with porosity in PANI/N-rGO composite facilitates rapid ion diffusion which enhances the charge transport properties of the composite and results in high specific capacitance [19].

Table 4.1 Surface area and porosity characteristics of PANI, PANI/rGO, and PANI/N-rGO.

Sample	BET Surface area (m^2/g)	Total pore volume (cm^3/g)	Average pore diameter (nm)
PANI	26.62	0.15	29.03
PANI/rGO	59.21	0.19	12.86
PANI/N-rGO	82.80	0.21	11.73

Fourier Transform Infrared Spectroscopy (FTIR) studies were conducted to evaluate the presence of various functional groups in the synthesized material. Figure 4.3a shows the FTIR spectra of GO, rGO, and N-rGO. FTIR spectrum of GO consist of a series of absorption peaks related to the oxygenated functional groups, which proves the successful oxidation of graphite. A broad absorption peak centred at 3422 cm^{-1} is associated with the hydroxyl groups and adsorbed water molecules. The absorption peaks at 1726 cm^{-1}, 1620 cm^{-1}, 1383 cm^{-1}, 1051 cm^{-1}, and 872 cm^{-1} are assigned to the carbonyl (C=O) stretching, aromatic C=C stretching, carboxyl (COOH), epoxy (C-O-C) group, and C-H bending vibration, respectively. While the peak related to aromatic (C=C) stretching is shifted to 1588 cm^{-1} for rGO and the intensity of the peaks related to oxygen functional groups is reduced in rGO which is attributed to the partial reduction of GO. For N-rGO, the absorption peaks related to the oxygen functional groups were mostly eliminated and a new peak has appeared at 1290 cm^{-1} responsible for C-N stretching vibration, which confirms the high degree of reduction and N doping into the graphene framework. In addition, the absorption peak of aromatic C=C stretching (1583 cm^{-1}) is shifted to a lower wavenumbers side indicating the reconstruction of the graphene network in N-rGO nanosheets. Meanwhile, various characteristic absorption peaks were observed in the FTIR spectrum of PANI as shown in Fig. 4.3b. the main absorption peaks at 1476 cm^{-1} and 1570 cm^{-1} are related to the stretching vibration of C=C in quinoid and benzenoid rings of PANI. The other absorption peaks at 1287 cm^{-1} for C-N stretching amine, 1336 cm^{-1} for C-N^+ protonic stretching, 1238 cm^{-1} for C-H in the benzene ring, 1110 cm^{-1} for C-H in the quinoid ring, and 870 cm^{-1} for C-H out of plane bending. Whereas the peaks at 1476 cm^{-1} and 1336 cm^{-1} are shifted towards the lower wavenumber side indicating the strong interaction of polymer chain with graphene network [32]. The interaction of protonic C-N^+ bonds with the graphene network may be through π–π stacking/hydrogen bonding [33]. These different bonding interactions may facilitate the effective charge transfer between the polymer and graphene crosslinked network, thus improving electrochemical properties.

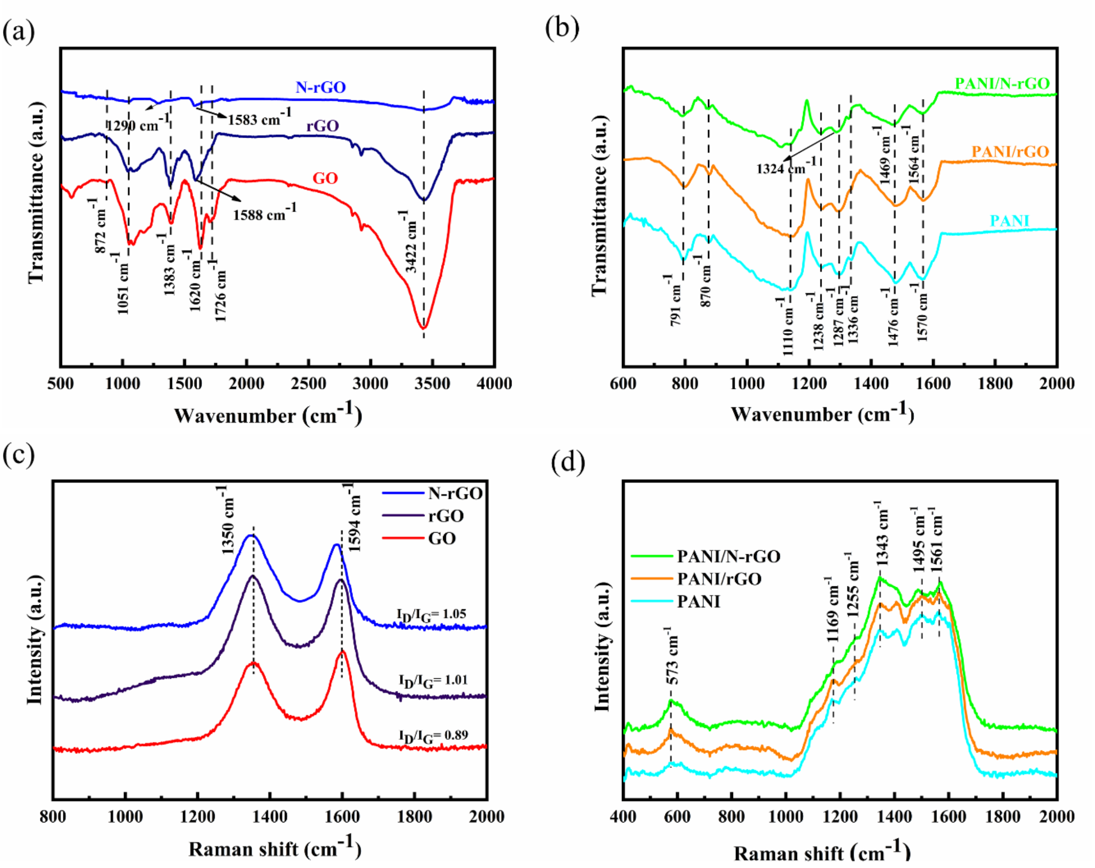

Figure 4.3 *FTIR spectrum: (a) GO, rGO, and N-rGO, (b) PANI, PANI/rGO, and PANI/N-rGO, and Raman spectrum: (c) GO, rGO, and N-rGO, (d) PANI, PANI/rGO, and PANI/N-rGO.*

Raman spectroscopy is the best spectroscopic technique for the analysis of carbon materials. Figure 4.3c illustrates the Raman spectra of GO, rGO, and N-rGO. Raman spectrum of GO consists of two strong vibrational bands at ~1350 cm^{-1} and ~1594 cm^{-1} referred to as D and G bands, respectively (Fig. 4.3c) [34]. Generally, the G band is observed in the wavenumber range of 1570 -1580 cm^{-1} for graphitic materials but the observed G band is shifted towards the higher wavenumber for GO (blue shift) indicating the higher degree of oxidation and formation of sp^3 carbon atoms in graphite lattice [35,36]. In comparison with GO, the G band is red-shifted in the case of rGO and N-rGO. The G band is observed at ~1586 cm^{-1} for rGO and ~1583 cm^{-1} for N-rGO. The shift in the G band could be associated with the removal of oxygen moieties during the reduction process and the reconstruction of sp^2 hybridized domains and the graphitic phase. Further, the intensity ratio of the D to G band (I_D/I_G) is interlinked with the disorder and structural defects in the graphene lattice which is found to be in the order of 0.89<1.01<1.05 of GO, rGO, and N-rGO, respectively. The higher value of I_D/I_G ratio for N-rGO elucidates higher degree of disorder in the graphene network due to the insertion of heterogeneous N atoms into graphene lattice by disrupting the sp^2 bonds of carbon atoms [37,38]. These results are well consistent with the results obtained from XRD. Furthermore, I_D/I_G ratio is also used to correlate the in-plane crystallite size (L_a) formed by a certain number of carbon rings using the following relation [36,39].

$$L_a(nm) = (2.4 \times 10^{-10})\lambda_l^4 (\frac{I_D}{I_G})^{-1} \tag{5}$$

Where λ_l is the Raman excitation wavelength ($\lambda_l = 532\,nm$). The calculated crystallite size values of GO, rGO, and N-rGO are 21 nm, 19 nm, and 18 nm, respectively. It is worth noting that, lower crystallize size of N-rGO produces a high surface area accessible to the electrolyte ions, which improves the capacitance of the device.

The Raman spectra of PANI, PANI/rGO, and PANI/N-rGO composite are displayed in Fig. 4.3d. It is observed that PANI/N-rGO, PANI/rGO, and pristine PANI possess similar kinds of Raman spectra. Pristine PANI consists of various characteristic peaks at 1169 cm^{-1} for C-H bending, 1343 cm^{-1} for C-N$^+$ vibration, 1495 cm^{-1} for C=N stretching, 1561 cm^{-1} for stretching vibration of C=C of the quinoid ring, suggesting the conductive emeraldine salt form of PANI, provides sufficient charge carriers to participate in a fast redox reaction with the electrolyte ions resulting in high capacitance [40]. In addition, the peak at 573 cm^{-1} is assigned to the phenazine type or the existence of the crosslinking structure in PANI [41,42]. The peak intensity at 573 cm^{-1} is high for PANI/N-rGO suggesting the formation of more crosslinking networks in PAN/N-rGO composite which is well supported by the XPS results. The formation of crosslinking favours efficient charge transportation with the electrode material. Further, we observed the shift in peaks related to C-N$^+$ vibration and C=N stretching towards the lower wavenumber side for PANI/rGO and PANI/N-rGO indicating well interaction between polymer chain and graphene sheets and these results are well consistent with the results obtained from FTIR.

XPS analysis is an effective technique to identify the surface chemical composition and doping level of the heteroatom in the graphene network. The survey spectra of rGO and N-rGO are shown in Fig. 4.4a and the surface atomic percentages of different elements present in the rGO and N-rGO are given in Table 4.2. The C 1s (285.6 eV) and O 1s (533.6 eV) peaks are detected in rGO while a well-defined N 1s (399.5 eV) peak is also appeared along with the C 1s (285.5 eV) and O 1s (533.5 eV) peaks in the survey spectrum of N-rGO, confirms the successful incorporation of N atoms into graphene lattice. From the survey spectra, it is observed that the peak intensity of O 1s and the O/C ratio is decreased in N-rGO (10.13%) in comparison with rGO (11.6%), which is indicating the reduction of GO is more prominent in the presence of reducing agent (Urea) during the hydrothermal process. Further, it is noticed that 6.8% of N atoms are present in N-rGO and the corresponding N/C atomic ratio (8.09%), indicating a higher degree of doping.

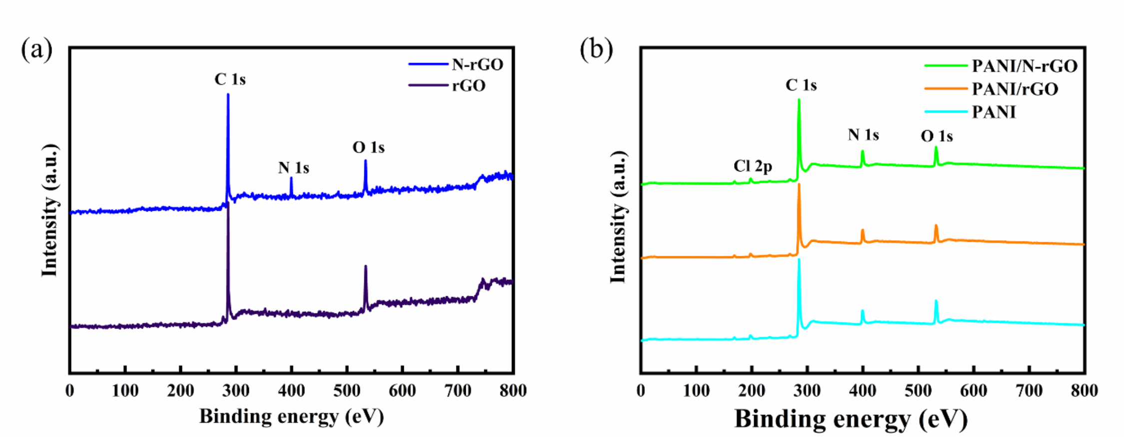

Figure 4.4 *XPS survey spectra of (a) rGO and N-rGO, (b) PANI, PANI/rGO, and PANI/N-rGO.*

The surface elemental composition of pristine PANI, PANI/rGO, and PANI/N-rGO composite was also investigated by XPS analysis, the survey spectra are depicted in Fig. 4.4b and the corresponding elemental composition is given in Table 4.2. From Fig. 4.4b, the survey spectra of all three samples show the existence of C 1s, N 1s, O 1s, and Cl 2p signals. It is observed that the atomic ratio of O/C is lesser and the atomic ratio of N/C is greater for PANI/N-rGO compared to PANI/rGO and PANI as given in Table 4.2, indicating the N content of PANI/N-rGO is increased with the incorporation of N-rGO sheets.

Table 4.2 Elemental composition of rGO, N-rGO, PANI, PANI/rGO, and PANI/N-rGO.

Material	**C 1s eV (at. %)**	**N 1s eV (at. %)**	**O 1s eV (at. %)**	**O/C (%)**	**N/C (%)**
rGO	285.6 (89.57)	-	533.6 (10.43)	11.6	-
N-rGO	285.6 (84.58)	399.5 (6.85)	533.6 (8.57)	10.13	8.09
PANI	285.1 (81.43)	399.5 (8.29)	532.5 (10.28)	12.62	10.18
PANI/rGO	285.1 (82.38)	399.5 (8.61)	532.5 (9.00)	10.09	10.45
PANI/N-rGO	285.1 (83.32)	399.5 (9.57)	532.5 (7.11)	8.53	11.48

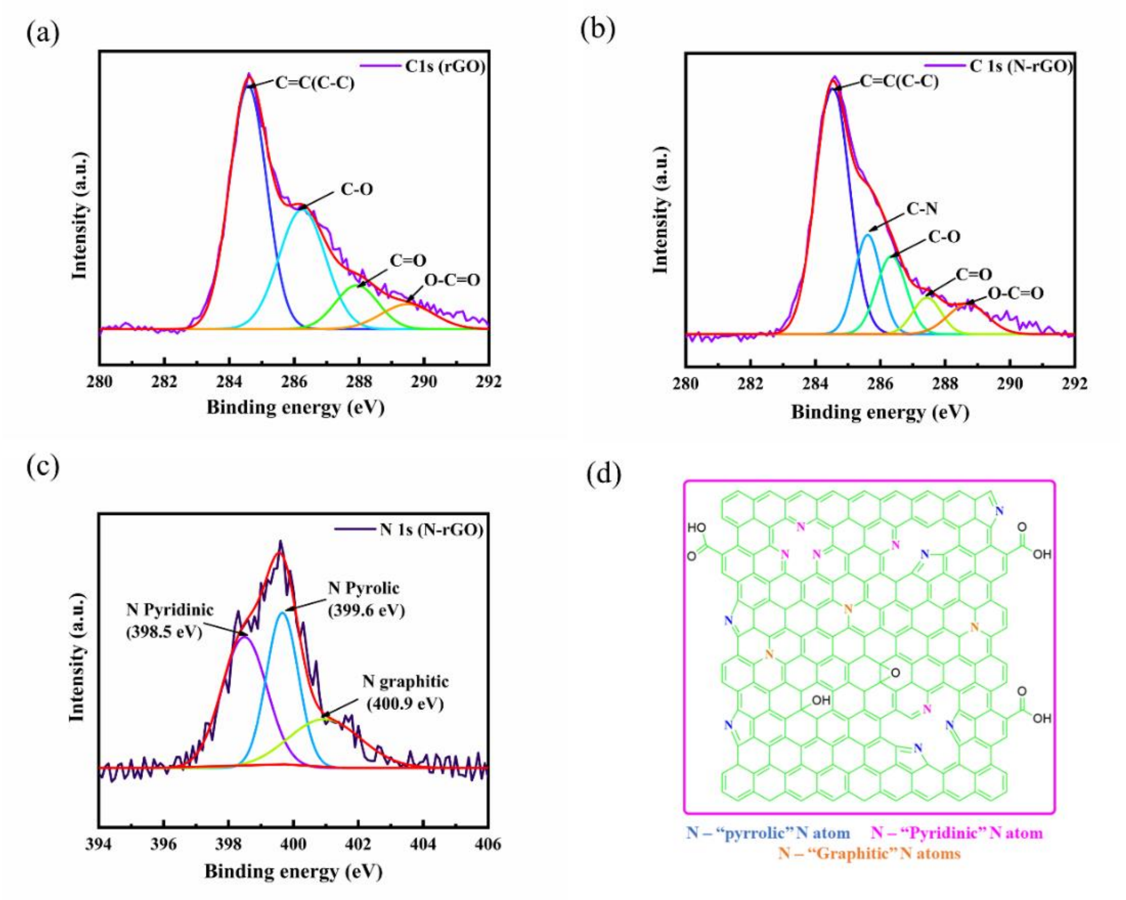

Figure 4.5 *High-resolution C 1s spectrum: (a) rGO, (b) N-rGO, (c) High-resolution N 1s spectra of N-rGO, and (d) chemical structure of N-rGO.*

The C 1s deconvolution spectrum of rGO and N-rGO showed in Fig. 4.5a&b. C 1s of rGO deconvoluted into four different peaks at binding energies of 284.5 eV, 286.2 eV, 287.9 eV, and 289.3 eV, related to C=C(C-C), C-O, C=O, and O-C=O, respectively [43]. Along with the above peaks, a new peak is noticed in the deconvoluted C 1s spectrum of N-rGO at a binding energy of ~285.6 eV corresponds to the C-N bond, confirming the doping of N atom into graphene network (Fig. 4.5b) [44]. It can be seen from Fig. 4.5c, the complex N 1s spectrum of N-rGO is composed of three main valence states of N at binding energies of 398.5 eV, 399.6 eV, and 400.9 eV, demonstrating the pyridinic N, pyrrolic N, and graphitic N, respectively [14]. The chemical structure of a single layer of N-rGO with different atomic configurations of N is shown in Fig. 4.5d. It is well known that different atomic configurations of N doping could play a different role in determining the supercapacitor behaviour. pyridinic N, pyrrolic N contributes additional pseudo capacitance and graphitic N can increase the conductivity of N-rGO. Insertion of N atoms into graphene lattice increases surface wettability resulting in a good electrochemical activity. Furthermore, the presence of high electronegative N atoms can facilitate a good interaction with the PANI chain and also provide mechanical strength to the polymer chain, which results in high-rate capability and better cycling stability of composite material.

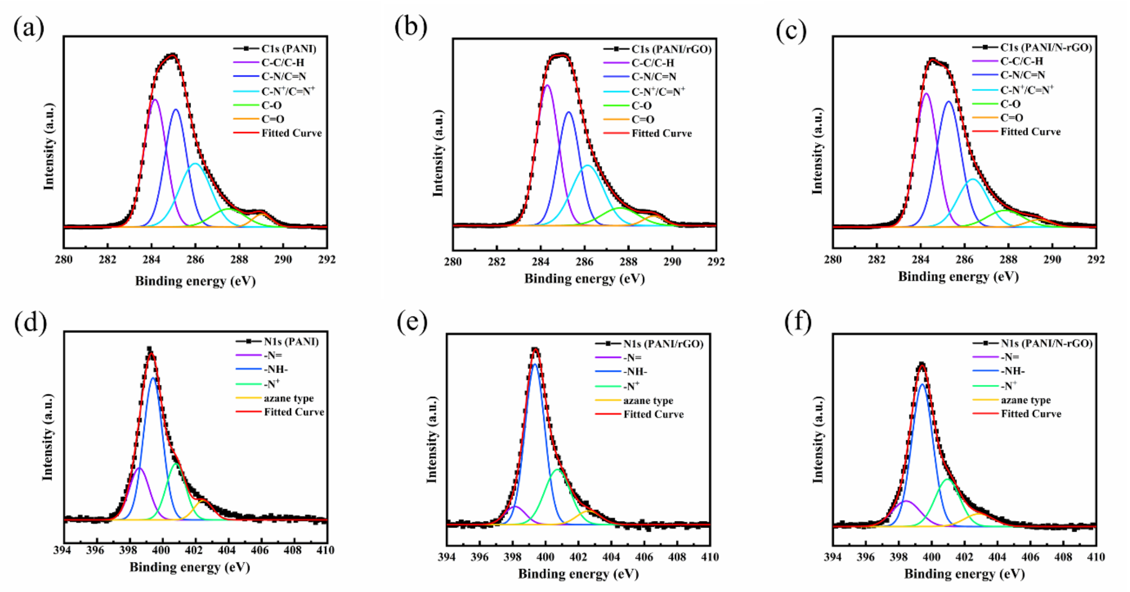

Figure 4.6 *High-resolution C 1s spectrum: (a) PANI, (b) PANI/rGO, (c) PANI/N-rGO, and High-resolution N 1s spectrum: (d) PANI, (e) PANI/rGO, (f) PANI/N-rGO.*

The high-resolution C 1s spectra of PANI (Fig. 4.6a) is split into five different bonding configurations located at 284.1 eV (C-C/C=C), 285.1 eV (C-N/C=N), 286 eV (C-N$^+$/C-O), 287.3 eV (C=O), and 289.01 eV (O-C=O) [33,45]. The presence of oxygen functional groups (C-O/C=O) are assigned to the degradation products hydroquinone (HQ) and benzoquinone (BQ) responsible for the decomposition of PANI [45,46]. We observed that the peak intensities of C=O and O-C=O are decreased for PANI/rGO (10.01%) and PANI/N-rGO (6.46%) compared to PANI (10.27%) indicating elimination of degradation products HQ and BQ from PANI, hence, the structural stability of PANI could be increased (Table 4.3). Further, we noticed a significant increase in the C-C/C=C bonds in PANI/rGO and PANI/N-rGO composites which could be assigned to the increase in sp^2 hybridized carbon atoms with the addition of rGO and N-rGO, respectively (Fig. 4.6b&c).

Table 4.3 Percentage of different C 1s bonding configurations of PANI, PANI/rGO, and PANI/N-rGO.

C1s	**C-C/C=C (%)**	**C-N/C=N (%)**	**C-N$^+$/C=N$^+$ (%)**	**C=O (%)**	**O-C=O (%)**
PANI	34.46	31.06	24.18	7.32	2.95
PANI/rGO	37.63	29.41	22.92	7.60	2.41
PANI/N-rGO	38.25	39.94	21.62	5.22	1.24

The XPS N 1s core-level spectra of PANI, PANI/rGO, and PANI/N-rGO are composed of four different configurations of N atoms with the binding energies at 398.6 eV for imine group (-N=), 399.3 eV for amine (-NH-), 400.7 eV and 402.4 eV assigned to the protonated N groups ($-N^+$) and cross-linking azane type N (Fig. 4.6(d-f)). We observed that the intensity of amine groups is increased for PANI/N-rGO (56.31%) compare to PANI (53.08%) and PANI/rGO (55.91%), which could be assigned to the existence of pyrrolic N (399.6 eV for N-rGO) in the composite (Table 4.4). Further, the doping level of PANI/N-rGO ($-N^+$) is slightly decreased and the concentration of azane-type N is high for PANI/N-rGO composite indicating the existence of more crosslinking between the polymer chain and N-rGO sheets, consistent with the Raman results. This may be possibly assigned to the good interaction of N atoms present in the N-rGO with the polymer chain and which can enhance the charge transfer property of the composite material.

Table 4.4 Percentage of different N 1s bonding configurations of PANI, PANI/rGO, and PANI/N-rGO.

N1s	**-N= (%)**	**-NH- (%)**	**$-N^+$ (%)**	**Azane type (%)**
PANI	19.89	53.08	20.97	6.05
PANI/rGO	18.20	55.91	19.19	6.69
PANI/N-rGO	17.48	56.31	18.25	7.95

The electrochemical properties of as-prepared samples were evaluated in a symmetrical supercapacitor by conducting a series of CV and GCD measurements in 1 M H_2SO_4 electrolyte. Figure 4.7a displays the CV curves of rGO, N-rGO, PANI, PANI/rGO, and PANI/N-rGO at 10 mV/s scan rates. The CV curve of the rGO is rectangular, which is characteristic of EDL energy storage. On the other hand, N-rGO displays a small hump in the CV curve, related to the pseudocapacitance charge storage behaviour. The additional pseudocapacitance of N-rGO is due to the presence of N atoms and attached oxygen functional groups in graphene lattice, which can participate in charge transfer reaction with electrolyte ions. Benefited from different types of N configurations, the N-rGO electrode produced a larger enclosed area in a CV than rGO. Furthermore, PANI/N-rGO, PANI/rGO, and PANI electrodes-based devices showed well-defined two pairs of redox peaks, implying to the energy storage comes from the pseudocapacitance behaviour of the electrodes. The two redox couples are related to the oxidation states associated with PANI. It could be noted that PANI/N-rGO displays a larger enclosed area of CV curve indicating the superior charge storage capability compared to pristine PANI and PANI/rGO composite. Hence, PANI/N-rGO composite possesses higher specific capacitance. Further, the variation of the current response of the sample is collected at scan rates of 10 - 100 mV/s as shown in Fig. 4.7b-f. PANI/N-rGO composite can able to deliver high currents with an increase in scan rates, attributed to the high redox activity, and improved electron diffusion pathways to the electrolyte ions. The redox peaks were overlapped and shifted towards higher potential and lower potential for anodic and cathodic peaks, respectively, which corresponds to the internal resistance of the electrodes (Fig. 4.17f) [47]. The shape of the CV curve is approximately unaltered even at higher scan rates suggesting the efficient charge transportation of the composite material. Furthermore, we have calculated the specific capacitance values of all the materials at various scan rates using the CV curves shown in Fig. 4.7(b-f). The change in the specific capacitance concerning scan rate for all the samples is shown in Fig. 4.7g. It is observed that the specific capacitance was decreased with the increase in scan rate for all the samples (Fig. 4.7g). PANI/N-rGO nanocomposite can deliver reasonably high specific capacitance at high scan rates, indicating high-rate capability among all the synthesized materials.

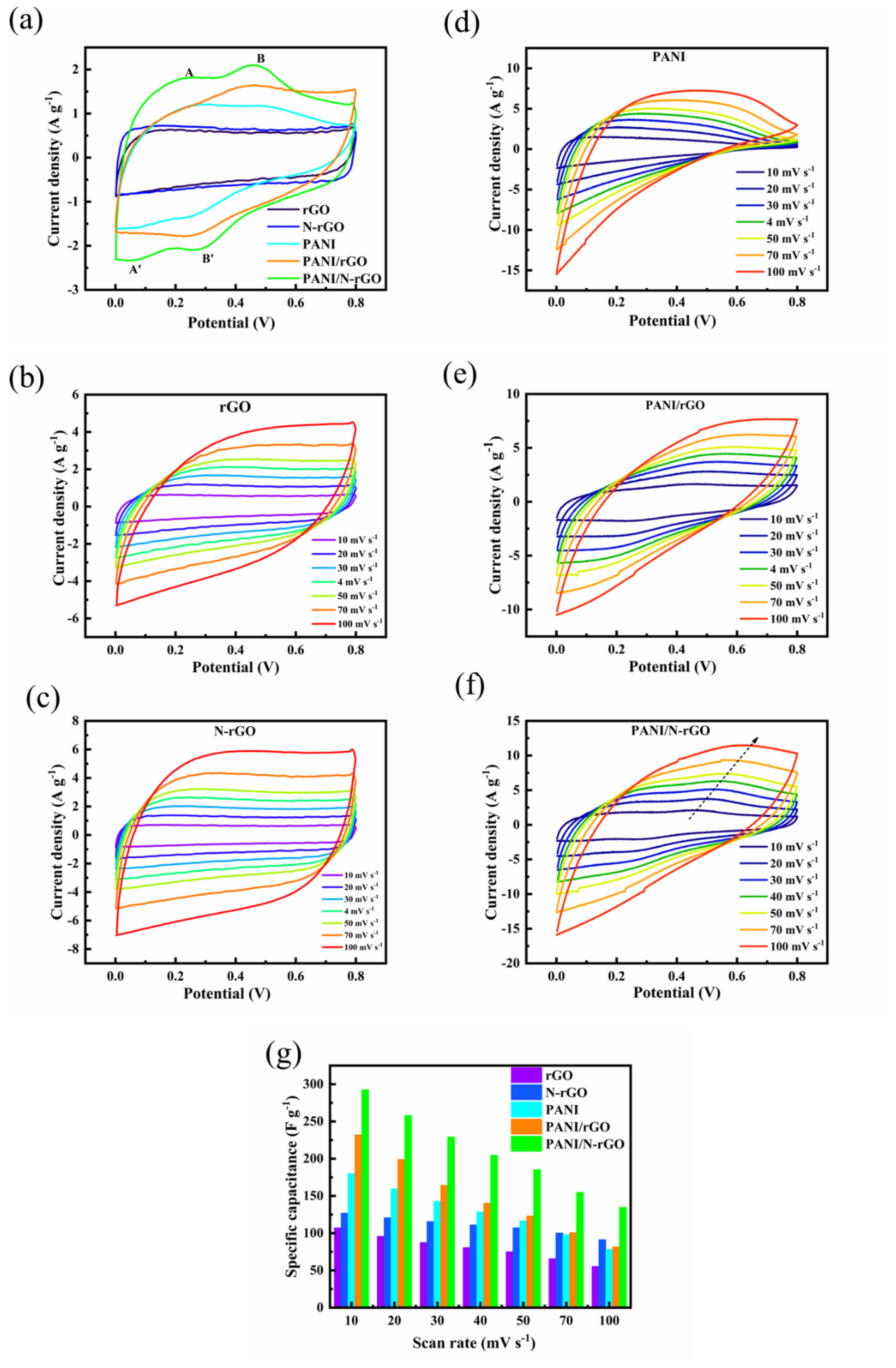

Figure 4.7 *(a) CV curves of rGO, N-rGO, PANI, PANI/rGO, and PANI/N-rGO at 10 mV/s, CV curves at scan rates of 10, 20, 30, 40, 50, 70, and 100 mV/s: (b) rGO, (c) N-rGO, (d) PANI, (e) PANI/rGO, and (f) PANI/N-rGO, and (g) Specific capacitance of rGO, N-rGO, PANI, PANI/rGO, and PANI/N-rGO at various scan rates.*

GCD studies were carried out to evaluate the capacitive performance of all the samples. Figure 4.8a illustrates the GCD plots of rGO, N-rGO, PANI, PANI/rGO, and PANI/N-rGO electrodes-based devices at a current density of 1 A/g. rGO exhibits a symmetrical triangular shape GCD curve, which reflects the characteristic of electric double-layer energy storage behaviour. A small deviation is observed in GCD curve of N-rGO further confirming the addition of pseudocapacitance behaviour, which originates from the presence of N atoms in graphene lattice. The specific capacitance value obtained for N-rGO (142.5 F/g) is higher than rGO (117.5 F/g) at a current density of 1 A/g. Meanwhile, pristine PANI, PANI/rGO, and PANI/N-rGO composite electrodes show a deviation in the GCD curve from the triangular shape, indicating the existence of pseudocapacitive nature. Moreover, the PANI/N-rGO composite possesses a longer discharging time than PANI and PANI/rGO, which proves that PANI/N-rGO composite possesses better charge storage capability. Furthermore, it is observed that all the materials have shown a sudden fall in potential value at the beginning of discharge process, which is related to the internal resistance (IR drop) of the device. The IR drop is originating from the equivalent series resistance (ESR), which includes electrode resistance, electrolyte resistance, and contact resistance at the interface between electrode and electrolyte. PANI/N-rGO composite possesses a lower voltage drop, indicating the high electrical conductivity of the composite material (Fig. 4.8a). A higher specific capacitance value is obtained for PANI/N-rGO (322.5 F/g) than PANI (212 F/g) and PANI/rGO (252.5 F/g) at 1 A/g current density. The enhanced specific capacitance of PANI/N-rGO nanocomposite could be achieved by the uniform distribution of PANI nanostructures over the N-rGO sheets. Further, to explore the rate capability of the samples, GCD measurements were obtained by varying current density from 1 - 5 A/g (Fig. 4.8b-f). Figure 4.8f depicts the GCD curves of PANI/N-rGO composite at current densities of 1 – 5 A/g. PANI/N-rGO nanocomposite is capable to deliver a high specific capacitance of 262.5 F/g at a high current density of 5 A/g which is higher than pristine PANI (125 F/g) and PANI/rGO (175 F/g) composite, shows its better rate capability. The variation of specific capacitance with increasing current density for all the samples is given in Fig. 4.8g. From Fig. 4.8g, it can be seen that the superior rate capability of PANI/N-rGO composite than PANI and PANI/rGO which could be attributed to the existence of better surface area and long-range interconnected crosslinking network as can be evident from BET and FESEM results. The formation of chain-like PANI nanostructures on N-rGO sheets creates more electroactive sites over the entire surface area of the electrode, thus increasing the rate capability. Furthermore, the combined features of both PANI and N-rGO greatly enhanced the performance of the composite material. The specific capacitance and the rate capabilities obtained for the PANI/N-rGO composite are comparable with the results obtained from the similar electrode materials studied in the two and three-electrode systems as shown in Table 4.5 [19,48–51].

Table 4.5 Comparison of the specific capacitance of similar electrode materials.

Material	Electrolyte/ Electrode system	Specific capacitance	Cyclic stability	Rate capability	Ref.
N-3D-rGO /PANI	1 M H_2SO_4/3 ele.	282 F/g at 1 A/g	69.9% (1000 cycles)	64.5% (1-8 A/g)	[19]
NG / PANI	1 M H_2SO_4/3 ele.	1058 F/cm^3 at 0.5 A/g	81.5% (5000 Cycles)	75% (0.5 -50 A/g)	[20]
3D NG/PANI	1 M H_2SO_4/2 ele.	528 F/g at 0.1 A/g	95.9% (5000 cycles)	50.7% (0.1-5 A/g)	[21]
H-NrGO-PANI	10% PVA-H_2SO_4/2 ele.	510 F/g at 1 A/g	74% (2000 cycles)	62% (1-20 A/g)	[22]
PANI-RGO-ZnO	1 M H_2SO_4/2 ele.	40.5 F/g at 0.05 A/g	86% (5000 cycles)	--	[52]
NG/PANI	1 M H_2SO_4/2 ele.	93.2 F/g at 1 A/g	79% (5000 cycles)	64% (1-10 A/g)	[48]
PANI/N-carbon	2 M KOH /3 ele.	276 F/g at 0.2 A/g	80% (5000 Cycles)	81.2% (0.2-5 A/g)	[49]
Graphene/ PANI	1 M H_2SO_4/3 ele.	257 F/g at 0.1 A/g	98% (1000 cycles)	58.7% (0.1-10 A/g)	[50]
N-carbon /PANI	1 M H_2SO_4/2 ele.	285 F/g at 0.5 A/g	80% (5000 Cycles)	73.7% (1-10 A/g)	[51]
PANI-NG-$CuCr_2O_4$	1 M H_2SO_4/3 ele.	443.4 F/g at 1 A/g	92% (10000 cycles)	--	[26]
ZnS/RGO/PANI	6 M KOH/2 ele.	722 F/g at 1 A/g	76.1% (1000 cycles)	50.0% (0.3-20 A/g)	[53]
PANI/GECF	1 M H_2SO_4/2 ele.	976.5 F/g at 0.1 A/g	89.2% (1000 cycles)	51.2% (0.4 -50 A/g)	[54]
SPANI/S-rGO	1 M H_2SO_4/2 ele.	347.5 F/g at 1 A/g	89% (2500 cycles)	68% (1-5 A/g)	[55]
PANI-FA	1 M H_2SO_4/2 ele.	208 F/g at 2.5 A/g	66% (5000 cycles)	-	[56]
rGO-Au@PANI	1 M H_2SO_4/2 ele.	212.8 F/g at 1 A/g	86.9% (5000 cycles)	89.5% (0.5-5 A/g)	[57]
CF@RGO/PANI	1 M H_2SO_4/2 ele.	868.5 F/g at 1 A/g	94.1% (2000 cycles)	95% (1-5 A/g)	[58]
PANI/rGO	1 M H_2SO_4/2 ele.	220 F/g at 0.2 A/g	75% (3000 cycles)	47% (0.2-20 A/g)	[59]
PANI/N-rGO	1 M H_2SO_4/2 ele.	322 F/g at 1 A/g	93% (1000 cycles)	81.39% (1- 5 A/g)	Present work

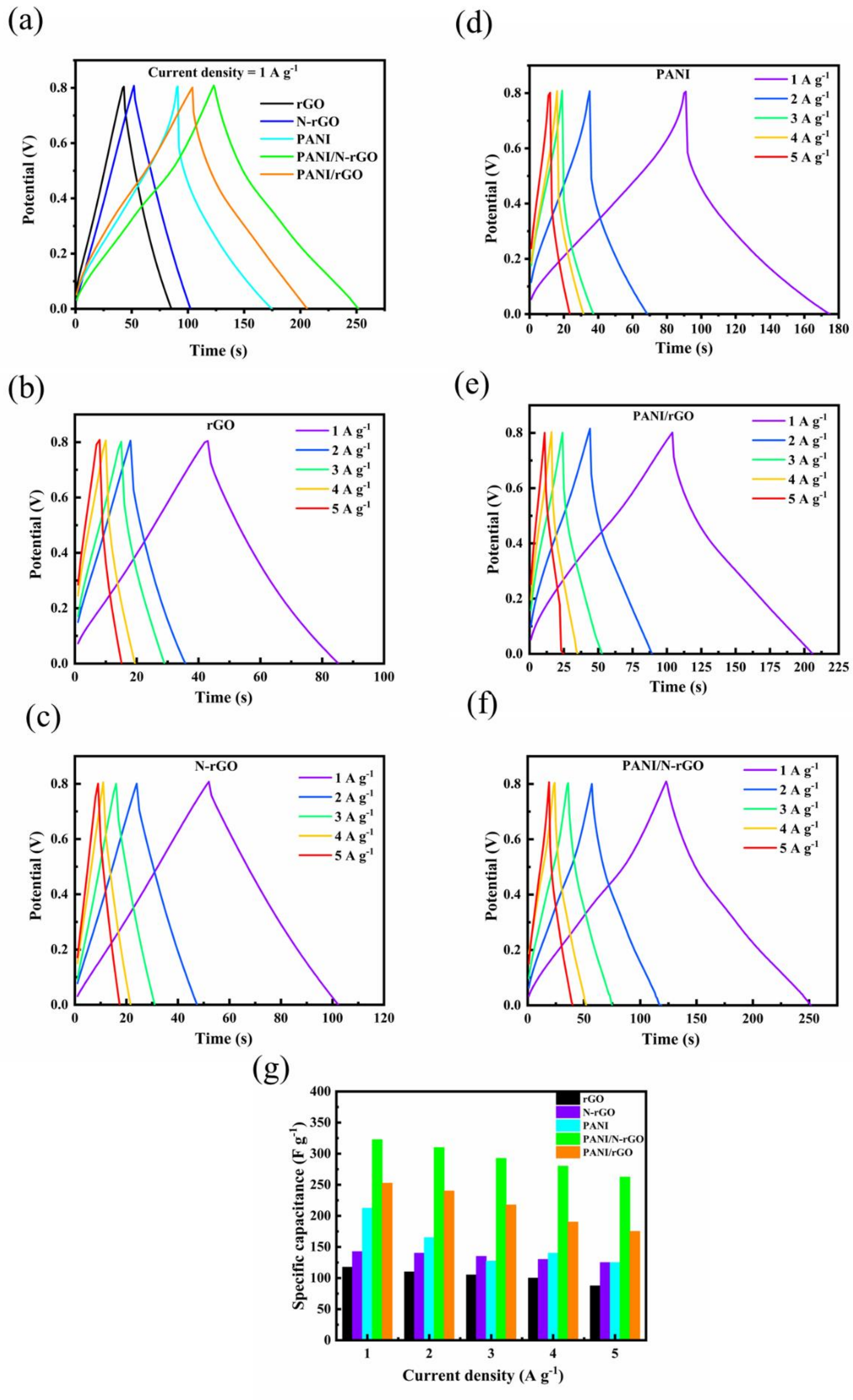

Figure 4.8 *(a) GCD curves of rGO, N-rGO, PANI, PANI/rGO, and PANI/N-rGO at 1 A/g, GCD curves at current densities of 1-5 A/g: (b) rGO, (c) N-rGO, (d) PANI, (e) PANI/rGO, and (f) PANI/N-rGO, and (g) Specific capacitance of rGO, N-rGO, PANI, PANI/rGO, and PANI/N-rGO at various current densities.*

Further, the specific energy and specific power are calculated for PANI/N-rGO composite at various current densities and the corresponding Ragone plot is given in Fig. 4.9a. The SSC device assembled by PANI/N-rGO composite possesses high specific energy of 27.95 Wh Kg and the corresponding specific power is 780.12 W kg. The specific energy remains 12.26 Wh kg even at a specific power of 2102.5 W kg. These results are also reasonably better than the graphene/PANI and other carbon/PANI composites [20,22,40,51,60].

Electrochemical impedance spectroscopy studies were obtained to evaluate the charge transfer kinetics at the electrode/electrolyte interface. Nyquist plots of rGO, N-rGO, PANI, PANI/rGO, and PANI/N-rGO are shown in Fig. 4.9b. All the samples exhibited a semi-circle in the high-frequency region and an inclined straight line in the low-frequency region. The observed semi-circle at the high-frequency region originates from the equivalent series resistance (ESR) and charge transfer resistance (R_{ct}) of the electrode material. It is known that the diameter value of the semi-circle is related to R_{ct}. PANI possesses a large-diameter semi-circle that shows its poor conductivity whereas, with the addition of rGO and N-rGO, the conducting properties of composites were greatly enhanced (Fig. 4.9b). Further, it is noted that PANI/N-rGO possesses a small diameter semi-circle compared to PANI/rGO, which indicates the lower charge transfer resistance. Furthermore, the slope of the inclined line in the low-frequency region is related to the diffusion resistance of electrolyte ions. PANI/N-rGO composite exhibits more vertical lines in the low-frequency region showing its better capacitance behaviour. The complete distribution of PANI nanostructure over the surface of N-rGO sheets facilitates more ion-accessible sites and provides more ion diffusion pathways which increase the charge transportation rates. The obtained values of R_s and R_{ct} for all the samples are given in Table 4.6.

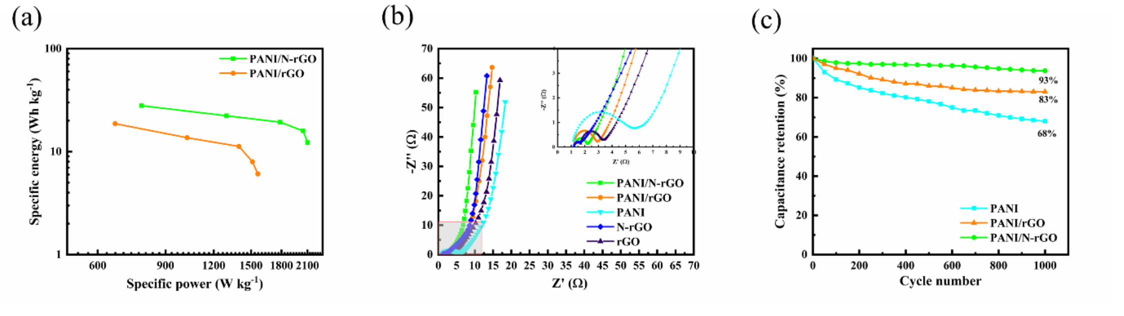

Figure 4.9 *(a) Ragone plots of PANI/rGO and PANI/N-rGO, (b) Nyquist plots of rGO, N-rGO, PANI, PANI/rGO, and PANI/N-rGO, (c) Cyclic performance of PANI, PANI/rGO, and PANI/N-rGO for 1000 cycles.*

The cyclic stability performance of assembled devices with pristine PANI, PANI/rGO, and PANI/N-rGO composite electrodes was conducted at a scan rate of 50 mV/s for 1000 cycles (Fig. 4.9c). The capacitance retention is only 68% for pristine PANI. The cycling stability of PANI is decreased due to volume changes occurring in polymer chain. The doping/de-doping of electrolyte ions during the continuous charge/discharge process causes structural instability in the polymer chain thus the cyclic stability is decreased. Meanwhile, the cycling stability of PANI is increased with the addition of rGO and N-rGO. The capacitance retention of PANI/N-rGO (93%) is higher than that of PANI/rGO (83%) after 1000 cycles. The higher capacitance retention of PANI/N-rGO nanocomposite revealed that the interaction of PANI nanostructures with graphene sheets is more effective in the presence of N atoms in the graphene sheets. The obtained results are shown in Fig. 4.9c, suggesting that the utilization of N-rGO sheets as a substrate for the growth of PANI nanostructures improved the structural stability of PANI and thus enhanced the electrochemical performance.

Table 4.6 Equivalent series resistance (R_s) and charge transfer resistance (R_{ct}) of rGO, N-rGO, PANI, PANI/rGO, PANI/N-rGO.

	rGO	N-rGO	PANI	PANI/N-rGO	PANI/rGO
R_s (Ω)	1.53	1.21	1.18	1.16	1.21
R_{ct} (Ω)	1.94	0.52	4.03	0.75	1.60

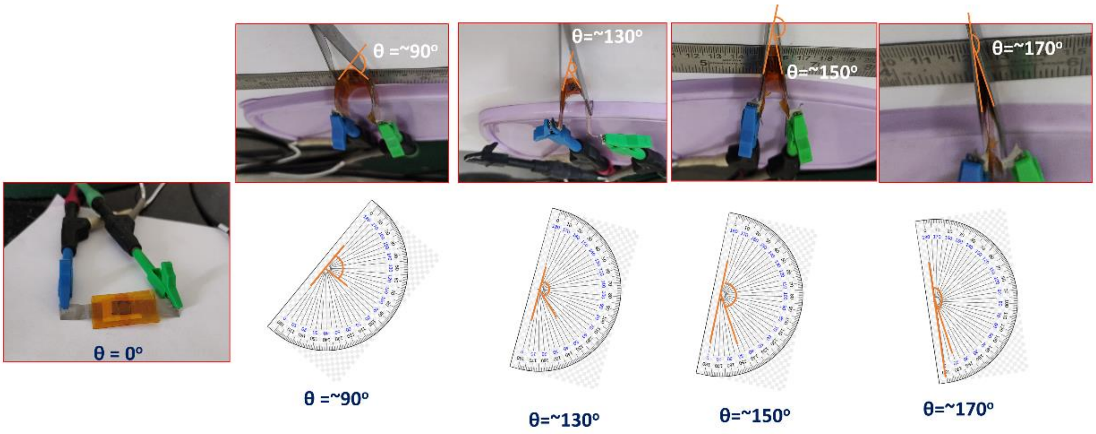

Figure 4.10 *Photographs of flexible SSC device assembled with PANI/N-rGO composite electrodes and the bending angle measurements.*

For the practical application of supercapacitors in flexible electronics, they should offer high flexibility with no loss in the electrochemical performance on bending the devices. We checked the flexibility of the supercapacitor device fabricated employing PANI/N-rGO flexible electrodes by carrying out the CV measurements by bending the devices at different bending angles. The photographs of the device upon bending are taken simultaneously while measuring CV curves at a scan rate of 50 mV/s are illustrated in Fig. 4.10 & Fig. 4.11a, respectively. The bending angle (θ) is measured by following Zhi's suggestion (Fig. 4.10) [61]. As seen in Fig. 4.11a, almost similar CV curves are obtained with the increasing bending angle indicating the good flexibility of the electrodes. The capacitance values are calculated from the CV curves, and the capacitance retention with the increased bending angles is plotted in Fig. 4.11b. It is noticed that only 3.5% of initial capacitance is lost after bending the device close to ~170^{o}, which is consistent with the flexibility tests reported elsewhere on PANI-based flexible supercapacitors [40,62–64]. These results suggest that the supercapacitor designed with PANI/N-rGO electrode material possesses considerably good flexibility and hence, has the potential to be used in flexible electronics.

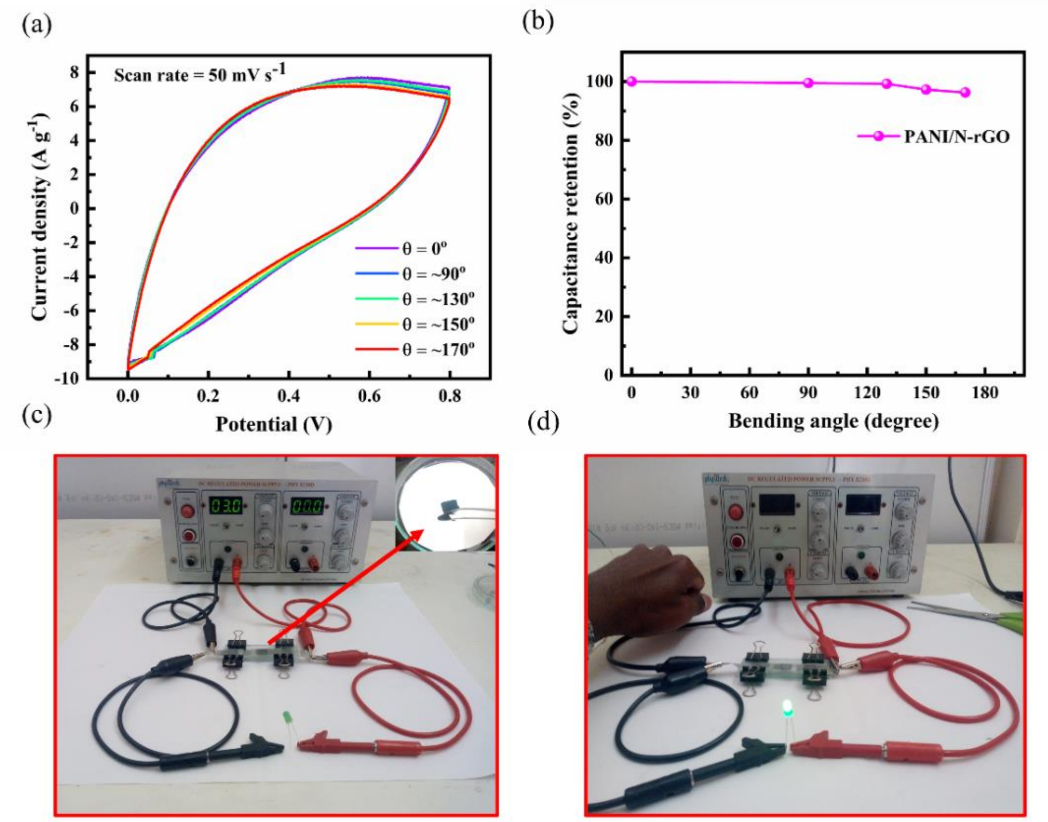

Figure 4.11 *(a) CV curves at respective bending angles measured with a scan rate of 50 mV/s, (b) Capacitance retention of supercapacitor device at different bending angles, and supercapacitor device (three cells) connected with regulated power supply: (c) before LED glow; and (d) after LED glow.*

Finally, to explore the supercapacitor performance of PANI/N-rGO composite further, an experiment is performed to drive an LED as a real-time application. Flexible film electrode of PANI/N-rGO composite are assembled into a prototype supercapacitor device as shown in Fig. 4.11c and the inset shows the flexible electrode of PANI/N-rGO composite. Three devices are connected in series and charged with a 3 V regulated power supply for 10 sec as shown in Fig. 4.11c. During discharge, an LED is connected in series with these devices, and with 10 sec of charging time the supercapacitor is found to drive the LED successfully with good intensity as shown in Fig. 4.11d. Therefore, the PANI/N-rGO nanocomposite electrode material could be a potential candidate for the development of flexible supercapacitor devices.

4.3 Conclusions

In summary, we reported a simple and robust approach for a readily scalable synthesis method for the preparation of PANI/N-rGO nanocomposites. N-rGO nanosheets are utilized as a platform to grow PANI nanostructures. Flexible electrodes are prepared to study the electrochemical properties of the composite material. In a symmetrical supercapacitor configuration, PANI/N-rGO exhibited enhanced electrochemical properties compared to PANI and PANI/rGO composite. A specific capacitance value of 322 F/g is obtained for PANI/N-rGO composite at a current density of 1 A/g. Further, PANI/N-rGO demonstrated high-rate capability and enhanced cycling stability (93% capacitance retention after 1000 cycles). The improved performance is attributed to the high surface area and long-range interconnected PANI nanostructures network in the composite material. Overall, the present work demonstrates a promising electrode material for flexible supercapacitor.

References

[1] F. Su, Z.S. Wu, A perspective on graphene for supercapacitors: Current status and future challenges, J. Energy Chem. 53 (2020) 354–357. https://doi.org/10.1016/j.jechem.2020.05.041.

[2] E.E. Miller, Y. Hua, F.H. Tezel, Materials for energy storage: Review of electrode materials and methods of increasing capacitance for supercapacitors, J. Energy Storage. 20 (2018) 30–40. https://doi.org/10.1016/j.est.2018.08.009.

[3] C.K. Chua, M. Pumera, Chemical reduction of graphene oxide: A synthetic chemistry viewpoint, Chem. Soc. Rev. 43 (2014) 291–312. https://doi.org/10.1039/c3cs60303b.

[4] R. Santhosh, S.R.S.S. Raman, S. Murali, V. Sandhya, S. Ghosh, N. Kumar, S. Punniyakoti, M. Karthik, P. Kollu, S. Kwan, A. Nirmala, S.M. Krishna, S. sai Ravuri, V. Sandhya, S. Ghosh, N.K. Sahu, S. Punniyakoti, M. Karthik, P. Kollu, S.K. Jeong, A.N. Grace, Heteroatom doped graphene based hybrid electrode materials for supercapacitor applications, Electrochim. Acta. 276 (2018) 284–292. https://doi.org/10.1016/j.electacta.2018.04.142.

[5] H. Liu, Y. Liu, D. Zhu, Chemical doping of graphene, J. Mater. Chem. 21 (2011)

3335–3345. https://doi.org/10.1039/c0jm02922j.

[6] D. Usachov, O. Vilkov, A. Grüneis, D. Haberer, A. Fedorov, V.K. Adamchuk, A.B. Preobrajenski, P. Dudin, A. Barinov, M. Oehzelt, C. Laubschat, D. V. Vyalikh, Nitrogen-doped graphene: Efficient growth, structure, and electronic properties, Nano Lett. 11 (2011) 5401–5407. https://doi.org/10.1021/nl2031037.

[7] A. Śliwak, B. Grzyb, N. Díez, G. Gryglewicz, Nitrogen-doped reduced graphene oxide as electrode material for high rate supercapacitors, Appl. Surf. Sci. 399 (2017) 265–271. https://doi.org/10.1016/j.apsusc.2016.12.060.

[8] H. Xu, L. Ma, Z. Jin, Nitrogen-doped graphene: Synthesis, characterizations and energy applications, J. Energy Chem. 27 (2018) 146–160. https://doi.org/10.1016/j.jechem.2017.12.006.

[9] L. Sun, L. Wang, C. Tian, T. Tan, Y. Xie, K. Shi, M. Li, H. Fu, Nitrogen-doped graphene with high nitrogen level via a one-step hydrothermal reaction of graphene oxide with urea for superior capacitive energy storage, RSC Adv. 2 (2012) 4498–4506. https://doi.org/10.1039/c2ra01367c.

[10] Z.Y. Sui, Y.N. Meng, P.W. Xiao, Z.Q. Zhao, Z.X. Wei, B.H. Han, Nitrogen-doped graphene aerogels as efficient supercapacitor electrodes and gas adsorbents, ACS Appl. Mater. Interfaces. 7 (2015) 1431–1438. https://doi.org/10.1021/am5042065.

[11] Z. Xing, Z. Ju, Y. Zhao, J. Wan, Y. Zhu, Y. Qiang, Y. Qian, One-pot hydrothermal synthesis of Nitrogen-doped graphene as high-performance anode materials for lithium ion batteries, Sci. Rep. 6 (2016) 1–10. https://doi.org/10.1038/srep26146.

[12] S. Dai, Z. Liu, B. Zhao, J. Zeng, H. Hu, Q. Zhang, D. Chen, C. Qu, D. Dang, M. Liu, A high-performance supercapacitor electrode based on N-doped porous graphene, J. Power Sources. 387 (2018) 43–48. https://doi.org/10.1016/j.jpowsour.2018.03.055.

[13] T. Wang, L. Wang, D. Wu, W. Xia, H. Zhao, D. Jia, Hydrothermal synthesis of nitrogen-doped graphene hydrogels using amino acids with different acidities as doping agents, J. Mater. Chem. A. 2 (2014) 8352–8361. https://doi.org/10.1039/c4ta00170b.

[14] T.K. Das, S. Banerjee, A. Kumar, A.K. Debnath, V. Sudarsan, Electrochemical performance of hydrothermally synthesized N-Doped reduced graphene oxide electrodes for supercapacitor application, Solid State Sci. 96 (2019) 105952. https://doi.org/10.1016/j.solidstatesciences.2019.105952.

[15] H. Wang, J. Lin, Z.X. Shen, Polyaniline (PANi) based electrode materials for energy storage and conversion, J. Sci. Adv. Mater. Devices. 1 (2016) 225–255. https://doi.org/10.1016/j.jsamd.2016.08.001.

[16] A. Eftekhari, L. Li, Y. Yang, Polyaniline supercapacitors, J. Power Sources. 347 (2017) 86–107. https://doi.org/10.1016/j.jpowsour.2017.02.054.

[17] F. Hekmat, S. Shahrokhian, Y. Mirzaei, Effect of Long-Chain Ionic Liquids on the Capacitive Performance of Carbon Nanotube-Sulfonated Polyaniline Hydrogels for Energy Storage Applications, J. Phys. Chem. C. 124 (2020) 9810–9821. https://doi.org/10.1021/acs.jpcc.0c02709.

[18] K. Gopalakrishnan, S. Sultan, A. Govindaraj, C.N.R. Rao, Supercapacitors based on composites of PANI with nanosheets of nitrogen-doped RGO, BC1.5N, MoS2 and WS2, Nano Energy. 12 (2015) 52–58.

https://doi.org/10.1016/j.nanoen.2014.12.005.

[19] Z. Liu, D. Li, Z. Li, Z. Liu, Z. Zhang, Nitrogen-doped 3D reduced graphene oxide/polyaniline composite as active material for supercapacitor electrodes, Appl. Surf. Sci. 422 (2017) 339–347. https://doi.org/10.1016/j.apsusc.2017.06.046.

[20] Z. Fan, Z. Cheng, J. Feng, Z. Xie, Y. Liu, Y. Wang, Ultrahigh volumetric performance of a free-standing compact N-doped holey graphene/PANI slice for supercapacitors, J. Mater. Chem. A. 5 (2017) 16689–16701. https://doi.org/10.1039/c7ta04384h.

[21] J. Zhu, L. Kong, X. Shen, Q. Chen, Z. Ji, J. Wang, K. Xu, G. Zhu, Three-dimensional N-doped graphene/polyaniline composite foam for high performance supercapacitors, Appl. Surf. Sci. 428 (2018) 348–355. https://doi.org/10.1016/j.apsusc.2017.09.148.

[22] J. Liu, P. Du, Q. Wang, D. Liu, P. Liu, Mild synthesis of holey N-doped reduced graphene oxide and its double-edged effects in polyaniline hybrids for supercapacitor application, Electrochim. Acta. 305 (2019) 175–186. https://doi.org/10.1016/j.electacta.2019.03.049.

[23] Y. Han, Y. Wu, M. Shen, X. Huang, J. Zhu, X. Zhang, Preparation and properties of polystyrene nanocomposites with graphite oxide and graphene as flame retardants, J. Mater. Sci. 48 (2013) 4214–4222. https://doi.org/10.1007/s10853-013-7234-8.

[24] K. Wang, L. Li, T. Zhang, Z. Liu, Nitrogen-doped graphene for supercapacitor with long-term electrochemical stability, Energy. 70 (2014) 612–617. https://doi.org/10.1016/j.energy.2014.04.034.

[25] X. Li, C. Zhang, S. Xin, Z. Yang, Y. Li, D. Zhang, P. Yao, Facile Synthesis of MoS2/Reduced Graphene Oxide@Polyaniline for High-Performance Supercapacitors, ACS Appl. Mater. Interfaces. 8 (2016) 21373–21380. https://doi.org/10.1021/acsami.6b06762.

[26] A. Raghavan, S. Sarkar, S. Ghosh, Dnevelopment of PANI based ternary nanocomposite with enhanced capacity retention for high performance supercapacitor application, Electrochim. Acta. 388 (2021) 138564. https://doi.org/10.1016/j.electacta.2021.138564.

[27] M. Shabani-Nooshabadi, F. Zahedi, Electrochemical reduced graphene oxide-polyaniline as effective nanocomposite film for high-performance supercapacitor applications, Electrochim. Acta. 245 (2017) 575–586. https://doi.org/10.1016/j.electacta.2017.05.152.

[28] P. Saini, V. Choudhary, B.P. Singh, R.B. Mathur, S.K. Dhawan, Polyaniline-MWCNT nanocomposites for microwave absorption and EMI shielding, Mater. Chem. Phys. 113 (2009) 919–926. https://doi.org/10.1016/j.matchemphys.2008.08.065.

[29] S. Palsaniya, H.B. Nemade, A.K. Dasmahapatra, Hierarchical Nylon-6/reduced graphene oxide/polyaniline nanocomposites with enhanced dielectric properties for energy storage applications, J. Energy Storage. 32 (2020) 101821. https://doi.org/10.1016/j.est.2020.101821.

[30] X. Li, Q. Zhong, X. Zhang, T. Li, J. Huang, In-situ polymerization of polyaniline on the surface of graphene oxide for high electrochemical capacitance, Thin Solid Films. 584 (2015) 348–352. https://doi.org/10.1016/j.tsf.2015.01.055.

[31] X. Liu, Y. Zheng, X. Wang, Controllable Preparation of Polyaniline-Graphene Nanocomposites using Functionalized Graphene for Supercapacitor Electrodes, Chem. - A Eur. J. 21 (2015) 10408–10415. https://doi.org/10.1002/chem.201501245.

[32] P. Asen, S. Shahrokhian, A.I. zad, Ternary nanostructures of Cr2O3/graphene oxide/conducting polymers for supercapacitor application, J. Electroanal. Chem. 823 (2018) 505–516. https://doi.org/10.1016/j.jelechem.2018.06.048.

[33] Y. Zou, Z. Zhang, W. Zhong, W. Yang, Hydrothermal direct synthesis of polyaniline, graphene/polyaniline and N-doped graphene/polyaniline hydrogels for high performance flexible supercapacitors, J. Mater. Chem. A. 6 (2018) 9245–9256. https://doi.org/10.1039/c8ta01366g.

[34] Z. Wang, L. Jiang, Y. Wei, C. Zong, In-situ polymerization to prepare reduced graphene oxide/polyaniline composites for high performance supercapacitors, J. Energy Storage. 32 (2020) 101742. https://doi.org/10.1016/j.est.2020.101742.

[35] K. Krishnamoorthy, M. Veerapandian, K. Yun, S.J. Kim, The chemical and structural analysis of graphene oxide with different degrees of oxidation, Carbon N. Y. 53 (2013) 38–49. https://doi.org/10.1016/j.carbon.2012.10.013.

[36] TUINSTRA F, KOENIG JL, Raman Spectrum of Graphite, J. Chem. Phys. 53 (1970) 1126–1130. https://doi.org/10.1063/1.1674108.

[37] N.R. Tanguy, M. Arjmand, N. Yan, Nanocomposite of Nitrogen-Doped Graphene/Polyaniline for Enhanced Ammonia Gas Detection, Adv. Mater. Interfaces. 6 (2019) 1–13. https://doi.org/10.1002/admi.201900552.

[38] P. Zhai, H. Jia, Z. Zheng, C.C. Lee, H. Su, T.C. Wei, S.P. Feng, Tuning Surface Wettability and Adhesivity of a Nitrogen-Doped Graphene Foam after Water Vapor Treatment for Efficient Oil Removal, Adv. Mater. Interfaces. 2 (2015) 1–8. https://doi.org/10.1002/admi.201500243.

[39] C. Zhang, L. Fu, N. Liu, M. Liu, Y. Wang, Z. Liu, Synthesis of nitrogen-doped graphene using embedded carbon and nitrogen sources, Adv. Mater. 23 (2011) 1020–1024. https://doi.org/10.1002/adma.201004110.

[40] F. Liu, S. Luo, D. Liu, W. Chen, Y. Huang, L. Dong, L. Wang, Facile processing of free-standing polyaniline/SWCNT film as an integrated electrode for flexible supercapacitor application, ACS Appl. Mater. Interfaces. 9 (2017) 33791–33801. https://doi.org/10.1021/acsami.7b08382.

[41] J.E. Pereira Da Silva, D.L.A. De Faria, S.I. Córdoba De Torresi, M.L.A. Temperini, Influence of thermal treatment on doped polyaniline studied by resonance Raman spectroscopy, Macromolecules. 33 (2000) 3077–3083. https://doi.org/10.1021/ma990801q.

[42] G.M. do Nascimento, C.H.B. Silva, C.M.S. Izumi, M.L.A. Temperini, The role of cross-linking structures to the formation of one-dimensional nano-organized polyaniline and their Raman fingerprint, Spectrochim. Acta - Part A Mol. Biomol. Spectrosc. 71 (2008) 869–875. https://doi.org/10.1016/j.saa.2008.02.009.

[43] S. Yang, Y. Lin, X. Song, P. Zhang, L. Gao, Covalently Coupled Ultrafine H-TiO2 Nanocrystals/Nitrogen-Doped Graphene Hybrid Materials for High-Performance Supercapacitor, ACS Appl. Mater. Interfaces. 7 (2015) 17884–17892. https://doi.org/10.1021/acsami.5b04368.

[44] D. Liu, Q. Li, S. Li, J. Hou, H. Zhao, A confinement strategy to prepare N-doped reduced graphene oxide foams with desired monolithic structures for supercapacitors, Nanoscale. 11 (2019) 4362–4368. https://doi.org/10.1039/c8nr09914f.

[45] J. Deng, T. Wang, J. Guo, P. Liu, Electrochemical capacity fading of polyaniline electrode in supercapacitor: An XPS analysis, Prog. Nat. Sci. Mater. Int. 27 (2017) 257–260. https://doi.org/10.1016/j.pnsc.2017.02.007.

[46] P. Zhang, X. Zhai, H. Huang, J. Zhou, X. Li, Y. He, Z. Guo, Capacitance fading mechanism and structural evolution of conductive polyaniline in electrochemical supercapacitor, J. Mater. Sci. Mater. Electron. 31 (2020) 14625–14634. https://doi.org/10.1007/s10854-020-04025-y.

[47] S. Lyu, Y. Chen, L. Zhang, S. Han, Y. Lu, Y. Chen, N. Yang, Z. Chen, S. Wang, Nanocellulose supported hierarchical structured polyaniline/nanocarbon nanocomposite electrode: Via layer-by-layer assembly for green flexible supercapacitors, RSC Adv. 9 (2019) 17824–17834. https://doi.org/10.1039/c9ra02449b.

[48] M. Ge, H. Hao, Q. Lv, J. Wu, W. Li, Hierarchical nanocomposite that coupled nitrogen-doped graphene with aligned PANI cores arrays for high-performance supercapacitor, Electrochim. Acta. 330 (2020) 135236. https://doi.org/10.1016/j.electacta.2019.135236.

[49] K. Xie, M. Zhang, Y. Yang, L. Zhao, W. Qi, Synthesis and Supercapacitor Performance of Polyaniline/Nitrogen-Doped Ordered Mesoporous Carbon Composites, Nanoscale Res. Lett. 13 (2018) 1–8. https://doi.org/10.1186/s11671-018-2577-3.

[50] Z.F. Li, H. Zhang, Q. Liu, L. Sun, L. Stanciu, J. Xie, Fabrication of high-surface-area graphene/polyaniline nanocomposites and their application in supercapacitors, ACS Appl. Mater. Interfaces. 5 (2013) 2685–2691. https://doi.org/10.1021/am4001634.

[51] Y. Hu, X. Tong, H. Zhuo, L. Zhong, X. Peng, Biomass-Based Porous N-Self-Doped Carbon Framework/Polyaniline Composite with Outstanding Supercapacitance, ACS Sustain. Chem. Eng. 5 (2017) 8663–8674. https://doi.org/10.1021/acssuschemeng.7b01380.

[52] S. Palsaniya, H.B. Nemade, A.K. Dasmahapatra, Hierarchical PANI-RGO-ZnO ternary nanocomposites for symmetric tandem supercapacitor, J. Phys. Chem. Solids. 154 (2021) 110081. https://doi.org/10.1016/j.jpcs.2021.110081.

[53] Z. Xu, Z. Zhang, H. Yin, S. Hou, H. Lin, J. Zhou, S. Zhuo, Investigation on the role of different conductive polymers in supercapacitors based on a zinc sulfide/reduced graphene oxide/conductive polymer ternary composite electrode, RSC Adv. 10 (2020) 3122–3129. https://doi.org/10.1039/c9ra07842h.

[54] S. He, X. Hu, S. Chen, H. Hu, M. Hanif, H. Hou, Needle-like polyaniline nanowires on graphite nanofibers: Hierarchical micro/nano-architecture for high performance supercapacitors, J. Mater. Chem. 22 (2012) 5114–5120. https://doi.org/10.1039/c2jm15668g.

[55] N. Macherla, K. Singh, M. Nerella, K. Kumari, R.G. Reddy Lekkala, Improved performance of flexible supercapacitor using naphthalene sulfonic acid-doped polyaniline/sulfur-doped reduced graphene oxide nanocomposites, Int. J. Energy

Res. 46 (2022) 6529–6542. https://doi.org/10.1002/er.7589.

[56] S.N. Karri, S.P. Ega, V. Perupogu, P. Srinivasan, Enhancing the Electrochemical Performance of Polyaniline Using Fly Ash of Coal Waste for Supercapacitor Application, ChemistrySelect. 6 (2021) 2576–2589. https://doi.org/10.1002/slct.202100513.

[57] Z. Çıplak, A. Yıldız, N. Yıldız, Green preparation of ternary reduced graphene oxide-au@polyaniline nanocomposite for supercapacitor application, J. Energy Storage. 32 (2020) 101846. https://doi.org/10.1016/j.est.2020.101846.

[58] X. Hong, Y. Lu, S. Li, X. Wang, X. Wang, J. Liang, Carbon foam@reduced graphene oxide scaffold grown with polyaniline nanofibers for high performance symmetric supercapacitor, Electrochim. Acta. 294 (2019) 376–382. https://doi.org/10.1016/j.electacta.2018.10.133.

[59] A. Moyseowicz, G. Gryglewicz, Hydrothermal-assisted synthesis of a porous polyaniline/reduced graphene oxide composite as a high-performance electrode material for supercapacitors, Compos. Part B Eng. 159 (2019) 4–12. https://doi.org/10.1016/j.compositesb.2018.09.069.

[60] K. Chi, Z. Zhang, J. Xi, Y. Huang, F. Xiao, S. Wang, Y. Liu, Freestanding graphene paper supported three-dimensional porous graphene-polyaniline nanocomposite synthesized by inkjet printing and in flexible all-solid-state supercapacitor, ACS Appl. Mater. Interfaces. 6 (2014) 16312–16319. https://doi.org/10.1021/am504539k.

[61] H. Li, Z. Tang, Z. Liu, C. Zhi, Evaluating Flexibility and Wearability of Flexible Energy Storage Devices, Joule. 3 (2019) 613–619. https://doi.org/10.1016/j.joule.2019.01.013.

[62] F. Hekmat, S. Shahrokhian, N. Taghavinia, Ultralight Flexible Asymmetric Supercapacitors Based on Manganese Dioxide-Polyaniline Nanocomposite and Reduced Graphene Oxide Electrodes Directly Deposited on Foldable Cellulose Papers, J. Phys. Chem. C. 122 (2018) 27156–27168. https://doi.org/10.1021/acs.jpcc.8b07464.

[63] J. Li, S. Qiu, B. Liu, H. Chen, D. Xiao, H. Li, Strong interaction between polyaniline and carbon fibers for flexible supercapacitor electrode materials, J. Power Sources. 483 (2021) 229219. https://doi.org/10.1016/j.jpowsour.2020.229219.

[64] L. Hou, X. Zhi, W. Zhang, H. Zhou, Boosting the electrochemical properties of polyaniline by one-step co-doped electrodeposition for high performance flexible supercapacitor applications, J. Electroanal. Chem. 863 (2020) 114064. https://doi.org/10.1016/j.jelechem.2020.114064.

FLEXIBLE SUPERCAPACITOR USING NSA DOPED POLYANILINE/S-rGO COMPOSITES

5.1 Introduction

Conducting polymers (CPs), transition metal oxides (TMOs), and transition metal chalcogenides (TMCs) fall in the class of pseudocapacitor electrode materials and offer high specific capacitance thereby increasing energy density [1]. In Pseudocapacitors, charge storage is happened based on the reversible fast-redox reactions which occurred at the electrode/electrolyte interface and the near surface of electrode material. In the context to design a flexible SC, many research groups are motivated to develop new advancements in CPs since their notable features like excellent conductivity and flexibility to fabricate flexible SCs [2]. Among the different types of CPs, Polyaniline (PANI) has attained an immense research interest owing to its impressive characteristic features including easy synthesis, flexible structure, tuneable electrical conductivity, non-toxic and multiple redox chemistries [3,4]. The nature of dopant and concentration has a significant impact on the morphology and electrical conductivity of PANI [5,6]. A wide variety of synthesis approaches, such as chemical polymerization, electrochemical polymerization, interfacial polymerization, seeding polymerization, hard template, and soft template methods were explored to obtain different micro and nanostructured forms of PANI [7–11]. Among them, the soft template method is considered to be a well-suited synthesis method to synthesize PANI with controlled morphology and excellent electrochemical properties. Several different types of organic sulfonic acids are used as surfactant-based soft templates as well as dopants to grow PANI nanostructures for improved electrochemical properties [12–14]. In this method, strong wander wall forces, hydrogen bonding, and other driving forces acted on the supermolecules to self-assemble themselves in the desired morphology [14,15]. Yield is relatively high as compared to electrochemical and interfacial polymerization, so bulk synthesis is also possible with this method. On the other hand, PANI suffers from some drawbacks when it is used as electrode material for supercapacitors, such as short cycle life and lower rate capability due to the continuous volume changes that occur in the polymer chain during the long charging-discharging process. Therefore, one of the key approaches is the incorporation of carbon materials, they can restrict the structural deformation of PANI and also provide additional capacitance based on their electrical double layer charge (EDLC) storage behaviour. Reduced graphene oxide (rGO) considered being a potential candidate to composite with PANI to improve structural stability and its electrochemical performance by providing additional EDL capacitance [16]. The two-dimensional layered structure of rGO act as a stable platform to grow one dimensional PANI nanostructures. In addition, rGO can also act as a counterion of PANI, which enhance chemical stability and increase electrical conductivity [17]. Moreover, heteroatom doping into graphene network is considered to further enhance the properties of rGO by tuning local charge density which would lead to an increase in the double-layer capacitance. In addition, doping creates the trap centres in graphene lattice to store charge carriers which eventually leads to an increase in the storage capacity [18]. For instance, Hao *et al.* have reported a specific capacitance of 241 and 189 F/g at 0.5 A/g in 1 M H_2SO_4 and 6 M KOH electrolytes, respectively in symmetrical supercapacitor assembly using sandwich-like polyaniline/B-doped graphene material [19]. Fan *et al.* synthesized sulfonated graphene/polyaniline nanocomposite paper and observed a maximum specific capacitance of 478 F/g at 0.5 A/g in three-electrode configurations [20]. Recently, Du *et al.* have prepared N, S-co-doped graphene/polyaniline composite hydrogel. The resultant composite delivered a maximum specific capacitance of 236.5 F/g at 0.5 A/g based on a three-electrode configuration [21]. Although the combination of heteroatom doped graphene with PANI is proved to be a promising approach to enhance the performance of electrode material, in most of the above referred reports, the synthesis of PANI nanostructures is carried out by applying conventional route of *in-situ* chemical oxidation of aniline in acidic media, which offer more tendency to agglomerate PANI nanostructures. The agglomeration of PANI nanostructures restricts the diffusion of electrolyte ions thus resulting in lower performance. Hence, a suitable combination of heteroatom doped graphene and a better synthesis approach needs to be explored to improve the morphology and the overall electrochemical activity of the composite material. Moreover, to the best of our knowledge, only very few studies are explored the symmetrical supercapacitor studies based on the free-standing electrodes using SPANI/S-rGO composites.

In the present study, we followed a facile method to grow well-aligned PANI nanostructures on S-doped reduced graphene oxide nanosheets to provide high electroactive surface area for the electrolyte ions and rapid charge transfer with a short diffusion length. The effect of different S-rGO content on the structural, morphology and electrochemical performance of SPANI/S-rGO composites is evaluated. The SPANI/S-rGO10 (10 wt.% of S-rGO) composite electrode delivered a high specific capacitance of 347.5 F/g at a current density of 1 A/g in symmetrical supercapacitor assembly. Further, the SPANI/S-rGO10 composite electrode shown impressive cycling stability of 89% after 2500 cycles at a current density of 2 A/g. The enhanced performance is attributed to the optimum loading of S-rGO in designing binary composite, well-aligned growth of SPANI nanostructures on S-rGO sheets, and synergistic effect of both S-rGO and SPANI. The facile synthesized SPANI/S-rGO composite electrode material with the offer mentioned features is considered to be a promising material for the fabrication of supercapacitors.

5.2 Results and Discussion

XPS studies were conducted to identify the surface elemental composition and doping level of sulfur atoms in the graphene framework. XPS survey spectra of GO and S-rGO are displayed in Fig. 5.1a. The survey spectra of GO comprise the C 1s and O 1s peaks, whereas S-rGO contains a peak that corresponds to S 2p in addition to C 1s and O 1s peaks. The survey spectra of S-rGO confirm the successful doping of sulfur spaces in graphene networks. In addition, the XPS analysis revealed that the atomic ratios of C and O (C/O) are found to be increased from 2.93 (GO) to 14.49 for S-rGO indicating a higher degree of reduction in S-rGO. The elemental composition of GO and S-rGO is given in Table 5.1.

Table 5.1 Elemental composition of GO and S-rGO from XPS survey spectra.

Material	C (at. %)	S (at. %)	O (at. %)	C/O ratio
GO	74.56	-	25.44	2.93
S-rGO	90.89	2.85	6.27	14.49

Further, the high-resolution C 1s spectrum of GO is deconvoluted into four peaks, which are centered at ~284.4 eV, ~285.9 eV, ~287.5 eV, and 289.7 eV are assigned to the C=C/C-C, C-O, C=O, and O-C=O, respectively, indicating the higher oxidation level of GO (Fig. 5.1b) [22]. Whereas the C 1s spectrum of S-rGO is fitted into four peaks at ~284.5 eV, ~286.0, ~287.9 eV, and ~290 eV corresponding to C=C/C-C, C-S/C-O, C=O, and O-C=O bonds, respectively (Fig. 5.1c). It was noticed that the peaks associated with the oxygen functional groups are reduced owing to the reduction of GO during hydrothermal treatment. In addition, the peak centered at 286.0 eV is found to broaden which is an indication of the presence of C-S bonding configuration in the S-rGO sample. As we observed from the deconvolution spectra of S 2p of S-rGO, the peaks centred at 163.7 eV and 165.4 eV reflected the covalent bonding configuration of C-S-C with spin-orbit coupling (Fig. 5.1d). The other peak at 168.1 eV is owing to the formation oxidation state of sulphur (C-SO_x-C) in the S-rGO sample. From the results obtained from the XPS spectra, it is concluded that the successful reduction of GO and doping of sulfur atoms into graphene lattice for the S-rGO sample. The presence of higher atomic size S atoms creates defective sites due to the higher bond length of C-S than C-C. These defective sites act as redox-active surface areas and contribute to additional pseudocapacitance [23].

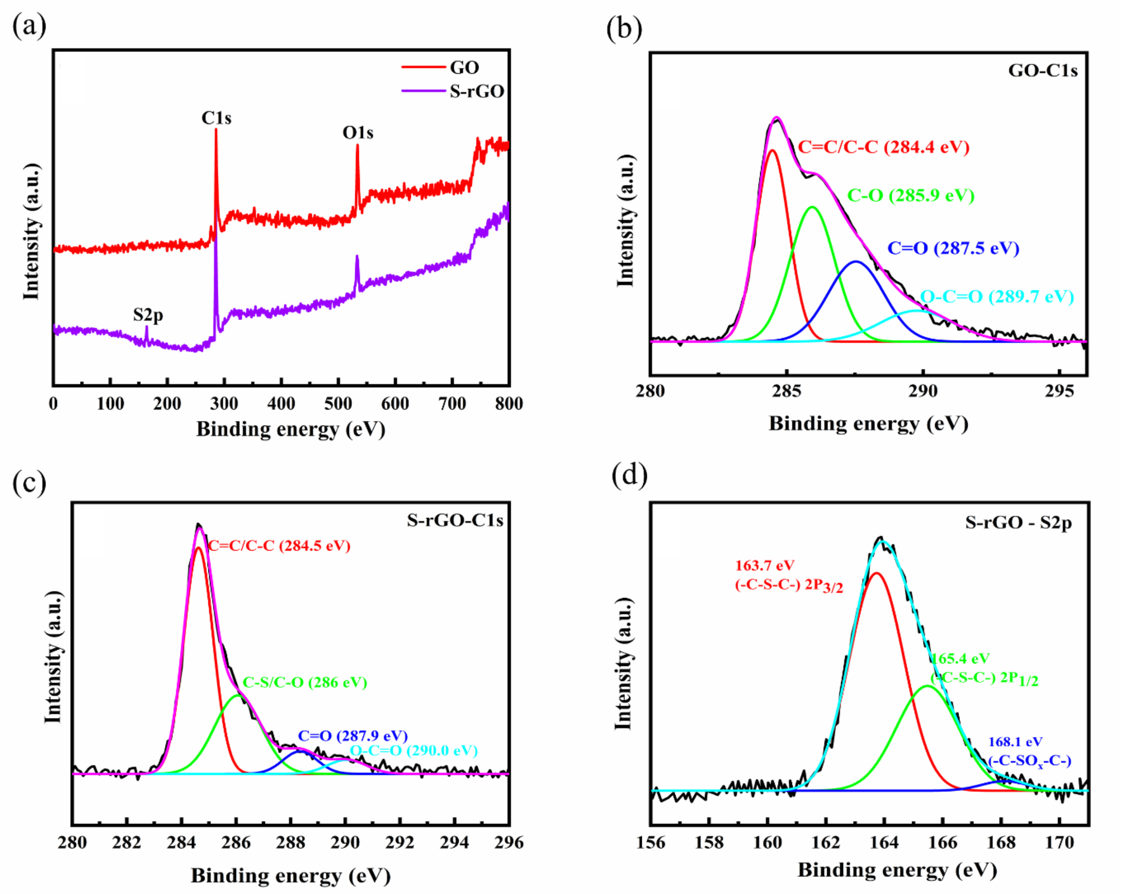

Figure 5.1 *(a) XPS survey spectra of GO and S-rGO (b) Deconvolution C 1s Spectra of GO, Deconvolution (c) C 1s Spectra, and (d) S 2p spectra of S-rGO.*

Figure 5.2 illustrates the Raman spectra of GO and S-rGO. Raman spectrum of GO, S-rGO exhibited a well-defined two vibrational bands related to D band and G bands, which are consistent with the reported literature. For GO, the peaks centred at ~1350 cm^{-1} and 1594 cm^{-1} are referred to as D and G bands, respectively [24]. The G band is related to the sp^2 hybridized carbon atoms it is observed in the wavenumber range of 1570 -1580 cm^{-1} for graphite but the observed G band for GO is shifted towards the higher wavenumber side for GO (blue shift) indicates the higher degree of oxidation and the formation of sp^3 carbon atoms in graphite lattice. In comparison with GO, the G band is red-shifted in the case of S-rGO and it is located at 1585 cm^{-1}. The shift in the G band could be associated with the removal of oxygen moieties during the reduction process and the reconstruction of sp^2 hybridized domains and the graphitic phase. Further, the intensity ratio of D to G band (I_D/I_G) is interlinked with the disorder and structural defects in the graphene lattice. The I_D/I_G ratio of GO and S-rGO are found to be 0.93 and 1.09, respectively. The higher value of I_D/I_G ratio for S-rGO elucidates the higher degree of disorder in the graphene network due to the insertion of bigger sized sulphur atoms into graphene lattice by disrupting the sp^2 bonds of carbon atoms. The results obtained from the Raman spectra confirm the doping of sulfur atoms into graphene layers and introduced more defects in the graphene framework. The defective structure of S-rGO can enhance the specific surface area and improves electrochemical performance.

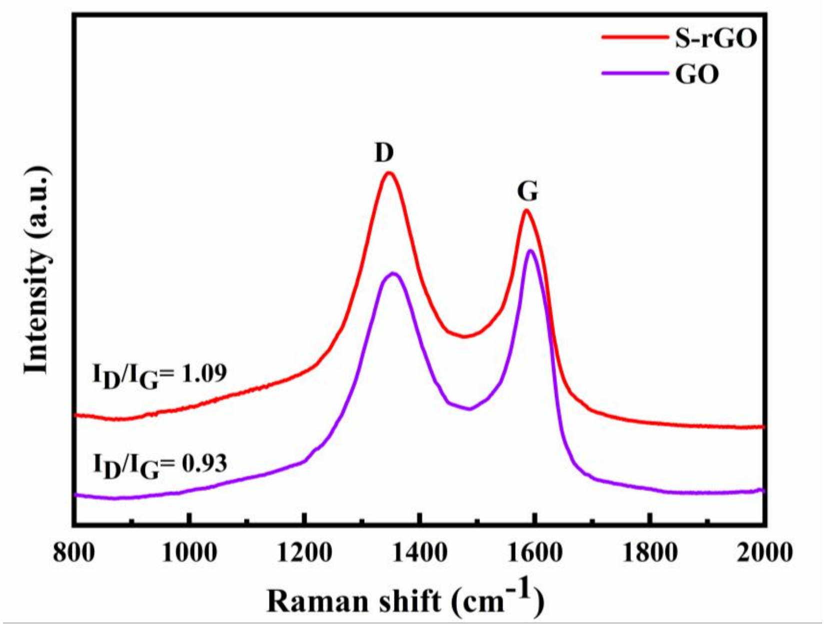

Figure 5.2 *Raman spectra of GO and S-rGO.*

XRD patterns of S-rGO, SPANI, SPANI/S-rGO composites are shown in Fig. 5.3. S-rGO possessed a broad diffraction peak ~25° corresponding to the (002) reflection indicating the reduction of GO and restoration of graphene structure in S-rGO (Fig. 5.3a). SPANI exhibited less intensive diffraction peaks at 19° are 25° confirms the conductive emeraldine salt form of SPANI and these peaks are related to the periodicity perpendicular and parallel to the polymer chain, respectively [15,25,26]. For SPANI/S-rGO composites, similar XRD patterns are observed. From the XRD plots of SPANI/S-rGO composites, it is noticed that the intensity of diffraction peak at 25° is increased with increasing concentration of S-rGO, indicating the successful incorporation of S-rGO nanosheets in the composites (Fig. 5.3a). An additional small intensity peak is also observed at 2θ of 43° in SPANI/S-rGO composites, which is related to the graphitic phase of S-rGO.

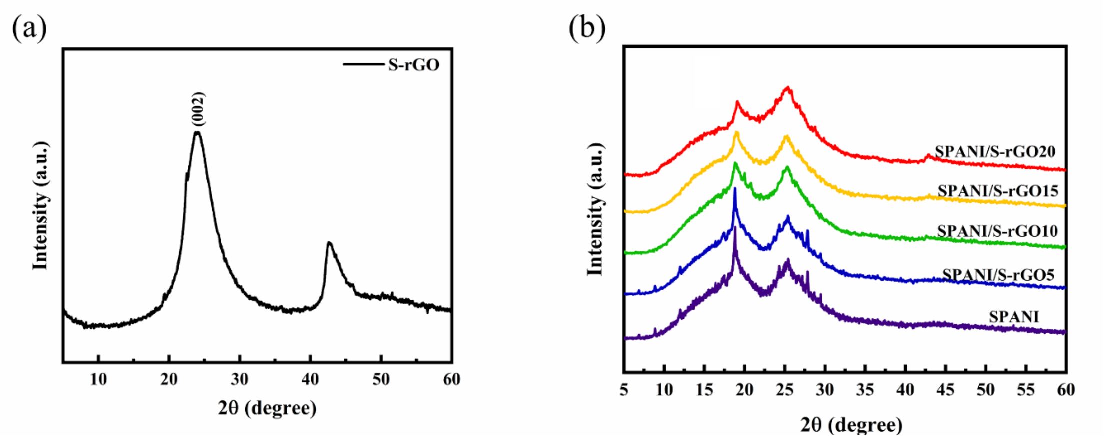

Figure 5.3 *XRD patterns of (a) S-rGO, and SPANI and SPANI/S-rGO composites.*

The surface morphology images of S-rGO, SPANI, and SPANI/S-rGO composites are shown in Fig. 5.4. From Fig. 5.4a, agglomerated crumbled layers with the defective structure are observed for S-rGO. These defective structures are created due to the doping of higher atomic size S atoms. Further, it is noticed that the graphene layers are stacked together due to the removal of oxygen functional groups during hydrothermal reduction. For SPANI, vertically aligned nanorod like morphology is observed (Fig. 5.4b). During the polymerization, NSA act as a soft template as well as a dopant for the SPANI nanostructures. For SPANI/S-rGO5 composite, with the incorporation of S-rGO, PANI maintained its nanorod like morphology over the surface of graphene layers (Fig. 5.4c). In SPANI/S-rGO10 composite, growth of SPANI nanorods structure is more prominent and which are vertically aligned in all directions with the support of S-rGO sheets. (Fig. 5.4d). The well-aligned nanostructures of SPANI/S-rGO10 could be results in an increased contact area for the electrolyte ions to diffuse and enhance the charge transfer property of the material. The better morphology of SPANI/S-rGO10 could be realised by the strong interaction of S-rGO and SPANI chains. Further, increase in wt.% of S-rGO for SPANI/S-rGO15 and SPANI/S-rGO20 leads to the stacking of S-rGO sheets which covered the SPANI nanostructures (Fig. 5.4e&f). The overlapping of S-rGO results in a decrease in the surface area accessible to the electrolyte ions. The overlapped structure of SPANI/S-rGO15 and SPANI/S-rGO20 restrict charge transfer kinetics and results in lower specific capacitance.

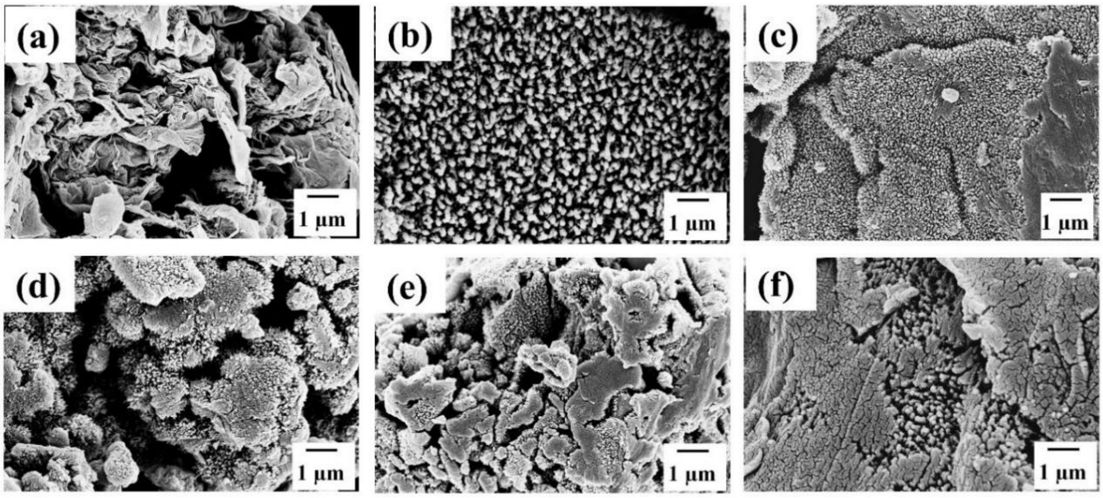

Figure 5.4 *FESEM images of (a) S-rGO, (b) SPANI, and (c) SPANI/S-rGO5, (d) SPANI/S-rGO10, (e) SPANI/S-rGO15, and (f) SPANI/S-rGO20 composites.*

Fourier Transform Infrared Spectroscopy (FTIR) studies were conducted to evaluate the presence of various functional groups in the synthesized material. Figure 5.5a shows the FTIR spectra of SPANI and SPANI/S-rGO composites. SPANI exhibited various characteristic vibrational peaks. The main vibrational peaks at 1565 cm^{-1} and 1490 cm^{-1} originated from the C=C stretching of quinonoid ring and benzenoid ring, respectively [27]. The other peaks at 3400, 1294, 1237, 1141, and 814 cm^{-1} are related to the -NH- stretching, –C-N^{+} protonic stretching, –C-N stretching of amine groups, and -B-NH+-Q stretching, –C-H bending vibration in benzene ring [27,28]. The peaks at 1029, and 671 cm^{-1} arising from the -SO$_3^-$ symmetric stretching confirm the NSA doping [29]. All the vibrational peaks which are related to SPANI are also observed in SPANI/S-rGO composites but the intensity of all peaks is reduced with increasing concentration of S-rGO. The peak intensity ratio of the quinoid ring (I_Q) and benzenoid ring (I_B) is useful to estimate the degree of oxidation and the interaction between SPANI and S-rGO layers. Figure 5.5b gives a clear view of quinonoid ring (I_Q) and benzenoid ring (I_B) peaks. We found that the intensity ratio (I_Q/I_B) is increased with the increasing wt.% of S-rGO indicating the presence of high number of quinoid rings in the composite. The increase in quinoid rings in SPANI/S-rGO composites suggests a strong interaction between S-rGO layers and conjugated PANI chains. This can be supported by the existence of a weak charge transfer complex formed between SPANI and S-rGO layers during polymerization where aniline loses an electron to the S-rGO layers [28]. Due to the formation of charge-transfer complex in SPANI/S-rGO composite, S-rGO can also act as a dopant to the SPANI and which leads increase in electrical conductivity, and hence, we observe an improved electrochemical performance.

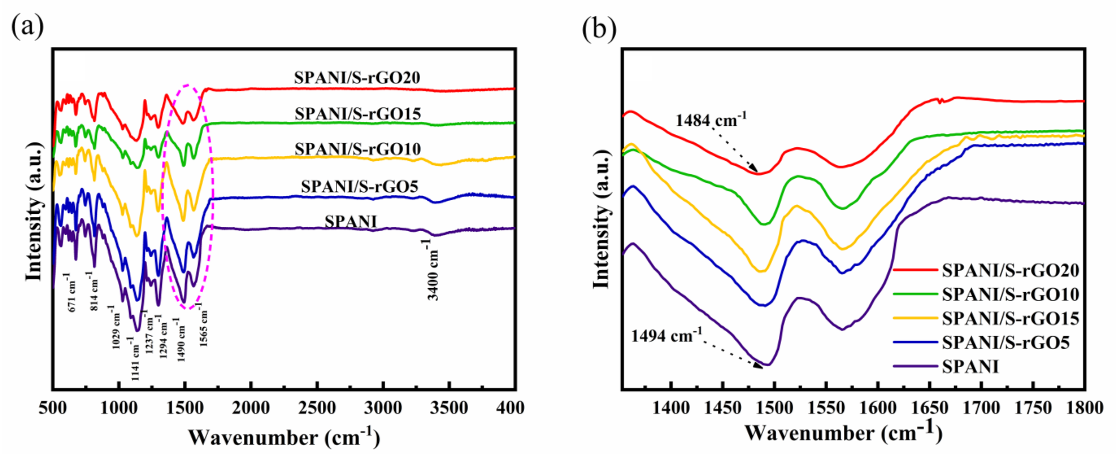

Figure 5.5 *(a) FTIR spectrum of SPANI and SPANI/S-rGO composites, (b) Zoomed view of FTIR spectra at quinoid and benzenoid ring region of SPANI and SPANI/S-rGO composites.*

The electrical conductivity measurements for SPANI, SPANI/S-rGO composites are obtained from a four-probe method. powder samples are pressed into pellets of a diameter of 1.3 cm and thickness ~0.05 – 0.06 cm using a hydraulic press. Measurements are repeated 5 times for each sample and the average values are given in Table 5.2. Here, we noticed that the electrical conductivity for all the SPANI/S-rGO composite samples is relatively higher compared to the electrical conductivity of pristine pure PANI. This is owing to the strong π-π stacking interaction and formation of charge transfer complex between the SPANI nanostructures and S-rGO layers and it is consistent with the FTIR studies.

Table 5.2 Electrical conductivity of S-rGO, SPANI, SPANI/S-rGO composites.

Samples	SPANI	SPANI/S-rGO5	SPANI/S-rGO10	SPANI/S-rGO15	SPANI/S-rGO20
Conductivity (S/cm)	0.06	0.95	2.63	2.24	2.22

The electrochemical properties of the electrode materials are studied using CV, GCD and EIS methods. Figure 5.6a shows the CV curves of S-rGO, SPANI, and SPANI/S-rGO composites at a 10 mV/s scan rate. It is observed that a nearly rectangular shape CV curve with a small hump at the low potential side for S-rGO, shows the contribution of pseudocapacitance from the S and residual oxygen species. Whereas, SPANI exhibiting typical pseudocapacitive behaviour originated from the SPANI nanostructures [26]. From Fig. 5.6a, all the SPANI/S-rGO composites show the combined features of EDLC and pseudocapacitive nature. However, it is noticed that the increasing concentration of S-rGO in composites, shows the increased area surrounded by the CV curve. It is known that the specific capacitance of a material is directly proportional to the area covered by the CV curve. The integrated area covered by the CV curve is maximum for the SPANI/S-rGO10 composite and with further increase in the S-rGO concentration, the area is decreased. Therefore, the SPANI/S-rGO10 composite possessed high specific capacitance. As we see from the FESEM results, increasing the concentration of S-rGO in composites causes the overlapping of SPANI nanostructures with S-rGO sheets, which restricts the accessible area of SPANI for the electrolyte ions. CV curves obtained at different scan rates from 10 mV/s to 100 mV/s are shown in Fig. 5.6(b-e) for SPANI/S-rGO composites. The CV curves are altered with increased scan rate for the SPANI indicating poor structural stability of SPANI at higher scan rates (Fig. 5.6b). However, within the incorporation of S-rGO in composites, the structural stability of the electrode materials is improved and it is seen in Fig. 5.6d. The SPANI/S-rGO10 composite material possesses the combined features of both EDLC and Pseudocapacitive behaviour. It is worth noting that the CV curves of SPANI/S-rGO10 composite are approximately remaining same with increased scan rate and are nearly rectangular at a scan rate of 75 mV/s and 100 mV/s. At higher scan rates, electrolyte ions do not have enough time to diffuse through the electrode material, as a result, the specific capacitance is decreased with increased scan rate. The specific capacitance values with increased scan rates for all the materials are calculated using the CV curves shown in Fig. 5.6(b-e). The specific capacitance vs scan rate curves are depicted in Fig. 5.6f, it is noticed that the SPANI/S-rGO10 composite possessed higher specific capacitance at higher scan rates, indicating the high-rate capability of the composite material.

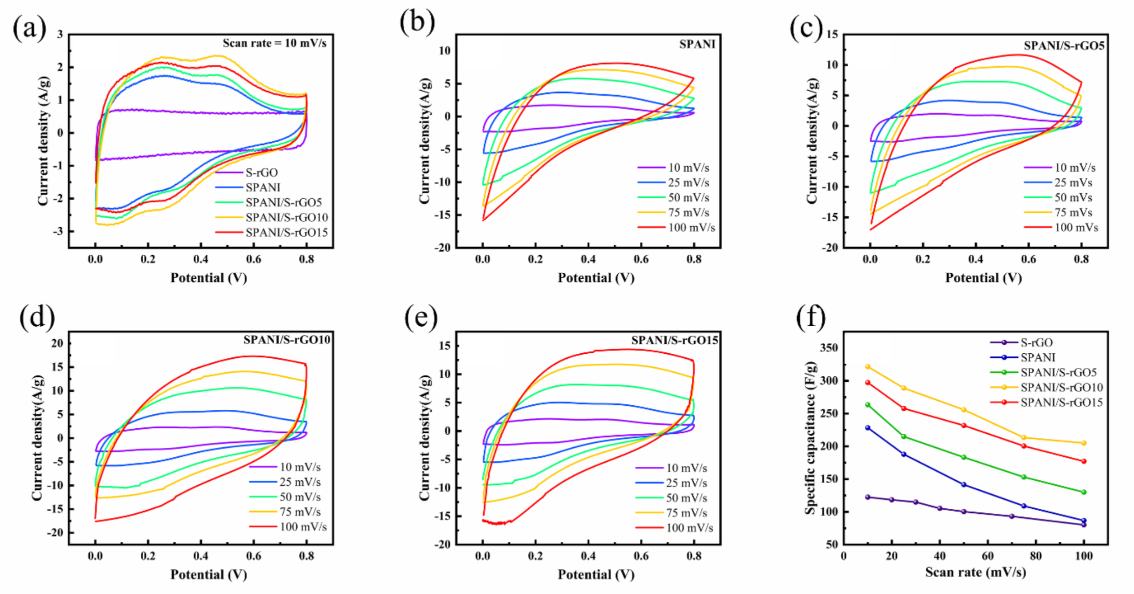

Figure 5.6 *(a) CV curves of S-rGO, SPANI, SPANI/S-rGO composites at a scan rate of 10 mV/s, CV curves of at scan rate from 10 mV/s to 100 mV/s: (b) SPANI, (c) SPANI/S-rGO5, (d) SPANI/S-rGO10, (e) SPANI/S-rGO15, and (f) scan rate vs specific capacitance curves of S-rGO, SPANI, and SPANI/S-rGO composites.*

The GCD curves of S-rGO, SPANI, and SPANI/S-rGO composite electrode materials are obtained at a constant current density of 1 A/g and the plots are shown in Fig. 5.7a. All the samples displayed a deviation in GCD curves from the triangular shape indicating their pseudocapacitive behaviour. The specific capacitance values of all the materials are calculated using Eqn. 2.3. The specific capacitance of 132.5 F/g for S-rGO, 240 F/g for SPANI, 287.5 F/g for SPANI/S-rGO5, 347.5 F/g for SPANI/S-rGO10, and 330 F/g for SPANI/S-rGO15 observed. SPANI/S-rGO10 possessed a high specific capacitance value suggesting the 10 wt.% S-rGO is the optimal quantity for composite material. Further, an increase in S-rGO wt.% shows the decrease in specific capacitance due to the overlapping of S-rGO layers. Further, the SPANI/S-rGO10 also exhibited better rate capability at high current density compared to pristine SPANI, and other SPANI/S-rGO composites, as shown in Fig. 5.7(b-e). The change in specific capacitance of all the samples at different current densities is shown in Fig. 5.7d. The specific capacitance values of S-rGO, SPANI, SPANI/S-rGO5, and SPANI/S-rGO15 are calculated using GCD curves (Fig. 5.7(b-e)). From Fig. 5.7f, it is observed that the SPANI/S-rGO10 composite is able to retain 68% of its initial capacitance at a current density of 5 A/g whereas pure SPANI retained only 57% of its initial capacitance. The improved performance of SPANI/S-rGO10 composite could be attributed to uniform growth of SPANI nanostructures on S-rGO sheets with better morphology (Fig. 5.4d), availability of electroactive surface area for electrolyte ions to perform fast redox reaction and formation of a charge-transfer complex between polymer chain and S-rGO as we seen in FTIR spectra (Fig. 5.5). The obtained values of specific capacitance and the rate capabilities are comparable with the results obtained from the similar electrode materials shown in Table 5.3.

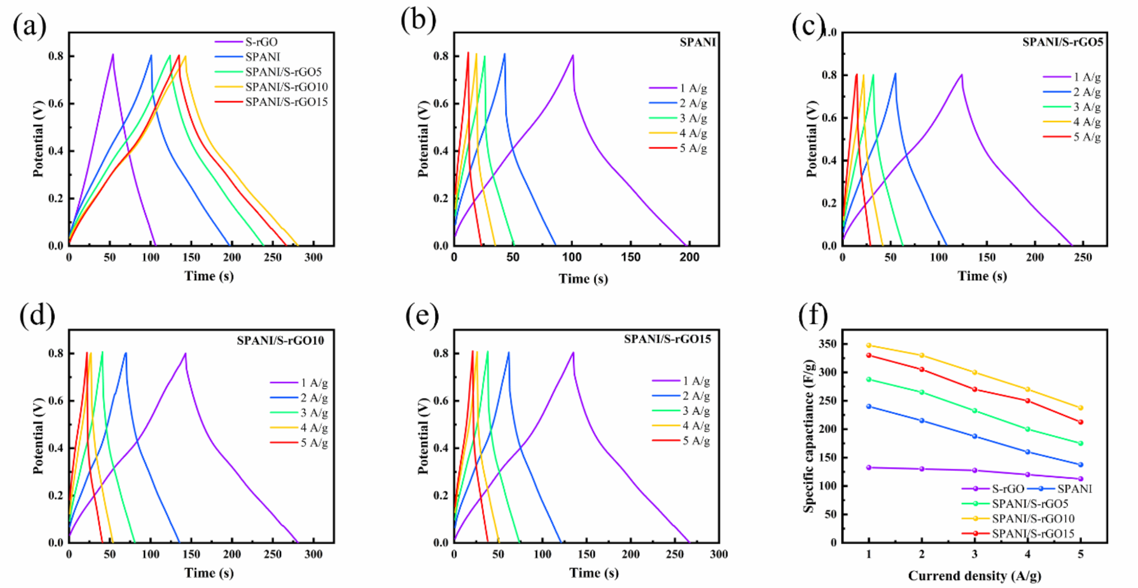

Figure 5.7 *(a) GCD curves of S-rGO, SPANI, and SPANI/S-rGO composites at a current density of 1 A/g, GCD curves at current densities from 1 to 5 A/g: (b) SPANI, (c) SPANI/S-rGO5, (d) SPANI/S-rGO10, (e) SPANI/S-rGO15 and (f) current density vs specific capacitance curves of S-rGO, SPANI, and SPANI/S-rGO composites.*

From the GCD curves, we have calculated the specific energy and specific power values of the device assembled by SPANI/S-rGO10 composite. The specific energy and specific power are the two important parameters to further evaluate the performance of a supercapacitor device. The obtained values of specific energy and specific power at different current densities are displayed in the Ragone plot (Fig. 5.8a). The SPANI/S-rGO10 composite based device has a specific energy of 12.87 Wh/Kg and the corresponding specific power of 333.06 W/Kg at a current density of 1 A/g which is comparable with reported literature based on PANI carbon composite materials [7,18,30–32].

Table 5.3 Comparison of the specific capacitance of similar electrode materials.

Material	Electrolyte/ Electrode system	Specific capacitance	Cyclic stability	Rate capability	Ref.
PANI/GO	1 M H_2SO_4/2 ele*	447 F/g at 0.5 A/g	95.7% (5000 cycles)	46% (0.5 – 20 A/g)	[6]
$Ni(OH)_2$@PANI	3 M KOH/2 ele*	120 F/g at 1 A/g	86% (5000 cycles)	77.5% (1-5 A/g)	[14]
3D rGO/PANI	1 M H_2SO_4/2 ele*	438.8 F/g at 0.5A/g	76.5% (2000 cycles)	91.4% (0.5–4 A/g)	[16]
S, N-GQD/PANI	1 M H_2SO_4/2 ele*	124.2 F/g at 1 A/g	90% (1000 cycles)	-	[18]
PANI/FrGO	PVA/H_2SO_4/2 ele$^\#$	324.4 F/g at 1 A/g	83.3% (1000 cycles)	--	[30]
N-carbon/PANI	1 M H_2SO_4/2 ele*	285 F/g at 0.5 A/g	80% (5000 Cycles)	73.7% (1-10 A/g)	[31]

PANI-GNRs	1 M H_2SO_4/2 ele*	340 F/g at 0.25 A/g	90% (4200 cycles)	75% (0.25 – 4 A/g)	[32]
NG/PANI	1 M H_2SO_4/2 ele$^{\$}$	93.2 F/g at 1 A/g	79% (5000 cycles)	64% (1-10 A/g)	[33]
HCM/PANI	1 M H_2SO_4/2 ele$^{\#}$	76 F/g at 0.2 A/g	90.6% (1000 cycles)	64% (0.2 – 10 A/g)	[34]
N-GNS-PdNP-PANI	1 M H_2SO_4/2 ele$^{\$}$	230 F/g at 0.1 A/g	96% (3000 cycles)	88% (3.8 -15 A/g)	[35]
ZnS/RGO/PANI	6 M KOH/2 ele$^{\#}$	722 F/g at 1 A/g	76.1% (1000 cycles)	50.0% (0.3-20 A/g)	[36]
PANI/GECF	1 M H_2SO_4/2 ele$^{\#}$	976.5 F/g at 0.1 A/g	89.2% (1000 cycles)	51.2% (0.4 -50 A/g)	[37]
PANI-FA	1 M H_2SO_4/2 ele$^{\#}$	208 F/g at 2.5 A/g	66% (5000 cycles)	-	[38]
rGO-Au@PANI	1 M H_2SO_4/2 ele$^{\#}$	212.8 F/g at 1 A/g	86.9% (5000 cycles)	89.5% (0.5-5 A/g)	[39]
CF@RGO/PANI	1 M H_2SO_4/2 ele*	868.5 F/g at 1 A/g	94.1% (2000 cycles)	95% (1-5 A/g)	[40]
PANI/rGO	1 M H_2SO_4/2 ele$^{\#}$	220 F/g at 0.2 A/g	75% (3000 cycles)	47% (0.2-20 A/g)	[41]
CC–PANI–CBf	1 M H_2SO_4/2 ele$^{\$}$	1039 F/g at 0.3 A/g	>80% (1000 cycles)	7.4% (0.3 – 13.7 A/g)	[42]
PF-rGO/PANI	1 M H_2SO_4/2 ele*	489 F/g at 0.5 A/g	89% (2000 cycles)	--	[43]
PANI-IPDI-rGO	PVA/H_2SO_4/2 ele$^{\$}$	485 F/g at 1 A/g	95% (2000 cycles)	73.2% (1-15 A/g)	[44]
SPANI/S-rGO10	1 M H_2SO_4/2 ele$^{\#}$	347.5 F/g at 1 A/g	89% (2500 cycles)	68% (1-5 A/g)	Present work

$^{\#}$ Capacitance calculated using single electrode, * based two electrodes, $^{\$}$Not mentioned

To further understand the superiority of the composite materials, electrochemical impedance spectroscopy studies are obtained for all the samples. Figure 5.8b shows the Nyquist plots of S-rGO, SPANI, SPANI/S-rGO composites. It is seen from the insight of Fig. 5.8b, all the samples exhibit a similar Nyquist plot with a semi-circle in the high frequency to mid-frequency region, a slope in the mid-frequency region, and a straight line in high-frequency region. In general, the touching point of the semi-circle on x-axis at high frequency indicates the equivalent series resistance (R_s) which is the sum of the resistance of electrode material, bulk resistance of electrolyte, and contact resistance [45]. The diameter of the semicircle corresponds to the charge transfer resistance (R_{ct}) which is corresponds to the charge transfer at electrode/electrolyte interface and the slope at the mid-frequency region shows the diffusion behaviour of electrolyte ions [7,46]. The charge transfer resistance is one important factor that limits the power densities of supercapacitors. The values of R_s and R_{ct} of all the samples are given in Table 5.4. The obtained values of R_s and R_{ct} of SPANI/S-rGO10 composite are lower than that of pure SPANI and S-rGO and other composite materials indicating the high conductivity of electrode material. The lower charge transfer resistance for SPANI/S-rGO10 is attributed to the strong interaction between S-rGO sheets and SPANI nanostructures.

Table 5.4 Equivalent series resistance (R_s) and charge transfer resistance (R_{ct}) of S-rGO, SPANI, SPANI/S-rGO composites.

	S-rGO	**SPANI**	**SPANI/S-rGO5**	**SPANI/S-rGO10**	**SPANI/S-rGO15**
R_s (Ω)	0.85	1.2	1.6	1.3	1.4
R_{ct} (Ω)	1.4	2.5	1.5	0.9	1.0

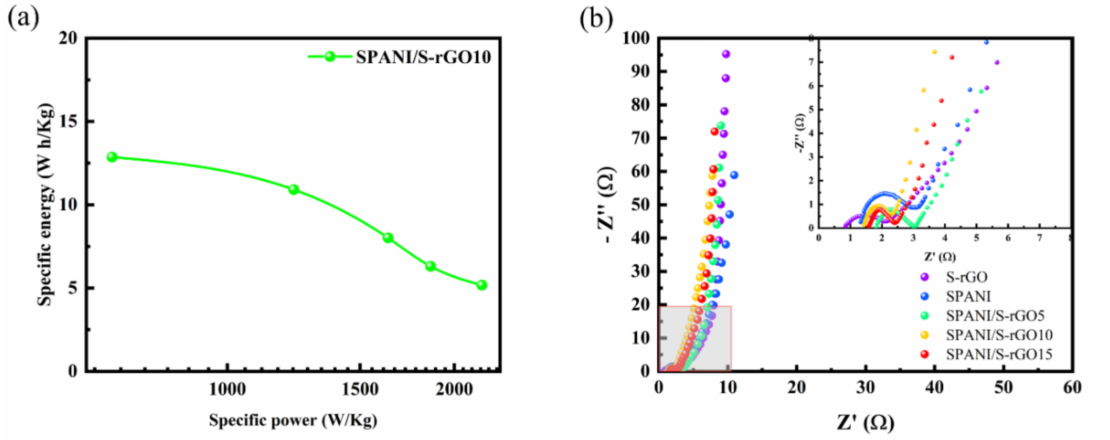

Figure 5.8 *(a) Ragone plot of SPANI/S-rGO10 composite, and (b) Nyquist plots of S-rGO, SPANI, and SPANI/S-rGO composites.*

The cycling stability studies are performed to understand the long-term stability of the composite material. The charge/discharge curves of SPANI and SPANI/S-rGO10 composite are obtained at a current density of 2 A/g for 2500 cycles (Fig. 5.9). It is noticed that the specific capacitance of both samples is decreased rapidly at the initial 200 cycles. The SPANI/S-rGO composite lost 8% of its initial capacitance in the first 200 cycles whereas SPANI lost 17%. The decrease in capacitance during initial cycling might be due to the surface redox reactions and loosely attached fragments of polymer. During the cycling process, the continuous doping/dedoping has occurred in PANI which causes the volume expansion/contraction and even degradation of PANI film, resulting in fading of capacitance [47]. From the 200 cycles to 2500 cycles the composite materials lost only 3% which is very much lower than that of SPANI 21%. The cycling stability of SPANI is greatly improved with the addition of S-rGO sheets in the composite material. The enhanced cycling stability of the composite material indicates the superiority of the electrode material in the composite form. Therefore, the composite with optimized wt.% of S-rGO could be a potential candidate for the high-performance supercapacitor.

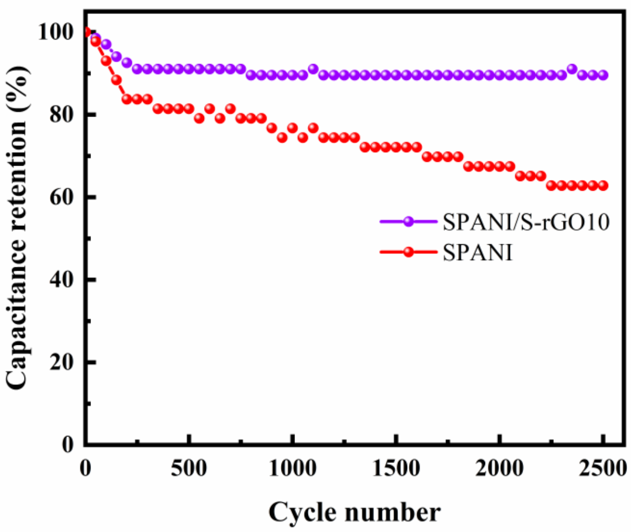

Figure 5.9 *Capacitance retention with the number of cycles at a current density of 2 A/g for SPANI/S-rGO10 and SPANI samples.*

To further demonstrate the flexibility of the SPANI/S-rGO10 composite material, CV measurements are carried out by bending the supercapacitor device fabricated using SPANI/S-rGO10 flexible electrodes (Fig. 5.10b). The photographs of the device upon bending were recorded simultaneously while measuring CV curves at a scan rate of 50 mV/s are illustrated in Fig. 5.10a. Precisely, the bending angle (θ) is measured using Zhi's suggestion, it is given in Fig. 5.10a of supplementary information [48]. We observed that the CV curves are identical with increasing bending angles demonstrating the good flexibility of the electrode materials. The results obtained from the flexibility studies are consistent with the flexibility tests reported elsewhere on PANI based flexible supercapacitors [49–52].

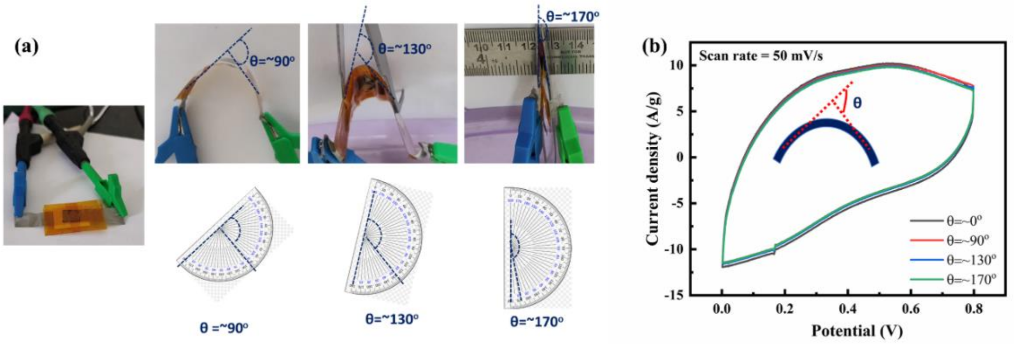

Figure 5.10 *(a) Bending angle measurements for the SPANI/S-rGO10 composite based SSC, and (b) CV curves at recorded at different bending angles with a scan rate of 50 mV/s.*

5.3 Conclusions

Two-dimensional S-doped reduced graphene oxide layers are used as support to grow Naphthalene sulfonic acid doped polyaniline nanostructures using a facile method containing hydrothermal reduction followed by an in-situ polymerization method. The well-designed SPANI/S-rGO electrode exhibited enhanced electrochemical performance. The binary composite with 10 wt.% of S-rGO, i.e., SPANI/S-rGO10 electrode delivered a high specific capacitance of 347.5 F/g at a current density of 1 A/g in 1 M H_2SO_4 and improved cycling stability (~89% after 2500 cycles at a current density of 2 A/g). The results depicted that the enhanced performance is attributed to the optimum loading of S-rGO in designing binary composite, well-aligned growth of SPANI nanostructures on S-rGO sheets, and synergistic effect of both S-rGO and SPANI. The facile synthesized SPANI/S-rGO composite electrode material with the offer mentioned features is considered to be a promising candidate for high-performance supercapacitor.

References

[1] E.E. Miller, Y. Hua, F.H. Tezel, Materials for energy storage: Review of electrode materials and methods of increasing capacitance for supercapacitors, J. Energy Storage. 20 (2018) 30–40. https://doi.org/10.1016/j.est.2018.08.009.

[2] Z. Liu, Z. Zhao, A. Xu, W. Li, Y. Qin, Facile preparation of graphene/polyaniline composite hydrogel film by electrodeposition for binder-free all-solid-state supercapacitor, J. Alloys Compd. 875 (2021) 159931. https://doi.org/10.1016/j.jallcom.2021.159931.

[3] Z. Zhao, Z. Liu, Q. Zhong, Y. Qin, A. Xu, W. Li, J. Shi, In Situ Synthesis of Trifluoroacetic Acid-Doped Polyaniline/Reduced Graphene Oxide Composites for High-Performance All-Solid-State Supercapacitors, ACS Appl. Energy Mater. 3 (2020) 8774–8785. https://doi.org/10.1021/acsaem.0c01309.

[4] K. Gholami laelabadi, R. Moradian, I. Manouchehri, Facile Method of Fabricating Interdigitated and Sandwich Electrodes for High-Performance and Flexible Reduced Graphene Oxide@Polyaniline Nanocomposite Supercapacitors, ACS Appl. Energy Mater. 4 (2021) 6697–6710. https://doi.org/10.1021/acsaem.1c00754.

[5] S. Sinha, S. Bhadra, D. Khastgir, Effect of dopant type on the properties of polyaniline, J. Appl. Polym. Sci. 112 (2009) 3135–3140. https://doi.org/10.1002/app.29708.

[6] A.G. Tabrizi, N. Arsalani, A. Mohammadi, L.S. Ghadimi, I. Ahadzadeh, H. Namazi, A new route for the synthesis of polyaniline nanoarrays on graphene oxide for high-performance supercapacitors, Electrochim. Acta. 265 (2018) 379–390. https://doi.org/10.1016/j.electacta.2018.01.166.

[7] N. Macherla, K. Singh, M.S. Santosh, K. Kumari, R. Gopal, R.G.R. Lekkala, Heat assisted facile synthesis of nanostructured polyaniline/reduced crumbled graphene oxide as a high-performance flexible electrode material for supercapacitors,

Colloids Surfaces A Physicochem. Eng. Asp. 612 (2021) 125982. https://doi.org/10.1016/j.colsurfa.2020.125982.

[8] O. Sadak, M.U.A. Prathap, S. Gunasekaran, Facile fabrication of highly ordered polyaniline–exfoliated graphite composite for enhanced charge storage, Carbon N. Y. 144 (2019) 756–763. https://doi.org/10.1016/j.carbon.2018.12.062.

[9] Y. He, X. Wang, H. Huang, P. Zhang, B. Chen, Z. Guo, In-situ electropolymerization of porous conducting polyaniline fibrous network for solid-state supercapacitor, Appl. Surf. Sci. 469 (2019) 446–455. https://doi.org/10.1016/j.apsusc.2018.10.180.

[10] Y. Shen, Z. Qin, T. Li, F. Zeng, Y. Chen, N. Liu, Boosting the supercapacitor performance of polyaniline nanofibers through sulfonic acid assisted oligomer assembly during seeding polymerization process, Electrochim. Acta. 356 (2020) 136841. https://doi.org/10.1016/j.electacta.2020.136841.

[11] P. Fan, S. Wang, H. Liu, L. Liao, G. Lv, L. Mei, Polyaniline nanotube synthesized from natural tubular halloysite template as high performance pseudocapacitive electrode, Electrochim. Acta. 331 (2020) 135259. https://doi.org/10.1016/j.electacta.2019.135259.

[12] T. Li, P. Liu, Y. Gao, S. Diao, X. Wang, B. Yang, X. Wang, High electrochemical performance of supercapacitor electrode with para-aminophenyl graphene/polyaniline cross-linking nanocomposites, Mater. Lett. 244 (2019) 13–17. https://doi.org/10.1016/j.matlet.2019.02.046.

[13] R. Awata, M. Shehab, A. El Tahan, M. Soliman, S. Ebrahim, High performance supercapacitor based on camphor sulfonic acid doped polyaniline/multiwall carbon nanotubes nanocomposite, Electrochim. Acta. 347 (2020) 136229. https://doi.org/10.1016/j.electacta.2020.136229.

[14] M. Bhaumik, K. Raju, I. Arunachellan, T. Ludwig, M.K. Mathe, A. Maity, S. Mathur, High-performance supercapacitors based on S-doped polyaniline nanotubes decorated with Ni(OH)2 nanosponge and onion-like carbons derived from used car tyres, Electrochim. Acta. 342 (2020) 136111. https://doi.org/10.1016/j.electacta.2020.136111.

[15] Z. Wei, Z. Zhang, M. Wan, Formation mechanism of self-assembled polyaniline micro/nanotubes, Langmuir. 18 (2002) 917–921. https://doi.org/10.1021/la0155799.

[16] X. Hong, B. Zhang, E. Murphy, J. Zou, F. Kim, Three-dimensional reduced graphene oxide/polyaniline nanocomposite film prepared by diffusion driven layer-by-layer assembly for high-performance supercapacitors, J. Power Sources. 343 (2017) 60–66. https://doi.org/10.1016/j.jpowsour.2017.01.034.

[17] C. Vallés, P. Jiménez, E. Muñoz, A.M. Benito, W.K. Maser, Simultaneous reduction of graphene oxide and polyaniline: Doping-assisted formation of a solid-state charge-transfer complex, J. Phys. Chem. C. 115 (2011) 10468–10474. https://doi.org/10.1021/jp201791h.

[18] H. Kuzhandaivel, S. Manickam, S.K. Balasingam, M.C. Franklin, H.J. Kim, K.S. Nallathambi, Sulfur and nitrogen-doped graphene quantum dots/PANI nanocomposites for supercapacitors, New J. Chem. 45 (2021) 4101–4110. https://doi.org/10.1039/d1nj00038a.

[19] Q. Hao, X. Xia, W. Lei, W. Wang, J. Qiu, Facile synthesis of sandwich-like

polyaniline/boron-doped graphene nano hybrid for supercapacitors, Carbon N. Y. 81 (2015) 552–563. https://doi.org/10.1016/j.carbon.2014.09.090.

[20] T. Fan, S. Tong, W. Zeng, Q. Niu, Y. Liu, C. Kao, J. Liu, W. Huang, Y. Min, A.J. Epstein, Self-assembling sulfonated graphene / polyaniline nanocomposite paper for high performance supercapacitor, Synth. Met. 199 (2015) 79–86. https://doi.org/10.1016/j.synthmet.2014.11.017.

[21] X. Du, X. Shi, Y. Li, K. Cao, Construction of N, S-co-doped graphene/polyaniline composite as free-standing electrode material, Int. J. Energy Res. 45 (2021) 6227–6238. https://doi.org/10.1002/er.6243.

[22] M. Chen, Y. Zhang, Y. Liu, Q. Wang, J. Zheng, C. Meng, Three-Dimensional Network of Vanadium Oxyhydroxide Nanowires Hybridize with Carbonaceous Materials with Enhanced Electrochemical Performance for Supercapacitor, ACS Appl. Energy Mater. 1 (2018) 5527–5538. https://doi.org/10.1021/acsaem.8b01109.

[23] A. Urbieta, A. González-Beltrán, S. Ben Mokhtar, M. Anwar Hossain, L. Capra, Adaptive and context-aware service composition for IoT-based smart cities, Futur. Gener. Comput. Syst. 76 (2017) 262–274. https://doi.org/10.1016/j.future.2016.12.038.

[24] Y. Zhang, M. Chen, T. Hu, C. Meng, 3D Interlaced Networks of VO(OH)2 Nanoflakes Wrapped with Graphene Oxide Nanosheets as Electrodes for Energy Storage Devices, ACS Appl. Nano Mater. 2 (2019) 2934–2945. https://doi.org/10.1021/acsanm.9b00364.

[25] M. Bhaumik, A. Maity, T.S. Mahule, V. V. Srinivasu, Tunability of localization length in naphthalene sulfonic acid doped polyaniline/nickel ferrite composite nanorods system, J. Appl. Phys. 126 (2019) 035102. https://doi.org/10.1063/1.5085161.

[26] F. Xie, M. Zhou, G. Wang, Q. Wang, M. Yan, H. Bi, Morphology-dependent electrochemical performance of nitrogen-doped carbon dots@polyaniline hybrids for supercapacitors, Int. J. Energy Res. 43 (2019) 7529–7540. https://doi.org/10.1002/er.4678.

[27] D. Ge, L. Yang, A. Honglawan, J. Li, S. Yang, In situ synthesis of hybrid aerogels from single-walled carbon nanotubes and polyaniline nanoribbons as free-standing, flexible energy storage electrodes, Chem. Mater. 26 (2014) 1678–1685. https://doi.org/10.1021/cm404025g.

[28] M. Mitra, C. Kulsi, K. Chatterjee, K. Kargupta, S. Ganguly, D. Banerjee, S. Goswami, Reduced graphene oxide-polyaniline composites - Synthesis, characterization and optimization for thermoelectric applications, RSC Adv. 5 (2015) 31039–31048. https://doi.org/10.1039/c5ra01794g.

[29] C. Basavaraja, K. Il Kim, G.H. Jung, D.S. Huh, Electrical properties of colloidal polyaniline-2-naphthalene sulfonic acid/graphene nanoparticle composite films, Polym. Compos. 35 (2014) 60–67. https://doi.org/10.1002/pc.22634.

[30] K. Jin, W. Zhang, Y. Wang, X. Guo, Z. Chen, L. Li, Y. Zhang, Z. Wang, J. Chen, L. Sun, T. Zhang, In–situ hybridization of polyaniline nanofibers on functionalized reduced graphene oxide films for high-performance supercapacitor, Electrochim. Acta. 285 (2018) 221–229. https://doi.org/10.1016/j.electacta.2018.07.220.

[31] Y. Hu, X. Tong, H. Zhuo, L. Zhong, X. Peng, Biomass-Based Porous N-Self-

Doped Carbon Framework/Polyaniline Composite with Outstanding Supercapacitance, ACS Sustain. Chem. Eng. 5 (2017) 8663–8674. https://doi.org/10.1021/acssuschemeng.7b01380.

[32] L. Li, A.R.O. Raji, H. Fei, Y. Yang, E.L.G. Samuel, J.M. Tour, Nanocomposite of polyaniline nanorods grown on graphene nanoribbons for highly capacitive pseudocapacitors, ACS Appl. Mater. Interfaces. 5 (2013) 6622–6627. https://doi.org/10.1021/am4013165.

[33] M. Ge, H. Hao, Q. Lv, J. Wu, W. Li, Hierarchical nanocomposite that coupled nitrogen-doped graphene with aligned PANI cores arrays for high-performance supercapacitor, Electrochim. Acta. 330 (2020) 135236. https://doi.org/10.1016/j.electacta.2019.135236.

[34] L. Gao, L. Xiong, D. Xu, J. Cai, L. Huang, J. Zhou, L. Zhang, Distinctive Construction of Chitin-Derived Hierarchically Porous Carbon Microspheres/Polyaniline for High-Rate Supercapacitors, ACS Appl. Mater. Interfaces. 10 (2018) 28918–28927. https://doi.org/10.1021/acsami.8b05891.

[35] P.K. Kalambate, C.R. Rawool, S.P. Karna, A.K. Srivastava, Nitrogen-doped graphene/palladium nanoparticles/porous polyaniline ternary composite as an efficient electrode material for high performance supercapacitor, Mater. Sci. Energy Technol. 2 (2019) 246–257. https://doi.org/10.1016/j.mset.2018.12.005.

[36] Z. Xu, Z. Zhang, H. Yin, S. Hou, H. Lin, J. Zhou, S. Zhuo, Investigation on the role of different conductive polymers in supercapacitors based on a zinc sulfide/reduced graphene oxide/conductive polymer ternary composite electrode, RSC Adv. 10 (2020) 3122–3129. https://doi.org/10.1039/c9ra07842h.

[37] S. He, X. Hu, S. Chen, H. Hu, M. Hanif, H. Hou, Needle-like polyaniline nanowires on graphite nanofibers: Hierarchical micro/nano-architecture for high performance supercapacitors, J. Mater. Chem. 22 (2012) 5114–5120. https://doi.org/10.1039/c2jm15668g.

[38] S.N. Karri, S.P. Ega, V. Perupogu, P. Srinivasan, Enhancing the Electrochemical Performance of Polyaniline Using Fly Ash of Coal Waste for Supercapacitor Application, ChemistrySelect. 6 (2021) 2576–2589. https://doi.org/10.1002/slct.202100513.

[39] Z. Çıplak, A. Yıldız, N. Yıldız, Green preparation of ternary reduced graphene oxide-au@polyaniline nanocomposite for supercapacitor application, J. Energy Storage. 32 (2020) 101846. https://doi.org/10.1016/j.est.2020.101846.

[40] X. Hong, Y. Lu, S. Li, X. Wang, X. Wang, J. Liang, Carbon foam@reduced graphene oxide scaffold grown with polyaniline nanofibers for high performance symmetric supercapacitor, Electrochim. Acta. 294 (2019) 376–382. https://doi.org/10.1016/j.electacta.2018.10.133.

[41] A. Moyseowicz, G. Gryglewicz, Hydrothermal-assisted synthesis of a porous polyaniline/reduced graphene oxide composite as a high-performance electrode material for supercapacitors, Compos. Part B Eng. 159 (2019) 4–12. https://doi.org/10.1016/j.compositesb.2018.09.069.

[42] J. Sarkar, S. Bhattacharyya, Application of graphene and graphene-based materials in clean energy-related devices Minghui, Arch. Thermodyn. 33 (2012) 23–40. https://doi.org/10.1002/er.

[43] Z. Hou, S. Zou, J. Li, Morphology and structure control of amine- functionalized

graphene/polyaniline composite for high-performance supercapacitors, J. Alloys Compd. 827 (2020) 154390. https://doi.org/10.1016/j.jallcom.2020.154390.

[44] Y. Li, M. Zhou, Z. Xia, Q. Gong, X. Liu, Y. Yang, Q. Gao, Facile preparation of polyaniline covalently grafted to isocyanate functionalized reduced graphene oxide nanocomposite for high performance flexible supercapacitors, Colloids Surfaces A Physicochem. Eng. Asp. 602 (2020) 125172. https://doi.org/10.1016/j.colsurfa.2020.125172.

[45] K. Sharma, K. Pareek, R. Rohan, P. Kumar, Flexible supercapacitor based on three-dimensional cellulose/graphite/polyaniline composite, Int. J. Energy Res. 43 (2019) 604–611. https://doi.org/10.1002/er.4277.

[46] S. Goswami, G.R. Dillip, S. Nandy, A.N. Banerjee, A. Pimentel, S.W. Joo, R. Martins, E. Fortunato, Biowaste-derived carbon black applied to polyaniline-based high-performance supercapacitor microelectrodes: Sustainable materials for renewable energy applications, Electrochim. Acta. 316 (2019) 202–218. https://doi.org/10.1016/j.electacta.2019.05.133.

[47] P. Zhang, X. Zhai, H. Huang, J. Zhou, X. Li, Y. He, Z. Guo, Capacitance fading mechanism and structural evolution of conductive polyaniline in electrochemical supercapacitor, J. Mater. Sci. Mater. Electron. 31 (2020) 14625–14634. https://doi.org/10.1007/s10854-020-04025-y.

[48] H. Li, Z. Tang, Z. Liu, C. Zhi, Evaluating Flexibility and Wearability of Flexible Energy Storage Devices, Joule. 3 (2019) 613–619. https://doi.org/10.1016/j.joule.2019.01.013.

[49] F. Liu, S. Luo, D. Liu, W. Chen, Y. Huang, L. Dong, L. Wang, Facile processing of free-standing polyaniline/SWCNT film as an integrated electrode for flexible supercapacitor application, ACS Appl. Mater. Interfaces. 9 (2017) 33791–33801. https://doi.org/10.1021/acsami.7b08382.

[50] F. Hekmat, S. Shahrokhian, N. Taghavinia, Ultralight Flexible Asymmetric Supercapacitors Based on Manganese Dioxide-Polyaniline Nanocomposite and Reduced Graphene Oxide Electrodes Directly Deposited on Foldable Cellulose Papers, J. Phys. Chem. C. 122 (2018) 27156–27168. https://doi.org/10.1021/acs.jpcc.8b07464.

[51] J. Li, S. Qiu, B. Liu, H. Chen, D. Xiao, H. Li, Strong interaction between polyaniline and carbon fibers for flexible supercapacitor electrode materials, J. Power Sources. 483 (2021) 229219. https://doi.org/10.1016/j.jpowsour.2020.229219.

[52] L. Hou, X. Zhi, W. Zhang, H. Zhou, Boosting the electrochemical properties of polyaniline by one-step co-doped electrodeposition for high performance flexible supercapacitor applications, J. Electroanal. Chem. 863 (2020) 114064. https://doi.org/10.1016/j.jelechem.2020.114064.

CHAPTER 6

CORN HUSK BIOWASTE DERIVED POROUS CARBON FOR HIGH PERFORMANCE SUPERCAPACITOR

6.1 Introduction

The pollution caused by the combustion of fossil fuels for the generation of electrical energy has become a big issue that needs to be addressed in the modern day. Emissions produced by fossil fuels, such as carbon dioxide and other greenhouse gasses, are causing unpleasant climate changes and harming human health [1]. One of the most attractive options for replacing fossil fuels is the process of producing electrical energy from natural sources such as solar, wind, and so on. However, effective use of such time-limited resources can be accomplished by utilizing adequate energy storage systems such as rechargeable batteries and supercapacitors (SCs) [2–4]. In this regard, SCs are considered a featured electrochemical energy storage system, which meets high power requirements [5]. In general, two possible ways of energy storage there exist in SCs [6]. The energy stored in SCs by the accumulation of charges is called Electrical Double-Layer Capacitors (EDLC) and the charge storage by the reversible faradaic reaction at the electrode and electrolyte interface is called Pseudocapacitors [7,8]. The primary problem that hinders the practical application of SCs is their low energy density [9]. To enhance the energy density, it is important to focus on the development of new active materials with excellent capacitive and stability behaviours.

EDLC type SCs are commercially very much available due to their attractive characteristics like high-power capability, fast charge-discharge rate, and long cyclability [9,10]. In the past few decades, various types of carbon materials such as activated porous carbon [11–14], carbon nanotubes, carbide-derived carbons, carbon fibers, carbon quantum dots, and graphene-based material have been investigated as electrode materials for EDL capacitors [15–19]. Among them, porous carbons (PCs) derived from biomass/biowaste have been receiving significant research interest due to the low cost, natural abundance, renewable and are very meaningful in particular for “waste to wealth” purpose [1,4,13]. The type of precursor material, the activation process and the activation conditions play major roles in determining the properties of the resulting PCs including porosity, pore-size distribution, surface area and surface chemistry [20,21]. Many biowaste resources from plant and animal waste such as corncob [6], mangosteen peel [7], coconut shell [22], coffee grounds [11], soybean dregs [21], rice straw [23], wheat husk [24], corn Silk [25], citrus peel fiber [26], pomelo peel [27], fish seed [28], orange-peel [29], Setaria viridis [30], Sapindus trifoliatus nut shells [31], tamarind seed coat [32], etc. are used for the production of porous carbons. The general approaches to prepare biowaste derived PCs are direct pyrolysis, hydrothermal-assisted carbonization, and carbonization-activation under inert atmospheric conditions. Among them, carbonization-activation is an immensely studied approach, where initially the raw material is carbonized under inert conditions then activated through physical (CO_2 and H_2O steam activation) and/or chemical (KOH, NaOH, $ZnCl_2$, H_3PO_4, $KHCO_3$ etc.) procedure at relatively high temperature [33–35]. Chemical activation is considered to be a suitable route to prepare porous carbons with high surface area and tuneable porosity by changing the synthesis parameters (precursor to activating agent ratio, activation temperature, activation time) [12,35–37].

The PCs synthesised from the biomass should possess a high surface area along with suitable pore size distribution to enhance EDL capacitance [37,38]. Porous carbons which contain abundant micropores (<2 nm), provide high specific surface area and increase the energy storage at lower current density. mesopores and macropores are effective in minimizing the ion diffusion distances, low-resistant pathways for the ions and facilitating fast ion transportation at high current densities thus providing good rate capability [13,39]. Therefore, the synthesis of porous carbon with a high surface area and controlled porosity is essential to achieve high energy density along with good rate capability.

Corn or Maize is a “food crop” which is grown in large quantities all over the world without any geographical limitations and it produced more than 1075 million tons around the world in 2017 [40]. Corn has been recognized as the third most cultivated food crop in India, after rice and wheat., the total corn production in the country has increased to 193% from 1990 to 2016 [41]. The increase in corn production also increases solid waste corn husk (CH). CH is lignocellulose biowaste, composed of cellulose (38.2%) and hemicellulose (44.5%), as well as a little amount of lignin (6.6%) and ash (2.8%) [40,42]. However, the CH weighed 10% of corn stover, which is thrown away as waste, used as food for animals or burned which creates environmental pollution. Instead of wastage, the abundantly available, low cost, renewable resource of CH can be utilized as biowaste raw material for the preparation of value-added porous carbons. Hence, in the present study, we have used natural abundant biowaste of CH as a precursor for the synthesis of porous carbons (CHPCs) using carbonization and chemical activation method. The effect of activation temperature on the surface area and pore structure of the resultant carbons is studied. Further, how the surface area and porosity effected the electrochemical properties of the CHPCs is evaluated in a two-electrode supercapacitor system.

6.2 Results and Discussion

The macroscopic photograph of CH is shown in Fig. 6.1a and it has consisted of a fibrous surface with a prominent thick sheet-like structure. After the carbonization, CHBC maintained a similar flat surface structure without any pore development (Fig. 6.1b). The chemical activation using KOH imposed porosity which can be seen from the SEM images given in Fig. 6.1(c-f). CHPC-600 has less porosity due to the insufficient temperature for the reaction to start (Fig. 6.1c). During the chemical activation, stepwise reactions have happened between the CHBC and KOH. Initially, at a temperature of about 600 ^{o}C, KOH fully reacted with Carbon and form K_2CO_3. Further, increase in activation temperature to 700 and above, the as-formed K_2CO_3 is converted into K_2O and CO_2 at temperature. Then, these K_2O and CO_2 further react with C and release CO and Metallic K [26,33]. These intermediate products intercalate into a carbon framework and expand carbon lattices leading to a highly porous structure. Increasing activation temperature from 600 ^{o}C to 700 ^{o}C results in creating some pores in the sample (Fig. 6.d). Further increase in temperature from 700 ^{o}C to 800 ^{o}C created more porosity in the sample CHPC-800 which eventually enhance the surface area and pore volume of the sample (Fig. 6.1e&f). The irregular size and ordered open pores can be seen in CHPC-800 (Fig. 6.1e&f). It is worth noting that the open pores created in CHPC-800 are interconnected which allows low-resistant pathways for the ions and facilitates fast ion transportation thus improving the capacitive performance.

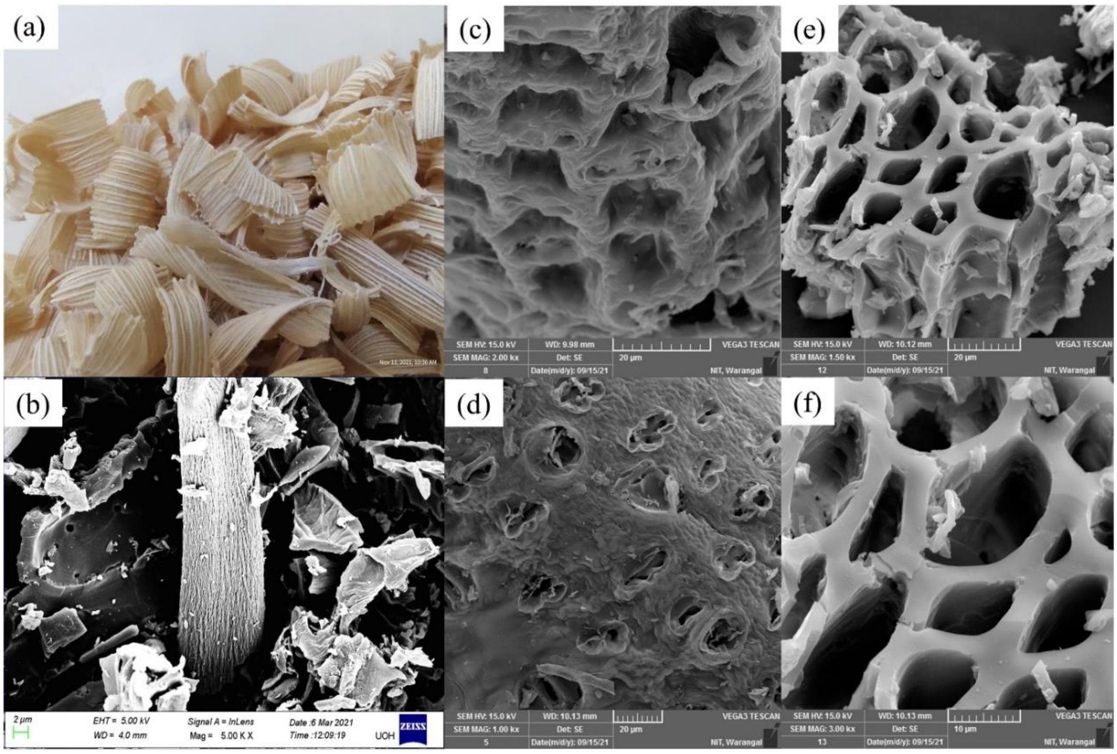

Figure 6.1 *(a) Photograph of CH, SEM images of (b) CHBC (c) CHPC-600, (d) CHPC-700, and (e)& (f) CHPC-800.*

The effect of temperature on the specific surface area and porosity is investigated using N_2 adsorption-desorption isotherm analysis. The isotherm plots of CHPC-600, CHPC-700, and CHPC-800 are shown in Fig. 6.2a. The samples activated at temperatures 600 ^oC and 700 ^oC are showing type-I isotherm with abundant microporosity. Whereas the sample CHPC-800 exhibited type-IV hysteresis with both micro and mesoporous behaviour. The obtained specific surface area values are 881 m^2/g for CHPC-600, 1458 m^2/g for CHPC-700, and 1583 m^2/g for CHPC-800. For sample activated at 600 ^oC is having high microporosity, when the temperature increases to 700 ^oC, 60% of increment is observed in specific surface area (Table 6.1). For CHPC-800, a little increase in surface area is observed and micropores are collapsed and formed into mesoporous (Table 6.1). The equal distribution of both micro and meso porosity is highly beneficial for the charge accumulation and electrolyte ions diffusion. The pore size distribution curves are given in Fig. 6.2b and the insight shows the mesopores region. From the microporous region, for CHPC-600 and CHPC-700 all the pores are distributed only in the micropore region and for CHPC-800 the pores are distributed in both micropore and mesopore regions with pore radius <10 nm.

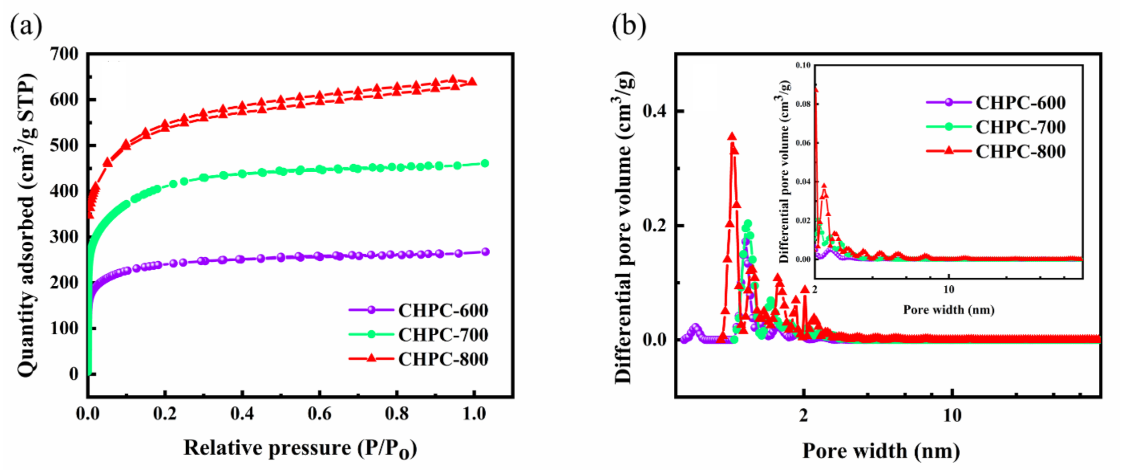

Figure 6.2 *(a) N_2 adsorption-desorption isotherms and (b) Pore size distribution curves, inset shows the mesopore region.*

Table 6.1 Surface area summary results of CHPCs.

Sample	S_{tot} (m^2 g^{-1})	S_{mic} (m^2 g^{-1})	S_{meso} (m^2 g^{-1})	V_t (cm^3 g^{-1})	V_{mic} (cm^3 g^{-1})
CHPC-600	881	873	8	0.41	0.39
CHPC-700	1458	1433	25	0.71	0.66
CHPC-800	1583	783	800	0.99	0.48

$\mathbf{S_{tot}}$: total surface is by BET method; $\mathbf{S_{mic}}$: Micropore surface area by t-plot method, $\mathbf{S_{meso}}$: Mesopore surface area, $\mathbf{V_t}$: Total pore volume by single point method, $\mathbf{V_{mic}}$: Micropore volume by t-plot.

The total pore volume is obtained by the single-point method at a relative pressure (P/P_o) =0.99 and the micropore volume is calculated from the t-plot method and the values are given in Table 6.1. Both micro and total pore volumes are high in the CHPC-800 sample. It is well known that the type of porosity present in electrode material plays a key role in charge transfer and electrolyte ion diffusion. The higher amounts of either micropores or mesopores are not suitable to obtain a high performance in SCs. Equal distribution of micro and meso porosity is highly beneficial for charge accumulation and diffusion of electrolyte ions through the pores. Therefore, the sample CHPC-800 is could be expected to deliver high performance in SCs application.

The XRD patterns of CHPC-800 are shown in Fig. 6.3a. the sample is exhibited less intensive broad diffraction peaks at 2θ values around 23-24° and 43° reflection from (002) and (001) planes of graphitic carbon (JCPDS card no. 41-1487) and the peak broadening and less intensity suggesting the amorphous and disordered nature of CHPC-800 [7,25]. The FTIR spectra (Fig. 6.3b) of CHPC-800 contain a series of peaks. The broad peak at ~3400 cm^{-1} due to OH stretching, 2923 cm$^{-1,}$ and 2853 cm^{-1} are related to CH and CH$_2$ bands. The peaks in the wavenumber range from 1730 -1613 cm^{-1} correspond to C=O groups. The peak that appeared at 1588 cm^{-1} is due to the stretching of an aromatic ring. The other peaks at 1404 cm^{-1} and 1088 cm^{-1} are assigned to the carboxyl group vibration and C-O group, respectively. It is observed from the FTIR spectra of CHPC-800, that the presence of oxygen functional groups (-OH, COOH, C=O) can increase the wettability of the electrodes in the electrolyte solution thus contributing to high energy storage [43].

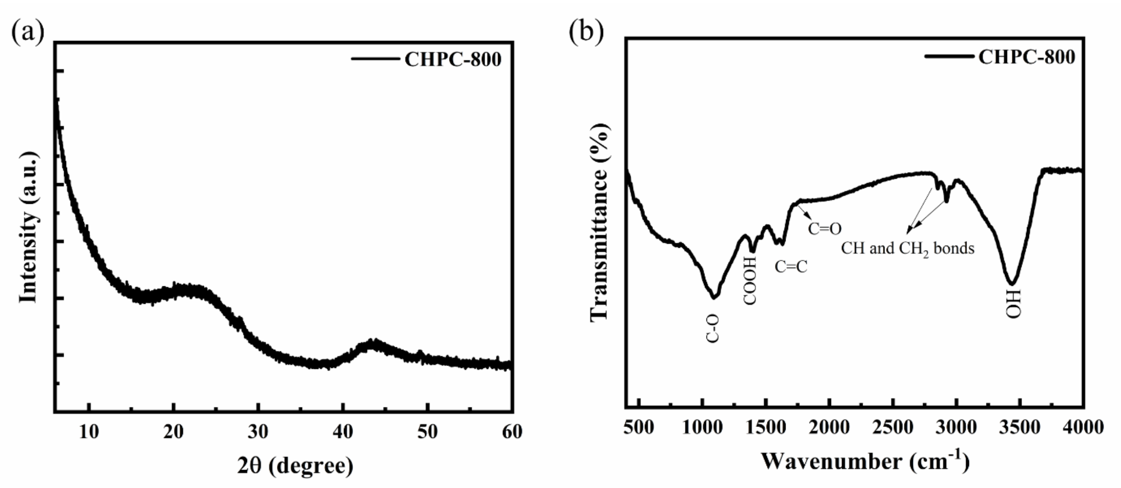

Figure 6.3 *(a) XRD and (b) FTIR plots of CHPC-800.*

The XPS studies were adopted to determine the surface elemental functionalities and bonding configuration. The survey spectrum of CHPC-800 depicts the characteristic peaks of C 1s (87.35%) and O 1s (12.65%) at binding energies of 284.8 eV and 532.8 eV, respectively (Fig. 6.4a). The high-resolution C 1s spectrum shown in Fig. 6.4b, is deconvoluted into four peaks located at 284.6, 285.6, 286.7 and 289.2 eV are assigned to C=C, C-C, C-O and C=O, respectively [44]. The O1s spectrum shown in Fig. 6.4c is fitted into two peaks centred at the binding energies of 531.7 eV and 533.1 eV, which are attributed to the C=O (oxygen in carbonyl and Quinone group) and C-O (oxygen in ester and hydroxyl group), respectively [6]. The existence of carbon-oxygen functional groups plays a major role in enhancing the surface wettability of the electrodes and also contributes an additional pseudo capacitance by participating in faradaic reaction at the electrode/electrolyte interface [28,45,46].

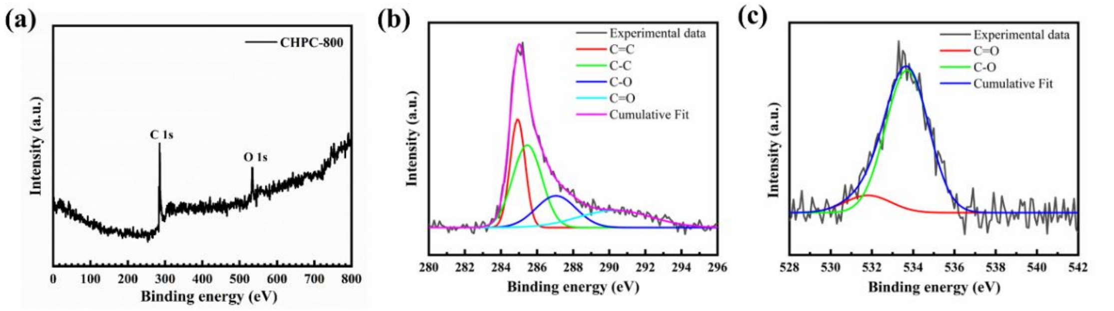

Figure 6.4 *(a) XPS spectra of CHPC-800, (b) High-resolution XPS spectra of CHPC-800: (b) C 1s, and (c) O 1s.*

The electrochemical properties evaluation is carried out for CHPC-600, CHPC-700 and CHPC-800 using CV, GCD and EIS. The CV curves obtained at a scan rate of 10 mV/s are shown in Fig. 6.5a. CHPC-800 exhibited a nearly shape CV curve indicating the dominating EDLC behaviour in the samples [47]. In all the CHPC samples, it is noticed a small hump at the lower potentials indicating the additional pseudocapacitance commenced from the presence of oxygen functionalities as we have seen in FTIR and XPS spectra [46]. A larger CV area is an indication of a high specific capacitance of the CHPC-800 material. Figure 6.5b shows the CV curves of CHPC-800at various scan rates, respectively. At higher scan rates, we observe a deviation in the cv curves and which were become more of like ovel shape. The deviation in the curves from rectangular to ovel shape is due to the insufficient time for the electrolyte ions to diffuse through the pores. Moreover, the micro pores present in the sample are not accessible to the electrolyte ions at high scan rate increasing the electrode resistance. Hence, we observed a deviation in the CV curved with increase in scan rate.

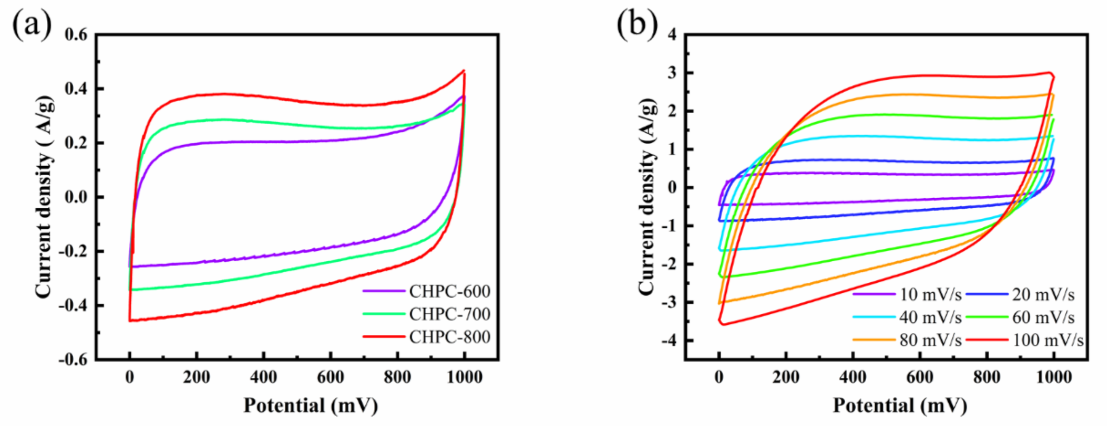

Figure 6.5 *(a) CV curves of CHPCs at a scan rate of 10 mV/s, (b) CV curves of CHPC-800 at different scan rates.*

The GCD graphs of CHPC-600, CHPC-700 and CHPC-700 at a current density of 1 A/g are shown in Fig. 6.6a. the typical triangular shape GCD curve is observed in all CHPC samples. CHPC-800 based SCs device exhibited higher discharge time than other samples, showing the enhanced charge storage in CHPC-800. The calculated specific capacitance value is 133.3 F/g for CHPC-800 at a current density of 1 A/g. The capacitance obtained for the CHPC-800 is higher and comparable with the reported results based on biomass-derived carbons in SSC (Table 6.2). Further, the rate capability studies are carried out at higher current densities (Fig. 6.6b-d). CHPC-800 can charge and discharge at a high current density of 10 A/g. The enhanced performance of CHPC-800 is attributed to the increased surface area of the sample and equally distributed micro and meso porosity. Generally, electrolyte ions diffuse through the pores of the electrode material which results in increased energy density and capacitive performance. At high current densities, most of the micropores are inaccessible and ions are diffuse through mesopores only. From Fig. 6.6e, it is noticed that CHPC-800 has retained 79% of initial capacitance at a current density of 10 A/g. This increase in rate capability is due to the sufficient amount of meso porosity present in the CHPC-800. The specific energy and the specific power are the two important parameters of the device to analyse the potential utilization for energy storage. The E_d and P_d values obtained from GCD curves of CHPC-800 are plotted in Fig. 6.6f. High specific energy of 17.09 Wh/kg at 960 W/kg for CHPC-800. Even at a high specific power of 5885 W/kg, the specific energy is remaining a high value of 5 Wh/kg. This result reveals the fast diffusion of electrolyte ions due to the presence of open mesopores and the high surface area of electrode material.

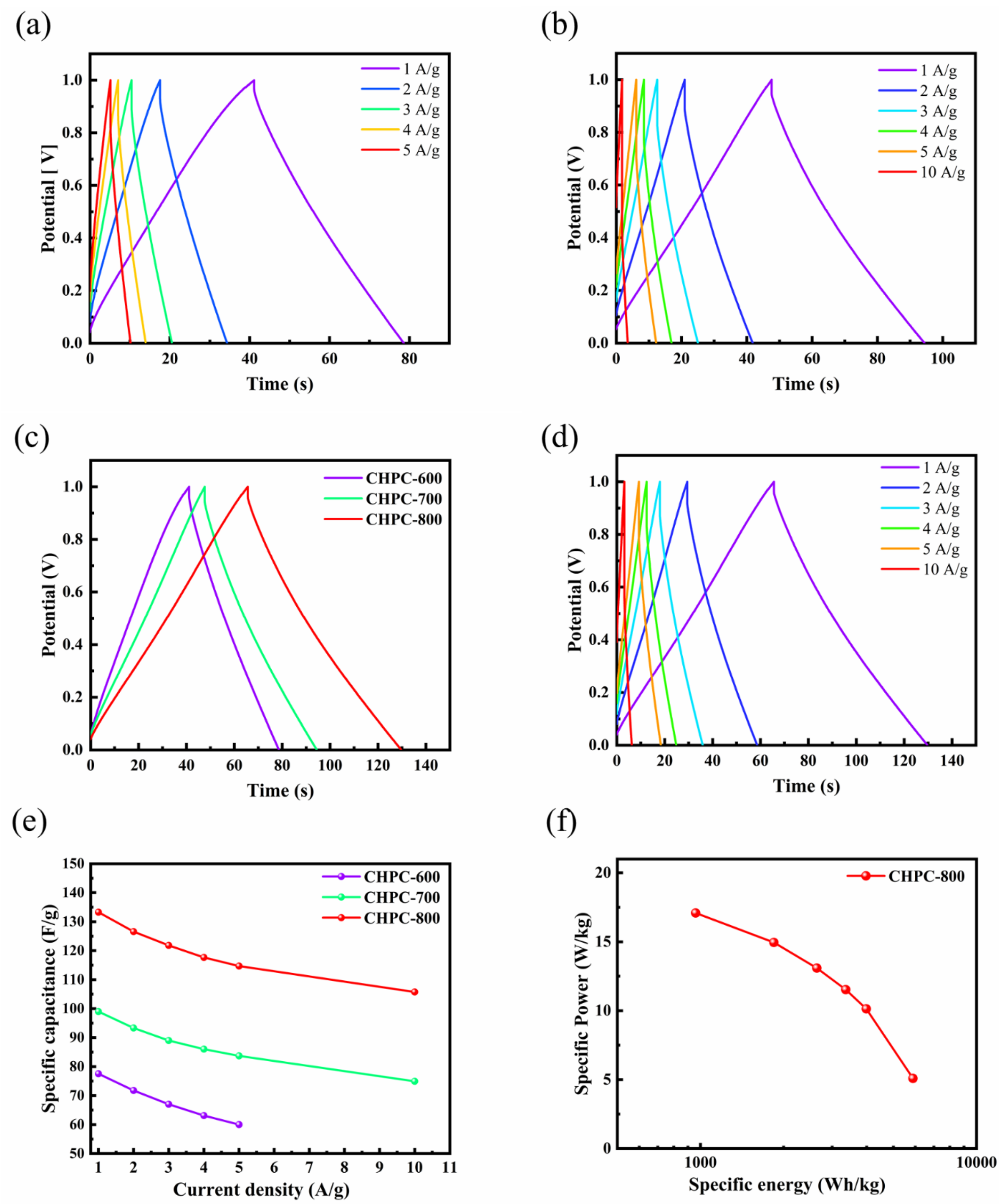

Figure 6.6 *(a) GCD curves of CHPCs at a current density of 1 A/g, GCD curves at various current densities: (b) CHPC-600, (c) CHPC-700, (d) CHPC-800, and (e) change in specific capacitance with current density for CHPCs and (f) Ragone plot of CHPC-800.*

The capacitive performance and charge transfer kinetics of the electrode materials are further analysed using EIS studies. The Nyquist plots of CHPC samples are shown in Fig. 6.7a. All the samples have shown a semi-circle in low high frequency region and straight line in low frequency region. The semi-circle corresponds to the series resistance and charge transfer resistance and straight line region corresponds to the double layer capacitance behaviour of the material [23]. In high-frequency region, a semicircle with a 45° angle slope suggests the combination of charge transfer and ion diffusion behaviour of the SC [11]. The intercept of Nyquist plot on the x-axis at high-frequency region represents the equivalent series resistance (R_s) and the diameter of the semicircle is corresponding to the charge transfer resistance (R_{ct}) of the samples [11,43]. All the samples have shown lower R_s. It can be seen that the shorter diameter of semicircle for CHPC-800 reveals the low R_{ct} than CHPC-600 and CHPC-700 which further confirms the better electrochemical performance of the sample.

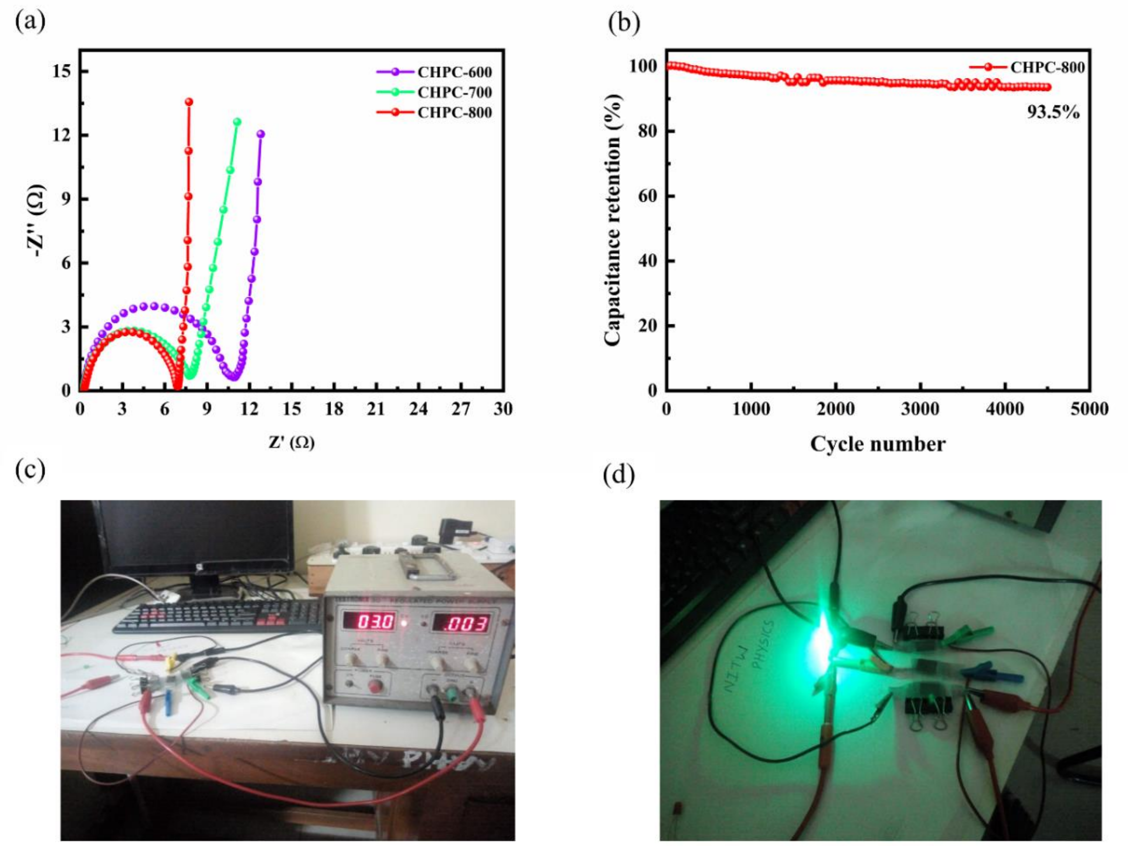

Figure 6.7 *(a) Nyquist plots of CHPCs and (b) Cycling stability of CHPC-800 at a current density of 5 A/g, A series-connected three supercapacitor devices charging with regulated power supply: (c)before LED glow, and (d) green LED glowing.*

Further, the cycling stability studies are also performed for CHPC-800, to evaluate the long-term durability of the electrode materials. The cycling stability is obtained from GCD curves for 4500 cycles at a current density of 1 A/g. the Specific capacitance retention (%) is plotted with increasing cycles as given in Fig. 6.7b. The CHPC-800 sample has shown 93.5% of its initial capacitance after 4500 charge-discharge cycles.

Finally, to prove the potential application of porous carbon for energy storage, A three cell SSC device is fabricated to lighten the LED. To increase the overall voltage of the SSC device, three cells are connected in series and charged with a 3V DC power supply shown in Fig. 6.7c&d. The SSC device successfully lights up the green LED after charging for 1 min. On the basis above results, we can believe that the CHPC-800 could be one of the best electrode materials for SC.

Table 6.2 Electrochemical performance comparison of porous carbons derived from various biomass/biowastes in symmetric supercapacitor.

Precursor	Activating agent	SSA m^2/g	Electrolyte & Voltage	Capacitance	Ref.
Hibiscus sabdariffa fruits	1:1 (KOH)	1720	0.5 M Na_2SO_4	29 F/g at 0.5 A/g	[5]
Mangosteen peel	1:3.5 (NaOH)	2623	1 M Li_2SO_4	76.8 F/g at 1 A/g	[7]
Onion	1:4 (KOH)	3150	3 M KNO_3	158 F/g at 0.5 A/g	[20]
Rice straw	1:3 (KOH)	1007	1 M H_2SO_4	156 F/g at 0.5 A/g	[23]
Corn silk	1:4 (KOH)	2285	6 M KOH	160 F/g at 1 A/g	[25]
Fish seed	1:3 (KOH)	3232	6 M KOH	250 F/g at 1 A/g	[28]
Buckwheat husk	1:2 (KOH)	2794	6 M KOH	75 F/g at 1 A/g	[39]
ardenia Jasminoides Ellis	1 M KOH	1637	6 M KOH	153 F/g at 0.5 A/g	[43]
lax seed residue	1:4 (KOH)	3230	6 M KOH	76 F/g at 0.5 A/g	[46]
Nettle leaf	1:4 (KOH)	1951	EMIM BF_4	163 F/g at 0.5 A/g	[48]
Waste tea	1:2 (H_3PO_4)	1130	6 M KOH	89.3 F/g at 1 A/g	[49]
American poplar fruits	1:2 (KOH)	942	6 M KOH	58.71 F/g at 1 A/g	[50]
Corn husk	1:4 (KOH)	1583	6 M KOH	133.3 F/g at 1 A/g	Present work

6.3 Conclusions

In summary, porous carbons are synthesised using biowaste corn husk as raw material. The activation temperature is optimized to improve the surface area and get the balance between the micro and mesopores. The FESEM and N_2 adsorption-desorption studies revealed the formation of both micro and mesopores in the sample activated using KOH at 800 ^oC. With the combination of micro and mesopores, CHPC-800 possessed a large specific surface area of 1583 m^2/g. The existence of oxygen functional groups in the CHPC-800 is confirmed from the FITR and XPS results which increases the surface wettability and contributes additional pseudocapacitance. As obtained CHPC-800 delivered a high specific capacitance of 133.3 F/g at 1 A/g with 93.5% capacitance reattained after 4500

GCD cycles. With the above-mentioned prominent features, CHPC-800 could be a prominent electrode material for SC.

References

[1] D.P. Yang, Z. Li, M. Liu, X. Zhang, Y. Chen, H. Xue, E. Ye, R. Luque, Biomass-Derived Carbonaceous Materials: Recent Progress in Synthetic Approaches, Advantages, and Applications, ACS Sustain. Chem. Eng. 7 (2019) 4564–4585. https://doi.org/10.1021/acssuschemeng.8b06030.

[2] W. Raza, F. Ali, N. Raza, Y. Luo, K.H. Kim, J. Yang, S. Kumar, A. Mehmood, E.E. Kwon, Recent advancements in supercapacitor technology, Nano Energy. 52 (2018) 441–473. https://doi.org/10.1016/j.nanoen.2018.08.013.

[3] B. Kale, S. Chatterjee, Electrochemical energy storage systems: India perspective, Bull. Mater. Sci. 43 (2020) 1–15. https://doi.org/10.1007/s12034-020-2042-7.

[4] H. Lu, X.S. Zhao, Biomass-derived carbon electrode materials for supercapacitors, Sustain. Energy Fuels. 1 (2017) 1265–1281. https://doi.org/10.1039/C7SE00099E.

[5] H.A. Hamouda, S. Cui, X. Dai, L. Xiao, X. Xie, H. Peng, G. Ma, Synthesis of porous carbon material based on biomass derived from hibiscus sabdariffa fruits as active electrodes for high-performance symmetric supercapacitors, RSC Adv. 11 (2020) 354–363. https://doi.org/10.1039/d0ra09509e.

[6] M. Karnan, K. Subramani, P.K. Srividhya, M. Sathish, Electrochemical Studies on Corncob Derived Activated Porous Carbon for Supercapacitors Application in Aqueous and Non-aqueous Electrolytes, Electrochim. Acta. 228 (2017) 586–596. https://doi.org/10.1016/j.electacta.2017.01.095.

[7] V. Yang, R.A. Senthil, J. Pan, A. Khan, S. Osman, L. Wang, W. Jiang, Y. Sun, Highly ordered hierarchical porous carbon derived from biomass waste mangosteen peel as superior cathode material for high performance supercapacitor, J. Electroanal. Chem. 855 (2019) 113616. https://doi.org/10.1016/j.jelechem.2019.113616.

[8] N. Macherla, K. Singh, M.S. Santosh, K. Kumari, R. Gopal, R.G.R. Lekkala, Heat assisted facile synthesis of nanostructured polyaniline/reduced crumbled graphene oxide as a high-performance flexible electrode material for supercapacitors, Colloids Surfaces A Physicochem. Eng. Asp. 612 (2021) 125982. https://doi.org/10.1016/j.colsurfa.2020.125982.

[9] C. Schütter, S. Pohlmann, A. Balducci, Industrial Requirements of Materials for Electrical Double Layer Capacitors: Impact on Current and Future Applications, Adv. Energy Mater. 9 (2019) 1–11. https://doi.org/10.1002/aenm.201900334.

[10] K. Surya, M.S. Michael, Novel interconnected hierarchical porous carbon electrodes derived from bio-waste of corn husk for supercapacitor applications, J. Electroanal. Chem. 878 (2020) 114674. https://doi.org/10.1016/j.jelechem.2020.114674.

[11] X. Liu, S. Zhang, X. Wen, X. Chen, Y. Wen, X. Shi, E. Mijowska, High yield conversion of biowaste coffee grounds into hierarchical porous carbon for superior capacitive energy storage, Sci. Rep. 10 (2020) 1–12. https://doi.org/10.1038/s41598-020-60625-y.

[12] J.H. Khan, F. Marpaung, C. Young, J. Lin, M.T. Islam, S.M. Alsheri, T. Ahamad,

N. Alhokbany, K. Ariga, L.K. Shrestha, Y. Yamauchi, K.C.W. Wu, M.S.A. Hossain, J. Kim, Jute-derived microporous/mesoporous carbon with ultra-high surface area using a chemical activation process, Microporous Mesoporous Mater. 274 (2019) 251–256. https://doi.org/10.1016/j.micromeso.2018.07.050.

[13] Z. Bi, Q. Kong, Y. Cao, G. Sun, F. Su, X. Wei, X. Li, A. Ahmad, L. Xie, C.M. Chen, Biomass-derived porous carbon materials with different dimensions for supercapacitor electrodes: A review, J. Mater. Chem. A. 7 (2019) 16028–16045. https://doi.org/10.1039/c9ta04436a.

[14] F.L. Braghiroli, A. Cuña, E.L. da Silva, G. Amaral-Labat, G.F.B. Lenz e Silva, H. Bouafif, A. Koubaa, The conversion of wood residues, using pilot-scale technologies, into porous activated biochars for supercapacitors, J. Porous Mater. 27 (2020) 537–548. https://doi.org/10.1007/s10934-019-00823-w.

[15] Z. Yang, J. Tian, Z. Yin, C. Cui, W. Qian, F. Wei, Carbon nanotube- and graphene-based nanomaterials and applications in high-voltage supercapacitor: A review, Carbon N. Y. 141 (2019) 467–480. https://doi.org/10.1016/j.carbon.2018.10.010.

[16] Y. Zhou, X. Zhou, C. Ge, W. Zhou, Y. Zhu, B. Xu, Branched carbon nanotube/carbon nanofiber composite for supercapacitor electrodes, Mater. Lett. 246 (2019) 174–177. https://doi.org/10.1016/j.matlet.2019.03.074.

[17] S. Zhu, J. Ni, Y. Li, Carbon nanotube-based electrodes for flexible supercapacitors, Nano Res. 13 (2020) 1825–1841. https://doi.org/10.1007/s12274-020-2729-5.

[18] J. Chen, C. Li, G. Shi, Graphene materials for electrochemical capacitors, J. Phys. Chem. Lett. 4 (2013) 1244–1253. https://doi.org/10.1021/jz400160k.

[19] J. Li, X. Yun, Z. Hu, L. Xi, N. Li, H. Tang, P. Lu, Y. Zhu, Three-dimensional nitrogen and phosphorus co-doped carbon quantum dots/reduced graphene oxide composite aerogels with a hierarchical porous structure as superior electrode materials for supercapacitors, J. Mater. Chem. A. 7 (2019) 26311–26325. https://doi.org/10.1039/c9ta08151h.

[20] N.M. Musyoka, B.K. Mutuma, N. Manyala, Onion-derived activated carbons with enhanced surface area for improved hydrogen storage and electrochemical energy application, RSC Adv. 10 (2020) 26928–26936. https://doi.org/10.1039/d0ra04556j.

[21] Z. Li, Z. Bai, H. Mi, C. Ji, S. Gao, H. Pang, Biowaste-derived porous carbon with tuned microstructure for high-energy quasi-solid-state supercapacitors, ACS Sustain. Chem. Eng. 7 (2019) 13127–13135. https://doi.org/10.1021/acssuschemeng.9b02303.

[22] L. Sun, C. Tian, M. Li, X. Meng, L. Wang, R. Wang, J. Yin, H. Fu, From coconut shell to porous graphene-like nanosheets for high-power supercapacitors, J. Mater. Chem. A. 1 (2013) 6462–6470. https://doi.org/10.1039/c3ta10897j.

[23] N. Sudhan, K. Subramani, M. Karnan, N. Ilayaraja, M. Sathish, Biomass-derived activated porous carbon from rice straw for a high-energy symmetric supercapacitor in aqueous and nonaqueous electrolytes, Energy and Fuels. 31 (2017) 977–985. https://doi.org/10.1021/acs.energyfuels.6b01829.

[24] M.M. Baig, I.H. Gul, Conversion of wheat husk to high surface area activated carbon for energy storage in high-performance supercapacitors, Biomass and Bioenergy. 144 (2021) 105909. https://doi.org/10.1016/j.biombioe.2020.105909.

[25] T. Mitravinda, K. Nanaji, S. Anandan, A. Jyothirmayi, V.S.K. Chakravadhanula, C.S. Sharma, T.N. Rao, Facile Synthesis of Corn Silk Derived Nanoporous Carbon for an Improved Supercapacitor Performance, J. Electrochem. Soc. 165 (2018) A3369–A3379. https://doi.org/10.1149/2.0621814jes.

[26] M. Mondal, D.K. Goswami, T.K. Bhattacharyya, Lignocellulose based Bio-waste Materials derived Activated Porous Carbon as Superior Electrode Materials for High-Performance Supercapacitor, J. Energy Storage. 34 (2021) 102229. https://doi.org/10.1016/j.est.2020.102229.

[27] J. Li, F. Luo, T. Lin, J. Yang, S. Yang, D. He, D. Xiao, W. Liu, Pomelo peel-based N, O-codoped hierarchical porous carbon material for supercapacitor application, Chem. Phys. Lett. 753 (2020) 137597. https://doi.org/10.1016/j.cplett.2020.137597.

[28] Y. Lu, F. Xu, L. Sun, Y. Wu, Y. Xia, X. Cai, N. Zhong, H. Zhang, B. Li, H. Chu, Facile method for preparation of porous carbon derived from biomass for high performance supercapacitors, Int. J. Electrochem. Sci. 14 (2019) 11199–11211. https://doi.org/10.20964/2019.12.54.

[29] C.K. Ranaweera, P.K. Kahol, M. Ghimire, S.R. Mishra, R.K. Gupta, Orange-Peel-Derived Carbon: Designing Sustainable and High-Performance Supercapacitor Electrodes, C. 3 (2017) 1–17. https://doi.org/10.3390/c3030025.

[30] R. Yan, K. Wang, X. Tian, X. Li, T. Yang, X. Xu, Y. He, S. Lei, Y. Song, Heteroatoms in situ-doped hierarchical porous hollow-activated carbons for high-performance supercapacitor, Carbon Lett. 30 (2020) 331–344. https://doi.org/10.1007/s42823-019-00102-3.

[31] M. Vinayagam, R. Suresh Babu, A. Sivasamy, A.L.F. de Barros, Biomass-derived porous activated carbon nanofibers from Sapindus trifoliatus nut shells for high-performance symmetric supercapacitor applications, Carbon Lett. 31 (2021) 1133–1143. https://doi.org/10.1007/s42823-021-00235-4.

[32] T. Ramesh, N. Rajalakshmi, K.S. Dhathathreyan, L.R.G. Reddy, Hierarchical Porous Carbon Microfibers Derived from Tamarind Seed Coat for High-Energy Supercapacitor Application, ACS Omega. 3 (2018) 12832–12840. https://doi.org/10.1021/acsomega.8b01850.

[33] J. Wang, P. Nie, B. Ding, S. Dong, X. Hao, H. Dou, X. Zhang, Biomass derived carbon for energy storage devices, J. Mater. Chem. A. 5 (2017) 2411–2428. https://doi.org/10.1039/c6ta08742f.

[34] M. Sevilla, A.B. Fuertes, A Green Approach to High-Performance Supercapacitor Electrodes: The Chemical Activation of Hydrochar with Potassium Bicarbonate, ChemSusChem. 9 (2016) 1880–1888. https://doi.org/10.1002/cssc.201600426.

[35] H. Zhang, Y. Zhang, L. Bai, Y. Zhang, L. Sun, Effect of physiochemical properties in biomass-derived materials caused by different synthesis methods and their electrochemical properties in supercapacitors, J. Mater. Chem. A. 9 (2021) 12521–12552. https://doi.org/10.1039/d1ta00790d.

[36] E. Elaiyappillai, R. Srinivasan, Y. Johnbosco, P. Devakumar, K. Murugesan, K. Kesavan, P.M. Johnson, Low cost activated carbon derived from Cucumis melo fruit peel for electrochemical supercapacitor application, Appl. Surf. Sci. 486 (2019) 527–538. https://doi.org/10.1016/j.apsusc.2019.05.004.

[37] A.A. Mohammed, C. Chen, Z. Zhu, Low-cost, high-performance supercapacitor

based on activated carbon electrode materials derived from baobab fruit shells, J. Colloid Interface Sci. 538 (2019) 308–319. https://doi.org/10.1016/j.jcis.2018.11.103.

[38] G. Zhang, Y. Chen, Y. Chen, H. Guo, Activated biomass carbon made from bamboo as electrode material for supercapacitors, Mater. Res. Bull. 102 (2018) 391–398. https://doi.org/10.1016/j.materresbull.2018.03.006.

[39] L. Qiang, Z. Hu, Z. Li, Y. Yang, X. Wang, Y. Zhou, X. Zhang, W. Wang, Q. Wang, Buckwheat husk-derived hierarchical porous nitrogen-doped carbon materials for high-performance symmetric supercapacitor, J. Porous Mater. 26 (2019) 1217–1225. https://doi.org/10.1007/s10934-019-00723-z.

[40] L. Hu, H. Du, C. Liu, Y. Zhang, G. Yu, X. Zhang, C. Si, B. Li, H. Peng, Comparative Evaluation of the Efficient Conversion of Corn Husk Filament and Corn Husk Powder to Valuable Materials via a Sustainable and Clean Biorefinery Process, ACS Sustain. Chem. Eng. 7 (2019) 1327–1336. https://doi.org/10.1021/acssuschemeng.8b05017.

[41] J. Jakobsen, The maize frontier in rural South India: Exploring the everyday dynamics of the contemporary food regime, J. Agrar. Chang. 20 (2020) 137–162. https://doi.org/10.1111/joac.12337.

[42] B. Barl, C.G. Biliaderis, E.D. Murray, A.W. Macgregor, Combined chemical and enzymic treatments of corn husk lignocellulosics, J. Sci. Food Agric. 56 (1991) 195–214. https://doi.org/10.1002/jsfa.2740560209.

[43] C. Qin, S. Wang, Z. Wang, K. Ji, S. Wang, X. Zeng, X. Jiang, G. Liu, Hierarchical porous carbon derived from Gardenia jasminoides Ellis flowers for high performance supercapacitor, J. Energy Storage. 33 (2021) 102061. https://doi.org/10.1016/j.est.2020.102061.

[44] S. Song, F. Ma, G. Wu, D. Ma, W. Geng, J. Wan, Facile self-templating large scale preparation of biomass-derived 3D hierarchical porous carbon for advanced supercapacitors, J. Mater. Chem. A. 3 (2015) 18154–18162. https://doi.org/10.1039/c5ta04721h.

[45] G.A. Yakaboylu, C. Jiang, T. Yumak, J.W. Zondlo, J. Wang, E.M. Sabolsky, Engineered hierarchical porous carbons for supercapacitor applications through chemical pretreatment and activation of biomass precursors, Renew. Energy. 163 (2021) 276–287. https://doi.org/10.1016/j.renene.2020.08.092.

[46] Y. Li, D. Zhang, Y. Zhang, J. He, Y. Wang, K. Wang, Y. Xu, H. Li, Y. Wang, Biomass-derived microporous carbon with large micropore size for high-performance supercapacitors, J. Power Sources. 448 (2020) 227396. https://doi.org/10.1016/j.jpowsour.2019.227396.

[47] L. Guan, L. Pan, T. Peng, C. Gao, W. Zhao, Z. Yang, H. Hu, M. Wu, Synthesis of Biomass-Derived Nitrogen-Doped Porous Carbon Nanosheests for High-Performance Supercapacitors, ACS Sustain. Chem. Eng. 7 (2019) 8405–8412. https://doi.org/10.1021/acssuschemeng.9b00050.

[48] W. Fan, H. Zhang, H. Wang, X. Zhao, S. Sun, J. Shi, M. Huang, W. Liu, Y. Zheng, P. Li, Dual-doped hierarchical porous carbon derived from biomass for advanced supercapacitors and lithium ion batteries, RSC Adv. 9 (2019) 32382–32394. https://doi.org/10.1039/c9ra06914c.

[49] S. Yaglikci, Y. Gokce, E. Yagmur, Z. Aktas, The performance of sulphur doped

activated carbon supercapacitors prepared from waste tea, Environ. Technol. (United Kingdom). 41 (2020) 36–48. https://doi.org/10.1080/09593330.2019.1575480.

[50] T.R. Kumar, R.A. Senthil, Z. Pan, J. Pan, Y. Sun, A tubular-like porous carbon derived from waste American poplar fruit as advanced electrode material for high-performance supercapacitor, J. Energy Storage. 32 (2020) 101903. https://doi.org/10.1016/j.est.2020.101903.

SUMMARY AND CONCLUSIONS

In this chapter summary and conclusions of the current thesis work are presented. The scope for future work in order to expand in the field of research work has also been suggested.

7.1 Summary of the thesis work

We have successfully developed electrode materials with good electrochemical properties by following a low cost, and easy synthesis processes. Improved specific capacitance and cycling stability are achieved for the polyaniline-reduced graphene oxide composite materials. The overall summary of the thesis work is given in below table 7.1.

Table 7.1 Summary of the thesis work.

S. No.	Materials	Synthesis method	Specific capacitance	Cyclic stability (%)
1	Polyaniline/reduced graphene oxide (PRGO2)	*in-situ* polymerization followed by hydrothermal reduction	299 F/g at 0.5 A/g	88% for 2000 cycles
2	Polyaniline/N-doped reduced graphene oxide (PANI/N-rGO)	hydrothermal reduction followed by *in-situ* polymerization	322 F/g at 1 A/g	93% for 1000 cycles
3	NSA-Polyaniline/ S-doped reduced graphene oxide (SPANI/S-rGO10)	hydrothermal reduction followed by *in-situ* polymerization	348 F/g at 1 A/g	89% for 2500 cycles
4	CHPC-800	carbonization followed by chemical activation	133 F/g at 1 A/g	93.5% after 4500 cycles

7.2 Conclusions

The conclusions derived from the thesis work performed on PANI/rGO based composites and porous carbon electrode materials for supercapacitors are given below:

- The GO is successfully synthesized using a modified Hummer’s method. Various characterization studies (XRD, FTIR, Raman, and XPS) are conducted to confirm the GO formation.

- polyaniline-reduced graphene oxide composites (PRGO) were synthesized using *in-situ* polymerization followed by low-temperature hydrothermal treatment with different weight ratios of GO to Aniline (1 wt.% (1:100), 2 wt.% (1:50), 4 wt.% (1:25)).
- The XRD results revealed that the successful reduction of GO by hydrothermal treatment and PANI nanostructures were firmly settled on the surface of the graphene sheets and retained their crystal structures.
- Surface morphologies studies conducted by FESEM have shown that the formation of densely packed nanoclusters over the surface of graphene layers and higher weight ratio of GO (PRGO4) leads to more densely packed structures which restrict the surface area accessible for the electrolyte ions.
- From the FTIR and Raman studies, it is confirmed a strong interfacial interaction between graphene layers and PANI chains which facilitates high electron transport and enhances electrochemical properties of composite materials.
- XPS spectra of pristine PANI and PRGO2 composites having peaks corresponding to C1s, N 1s, O 1s, and Cl 2p. Further, the deconvoluted C1s spectra of PRGO2 showed the higher oxygen functionalities (O-C=O) present PRGO2 composite indicating the interaction of imine groups of PANI with the oxygen functional groups of GO in the composites.
- Further, we obtained a high electrical conductivity for PRGO2 (σ=4.81 S/cm) compared to PRGO1 (σ=1.33 S/cm), and PRGO4 (σ=3.83 S/cm), pristine rcGO (σ=0.22 S/cm) and pure PANI (σ=0.89 S/cm) samples. This is owing to the strong π-π stacking between the PANI nanostructures and graphene layers and better morphology of the PRGO2 composite.
- The CV curves of PANI, PRGO1, PRGO2, and PRGO4 composites are having two pairs of redox peaks with rectangular shape indicating the conversion of Leucoemeraldine base to Emeraldine salt and Emeraldine salt to Pernigraniline base forms of PANI by redox reaction. Higher area under the curve is observed for PRGO2 composite confirming the higher specific capacitance of the electrode materials.
- From the GCD studies, PRGO composite with 2 wt.% of GO based electrode material has delivered maximum specific capacitance of 299 F/g at a current density of 0.5 A/g. Besides, this composite has shown good rate capability and capacitance retention (88%) at a current density of 2 A/g after 2000 charge-discharge cycles. The

enhanced electrochemical properties of PRGO2 composite are owing to high interfacial contact due to the densely packed structure.

- A robust and simple chemical method is followed for the synthesis of PANI/N-rGO composite where N-rGO is used as a supportive network for the growth of PANI nanostructures using *in-situ* polymerization.
- N-doping is carried out by hydrothermal treatment where urea is used as reducing agent as well as an N source.
- N-doping into graphene network is confirmed by FTIR, Raman, and XPS studies. A new peak at 1290 cm^{-1} responsible for C-N stretching vibration, is observed from the FTIR spectra, a well-defined N 1s (399.5 eV) peak is also appeared along with the C 1s (285.5 eV) and O 1s (533.5 eV) peaks in the XPS survey spectrum of N-rGO, and higher value of I_D/I_G ratio from Raman studies elucidates doping of N atoms into graphene lattice by disrupting the sp2 bonds of carbon atoms.
- FESEM and BET studies revealed that the PANI/N-rGO possessed longer length interconnected PANI nanostructures, which result in a higher surface area (82.80 m^2/g) compared to PANI/rGO ((59.21 m^2/g) and PANI (26.62 m^2/g).
- FTIR studies revealed the presence of various functional groups corresponding to PANI in its conductive emeraldine form. The shift in the main peaks of benzenoid and quinonoid rings of PANI in PANI/N-rGO indicates the strong interfacial interaction of the polymer chain with the graphene network.
- From the Raman results, it is found that PANI/N-rGO is having high intensity peak at 573 cm^{-1} corresponding to the phenazine type or the existence of the crosslinking structure, indicating the formation of more crosslinking networks between PANI and N-rGO sheets. due to the presence of N atoms in N-rGO, which is also supported by the XPS results, where the higher concentration of azane-type N is observed for PANI/N-rGO composite compared to PANI/rGO and pristine PANI.
- Electrochemical properties evaluated in symmetrical supercapacitor configuration also have shown enhanced capacitive performance for PANI/N-rGO.
- From the GCD studies, a maximum specific capacitance of 322 F/g is achieved for PANI/N-rGO composite at 1 A/g which is higher than PANI/rGO and PANI.
- Further, PANI/N-rGO composite possessed high cycling stability (93%) over 1000 cycles, which is attributed to the higher specific surface area, existence of strong cross linking between PANI and N-rGO which facilitates better electron transport within the electrode material.

- Furthermore, flexible supercapacitors assembled by PANI/N-rGO composite electrodes have offered good flexibility over a wide range of bending angles (0 ^{o}C – ~170 ^{o}C).
- S-doping into graphene lattice is successfully carried out by following simple hydrothermal method where Na_2S is used as S source.
- Reduction of GO and S-doping is confirmed by performing XRD, FTIR, Raman, and XPS studies.
- The XPS survey spectra of S-rGO contain peaks related to S 2p in addition to C 1s and O 1s peaks confirming the successful doping of Sulphur spaces in the graphene network.
- A well-aligned grown sulfonic acid doped PANI nanostructures on S-rGO (SPANI/S-rGO) composites are prepared by following a simple *in-situ* polymerization method where NSA is used as a dopant for PANI.
- The effect of different wt.% of S-rGO (5%, 10%,15%, and 20%) on the structural, morphology, and electrochemical performance of SPANI/S-rGO composites is evaluated.
- From the XRD plots of SPANI/S-rGO composites, it is noticed that the intensity of diffraction peak at 25^{o} is increased with increasing concentration of S-rGO, indicating the successful incorporation of S-rGO nanosheets.
- FTIR studies conformed the sulfonic acid doping into PANI and the existence of PANI in its conductive emeraldine form. Further, we found an increase in the intensity ratio of I_Q/I_B with the increasing wt.% of S-rGO indicating the presence of high number of quinoid rings in the composite. The increase in quinoid rings in SPANI/S-rGO composites suggests the formation of a week charge transfer complex between SPANI and S-rGO layers during polymerization where aniline loses an electron to the S-rGO layers. Due to the formation of charge-transfer complex in PANI/S-rGO composite, S-rGO can also act as a dopant to the PANI which leads to increase in electrical conductivity, and hence, we observe an improved electrochemical performance.
- FESEM studies revealed the growth of well-aligned SPANI nanostructures on S-rGO sheets. For PANI/S-rGO10 (10 wt.% of S-rGO), growth is more prominent, indicating the better morphology of the composite. Further, it is also noticed that an increase in wt.% of S-rGO to 15% and 20% lead to overlapping of PANI nanostructures with S-rGO which restricts the electroactive surface area accessible

for electrolyte ions. The well-aligned nanostructures of SPANI/S-rGO10 composite could result in high contact area for the electrolyte ions to diffuse and enhance the charge transfer property of the material.

- Flexible electrodes are prepared to study the electrochemical properties of the composite material in a symmetrical configuration using Swagelok cell.
- The CV curves show that the SPANI, SPANI/S-rGO composites exhibited two pairs of redox peaks responsible for the transformation of PANI through its oxidation states.
- From the CV curves, it is found that with the incorporation of S-rGO in SPANI/S-rGO composites, area covered by the CV curved is increased which indicates the combined features of both PANI and S-rGO.
- From the GCD curves, SPANI/S-rGO10 composite electrode delivered a maximum specific capacitance of 348 F/g at a current density of 1 A/g in a symmetrical supercapacitor and it is able to retain 68% of its initial capacitance at a current density of 5 A/g whereas pure SPANI retained only 57% of its initial capacitance.
- Further, SPANI/S-rGO composite electrode possessed impressive cyclic stability of 89 % after 2500 cycles at a current density of 2 A/g.
- The enhanced performance of SPANI/S-rGO10 is attributed to the optimum loading of S-rGO in designing binary composite and well-aligned growth of SPANI nanostructures on S-rGO sheets. This offers strong interfacial interaction between SPANI nanostructures and S-rGO sheets thus lowering the charge transfer resistance (0.91Ω).
- Porous carbons are successfully synthesized from nature-abundant biowaste of corn husk via carbonization and chemical activation process.
- The activation temperature is optimized to improve the surface area and get a balance between the micro and mesopores.
- Surface morphology studies carried out by FESEM revealed the existence of high porosity in the CHPC-800 sample compared to CHPC-600 and CHPC-700.
- The N_2 adsorption-desorption studies revealed that CHPC-800 possessed a high specific surface area of 1583 m^2/g along with micro and mesoporosity.
- The FTIR and XPS results revealed the presence of surface oxygen functional groups attached to the carbon network which can improve the surface wettability of the electrodes.

- In a symmetrical supercapacitor, CHPC-800 electrode material has delivered a maximum specific capacitance of 133 F/g at a current density of 1 A/g.
- Further, CHPC-800 also showed good cyclic stability, with 93% of capacitance retention after 4500 charge-discharge cycles at a current density of 5 A/g. The improved performance of CHPC-800 is attributed to the combination of both high surface area and porous structure of the material.
- Further, a LED was successfully driven with the series-connected SSC device made by CHPC-800 electrodes.

7.3 Scope for the future work

In the present work, some of the important features of PANI/rGO based composite materials have been addressed via a detailed study of their synthesis, structural, and electrochemical properties for supercapacitor electrodes. Other 2D materials such as MXenes, Metal chalcogenides, etc., can be explored for the preparation of binary and ternary composites to further improve the performance of supercapacitors. Further, natural abundant porous carbons are also developed and explored their properties for supercapacitor. These porous carbons can also be used as a supporting network to grow PANI nanostructures by developing (PANI-porous carbon) composites and studying their electrochemical properties for supercapacitors.

Publications in International Journals (SCI):

1. **Nagaraju Macherla**, Kuldeep Singh, M.S. Santosh, Kusum Kumari, and Ram Gopal Reddy Lekkala, "Heat Assisted Facile Synthesis of Nanostructured Polyaniline / Reduced Crumbled Graphene Oxide as a High-Performance Flexible Electrode Material for Supercapacitors", Colloids Surfaces A: Physicochem. Eng. Asp. 612, (2021), 125982. https://doi.org/10.1016/j.colsurfa.2020.125982.
2. **Nagaraju Macherla**, Kuldeep Singh, Kusum Kumari, and Ram Gopal Reddy Lekkala, "A robust approach for designing N-doped reduced graphene oxide/polyaniline nanocomposite-based electrodes for efficient flexible supercapacitors." Polym Adv Technol., (2022), 1- 16. doi:10.1002/pat.5670.
3. **Nagaraju Macherla**, Kuldeep Singh, Nerella Manjula, Kusum Kumari, and Ram Gopal Reddy Lekkala, "Improved performance of flexible supercapacitor using naphthalene sulfonic acid-doped polyaniline/sulfur-doped reduced graphene oxide nanocomposites", Int J Energy Res., 46, (2022), 6529- 6542. https://doi.org/10.1002/er.7589
4. **Nagaraju Macherla**, Kuldeep Singh, Nerella Manjula, Kusum Kumari, and Ram Gopal Reddy Lekkala, "Cornhusk biowaste derived porous carbon as a high-performance electrode material for symmetric supercapacitor", Submitted to Carbon Letters**, 2022** (Under review)

PAPERS PRESENTED AT NATIONAL AND INTERNATIONAL CONFERENCES

1. **Nagaraju Macherla**, Ram Gopal Reddy Lekkala, Kuldeep Singh, and Kusum Kumari, "Electrochemical analysis of polyaniline-graphene oxide composites for high-performance supercapacitors", in DAE Solid State Physics Symposium (DAE-SSPS), held at IIT Jodhpur, Rajasthan, 18th – 22nd December 2019.
2. **Nagaraju Macherla,** Ram Gopal Reddy Lekkala, Kuldeep Singh, and Kusum Kumari, "Conversion of corn husk to high surface area porous carbon for high performance supercapacitor", in International Conference on Energy & Advanced Materials Organized by Department of Physics and Materials Science & Engineering Jaypee Institute of Information Technology, Noida, India, during 21th -23th October, 2021.
3. **Nagaraju Macherla**, Nerella Manjula, Kuldeep Singh, Kusum Kumari, and Ram Gopal Reddy Lekkala, "A Facile synthesized S-doped reduced graphene oxide-polyaniline nanocomposite for energy storage application", in Virtual International Conference on Functional Materials and its Application Aspects (ICFMAA-2021), Organized by Department of Physics, Institute of Science and Humanities, Saveetha School of Engineering, Chennai, India during 29th -30th October 2021.
4. **Nagaraju Macherla**, Nerella Manjula, Kusum Kumari, and Ram Gopal Reddy Lekkala, "Effect of heteroatom doping on the structural and electrochemical properties of reduced graphene oxide for energy storage", in International Conference on Advances in Chemical and Materials Sciences (ACMS 2022), Organized by Indian Institute of Chemical Engineers, Headquarters, Kolkata, India, during 14th-16th April 2022.